General Disclaimer

One or more of the Following Statements may affect this Document

- This document has been reproduced from the best copy furnished by the organizational source. It is being released in the interest of making available as much information as possible.

- This document may contain data, which exceeds the sheet parameters. It was furnished in this condition by the organizational source and is the best copy available.

- This document may contain tone-on-tone or color graphs, charts and/or pictures, which have been reproduced in black and white.

- This document is paginated as submitted by the original source.

- Portions of this document are not fully legible due to the historical nature of some of the material. However, it is the best reproduction available from the original submission.

Produced by the NASA Center for Aerospace Information (CASI)

(NASA-TM-86122) VIBRATIONAL AND ROTATIONAL EXCITATION OF CO IN COMETS. PART 1: NON-EQUILIBRIUM CALCULATIONS. PART 2: RESULTS OF THE CALCULATION FOR STANDARD BRIGHT COMET, COMET IRAS-ARAKI-ALCOCK AND N84-26545
Unclas
G3/91 19485

NASA

Technical Memorandum 86122

VIBRATIONAL AND ROTATIONAL EXCITATION OF CO IN COMETS:

PART I. NON-EQUILIBRIUM CALCULATIONS

PART II. RESULTS OF THE CALCULATION FOR STANDARD BRIGHT COMET, COMET IRAS-ARAKI-ALCOCK, AND COMET HALLEY

G. Chin
H. A. Weaver

JUL 1984
RECEIVED
NASA STI FACILITY
ACCESS DEPT.

MAY 1984

National Aeronautics and
Space Administration

Goddard Space Flight Center
Greenbelt, Maryland 20771

VIBRATIONAL AND ROTATIONAL EXCITATION OF CO IN COMETS:

PART I. NON-EQUILIBRIUM CALCULATIONS

PART II. RESULTS OF THE CALCULATION FOR STANDARD BRIGHT COMET, COMET IRAS-ARAKI-ALCOCK, AND COMET HALLEY

by

G. Chin and H. A. Weaver[1,2]

Laboratory for Extraterrestrial Physics

Infrared and Radio Astronomy Branch

NASA/Goddard Space Flight Center

Part I to be published in Astrophysical Journal, 15 October 1984, main journal.

[1]NAS/NRC Resident Research Associate at the Goddard Space Flight Center

[2]Visiting Astronomer, Kitt Peak National Observatory, which is operated by the Association of Universities for Research in Astronomy under contract with the National Science Foundation.

PART I. NON-EQUILIBRIUM CALCULATIONS

ABSTRACT

The vibrational and rotational excitation of the CO molecule in cometary comae has been investigated using a model which includes IR vibrational pumping by the solar flux, vibrational and rotational radiative decay, and collisional coupling among rotational states. Steady-state is not assumed in solving the rate equations. The evolution of a shell of CO gas is followed as it expands from the nucleus into the outer coma. Collisional effects are treated using a kinetic temperature profile derived from recent theoretical work on the coma energy balance. The kinetic temperature is assumed to be extremely cold in the inner coma, and this has important consequences for the CO excitation. If optical depth effects are ignored, only low J transitions will be significantly excited in comets which are observed at high spatial resolution. Ground-based observations of CO ro-vibrational and rotational transitions will be extremely difficult due to lack of sensitivity and/or terrestrial absorption, but CO should be detectable from a large comet with favorable observing geometry, if the CO is a parent molecule present at the 10% level (or greater) relative to H_2O. Observations using cooled, space-borne instruments should be capable of detecting CO emission from even moderately bright comets.

I. INTRODUCTION

Although strong circumstantial evidence indicates that H_2O ice is the dominant volatile constituent of cometary nuclei (Weaver et al. 1981, Delsemme 1982, Campins, Rieke, and Lebofsky 1983), ultraviolet (UV) observations of atomic carbon in cometary comae (summarized in Feldman 1982) clearly show that carbon-bearing compounds must comprise a significant fraction ($\gtrsim$10%) of the volatiles. CO is one likely source of this carbon.

Observations have demonstrated that CO is present in some cometary comae although the CO abundance can not always account for the amount of atomic carbon observed. Feldman and Brune (1976) observed several bands of the CO fourth positive group ($A^1\pi$-$X^1\Sigma^+$) in the UV spectrum of comet West (1976 VI). Feldman (1978) has analyzed these results and found that the CO production rate in this comet was $\sim$30% of the H_2O rate, and that the observed atomic carbon was derived from the CO. Fourth positive group emission was tentatively identified in International Ultraviolet Explorer (IUE) spectra of comet Bradfield (1979 X) (Feldman et al. 1980). A'Hearn and Feldman (1980) demonstrated that the CO production rate (assuming CO to be a "parent" molecule) could be no more than $\sim$2% of the H_2O production rate in this comet. On the other hand, Weaver (1981) argued that atomic carbon was relatively abundant in comet Bradfield (1979 X) (the production rate of the carbon parent was $\sim$10% of the H_2O production rate), and could not be derived from either CO or CO_2. Cosmovici et al. (1982) recently claimed to have detected a triplet system of CO ($d^3\Delta$-$a^3\pi$) in the visible spectrum of comet Bradfield (1980 XV). Thus, CO is an important constituent of at least some cometary nuclei, even though it may not be the ultimate source of atomic carbon in all comets.

Feldman (1983) has suggested that the relative abundance of CO may be one of the few fundamental characteristics which distinguish one comet from another. Such differences could provide clues to determine the formation regions of comets (Yamamoto, Nakagawa, and Fukui 1983). We have, therefore, investigated the vibrational and rotational excitation of the CO molecule in cometary comae. The IR and rotational transitions of CO are potentially important probes of the density, kinetic temperature, and the outflow velocities of cometary parent molecules in the inner coma.

Two recent papers have also addressed the problem of vibrational and rotational excitation of CO in comets. Krishna Swamy (1983) has apparently neglected the most important vibrational excitation mechanism, direct radiative pumping by absorption of solar IR radiation. Crovisier and Le Bourlot (1983) have considered IR pumping but have concentrated on calculations in the outer coma where fluorescence equilibrium prevails, and they only briefly discussed the case of an isothermal inner coma where collisional effects are important. They also pointed out that the time constants for the CO problem are long enough that steady state should not be assumed at every point in the coma in solving the rate equations.

In our approach to the CO excitation calculations, we have explicitly solved the time-dependent problem, i.e., we have followed the evolution of a shell of CO gas as it expands radially outward from the nucleus. In this manner, we have included the inner coma where collisional effects dominate the rotational excitation, the outer coma where radiative equilibrium dominates, and also the intermediate region from 10^3 to 10^5 km from the nucleus where neither collisional nor radiative equilibrium is attained. In addition, we have considered a non-isothermal temperature profile for the inner coma. Details of the model calculations will be given in sec. II. From the model, we

have determined conditions under which the CO millimeter and IR transitions should be observable. Recently we have attempted to observe some of the 4.7 μm and $J=1\rightarrow0$ CO transitions in comet IRAS-Araki-Alcock (1983d).

II. THE MODEL

Before the model calculations can be performed, certain physical conditions in the comet must be defined. The kinetic temperature of the gas directly above the nucleus determines one of the initial conditions of the excitation model. Thermodynamic considerations indicate that the temperature of a spherical, isothermal nucleus composed principally of H_2O ice is $T\sim187K$, for a comet at a heliocentric distance of 1 AU (Houpis and Mendis 1981). We adopt this value for the initial kinetic temperature of the gas leaving the nucleus. To calculate the effects of collisional excitation, the kinetic temperature profile of the inner coma must also be specified. Marconi and Mendis (1982) have demonstrated that, after release from the nucleus, the coma gas is rapidly cooled to extremely low temperatures ($\sim5K$ at a distance of ~50 km from the nucleus), followed by gradual photolytic heating beyond ~100 km. A figure in Marconi and Mendis (1982) is used to derive a polynomial fit to their calculated kinetic temperature profile and this fit is the profile we use in our calculations. Gases subliming from the surface of the nucleus are assumed to flow radially outward with a velocity of 0.8 km s^{-1} (Weaver and Mumma 1984). Densities are calculated using a Haser model (Festou 1981), with lifetimes taken from Huebner and Carpenter (1979). H_2O and CO are the only gaseous species considered, with H_2O being dominant. As a result, collisional effects are confined to $CO-H_2O$ interactions. The H_2O production rates are taken from observations of comets, but these are generally consistent with

values derived from thermodynamic models. The CO production rate is taken to be 10% of the H_2O production rate, but observed rates (or upper limits) are used for specific comets, whenever this is possible. We assume that the radiation field in the coma is determined solely by the solar field, with further details given below.

Only the CO v=0 and v=1 levels of the ground electronic state ($^1\Sigma^+$) are considered in the present analysis (see discussion in Crovisier and Le Bourlot 1983). Within each vibrational level we use 21 rotational states since the results of the present work and of Crovisier and Le Bourlot (1983) show no need for including rotational states higher than J=20. A Dunham expansion with coefficients from Kildal, Eng, and Ross (1974) is used to calculate the energies of the states, and the allowed transition frequencies are derived using these energies.

The excitation of an expanding shell of CO gas is determined primarily by radiative pumping due to absorption of solar photons in ro-vibrational transitions of the IR (1,0) band, radiative relaxation in the ro-vibrational lines of the IR (1,0) band and in the rotational lines of each vibrational level, and collisional coupling among the rotational states of each vibrational level. Collisional coupling of the vibrational levels is negligible throughout the coma (Weaver and Mumma 1984). It is easily demonstrated that stimulated emission in the ro-vibrational and rotational lines can be neglected, and that stimulated absorption in the rotational lines can also be omitted. The optical depths of some low J lines (in both the IR (1,0) band and the rotational lines) may exceed unity close to the nucleus ($r \lesssim 1000$ km). However, considering the increased complexity of a full radiative transfer treatment, we have assumed that all radiative transitions

ORIGINAL PAGE IS
OF POOR QUALITY

are optically thin. The problem of radiative transfer is, therefore, completely decoupled from the rate equations.

Thus, the rate equations for our model are given by:

$$dn_J^v/dt = A^{1,0}_{J+1,J}n^1_{J+1} + A^{1,0}_{J-1,J}n^1_{J-1} + A^{0,0}_{J+1,J}n^0_{J+1} + \sum_k C_{k,J}n^0_J - [B^{0,1}_{J,J+1}\rho + B^{0,1}_{J,J-1}\rho + A^{0,0}_{J,J-1} + \sum_k C_{J,k}]n^0_J$$

for v=0, and (1)

$$dn_J^v/dt = B^{0,1}_{J+1,J}\rho n^0_{J+1} + B^{0,1}_{J-1,J}\rho n^0_{J-1} + A^{1,1}_{J+1,J}n^1_{J+1} + \sum_k C_{k,J}n^1_k - [A^{1,0}_{J,J+1} + A^{1,0}_{J,J-1} + A^{1,1}_{J,J-1} + \sum_k C_{J,k}]n^1_J$$

for v=1.

The rate equations given by (1) have the vibrational states indicated by superscripts and the rotational states indicated by subscripts. When two superscripts or subscripts are used, the first refers to the initial state and the second to the final state. The vibrational index, v, can take values v=0 and v=1, while the rotational index, J, runs from J=0 to J=20. The unknown quantities are the n_J^v's which are the <u>fractional populations</u> of the rotational states of CO.

Einstein A-coefficients for the ro-vibrational transitions (Nuth and Donn 1981) are given by:

$$\text{P branch: } A^{1,0}_{J,J+1} = (64\pi^4/3h)(TM)^2\omega^3(J+1)/(2J+1) = 3.39\times10^{-9}\omega^3(J+1)/(2J+1) \quad (2)$$

$$\text{R branch: } A^{1,0}_{J,J-1} = 3.39\times10^{-9}\omega^3\, J/(2J+1),$$

where the transition frequencies (ω) are given in cm^{-1}, and the transition

moment (TM) is equal to 1.04×10^{-19} esu. Einstein B-coefficients are calculated in the usual way from the A-coefficients. We have expressed the radiative absorption rate constants in the IR (1,0) band as:

$$\begin{aligned} \text{P branch: } B^{0,1}_{J,J-1}\rho &= (F_{\odot}/8\pi c)\omega^{-2}(2J-1)/(2J+1)A^{1,0}_{J-1,J} \\ &= 33.2\omega^{-2}(2J-1)/(2J+1)A^{1,0}_{J-1,J} \qquad (3) \\ \text{R branch: } B^{0,1}_{J,J+1}\rho &= 33.2\omega^{-2}(2J+3)/(2J+1)A^{1,0}_{J+1,J}. \end{aligned}$$

The absorption rate constant in the IR (1,0) band is calculated assuming a constant solar flux over the (1,0) band of $F_{\odot}=2.5 \times 10^{13}$ photons $cm^{-2}s^{-1}/cm^{-1}$ at 1 AU (Labs and Neckel 1968).

Rotational Einstein A's are given by (Somerville 1977):

$$\begin{aligned} A^{0,0}_{J,J-1} &= (64\pi^4/3hc^3)\nu^3\mu_0^2 J/(2J+1) \\ &= 1.164 \times 10^{-20}\nu^3\mu_0^2 J/(2J+1) \qquad (4) \\ A^{1,1}_{J,J-1} &= 1.164 \times 10^{-20}\nu^3\mu_1^2 J/(2J+1), \end{aligned}$$

with the transition frequencies (ν) in MHz, and with dipole moments (μ_0=0.1098 and μ_1=0.0848 Debyes) derived from the constants given in the work of Kirschner <u>et al</u>. (1977).

The collision rate constants have the following form:

$$C_{J,J'} = n_{H2O}\sigma_{J,J'}\bar{v}, \qquad (5)$$

where n_{H2O} is the H_2O number density (cm^{-3}), $\sigma_{J,J'}$ is the cross section (cm^2) for the transition from the J-th to the J'-th level of CO produced by

collisions with H_2O, and $\bar{v}$ is the average relative speed (cm s^{-1}) of the H_2O and CO molecules.

The collision cross sections deserve some discussion because of the difficulties in estimating their magnitude. Crovisier and Le Bourlot (1983) point out that both experimental and theoretical data on this problem are scarce. In their calculations, they assume a cross section of $\sigma=2\times10^{-15}$ cm^2 (presumably this does not refer to a transition from one specific rotational state to another state, but to the <u>total</u> rate out of one rotational state), which they call the "geometrical" cross section. However, we calculate the geometrical cross section to be about an order of magnitude smaller than this (from Herzberg 1945, the separation C-O in CO is 1.13 Å while the separation H-O in H_2O is 0.958 Å).

A better estimate for the collision cross section than the geometrical value can be obtained by considering the data of Varghese and Hanson (1981), who have investigated the broadening of CO lines in the IR (1,0) band by collisions with H_2O. Using the theory outlined in Draegert and Williams (1968), we can use these data to derive a <u>total</u> cross section for the de-excitation and excitation of a CO rotational state by collisions with H_2O:

$$\sigma_{tot} = 1.32\times10^{-14} \quad cm^2. \qquad (6)$$

Strictly speaking this cross section is valid only at room temperature (~294-298K), but these cross sections generally show little variation with temperature (S. Green, private communication). We have used this value throughout the coma.

In addition, we must also know how collisions connect individual states. We assume that the cross section is a function of ΔJ only, with the explicit

dependence given by Table 1. This dependence on ΔJ is somewhat arbitrary, but was suggested to us by S. Green (private communication), based on his experience with other molecules. By experimentation, we have found that our model is rather insensitive to the explicit ΔJ dependence of the cross sections, as long as the total cross section remains fixed (compare this with results of H_2-CO collisional excitation in Goldsmith 1972, and McKee et al. 1982). We force the total cross section to always equal 1.32×10^{-14} cm^2. Excitation cross sections are related to de-excitation cross sections by the detailed balance condition (cf., Goldsmith 1972).

To complete the expression for the collisional rate constants, the relative thermal velocities ($\bar{v}$) are calculated assuming a Maxwellian distribution of velocities (which is incorrect, but we neglect this fact) and the kinetic temperature profile of Marconi and Mendis (1982). When the collisional rates are larger than the radiative rates, then the detailed balance condition will ensure that the rotational excitation temperature is equal to the local kinetic temperature, i.e., rotational LTE will be satisfied.

With all the necessary physical parameters of the comet model defined, equations (1) lead to 42 coupled, linear differential equations (LDEs) with only the collisional rate constants explicit functions of time. Since we assume that a shell of CO gas expands uniformly once released from the nucleus, we have $r=vt$, where r is the distance from the nucleus, v is the expansion velocity (0.8 km s^{-1}), and t is the time. Therefore, a solution of our coupled LDEs will give the excitation of CO as a function of time, which is easily translated to distance from the nucleus.

An IMSL (International Mathematical and Statistical Libraries) subroutine, DGEAR, which employs a Gear method (Gear 1971) for "stiff" equations, was used in solving the system of coupled LDEs given in (1). A system is said to be

"stiff" when the time constants in the problem are of very different magnitudes. Since the comet model involves rate constants ranging from $\sim 10^2$ s^{-1} (collision rate constants near the nucleus) to $\sim 10^{-8}$ s^{-1} (rotational Einstein A for the J=1→0 transition), this numerical technique is clearly necessary. Other techniques for solving LDEs, such as Runge-Kutta methods, were attempted on equations (1), but with little success.

The initial conditions for equations (1) are obtained by setting $dn_J^v/dt=0$ at the surface of the nucleus, and solving the resultant set of simultaneous linear equations. The density and kinetic temperature are assumed to be values appropriate for r=2.5 km. Of the 42 equations of the homogeneous system, only 41 are independent, so we replace one of the equations by the normalization condition:

$$\sum_v \sum_J n_J^v = 1. \qquad (7)$$

The 42 linear equations are then solved by use of an IMSL routine LEQT2F.

With the initial conditions as input, the DGEAR package attempts to integrate the coupled LDEs in time. As the program steps into different regions of the coma (or, equivalently, steps forward in time), rate constants are updated to take into account the density dilution due to expansion and lifetime effects, as well as the changing kinetic temperature. The DGEAR package automatically takes as small a step as necessary in order to give consistent results in adjacent steps. The solution consists of a set of relative populations for each energy level throughout the coma. We generate output on a logarithmic scale, using 10 points/decade (in km space) ranging from 10 km to 10^5 km. The program was run on a Digital Equipment Corporation VAX 11/780, and a complete solution takes $\sim$12 hours of cpu time.

The relative fractional populations are used to calculate volume emission rates using:

$$j^{v,v'}_{J,J'}(r) = n^{v}_{J}(r) A^{v,v'}_{J,J'} n_{CO}(r)/(4\pi), \qquad (8)$$

where $j^{v,v'}_{J,J'}(r)$ is the volume emission rate (photons cm^{-3} s^{-1} sr^{-1}) for the transition from initial state J to final state J' at the position r, $n_{CO}(r)$ is the total number density of CO molecules at position r, and v and v' are the initial and final vibrational levels respectively. Emission rates for the IR (1,0) band are calculated using v=1 and v'=0, while rotational transitions are calculated using v=v'=0.

The surface (column) brightness is calculated by integrating $j^{v,v'}_{J,J'}(r)$ along a given line of sight. This integration is done numerically using a path length that extends over 12 decades (in cm space; from 10^{0} cm to 10^{12} cm), employing 18 points/decade. Since the line of sight integration requires volume emission rates for many more points than are output from our model, we use a logarithmic interpolation procedure to fill in between the calculated points. For comparison with observations, we average the surface brightness over the field of view (FOV) of the instrument.

III. RESULTS AND DISCUSSION

Calculations have been performed using a variety of model input parameters. Our standard "bright" comet has an H_2O production rate of $Q_{H2O}=2\times10^{29}$ mol s^{-1} and a CO production rate of $Q_{CO}=2\times10^{28}$ mol s^{-1}. Since the Marconi and Mendis kinetic temperature profile is strictly valid only at R (heliocentric distance) = 1 AU, we have concentrated on calculations for

comets at or near this value. However, in order to gauge the effects of fluorescent pumping, we have varied the solar flux to approximate the conditions of a comet at R=2 AU and R=0.5 AU (production rates and other parameters remain identical to their values at R=1 AU). Using measured H_2O production rates and upper limits on the CO production rate (Feldman, private communication), we have also considered the case of comet IRAS-Araki-Alcock (1983d), a comet which passed very close to the earth (minimum distance = 0.032 AU) in the spring of 1983. For the week during which comet 1983d was observable from the northern hemisphere, its heliocentric distance was nearly constant with R=1 AU. Finally, we have considered three optimum viewing aspects during the apparition of comet Halley in 1985-1986. The complete set of model results can be found in Chin and Weaver (1984).

Here, we concentrate on the most important effects which determine the excitation of CO in a cometary coma, and compare the non-equlibrium calculations with those assuming steady-state at each point in the coma. The rotational excitation of the v=0 and v=1 levels are examined in detail as a function of distance from the nucleus. By neglecting the rotational structure we also elucidate several inportant points concerning the vibrational excitation. Finally, we average our results over different fields of view to determine which unique aspects of the non-equilibrium model would be observable.

Figure 1 shows typical results from the non-equilibrium model (hereafter referred to as the DGEAR model) for the standard bright comet. A single contour in Figure 1 represents a fixed relative population. The contour levels are given in logarithmic units so that, for example, the curve labeled -1.0 represents a relative population of 10%. The vertical scale is the distance from the nucleus, while the solid and dotted vertical lines represent

the J values for the various energy levels. The regions between the vertical lines have no physical significance. Similarly, Figure 2 gives the contour plot for the excitation temperature, T_{ex}, calculated between adjacent rotational states within a vibrational level ($T_{ex} \equiv (E^v_{J-1} - E^v_J)/k/\ln[(n^v_J/n^v_{J-1})(2J-1)/(2J+1)]$), where E is the energy of the state. Relative populations and excitation temperatures are plotted for both the v=0 and v=1 levels. The results are shown in this way because the contour plot is a convenient way to present data obtained for <u>all</u> states simultaneously.

Several important points are apparent upon examination of the contour plots. In general, the results of the calculations behave in the expected manner. For $r<10^3$ km, the rotational states are maintained in an extremely cold distribution; i.e., only the lower J states are substantially populated. In this region, the H_2O density is high and the rotational excitation temperature is expected to follow, at least approximately, the local kinetic temperature profile (however, see discussion below). In the outer coma ($r \sim 10^5$ km) the rotational distribution is spread over many states as the molecules approach fluorescence equilibrium. For practical purposes, a fluorescence equilibrium distribution can be assumed whenever $r>10^5$ km. The region between 10^3 and 10^5 km from the nucleus is a transition region in which radiative effects begin to take over from collisional effects.

Figures 3 and 4 illustrate more clearly the behavior we have outlined. These show the fractional populations for the J=0 rotational state of the v=0 and v=1 vibrational levels, respectively. The results for the DGEAR model output, a single cut along the J=0 line in Figure 1, and for a homogeneous solution, which assumes steady-state throughout the coma, are plotted together in Figures 3 and 4. The solid curve represents the fractional population if

local thermodynamic equilibrium (LTE) is achieved everywhere. In general, the fractional population of the v=0 level follows an LTE distribution in the inner coma as can be seen in Figure 3. Both the DGEAR and homogeneous model results closely follow the solid curve for $r<10^3$ km. However, as Figure 4 shows, rotational LTE is never achieved anywhere in the coma for the J=0, v=1 state. In fact, rotational LTE is not achieved anywhere in the coma for any rotational state in the v=1 level. We will discuss this point in more detail when we examine vibrational excitation later.

We also see from Figure 3 that for the v=0 level the DGEAR result departs from LTE at a much smaller radius ($r\sim250$ km) than does the homogeneous solution ($r\sim4000$ km). This is to be expected for several reasons. First, the H_2O density is decreasing at increasing distances from the nucleus, implying that the collisional rate constants, which determine the equilibration time, are also decreasing. In addition, the kinetic temperature profile changes dramatically in this region of the coma, reaching a minimum at ~50 km but heating up at larger radii. Since the collisional rate constants are proportional to the square root of the temperature ($C_{J,J'}\propto\bar{v}$ and $\bar{v}\propto T^{1/2}$), the rate constants will also exhibit a fairly large variation. This combination of small and rapidly changing rate contants means that the DGEAR solution cannot adjust to the changing kinetic temperature and, thus, lags behind the homogeneous solution, which assumes that steady-state has been achieved. In effect, the DGEAR solution retains a "memory" of the coldest portion of the coma, even as the coma temperature increases. The populations in the DGEAR solution change in a smoother fashion than the homogeneous result, especially in the intermediate region (10^3-10^4 km) when the homogeneous solution continues to adhere to LTE.

A further consequence of the smooth departure of the DGEAR solution from an LTE distribution is illustrated in Figure 5, which shows the excitation temperature for the J=1→0 transition in the v=0 vibrational level. Again we plot a DGEAR solution, a homogeneous solution, and a solid curve which represents the assumed kinetic temperature profile. The homogeneous solution shows an excitation temperature which remains thermalized to $\sim 10^4$ km, as is expected by comparing the collisional rate constants with the rotational Einstein A-coefficients (the disequilibrium distance in Weaver and Mumma 1984). However, the DGEAR solution departs from the kinetic temperature at a much smaller distance from the nucleus ($r \sim 700$ km) and becomes highly suprathermal, even inverted, in the transition region. Once again, this is a consequence of the "relaxation" required by the DGEAR model as the distribution evolves from LTE to fluorescence equilibrium. While the J=1→0 transition becomes suprathermal or inverted, all other transitions depart from LTE by becoming subthermal for the DGEAR solution.

A DGEAR solution using an isothermal (T=200K) temperature profile with the physical parameters of the standard bright comet does not show any temperature inversions in the transition region. This result is expected since the fractional populations of a 200K and fluorescence equilibrium distribution do not differ greatly; essentially no "relaxation" is necessary to connect the thermalized inner coma to the radiatively determined outer coma. It is the combination of a rapidly changing temperature profile and the use of the DGEAR method which results in the large deviations from thermalized populations and excitation temperatures.

Temperature inversions occur for several rotational states in both the v=0 and v=1 levels when other model parameters are used (see results in Chin and Weaver 1984). Since the rotational Einstein A's increase as J^3, there is a

tendency to form a bottleneck in the lower J levels, which have low decay rates (especially in CO which has a small dipole moment). Inversion will result if no competitive excitation mechanism, such as collisional excitation or radiative pumping, is strong enough to distribute the rotational population among a number of J levels. For example, in the case of comets with low gas production rates or at large heliocentric distances, the lower J states in CO can easily become suprathermal or inverted.

No appreciable amplification is expected from the inverted regions in the coma. An upper limit to the expected gain is <0.01% in our bright comet model. Indeed, we can continue to assume that the coma is optically thin. The excitation problem remains decoupled from the radiative transfer problem and the emergent radiation from the coma can be calculated in the usual manner (i.e., use equation 8).

The relative populations of the upper and lower (v=1 and v=0) vibrational levels are determined only by the solar flux (collisional excitation is neglible between vibrational levels, as discussed earlier). If we ignore the rotational structure for the moment, statistical equilibrium gives the following steady-state vibrational distribution:

$$n^1/n^0 = B\rho/A, \qquad (9)$$

where A and B represent the band values for the Einstein A and B coefficients and ρ is the density of the solar radiation field. This solution represents a system which is in equilibrium with the solar radiation field and fixes the ratio, n^1/n^0, at 7.28×10^{-6} when R=1 AU. The sun at a distance of 1 AU has an "equivalent" blackbody temperature of 261K at $\sim$4.7 μm, and that is the vibrational excitation temperature given by equation (9). The output of our

model is consistent with this value and forms an important check on the correctness of the calculations.

The explicit form for vibrational excitation as a function of time is given by (see the Appendix):

$$n^1/n^0 = B\rho/A + R_0 e^{-At}, \qquad (10)$$

where R_0 is a constant determined by the initial conditions. We see that the steady-state vibrational distribution is achieved very rapidly. The time constant for equilibration is 1/A (or 0.029 s), not $1/B\rho$ (or 4.14×10^3 s), as might be expected. For $t \gg 1/A$, equation (10) gives the steady-state value.

It is illustrative to examine the case when only the lower state is initially populated ($n^1/n^0=0$ at $t=0$) and for $t \ll 1/A$. Then equation (10) reduces to $n^1/n^0=B\rho t$, and the vibrational excitation is determined initially only by the solar pump rate constant ($B\rho$). However, once some population is achieved in the upper level, radiative decay quickly determines the equilibrium value. This is due to the fact that since the radiative decay rate constant is so large compared to the pump rate constant, the equilibrium value must be very small (i.e., $B\rho/A \ll 1$).

Since the relative vibrational populations reach equilibrium almost instantly after release from the nucleus, the <u>band</u> excitation factor, or g_{band}, is fixed at a value of 2.4×10^{-4} s^{-1} throughout the entire coma for R=1 AU.

The intensities of individual transitions within the IR (1,0) band are determined by the rotational distribution of the v=1 level. As discussed earlier, the v=1 level is never in rotational LTE anywhere in the coma. Figure 4 shows the fractional population of the J=0, v=1 state for the DGEAR

solution, the homogeneous solution, and the LTE distribution. Both the DGEAR and homogeneous solutions give similiar results in the inner coma, an essentially flat distribution which is depressed by a factor of 2.5 - 3 from the peak of the LTE distribution at $r \sim 100$ km. Figure 6 shows the excitation temperature for the $J=1 \rightarrow 0$ $v=1$ transition for the DGEAR and homogeneous models, as well as the assumed kinetic temperature profile. Departure from the kinetic temperature profile is most pronounced at $r \sim 100$ km, and both the DGEAR and homogeneous solutions give similiar suprathermal results throughout the inner coma.

By examining equations (1) separately for the $v=1$ and $v=0$ cases, we can understand why LTE is maintained in the $v=0$ level at the same time LTE is violated in the $v=1$ level. It is important to recognize the difference between the rate constants and the rates in equations (1). The rate constants are the B_ρ's, A's, and $C_{J,J'}$'s which multiply the fractional populations. The rates are the products of the rate constants and the fractional populations. In order to determine the dominant excitation processes for each vibrational level, it is necessary to determine the dominant <u>rates</u> in (1).

Although the collisional rate constants can be rather large (~ 50 s^{-1} at $r=10$ km) with respect to $B^{0,1}{}_\rho$ ($\sim 10^{-4}$ s^{-1}) and $A^{1,0}$ ($\sim 10-33$ s^{-1}) in the inner coma, for the $v=1$ states the collisional <u>rates</u> ($\Sigma C_{J,J'} n^1$) are much smaller ($\sim 10^{-5}$ s^{-1}) and must be compared to $B^{0,1}{}_\rho n^0$ ($\sim 10^{-5}$ s^{-1}) and $A^{1,0} n^1$ ($\sim 10^{-5}$ s^{-1}). We see, therefore, that qualitatively the collisional and radiative rates are about equal in the $v=1$ level. When the collisional rates decrease, for example when the kinetic temperature or the H_2O density decreases, the radiative rates dominate. The largest departures from rotational LTE in the $v=1$ level occur in the coldest regions of the inner coma. On the other hand, in the $v=0$ level rotational LTE is maintained within the inner coma.

The usual formula for the g-factor can be derived from equations (1) by assuming that radiative rates dominate the excitation. If we neglect all collisional and rotational radiative decay terms, and assume steady-state, we get:

$$n_J^1 = [B_{J+1,J}^{0,1}\rho n_{J+1}^0 + B_{J-1J}^{0,1}\rho n_{J-1}^0]/(A_{J,J+1}^{1,0} + A_{J,J-1}^{1,0}). \qquad (11)$$

The g-factor is obtained simply by multiplying (11) by the appropriate radiative decay rate. For example, g_{RO} is given by (with the transitions properly identified):

$$g_{RO} = [(B\rho)_{RO}n_0^0 + (B\rho)_{P2}n_2^0][A_{RO}/(A_{RO}+A_{P2})]. \qquad (12)$$

The g-factor can then be evaluated by assuming a rotational distribution for the v=0 level. Comparing the values of g_{RO} obtained by evaluating (12) assuming a rotational LTE distribution for v=0, to those obtained directly from the results of the DGEAR model, we get g_{RO}(DGEAR)/g_{RO}(radiative)=1.11 at r=10 km. Since g_{RO}(DGEAR)/g_{RO}(radiative) is also equal to n_1^1(DGEAR)/n_1^1(radiative), we find that the radiative formula, equation (11), gives very good approximations to the actual fractional populations even at r=10 km, where collisional effects are strong.

The rotational states in the v=1 level retain some information about the rotational distribution of the v=0 level through equation (11). Although it appears that the v=1 level is in rotational LTE within the inner coma (the general trend of the contour lines for both v levels in Figure 1 are quite similiar), in fact, the upper v states are merely reflecting the LTE distribution of the v=0 level.

Many of the differences between the DGEAR and homogeneous models are averaged out by the line of sight integration used in calculating column brightnesses. For example, Figure 7 shows the P1 column brightness versus the projected distance from the nucleus for both the DGEAR and homogeneous models, using the standard bright comet parameters at R=1 AU. The CO column density is also plotted on the same graph. The column density falls off inversely with the impact parameter until $\sim 10^5$ km when photolysis becomes important. The P1 column brightnesses in Figure 7 differ significantly only when the impact parameter is $\sim 10^3$-10^5 km (i.e., when the line of sight is about tangent to the transition regions in the coma). The maximum differences between the two models are $\sim$40%. For higher J transitions, differences between the DGEAR and homogeneous results are also found in the inner coma, in addition to the transition region, with maximum differences reaching $\sim$50% (these results can be found in Chin and Weaver 1984). At a distance of $\sim 10^5$ km, where fluorescence equilibrium is achieved, column brightnesses for all transitions become proportional to the column density, as expected.

Figure 8 shows column brightnesses for the P1 and P7 transitions using only the DGEAR model. The P7 brightness is essentially flat for impact parameters $\lesssim 10^3$ km with a slight increase close to the nucleus. This behavior is indicative of the cold rotational distribution in the inner coma where higher J states are not significantly populated and, therefore, contributions to the line of sight integration can only come from outside of this region. The reverse is true for the P1 transition for which the inner coma contributes significantly to the intensity.

The intensity distribution in the IR (1,0) band changes dramatically for different fields of view. Table 2 gives aperture-averaged absolute intensities (in W cm^{-2} sr^{-1}) for lines in the IR (1,0) band for two fields of

view ($1\hat{'}$ and $4\hat{''}$) when our standard bright comet is 1 AU from the sun and 0.62 AU from the earth. The detectability of these lines will be discussed in the next section. Figure 9 shows the aperture-averaged g-factors (which are directly proportional to the intensities) for the $1\hat{'}$ FOV. At a geocentric distance (Δ) of 0.62 AU, a $1\hat{'}$ aperture subtends a radius of 1.35×10^4 km. We plot the results for the DGEAR and homogeneous models, and, for comparison, an LTE distribution using the assumed kinetic temperature profile shown in Figures 4 and 6. For this FOV and observing aspect, a large portion of the coma is averaged into the measurement, and the intensity is distributed among many J states. For the DGEAR and homogeneous models, the peak intensity is reached at J=6 or 7, while the LTE distribution is peaked at even higher J and exhibits a "flatter" spectral profile. The "hot" LTE distribution is due to the assumption of high kinetic temperatures ($T \sim 500$K when $r \gtrsim 10^4$ km) in the outer coma.

In contrast, Figure 10 shows the g-factors for the IR (1,0) band averaged over a $4\hat{''}$ diameter circular aperture at the same heliocentric and geocentric distances. Here the projected radius is 900 km, so that the measurement is primarily sampling the inner coma. In this case, the DGEAR, homogeneous, and LTE distributions all give similiar results. Note that for a $4\hat{''}$ aperture, the peak g-factors are almost three times as strong as the peak values for a $1\hat{'}$ aperture. Only the low J transitions are significantly excited in the cold inner coma, so that almost all the intensity in the band is concentrated into these few lines. The differences between the model calculations and the LTE distribution result from the fact that the v=1 rotational states are not in LTE (as discussed above).

Previous studies have obtained similiar values for the band g-factor (Crovisier and Le Bourlot 1983 derive $g_{band}=2.6 \times 10^{-4}$ s^{-1}, while Weaver and

Mumma 1984 give 2.5×10^{-4} s^{-1}, compared to 2.4×10^{-4} s^{-1} from our model calculations). The small differences arise from the different values used for the Einstein B-coefficients and for the solar flux. However, the earlier works make very different assumptions concerning rotational excitation in the coma, and, thus, derive different intensity distributions within the IR (1,0) band. Crovisier and Le Bourlot concentrated on a fluorescence equilibrium distribution and their results are similiar to ours for comets which are observed with large apertures at large geocentric distances. Weaver and Mumma assumed an LTE distribution for the v=0 level with T=200K; their results are similiar to those obtained assuming fluorescence equilibrium. For small fields of view, our calculations become critically dependent upon the assumed kinetic temperature profile in the inner coma. The "cold" IR intensity distribution predicted for observations with a 4" FOV is a reflection of the extremely cold kinetic temperature profile used in our calculations.

Table 3 shows the intensities of the rotational transitions for the bright comet model at R=1 AU Δ=0.62 AU for both 1' and 4" fields of view. The intensities in Table 3 are calculated assuming a line width of 1.6 km s^{-1} and are expressed as brightness temperatures in the Rayleigh-Jeans limit. The Crovisier and Le Bourlot (1983) results are not directly comparable to ours, since there are numerous differences between the two models. However, if we assume the same conditions as Crovisier and Le Bourlot (i.e., 0.5' FOV, Δ=1 AU, and use the same Haser model input parameters and cometary line width), we calculate significantly different intensities for some of the rotational lines (the largest difference is 1.8 for the J=1→0 transition). Again, the higher spatial resolution results in Table 3 show enhanced values for the low J transitions and are a reflection of the "cold" kinetic temperature profile we have assumed for the inner coma.

IV. OBSERVATIONS

The preceding discussion has important implications for the detectability of cometary emission in the IR (1,0) band and from the millimeter-wavelength rotational transitions. The strongest IR line in a 4" FOV when Δ=0.62 AU is expected to be the P2 transition with an average brightness of 1.6×10^{-10} Watts cm^{-2} sr^{-1} (see Table 2). The sensitivity of the Kitt Peak National Observatory (KPNO) Fourier Transform Spectrometer (FTS) at the 4-meter Mayall Telescope in the region of the CO IR (1,0) band, for a one hour integration period, using its highest resolution (0.0216 cm^{-1}), is $\sim 8 \times 10^{-11}$ Watts cm^{-2} sr^{-1} (1 σ limit). This sensitivity limit can be achieved for cometary observations when they are performed at low air mass ($\sim$1), and if the cometary line is Doppler-shifted far enough away from the peak of telluric CO absorption that the transmittance at the position of the cometary emission is essentially the continuum transmittance. Cometary geocentric velocities greater than 30 km s^{-1} are necessary in order to accomplish this, but such velocities are not unusual. Thus, it appears possible, although difficult, to do ground-based observations of the CO IR (1,0) band emission from a bright comet if the CO abundance is >10% of the H_2O abundance.

Ground-based FTS observations are background noise limited in this spectral region. Even when a narrow filter is used to limit the bandwidth to $\sim$100 cm^{-1}, covering most of the CO (1,0) band, background noise is still about two orders of magnitude above detector noise limited sensitivity. On the other hand, an FTS on a cooled, space-borne instrument, like the Shuttle Infrared Telescope Faciltiy (SIRTF), should easily detect cometary CO emission in the (1,0) band.

Ground-based searches for rotational transitions will be confined primarily to low J transitions like J=1→0 and J=2→1, since higher J transitions are difficult to observe from the ground and no sensitive receivers are currently available for J>4 transitions (see Wilson 1983). Since typical millimeter-wavelength telescopes have rather large beam sizes, the relevant intensities to examine in Table 3 are the average values in a 1′ FOV. Millimeter-wave receivers can now achieve sensitivity limits approaching ∿10 mK (1σ) for the J=1→0 transition. As can be seen from Table 3, the highest possible sensitivities are required to observe this transition from the ground for a bright comet. Receiver sensitivities are not as good for the J=2→1 transition but since this transition will generally be brighter in the comet, it would not be unreasonable to also search for this line. The prospects of detecting either of these lines drop dramatically when the comet's geocentric distance becomes large (Δ>1 AU; see earlier discussion). Since the CO brightness peaks strongly towards the nucleus if CO is a parent molecule, accurate ephemerides are essential for centering the beam on the nucleus to improve the sensitivity of any observation.

The apparition of comet IRAS-Araki-Alcock (1983d) in May 1983 provided a favorable opportunity to perform sensitive IR and radio searches for CO. We searched for individual lines of the IR (1,0) band on 1983 May 10 (∿10:20-11:31 UT) using the KPNO FTS at the Mayall 4-meter telescope (These observations are summarized in Weaver et al. 1983). We estimate that the atmospheric transmittance for the strongest CO line was ∿0.25 (the comet was observed at ∿2 air masses). No CO lines were detected. Our upper limit (1σ) for the average CO column density in the 4″ FOV is 1.3×10^{14} cm^{-2}, which translates into a CO production rate of $\sim1\times10^{27}$ mol s^{-1}. From IUE

observations of OH emission, the H_2O production rate is estimated to be between $1.5-4 \times 10^{28}$ mol s^{-1}.

A search was conducted for the CO J=1→0 radio transition on 3 nights (1983 May 7,10, and 11 UT) using the Bell Laboratories 7-meter telescope in Holmdel, New Jersey (These observations are also described briefly in Weaver et al. 1983). Telescope pointing and tracking were verified using a TV guider system that was co-aligned with the radio telescope. The small geocentric distances ($\Delta \sim 0.07-0.03$ AU) of the comet ensured that the coldest region of the coma was observed (the beam size was ~ 100 $''$), and that there would be reasonable expectations for observing the J=1→0 line. Unfortunately, no CO emission was detected. The upper limit on the CO production rate based on the radio results is virtually identical to the number derived above from the IR observations (e.g., $Q_{CO} < 1 \times 10^{27}$ mol s^{-1}).

This upper limit is also consistent with the upper limit placed on CO production from IUE observations (fourth positive group emissions were not seen in the IUE spectra). The IUE limit ($Q_{CO} < 4 \times 10^{26}$ mol s^{-1} on 5/12 UT; Feldman, private communication) is more sensitive than the IR and radio limits but, unlike the IR and radio observations, the IUE measurements would yield no direct information on the rotational excitation or outflow velocities of the CO molecules (the IUE resolution is not high enough to resolve individual lines within the CO bands). If CO were a parent molecule present at the same abundance relative to H_2O as for comet West (1976 VI) ($Q_{CO}/Q_{H2O} \sim 0.3$), then CO emission should have been detectable in all 3 spectral regions.

V. CONCLUSION

Our study takes two previously-neglected factors into account in

calculating the vibrational and rotational excitation of CO. First, we explicitly derive the fractional populations of CO as solutions to time-dependent differential equations, so that the physical parameters of the comet determine the evolution of the solution throughout the coma. Important differences between the DGEAR method and a steady-state solution occur, especially in the transition region ($r \sim 10^3$ to 10^5 km). The DGEAR solution predicts suprathermal and inverted populations for low J rotational transitions. Second, we consider a non-isothermal and cold kinetic temperature profile for the inner coma ($r \lesssim 10^3$ km). This leads to enhanced emissions for low J transitions in the IR (1,0) band and for millimeter-wavelength rotational transitions in the inner coma.

The predictions in this paper are crucially dependent upon our choice for the kinetic temperature profile. If the kinetic temperature is very different from that given by present models (e.g., Marconi and Mendis 1982, Shimizu 1976, Crovisier 1983), then many of our conclusions concerning the observations of comets using small fields of view or at small geocentric distances may be invalid. We have also neglected optical depth effects. Significant optical trapping could affect the excitation of CO in the inner coma, and this could alter our results. To our knowledge, a proper treatment of multi-level radiative transfer in comets has never been attempted, and is outside the scope of the present paper. Such a refined analysis of the CO problem may not be justified until suitable future observations of CO indicate that this approach is warranted.

The predicted intensities for our bright comet model show that IR (1,0) band and millimeter-wavelength observations of CO are feasible under certain favorable conditions and would be important probes of the excitation conditions in the comae of comets. The kinetic temperature of the inner comae

of comets is expected to be cold and IR and millimeter-wavelength observations of CO would directly test this hypothesis. Due to many factors, including terrestrial absorption, beam dilution, and lack of sensitivity, ground-based observations may only be accomplished for large comets passing reasonably close to the earth. Comet IRAS-Araki-Alcock (1983d) presented an excellent opportunity to test many of the predictions of our model calculations, since it passed within 0.032 AU of the earth. Unfortunately, 1983d proved to be a small comet with relatively low gas production rates (Large comets could have H_2O production rates a factor of 10 or more larger than comet 1983d at the same heliocentric distance).

Our calculations also indicate that comet Halley will not be a favorable target for ground-based observations of CO. During the second week of March in 1986 (one of the most favorable times for observing comet Halley; R=0.88 AU and 1 AU), parent molecular column densities may be lower by a factor of $\sim$7 compared to those of comet 1983d (We assume $Q_{H2O}=1.3\times10^{29}$ mol s^{-1} for comet Halley when R=0.88 AU). Moreover, the rather large geocentric distance will mean that ground-based observers will be viewing a CO population closely approaching fluorescence equilibrium, and this will further inhibit the detection of the low J IR (1,0) band and millimeter-wavelength transitions.

Although ground-based IR observations of CO emissions from comets will be extremely difficult, a completely different picture emerges when one considers observations from earth orbit using cooled instrumentation. An FTS instrument aboard a cooled telescope such as SIRTF could have up to two orders of magnitude increased sensitivity compared to similiar ground-based instruments in the CO IR (1,0) band. Thus, Earth orbiting instruments should be capable of monitoring CO emission from even moderately-bright comets.

ACKNOWLEDGEMENTS

We wish to thank Dr. J. Hillman for providing many of the sources for the CO molecular constants used in our calculations, and Dr. S. Green for helpful discussions on the collisional cross section problem. Dr. M. Allen emphasized the need for differentiating between rate constants and rates, provided helpful discussions on solving LDEs, and contributed other meaningful comments concerning this work. We thank Dr. D. Deming for providing several useful suggestions which improve the paper. Mr. F. Espenak and Drs. M. A'Hearn and B. Marsden supplied important ephemeris information for the observations of comet 1983d. Dr. K. Hinkle expertly supported the CO IR observations on the Mayall FTS. We express our sincere appreciation to Drs. J. Bally and A. Stark, who performed the CO radio observations on very short notice with the Bell Laboratory telescope. Finally, we thank Dr. M. Mumma who provided constant encouragement for us to undertake this investigation.

APPENDIX

We wish to solve the explicit time development for a two level system which is excited only by radiative processes. Let the upper state be denoted by n_1 and the lower state by n_0. We define R as

$$R \equiv n_1/n_0. \tag{A1}$$

From the normalization condition, $n_1+n_0=1$, we have:

$$dn_1/dt = -dn_0/dt. \tag{A2}$$

The time derivative of R is given by:

$$\begin{aligned} dR/dt &= (\partial R/\partial n_1)(dn_1/dt) + (\partial R/\partial n_0)(dn_0/dt) \\ &= (1/n_0)(dn_1/dt) - (n_1/n_0^2)(dn_0/dt) \\ &= -(1/n_0)(dn_0/dt) - (R/n_0)(dn_0/dt) \\ &= -(dn_0/dt)(1+R)/n_0, \end{aligned} \tag{A3}$$

using equations (A1) and (A2). The rate equation is:

$$\begin{aligned} dn_0/dt &= An_1 - B\rho n_0 \\ &= ARn_0 - B\rho n_0 \\ &= n_0(AR - B\rho), \end{aligned} \tag{A4}$$

where A is the radiative decay rate constant and $B\rho$ is the radiative pump rate constant. Substitution from equation (A4) into (A3) yields:

$$dR/dt = B\rho + (B\rho - A)R - AR^2. \tag{A5}$$

The equilibrium solution can be obtained by setting $dR/dt=0$, and solving the resultant quadratic equation. The roots of equation (A5) are $R=B\rho/A$, and $R=-1$ (this gives a non-physical solution). Setting equation (A4) to zero and solving for R also gives the equilibrium result $R=B\rho/A$. Dividing equation (A5) by $-A$, and ignoring terms in R^2 and $(B\rho/A)R$ ($R<<1$ and $B\rho/A<<1$) gives:

$$-(1/A)dR/dT = R - B\rho/A. \tag{A6}$$

Equation (A6) can be rewritten as

$$dR/(R-B\rho/A) = -Adt. \tag{A7}$$

Equation (A7) can be integrated immediately to yield:

$$\ln(R-B\rho/A) = -At + C, \tag{A8}$$

which can be exponentiated to give:

$$R = B\rho/A + R_0 e^{-At}, \tag{A9}$$

where R_0 is determined by the initial conditions. Note that the time-constant in equation (A9) is dependent only on A, and not on the pumping rate.

TABLE 1

$CO-H_2O$ Collision Cross Section Information[a]

ΔJ ($\equiv J_{upper}-J_{lower}$)	Fraction of Total De-Excitation
1	0.34
2	0.25
3	0.20
4	0.10
5	0.07
6	0.05
>6	0

[a]The total cross section is always forced to equal 1.32×10^{-14} cm^{-2}. Excitation cross sections are derived from de-excitation cross sections by using the detailed balance relationship.

TABLE 2

Predicted Intensities for the CO IR (1,0) Band: Bright Comet[a]

Transition	Frequency (cm^{-1})	Intensity (10^{-11} W cm^{-2} sr^{-1}) 1' FOV	4" FOV
P12	2094.863	0.162	0.344
P11	2099.083	0.209	0.503
P10	2103.270	0.256	0.732
P9	2107.424	0.298	1.08
P8	2111.543	0.333	1.62
P7	2115.629	0.355	2.51
P6	2119.681	0.365	4.00
P5	2123.699	0.361	6.43
P4	2127.683	0.343	10.3
P3	2131.632	0.310	15.1
P2	2135.547	0.241	15.8
P1	2139.427	0.131	9.41
R0	2147.082	0.123	8.06
R1	2150.856	0.214	10.4
R2	2154.596	0.270	8.12
R3	2158.300	0.308	5.49
R4	2161.969	0.329	3.61
R5	2165.601	0.335	2.36
R6	2169.198	0.324	1.58
R7	2172.759	0.300	1.08
R8	2176.284	0.264	0.755
R9	2179.772	0.221	0.532
R10	2183.224	0.175	0.372

[a]The CO production rate is 2×10^{28} mol s^{-1} and the H_2O production rate is 2×10^{29} mol s^{-1}. The heliocentric distance is 1 AU and the geocentric distance is 0.62 AU. The average CO column density in the 1' circular field of view (FOV) is 8.55×10^{13} cm^{-2}, while that in the 4" circular FOV is 1.38×10^{15} cm^{-2}. All intensities are aperture-averaged values calculated using the non-equilibrium (DGEAR) model.

TABLE 3

Predicted Intensities for the CO Rotational Transitions: Bright Comet[a]

Transition	Frequency (GHz)	Brightness Temperature[b] (K) 1' FOV	4" FOV
J = 1→0	115	0.008	0.595
2→1	231	0.027	1.18
3→2	346	0.050	1.28
4→3	461	0.076	1.15
5→4	576	0.101	0.940
6→5	691	0.123	0.746
7→6	807	0.138	0.588
8→7	922	0.144	0.465
9→8	1037	0.141	0.369
10→9	1152	0.128	0.289

[a]The CO production rate is 2×10^{28} mol s^{-1} and the H_2O production rate is 2×10^{29} mol s^{-1}. The heliocentric distance is 1 AU and the geocentric distance is 0.62 AU. The average CO column density in the 1' circular field of view (FOV) is 8.55×10^{13} cm^{-2}, while that in the 4" circular FOV is 1.38×10^{15} cm^{-2}. All intensities are aperture-averaged values calculated using the non-equilibrium (DGEAR) model.

[b]The Brightness Temperature is calculated in the Rayleigh-Jeans limit assuming a rectangular line width of 1.6 km s^{-1}.

REFERENCES

A'Hearn, M.F., and Feldman, P.D. 1980, Ap. J. (Letters), 242, L187.

Campins, H., Rieke, G.H., and Lebofsky, M.J. 1983, Nature, 301, 405.

Chin, G., and Weaver, H.A. 1984, Part II of this Technical Memorandum.

Cosmovici, C.B., Barbieri, C., Bondi, C., Bortoletto, F., and Hamzaoglu, E. 1982, Astr. Ap., 114, 373.

Crovisier, J., and Le Bourlot, J. 1983, Astr. Ap., 123, 61.

Crovisier, J. 1983, Astr. Ap., in press.

Draegert, D.A., and Williams, D. 1968, JOSA, 58, 1399.

Delsemme, A.H., 1982, in Comets, ed. L.L. Wilkening (Tucson: University of Arizona Press), p. 85.

Feldman, P.D. 1978, Astr. Ap., 70, 547.

_____. 1982, in Comets, ed. L.L. Wilkening (Tucson: University of Arizona Press), p. 461.

_____. 1983, Science, 219, 347.

Feldman, P.D., et al. 1980, Nature, 286, 132.

Feldman, P.D., and Brune, W.H. 1976, Ap. J. (Letters), 209, L45.

Festou, M. 1981, Astr. Ap., 95, 69.

Gear, C.W. 1971, Numerical Initial Value Problems in Ordinary Differential Equations (Englewood Cliffs, New Jersey: Prentice-Hall, Inc.).

Goldsmith, P.F. 1972, Ap. J., 176, 597.

Herzberg, G. 1954, Molecular Spectra and Molecular Structure, Vol. 2, Infrared and Raman Spectra of Polyatomic Molecules (New York: D. Van Nostrand).

Houpis, H.L.F., and Mendis, D.A. 1981, Ap. J., 243, 1088.

Huebner, W.F., and Carpenter, C.W. 1979, Los Alamos Sci. Lab. Rept., LA-8085-MS.

Kildal, H., Eng, R.S., and Ross, A.H.M. 1974, J. Mol. Spectrosc., 53, 479.

Kirschner, S.M., LeRoy, R.J., Ogilvie, J.F., and Tipping, R.H. 1977, J. Mol. Spectrosc., 65, 306.

Krishna Swamy, K.S. 1983, Ap. J., 267, 1983.

Labs, D., and Neckel, H. 1968, Zs. Ap., 69, 1.

Marconi, M.L., and Mendis, D.A. 1982, Ap. J., 260, 386.

McKee, C.F., Storey, J.W.V., Watson, D.M., and Green, S. 1982, Ap. J., 259, 647.

Nuth, J.A., and Donn, B. 1981, Ap. J., 247, 925.

Shimizu, M. 1976, Ap. Space Sci., 40, 149.

Somerville, W.B. 1977, in Advances in Atomic and Molecular Physics, Vol. 13, ed. D.R. Bates (New York: Academic Press), p. 383.

Varghese, P.L., and Hanson, R.K. 1981, J. Mol. Spectrosc., 88, 234.

Weaver, H.A. 1981, Doctoral Thesis, The Johns Hopkins University.

Weaver, H.A., Feldman, P.D., Festou, M.C., and A'Hearn, M.F. 1981, Ap. J., 251, 809.

Weaver, H.A., Chin, G., Mumma, M.J., Espenak, F., Bally, J., Stark, A., and Hinkle, K. 1983, BAAS, 15, 802.

Weaver, H.A., and Mumma, M.J. 1984, Ap. J., 276, in press.

Wilson, W.J. 1983, IEEE Trans. on Microwave Theory Tech., Vol. MTT-31, 873.

Yamamoto, T., Nakagawa, N., and Fukui, Y. 1983, Astr. Ap., 122, 171.

FIGURE CAPTIONS

Figure 1. Contour plots showing relative populations of CO rotational states as a function of distance from the nucleus. Each vertical line represents a different rotational state, starting with J=0 at the extreme left and incrementing by one until J=20 is reached at the extreme right. The regions between the vertical lines have no physical significance. The contours are given in logarithmic units so that, for example, the curve labeled -1.0 represents a relative population of 10%. Plots are shown for both the v=0 and v=1 vibrational levels of the ground electronic state. The non-equilibrium (DGEAR) excitation model is used to generate these results. The CO production rate is 2×10^{28} mol s^{-1}, the H_2O production rate is 2×10^{29} mol s^{-1}, and the heliocentric distance is 1 AU.

Figure 2. Contour plots showing the excitation temperatures for CO rotational transitions as a function of distance from the nucleus. Excitation temperatures are calculated between adjacent rotational levels (see text for explicit formula) with each transition represented by a vertical line. Excitation temperatures for the lowest frequency transition ($J=1\rightarrow0$) are given along the left most <u>dotted</u> vertical line. Notice that this transition for the v=0 level becomes inverted (negative excitation temperatures) in the region between 3000 and 13000 km from the nucleus (this region is cross-hatched in the figure). Plots are shown for both the v=0 and v=1 vibrational levels of the ground electronic state. The non-equilibrium (DGEAR) model is used to generate these results. The CO production rate is 2×10^{28} mol s^{-1}, the H_2O production rate is 2×10^{29} mol s^{-1}, and the heliocentric distance is 1 AU.

Figure 3. The fractional population of the J=0, v=0 level of CO is plotted as a function of distance from the nucleus. Three different profiles are shown corresponding to three different excitation models: the circles, O, represent results from the non-equlibrium (DGEAR) solution, the triangles, Δ, show the steady-state results, and the solid line is the profile if rotational LTE is valid everywhere in the coma. The CO production rate is 2×10^{28} mol s^{-1}, the H_2O production rate is 2×10^{29} mol s^{-1}, and the heliocentric distance is 1 AU.

Figure 4. Same as Figure 3, except for the J=0, v=1 level of CO.

Figure 5. The excitation temperature of the J=1→0, v=0 transition in CO is plotted as a function of distance from the nucleus. The circles, O, show the non-equilibrium (DGEAR) solution, the triangles, Δ, are the steady-state results, and the solid curve is the assumed kinetic temperature profile. For the DGEAR results there is a region in the coma (3000 km $\leq r \leq$ 13000 km) where the excitation temperature becomes negative (indicating a population inversion). For these points we plot the absolute value of the excitation temperature, and indicate that inversion has ocurred by arrows. The CO production rate is 2×10^{28} mol s^{-1}, the H_2O production rate is 2×10^{29} mol s^{-1}, and the heliocentric distance is 1 AU.

Figure 6. Same as for Figure 5, except for the J=1→0, v=1 transition in CO. In this case, there are no population inversions, but both the non-equilibrium (DGEAR) and steady-state results indicate suprathermal excitation temperatures in the inner coma.

Figure 7. Column densities and column brightnesses are plotted as a function

of projected distance from the nucleus. The brightnesses are shown for the P1 transition of the IR (1,0) band using two different excitation models: the circles, O, are the non-equilibrium (DGEAR) results and the triangles, Δ, represent the steady-state solution. Significant differences between the two models occur only when the projected distance from the nucleus is between 10^3 and 10^4 km. The spatial distribution of the brightness in the inner coma is different from that of the column density, which varies inversely with the projected distance from the nucleus. The CO production rate is 2×10^{28} mol s^{-1}, the H_2O production rate is 2×10^{29} mol s^{-1}, and the heliocentric distance is 1 AU.

Figure 8. Column densities and column brightnesses are plotted as a function of projected distance from the nucleus. The brightnesses are shown for the P1 and P7 transitions of the IR (1,0) band. The column density varies inversely with the projected distance from the nucleus out to $\sim 10^5$ km. The P1 and P7 brightnesses have different spatial distributions, with neither being directly proportional to the column density in the inner coma. The column brightnesses have been calculated using the non-equilibrium (DGEAR) model. The CO production rate is 2×10^{28} mol s^{-1}, the H_2O production rate is 2×10^{29} mol s^{-1}, and the heliocentric distance is 1 AU.

Figure 9. Average g-factors (in photons s^{-1} mol^{-1}) in a $1''$ field of view for the IR (1,0) band when the geocentric distance is 0.62 AU. Results from three different excitation models are shown: the circles, O, represent the non-equilibrium (DGEAR) solution, the triangles, Δ, are the steady-state results, and the crosses, +, represent the distribution when rotational LTE is achieved in the upper vibrational level (v=1). Notice that the intensity in

the IR (1,0) band is distributed among many lines in this example. The CO production rate is 2×10^{28} mol s^{-1}, the H_2O production rate is 2×10^{29} mol s^{-1}, and the heliocentric distance is 1 AU.

Figure 10. Same as Figure 9, except for a 4'' field of view. In this case the intensity in the band is concentrated into the low J transitions. The largest g-factor here is almost three times the largest value attained for the 1'' field of view.

ORIGINAL PAGE IS
OF POOR QUALITY

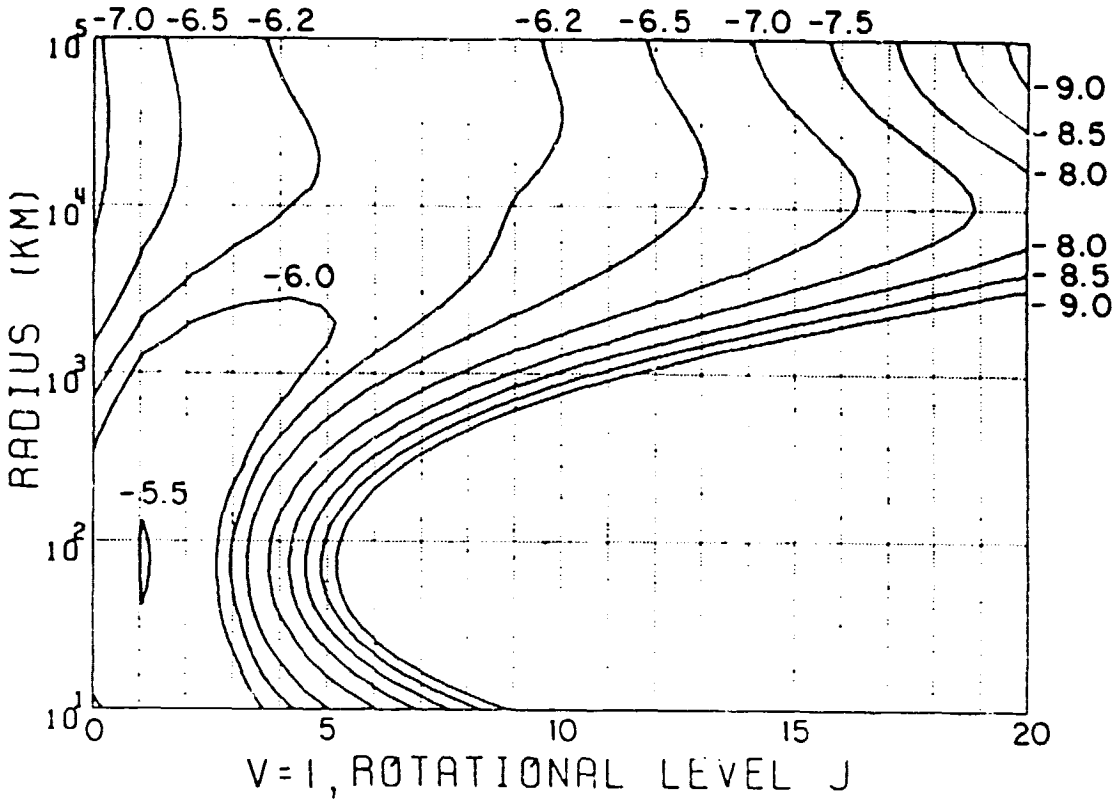

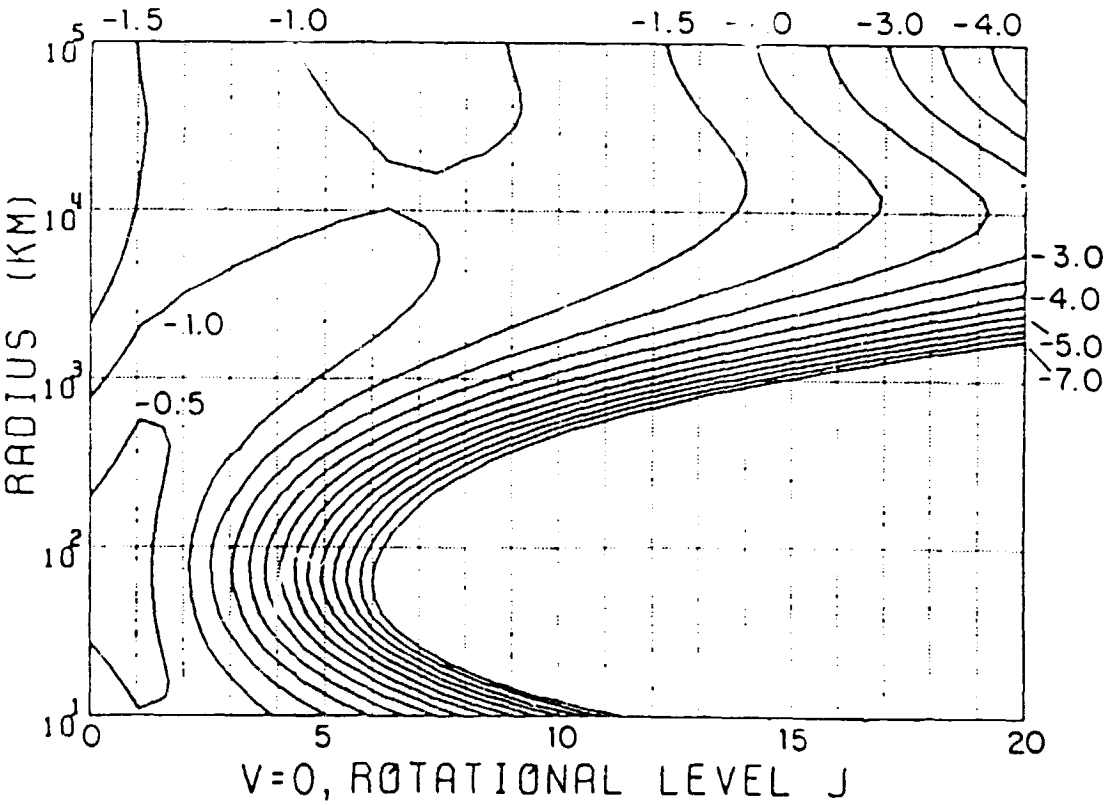

Figure 1.

ORIGINAL PAGE IS
OF POOR QUALITY

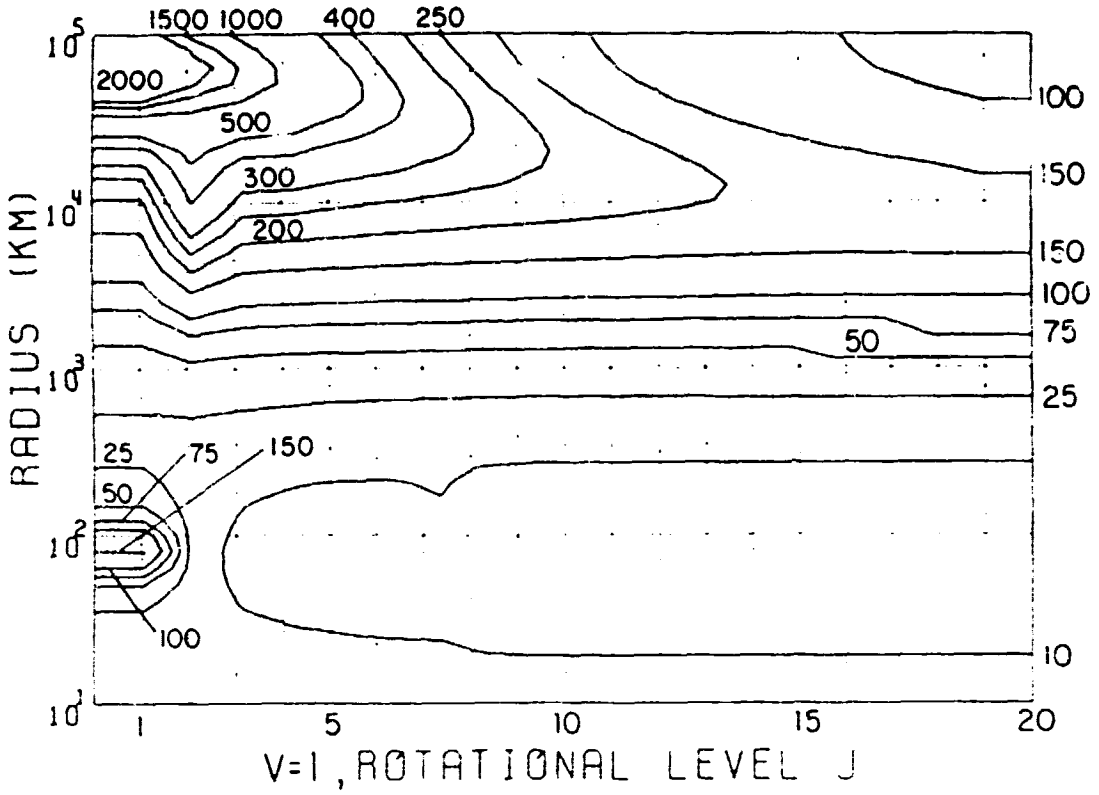

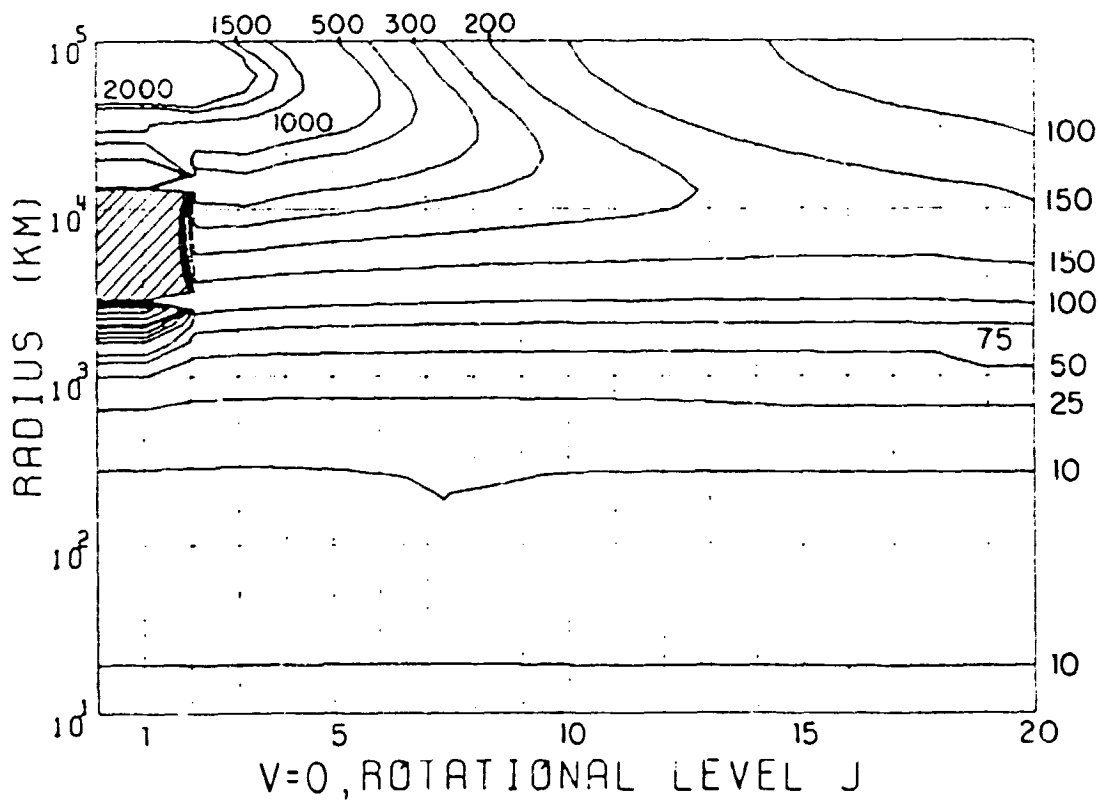

Figure 2.

ORIGINAL PAGE IS
OF POOR QUALITY

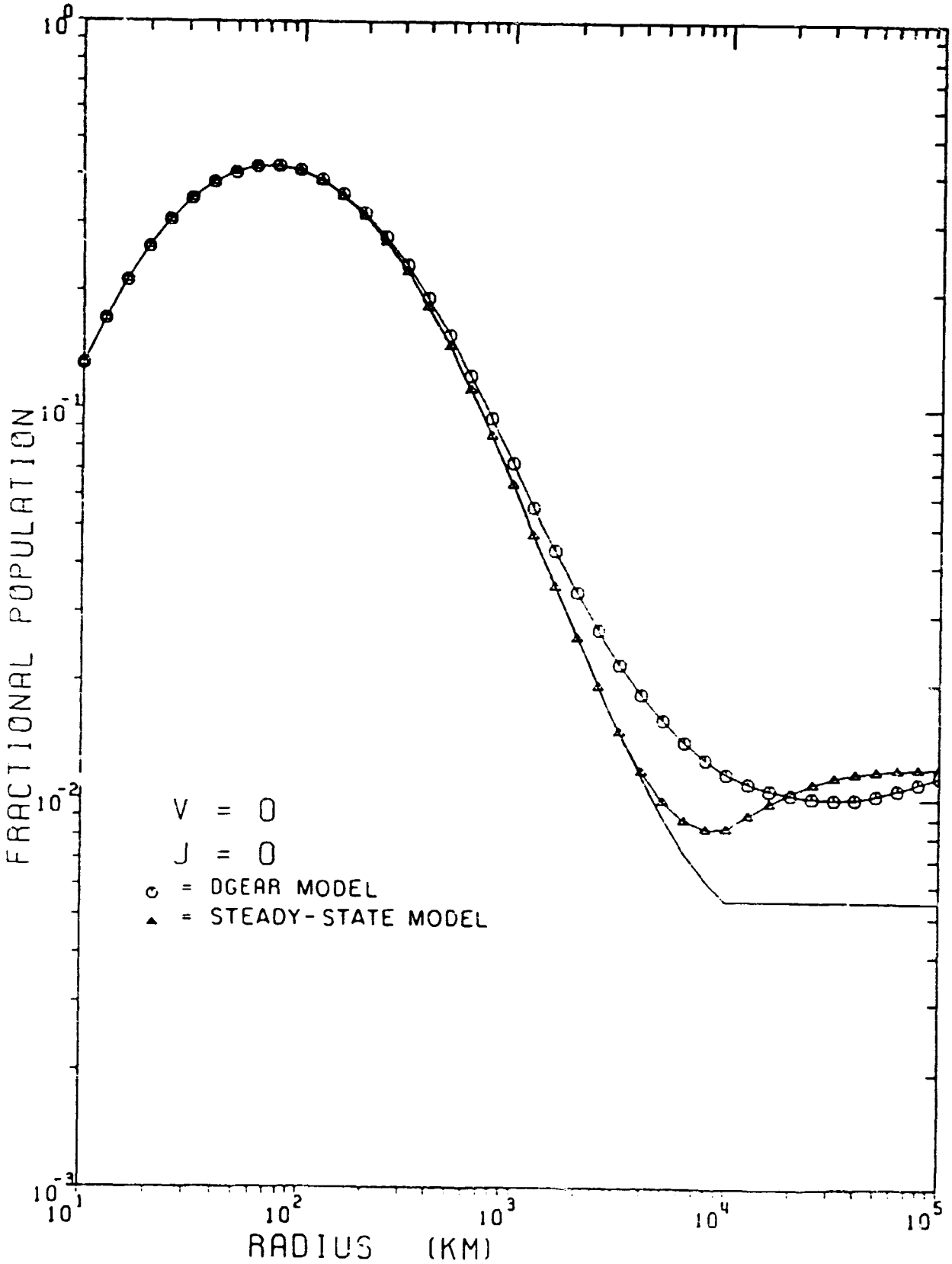

Figure 3

ORIGINAL PAGE IS
OF POOR QUALITY

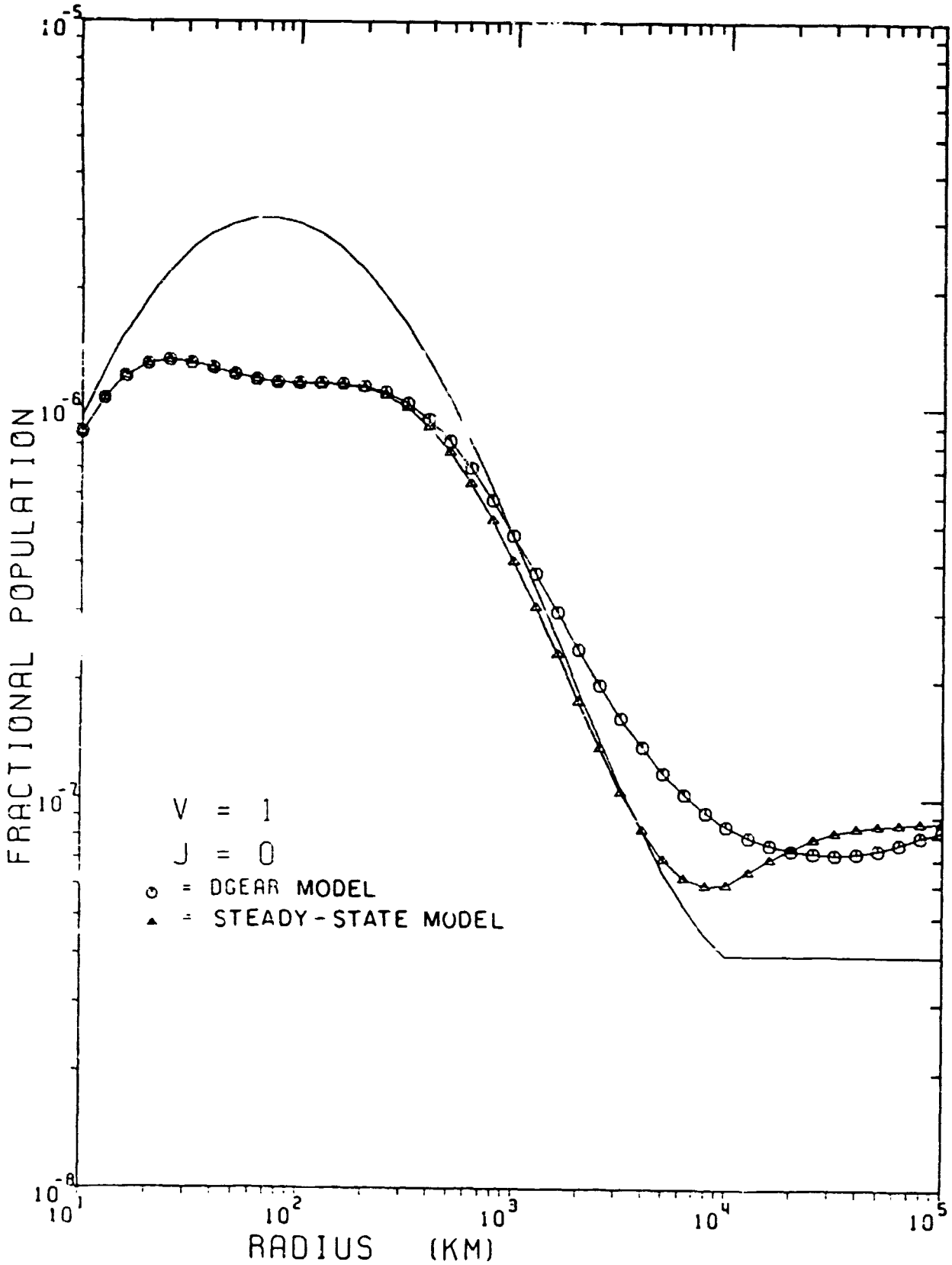

Figure 4.

ORIGINAL PAGE IS
OF POOR QUALITY

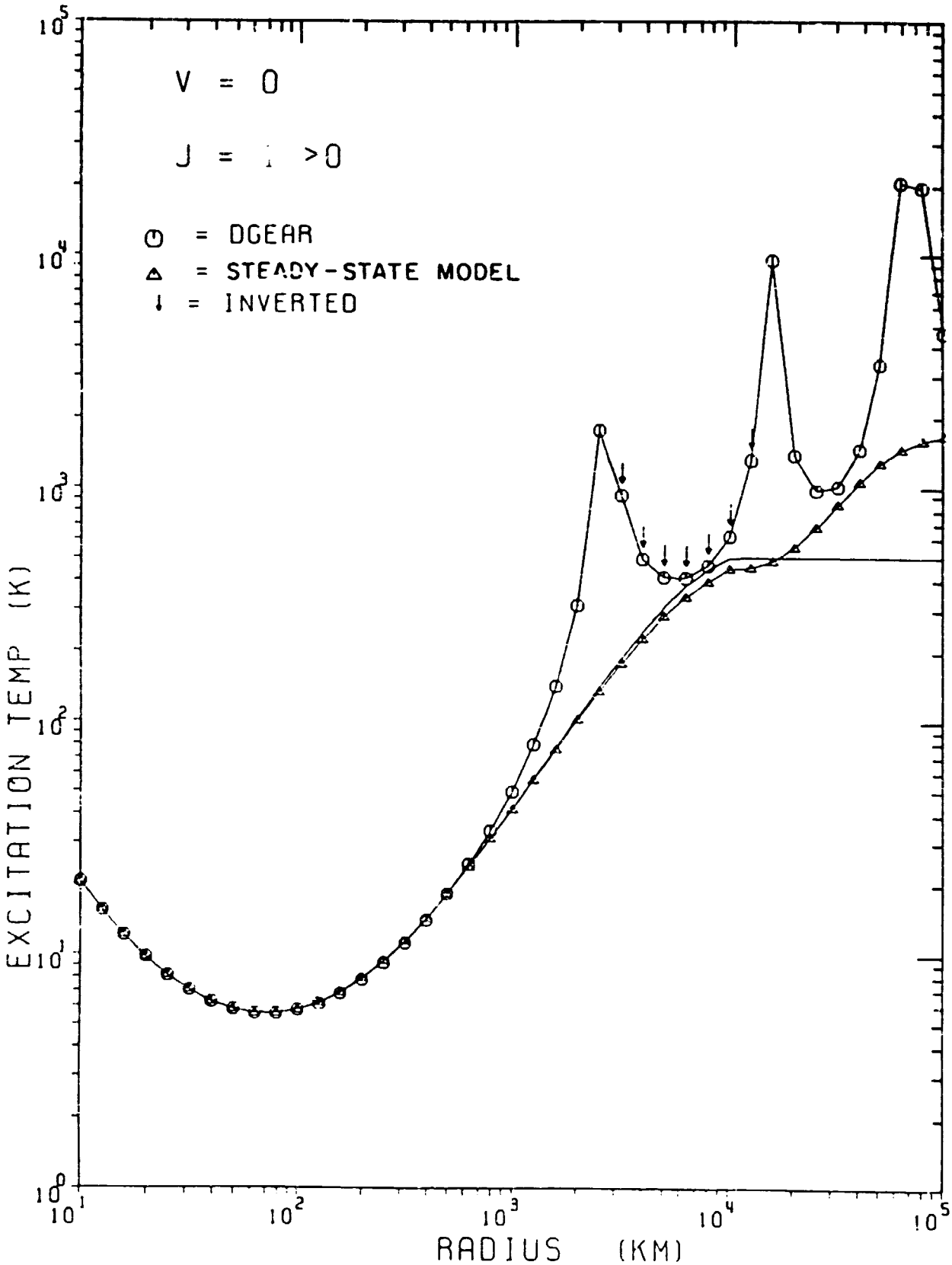

Figure 5.

ORIGINAL PAGE IS
OF POOR QUALITY

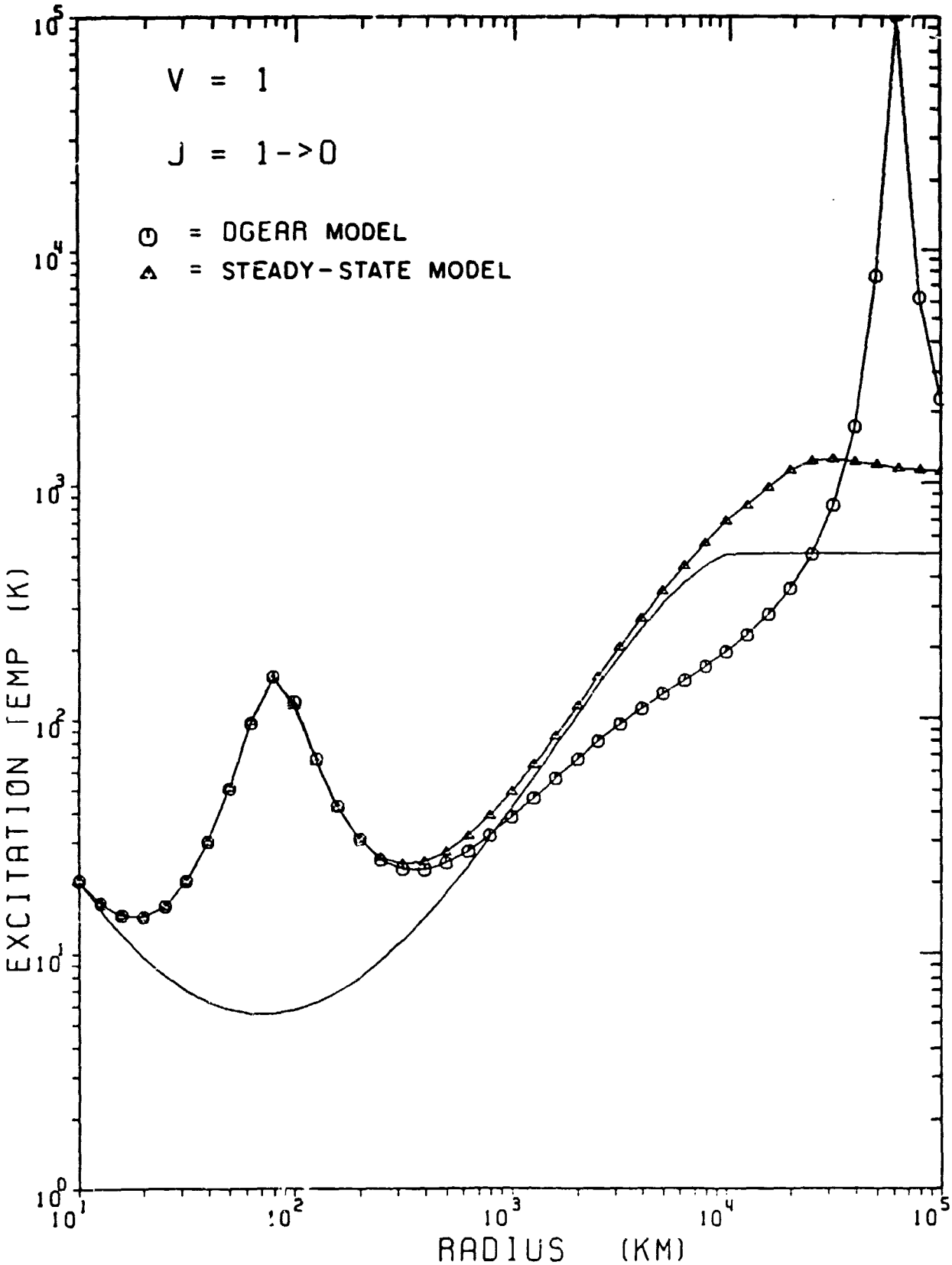

Figure 6.

ORIGINAL PAGE IS
OF POOR QUALITY

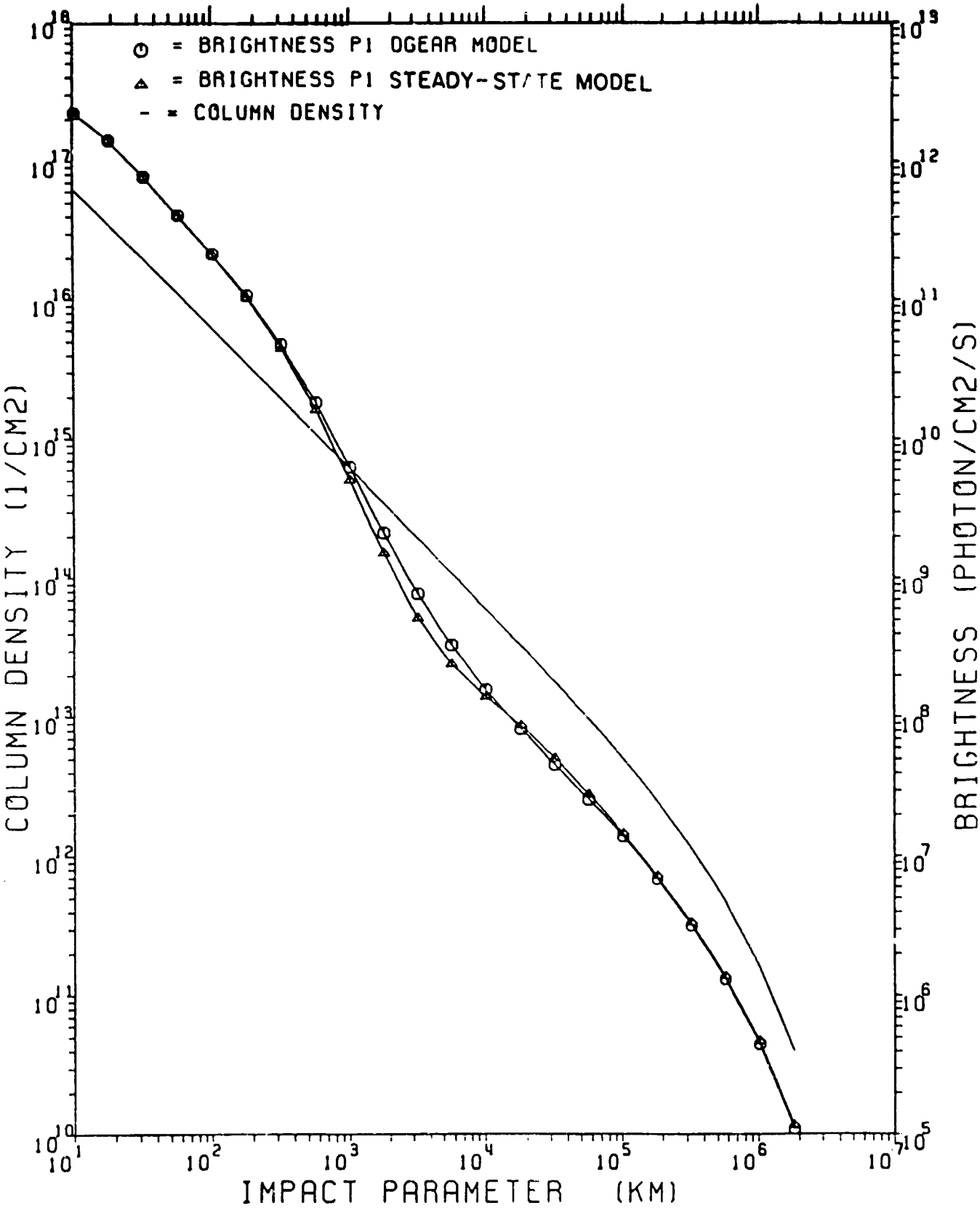

Figure 7.

ORIGINAL PAGE IS
OF POOR QUALITY

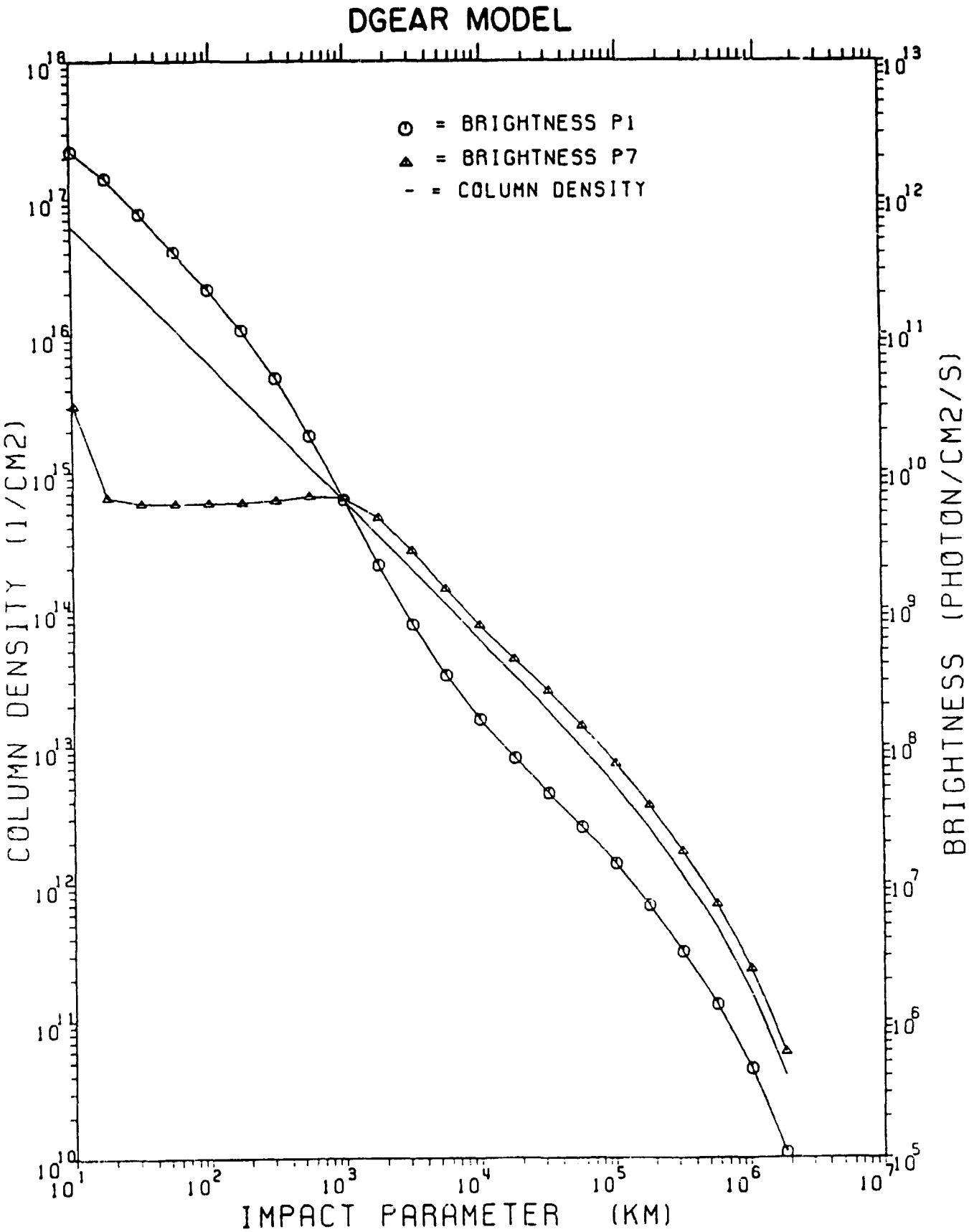

Figure 8.

ORIGINAL PAGE IS
OF POOR QUALITY

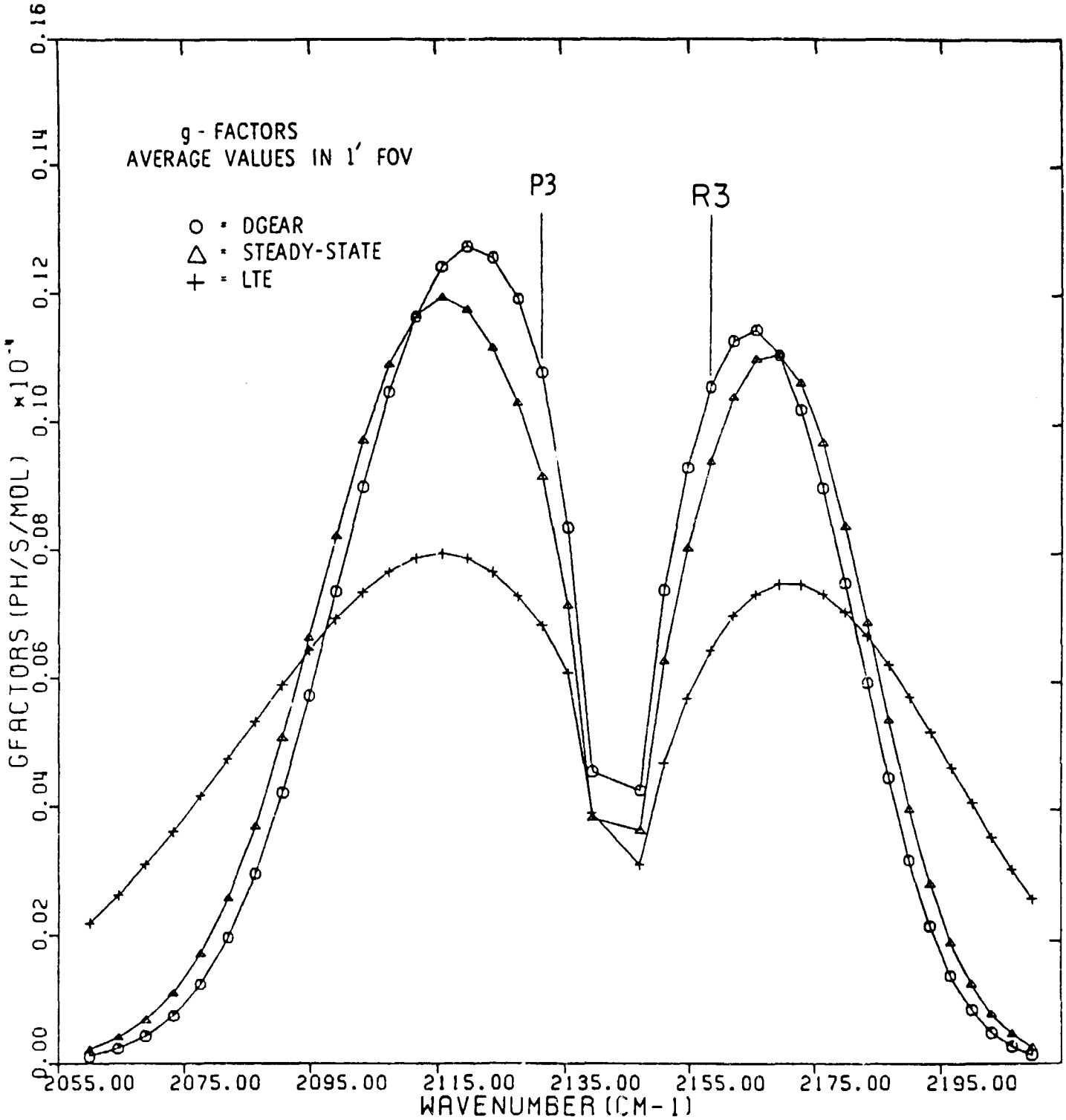

Figure 9.

ORIGINAL PAGE IS
OF POOR QUALITY

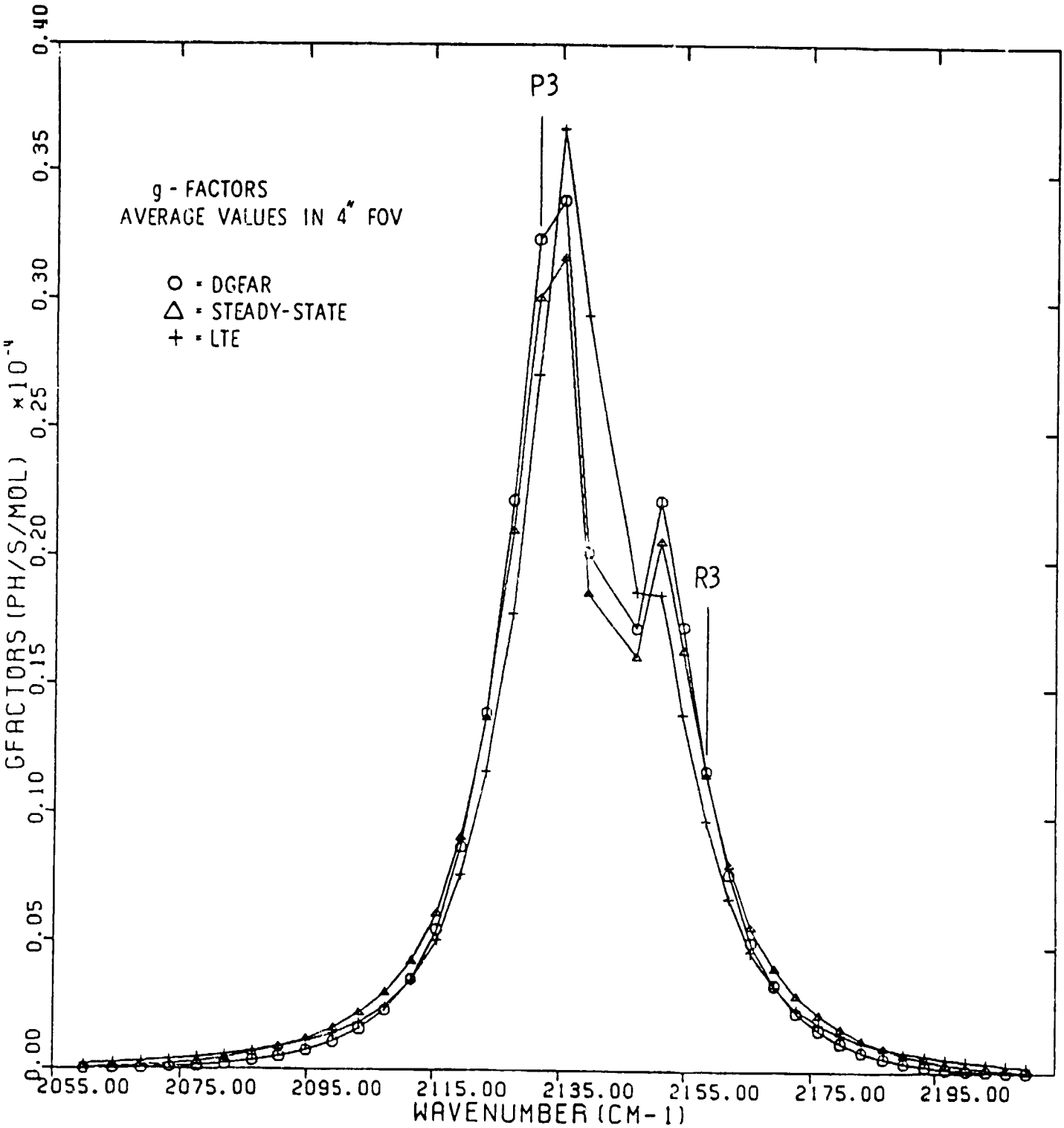

Figure 10

Gordon Chin: NASA/Goddard Space Flight Center, Infrared and Radio Astronomy Branch, Code 693, Laboratory for Extraterrestrial Physics, Greenbelt, MD 20771.

H.A. Weaver: Department of Physics, The Johns Hopkins University, Baltimore, MD 21218.

II. RESULTS OF THE CALCULATION FOR STANDARD BRIGHT COMET, COMET IRAS-ARAKI-ALCOCK, AND COMET HALLEY

INTRODUCTION

The results of the non-equilibrium calculation for different comet parameters are presented in this section. The details of the calculation are given in Part I. Here, we give results for three different comets; a standard "bright" comet, comet IRAS-Araki-Alcock (1983d), and comet Halley.

For the bright comet, we use a CO production rate, Q_{CO}, of 2×10^{28} mol s^{-1}, a water production rate, Q_{H2O}, equal to $10 \times Q_{CO}$, and a solar flux at R=1 AU. To gauge the effects of solar pumping on the CO excitation, we vary the solar flux to approximate the conditions of the comet at R=2 AU and R=0.5 AU (production rates and other parameters remain identical to their values at R=1 AU). For comparison, we also use the standard bright comet parameters to calculate a steady-state solution and a non-equilibrium solution with an isothermal temperature profile (T=200K) throughout the coma.

For comet IRAS-Araki-Alcock (1983d), we use H_2O production rates and upper limits on the CO production rate from <u>IUE</u> measurements (Feldman, private communication). We calculated two cases for comet 1983d; IRAS1 with $Q_{CO}=1 \times 10^{27}$ mol s^{-1} and $Q_{H2O}=40 \times Q_{CO}$, and R=1 AU, and IRAS2 with $Q_{CO}=5 \times 10^{26}$ mol s^{-1} and $Q_{H2O}=40 \times Q_{CO}$, and R=1 AU.

Three different observing aspects for comet Halley are used to calculate model predictions; HALLEY1 with $Q_{CO}=4.3 \times 10^{27}$ mol s^{-1}, $Q_{H2O}=10 \times Q_{CO}$, R=1.53 AU, and geocentric distance (Δ) of 0.62 AU, HALLEY2 with $Q_{CO}=1.3 \times 10^{28}$ mol s^{-1}, $Q_{H2O}=10 \times Q_{CO}$, R=0.88 AU, Δ=1.0 AU, and HALLEY3 with $Q_{CO}=5.7 \times 10^{27}$ mol s^{-1}, $Q_{H2O}=10 \times Q_{CO}$, R=1.33 AU, Δ=0.42 AU.

Results for the standard bright comet, comet IRAS-Araki-Alcock, and comet Halley are given in four groups:

Group I shows contour plots of the fractional populations for CO rotational transitions and excitation temperatures as a function of distance from the comet nucleus.

Group II shows the fractional population and excitation temperatures of selected rotational states of CO as a fuction of distance from the nucleus.

Group III shows column densities and brightnesses of selected CO IR (1,0) transitions.

Group IV. shows aperture averaged intensities and g-factors for the CO IR (1,0) band using a 1' and 4' field of view.

Figure Captions

NOTE: Since there are 94 figures, captions cannot be given for each. The figures have been divided into four groups. A general figure captions is given for each group followed by a listing, with a short identification for all the figures in that group.

I. Contour plots showing relative populations of CO rotational states and excitation temperatures for CO rotational transitions as a function of distance from the nucleus. The plots are arranged in pairs consisting of the plot for the relative populations followed by the excitation temperature plots. Different pairs of plots are distinguished by different comet conditions and/or the use of different excitation models. For the relative population plots, each vertical line represents a different rotational state, starting with J=0 at the extreme left and incrementing by one until J=20 is reached at the extreme right. The contours are given in logarithmic units so that, for example, the curve labeled -1.0 represents a relative population of 10%. Excitation temperature are calculated between adjacent rotational levels (see text for explicit formula) with each transition represented by a vertical line. Excitation temperatures for the lowest frequency transition ($J=1\rightarrow0$) are given along the left most dotted vertical line. Regions in which a transition becomes inverted (negative excitation temperatures) are cross-hatched. In all cases, plots are shown for both the v=0 and v=1 vibrational levels of the ground electronic state. Also, the regions between the vertical lines have no physical significance. Individual figure identifications follow.

Ia1 and Ia2: DGEAR (non-equilibrium) model with $Q_{CO}=2\times10^{28}$ mol s^{-1}, $Q_{H2O}=10\times Q_{CO}$, R=1 AU.

Ib1 and Ib2: Steady-state model with $Q_{CO}=2\times10^{28}$ mol s^{-1}, $Q_{H2O}=10\times Q_{CO}$, R=1 AU.

Ic1 and Ic2: DGEAR model with $Q_{CO}=2\times10^{28}$ mol s^{-1}, $Q_{H2O}=10\times Q_{CO}$, and R=2 AU.

Id1 and Id2: DGEAR model with $Q_{CO}=2\times10^{28}$ mol s^{-1}, $Q_{H2O}=10\times Q_{CO}$, and R=0.5 AU.

Ie1 and Ie2: Same as (a) except using an isothermal coma with $T_{kinetic}$=200K.

If1 and If2: DGEAR model for the conditions of IRAS1: $Q_{CO}=1\times10^{27}$ mol s^{-1}, $Q_{H2O}=40\times Q_{CO}$, and R=1 AU.

Ig1 and Ig2: DGEAR model for the conditions of IRAS2: $Q_{CO}=5\times10^{26}$ mol s^{-1}, $Q_{H2O}=40\times Q_{CO}$, and R=1 AU.

Ih1 and Ih2: DGEAR model for the conditions of HALLEY1: $Q_{CO}=4.3\times10^{27}$ mol s^{-1}, $Q_{H2O}=40\times Q_{CO}$, and R=1 AU.

Ii1 and Ii2: DGEAR model for the conditions of HALLEY2: $Q_{CO}=1.3\times10^{28}$ mol s^{-1}, $Q_{H2O}=10\times Q_{CO}$, and R=0.88 AU.

Ij1 and Ij2: DGEAR model for the conditions of HALLEY3: $Q_{CO}=5.7\times10^{27}$ mol s^{-1}, $Q_{H2O}=10\times Q_{CO}$, and R=1.33 AU.

II. The fractional populations of selected rotational states of CO and the excitation temperatures of selected rotational transitions are plotted as a function of distance from the nucleus. The figures are divided into five groups of twelve plots each. Each group represents a different set of comet conditions and/or the use of different excitation models. The first half of each group (six plots) shows fractional populations for the J=0, 4, and 10 rotational states, for both the v=0 and v=1 levels. In these figures, the solid curve represents the fractional population achieved assuming rotational LTE. The second half of each group shows excitation temperatures for the J=1→0, 5→4, and 10→9 rotational transitions, for both the v=0 and v=1 levels. For these plots,

the solid curve is the assumed kinetic temperature profile and population inversions (negative excitation temperatures) are indicated by arrows. Individual figure identifications follow.

II a1-a6: DGEAR (non-equilibrium, and Steady-State fractional populations. $Q_{CO}=2\times10^{28}$ mol s^{-1}, $Q_{H2O}=10\times Q_{CO}$, and R=1 AU.

II a7-12: DGEAR and Steady-State excitation temperatures. $Q_{CO}=2\times10^{28}$ mol s^{-1}, $Q_{H2O}=10\times Q_{CO}$, and R=1 AU.

II b1-b6: Fractional populations using DGEAR model for conditions of:

IRAS 1: $Q_{CO}=1\times10^{27}$ mol s^{-1}, $Q_{H2O}=40\times Q_{CO}$, and R=1 AU.

IRAS2: $Q_{CO}=5\times10^{26}$ mol s^{-1}, $Q_{H2O}=40\times Q_{CO}$, and R=1 AU.

II b7-b12: Excitation temperatures using DGEAR model for conditions of IRAS1 and IRAS2.

II c1-c6: Fractional populations using DGEAR model for R=2 AU and R=0.5 AU. In both cases, $Q_{CO}=2\times10^{28}$ mol s^{-1} and $Q_{H2O}=10\times Q_{CO}$.

II c7-c12: Fractional temperatures using DGEAR model for R=2 AU and R=0.5 AU.

II d1-d6: Fractional populations using DGEAR model for conditions of:

HALLEY1: $Q_{CO}=4.3\times10^{27}$ mol s^{-1}, $Q_{H2O}=10\times Q_{CO}$

HALLEY2: $Q_{CO}=1.3\times10^{28}$ mol s^{-1}, $Q_{H2O}=10\times Q_{CO}$

II d7-d12: Excitation temperatures using DGEAR model for conditions of HALLEY1 and HALLEY2.

II e1-e6: Fractional populations using DGEAR model but with two different kinetic temperature profiles. One case employs the Marconi and Mendis (1982) kinetic temperature profile (same as used above in all cases), while the other assumes an isothermal coma with $T_{kinetic}=200K$.

II e7-e12: Same as II e1-e6, except for excitation temperatures.

III. Column densities and column brightnesses are plotted as a function of projected distance from the nucleus.

III a-c: These figures compare results for the DGEAR (non-equilibrium) and Steady-State models for the P1, P6, and P8 lines, respectively, of the CO IR (1,0) band. For the P1 transition, significant differences between the two models occur only when the projected distance from the nucleus is between 10^3 and 10^4 km. For the P6 and P8 lines differences can also occur for small projected distances ($<10^3$ km), but for these lines the differences between the two model results are generally small ($\lesssim 10\%$).

III d-f: These figures are the results from the DGEAR model comparing spatial brightness distributions for two different lines. Figure IIId compares P1 and P2, IIIe compares P1 and P4, while IIIf compares P1 and P7. For all of the lines in the CO (1,0) band, the spatial brightness distribution in the inner coma is different from that of the column density, which varies inversely with the projected distance from the nucleus.

All of the above results have been calculated using $Q_{CO}=2\times10^{28}$ mol s^{-1}, $Q_{H2O}=10\times Q_{CO}$, and R=1 AU.

IV. Aperture-averaged intensities and g-factors for the CO IR (1,0) band are shown for two fields of view ($4''$ and $1'$). Individual figure identifications are given below.

IVa: DGEAR (non-equilibrium) and Steady-State model results using $Q_{CO}=2\times10^{28}$ mol s^{-1}, $Q_{H2O}=10\times Q_{CO}$, R=1 AU, Δ=0.62 AU, and a field of view (FOV) of $\hat{4}''$.

IVb: DGEAR model using FOV=$\hat{4}''$ for the conditions of:

HALLEY1: $Q_{CO}=4.3\times10^{27}$ mol s^{-1}, $Q_{H2O}=10\times Q_{CO}$, R=1.53 AU, Δ=0.62 AU

HALLEY2: $Q_{CO}=1.3\times10^{28}$ mol s^{-1}, $Q_{H2O}=10\times Q_{CO}$, R=0.88 AU, Δ=1.0 AU

HALLEY3: $Q_{CO}=5.7\times10^{27}$ mol s^{-1}, $Q_{H2O}=10\times Q_{CO}$, R=1.33 AU, Δ=0.42 AU

IVc: DGEAR model using FOV=$\hat{4}''$ for the conditions of:

BRIGHT: $Q_{CO}=2.0\times10^{28}$ mol s^{-1}, $Q_{H2O}=10\times Q_{CO}$, R=1 AU, Δ=0.062 AU

HALLEY2: $Q_{CO}=1.3\times10^{28}$ mol s^{-1}, $Q_{H2O}=10\times Q_{CO}$, R=0.88 AU, Δ=1.0 AU

IRAS1: $Q_{CO}=1.0\times10^{27}$ mol s^{-1}, $Q_{H2O}=10\times Q_{CO}$, R=1 AU, Δ=0.041 AU

IVd: Same as (a), except using FOV=$\hat{1}'$

IVe: Same as (b), except using FOV=$\hat{1}'$

IVf: Same as (c), except using FOV=$\hat{1}'$

IVg: g-factor x R^2 using FOV=$\hat{4}''$, Δ=0.62 AU, and the DGEAR model for three different values of R: 1 AU, 0.5 AU, and 2 AU. In all cases, $Q_{CO}=2\times10^{28}$ mol s^{-1} and $Q_{H2O}=10\times Q_{CO}$.

IVh: Same as (g), except using FOV=$\hat{1}'$.

ORIGINAL PAGE IS
OF POOR QUALITY

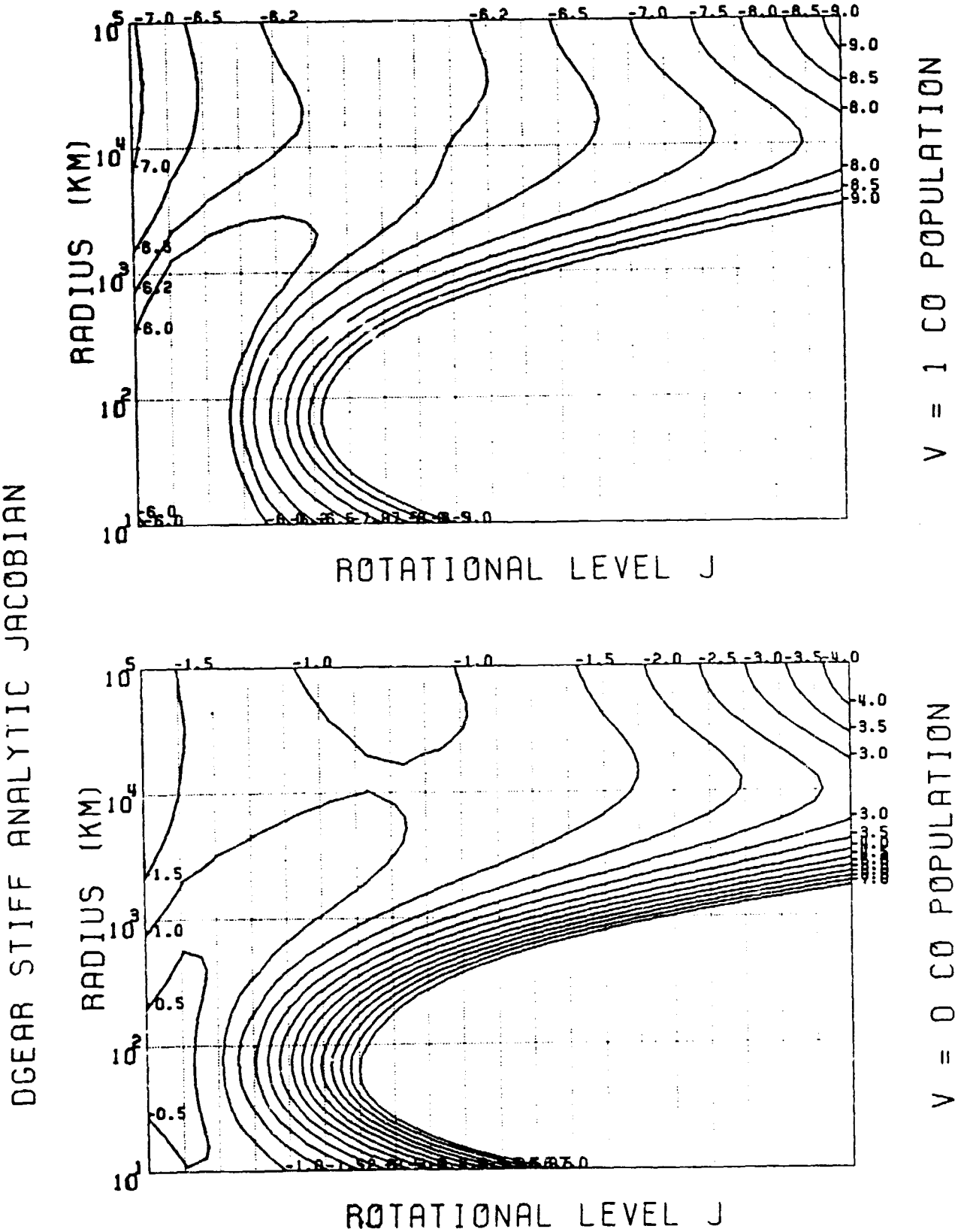

Figure Ia1.

ORIGINAL PAGE IS
OF POOR QUALITY

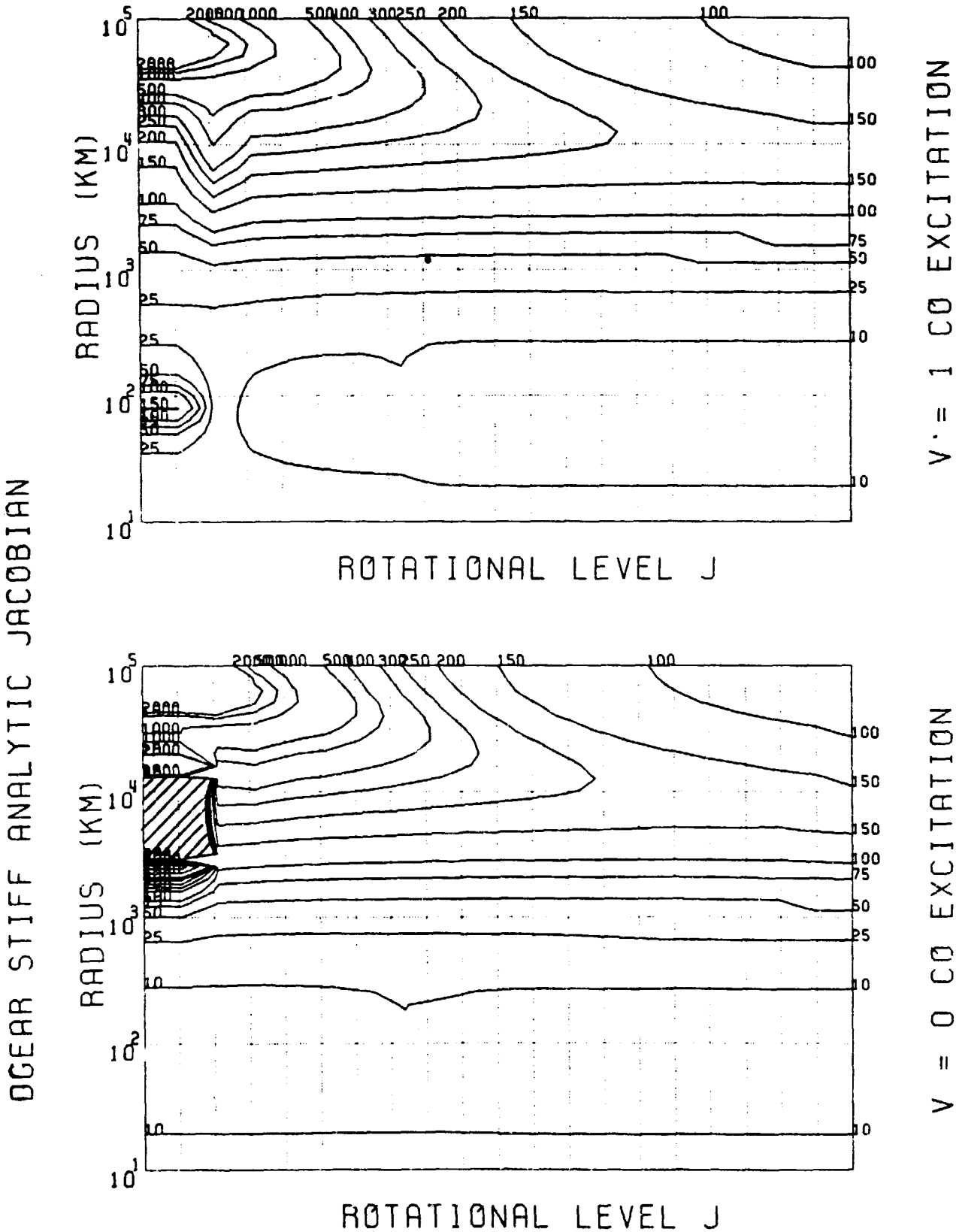

Figure Ia2.

ORIGINAL PAGE IS
OF POOR QUALITY

Steady-State

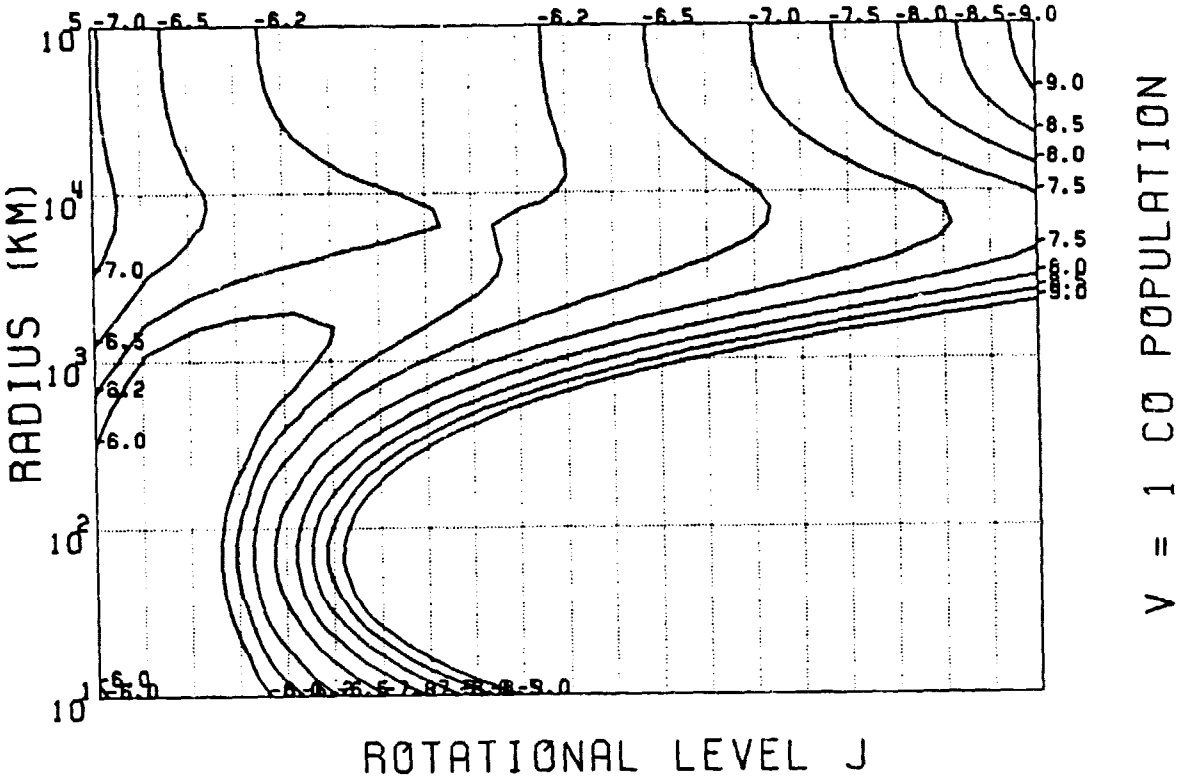

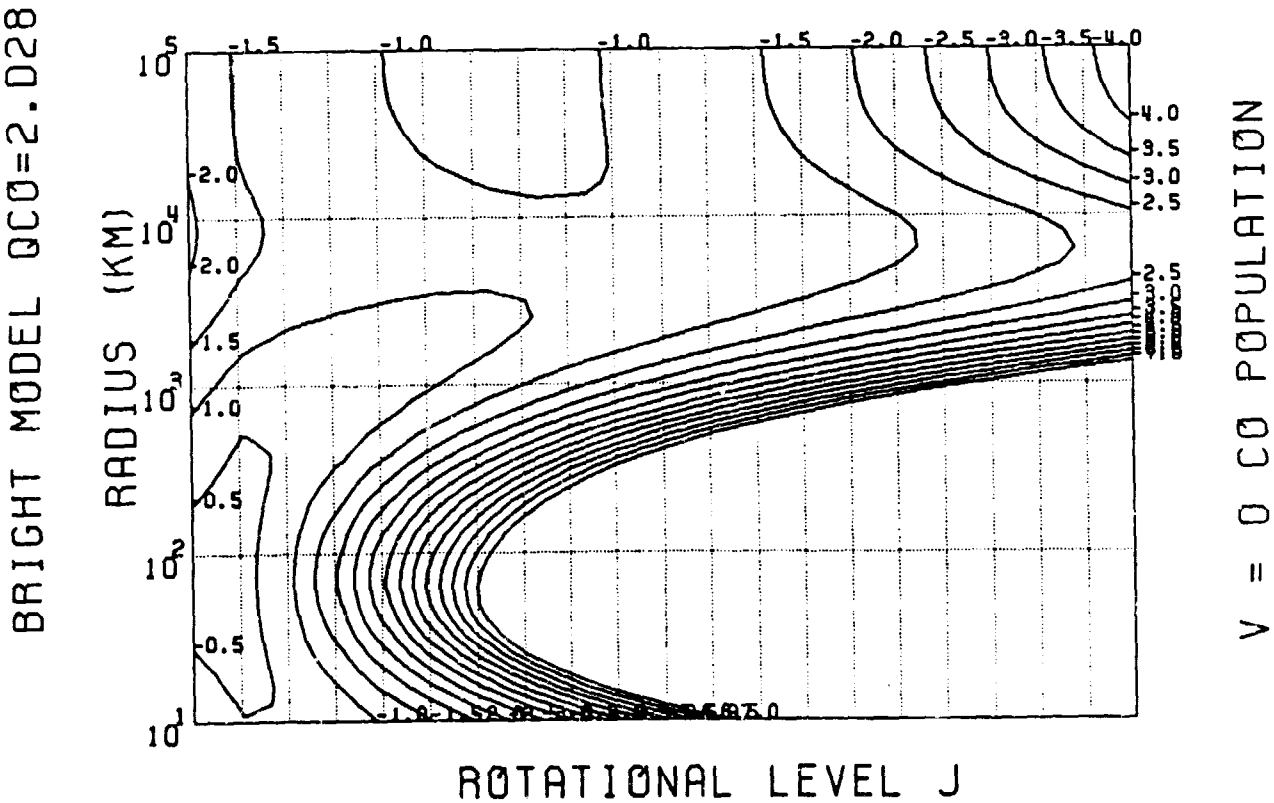

Figure Ib1.

ORIGINAL PAGE IS
OF POOR QUALITY

Steady-State

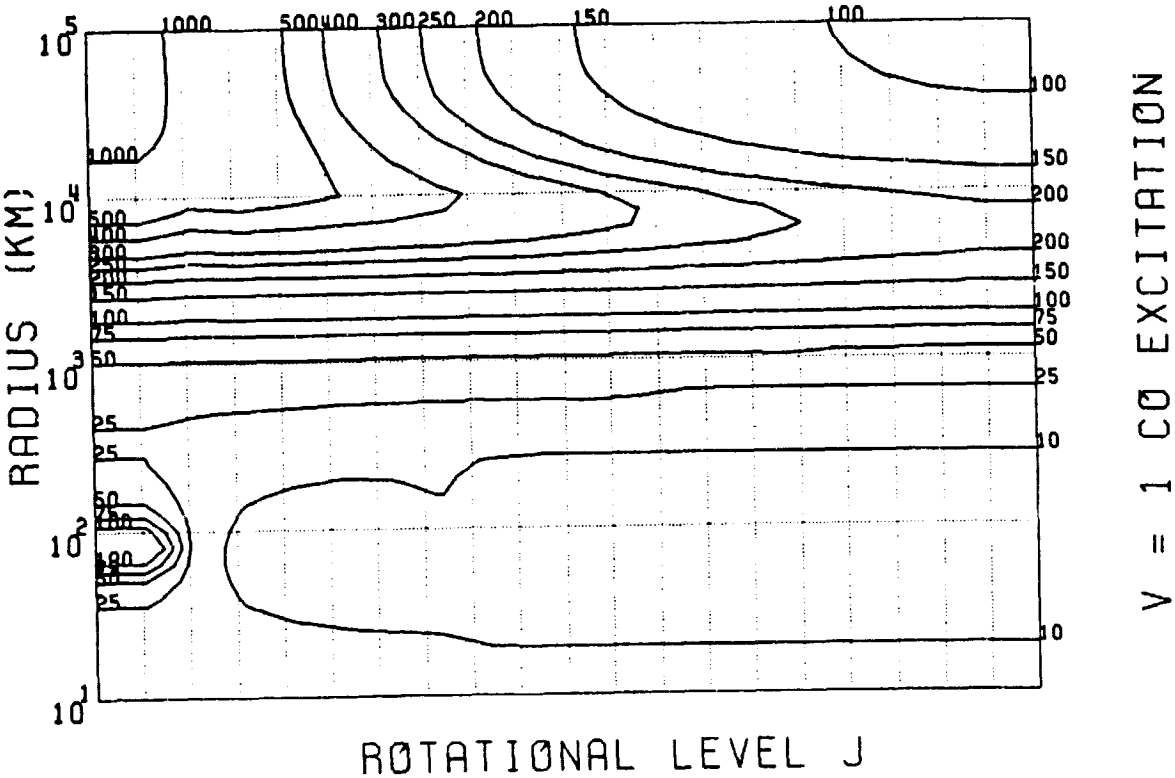

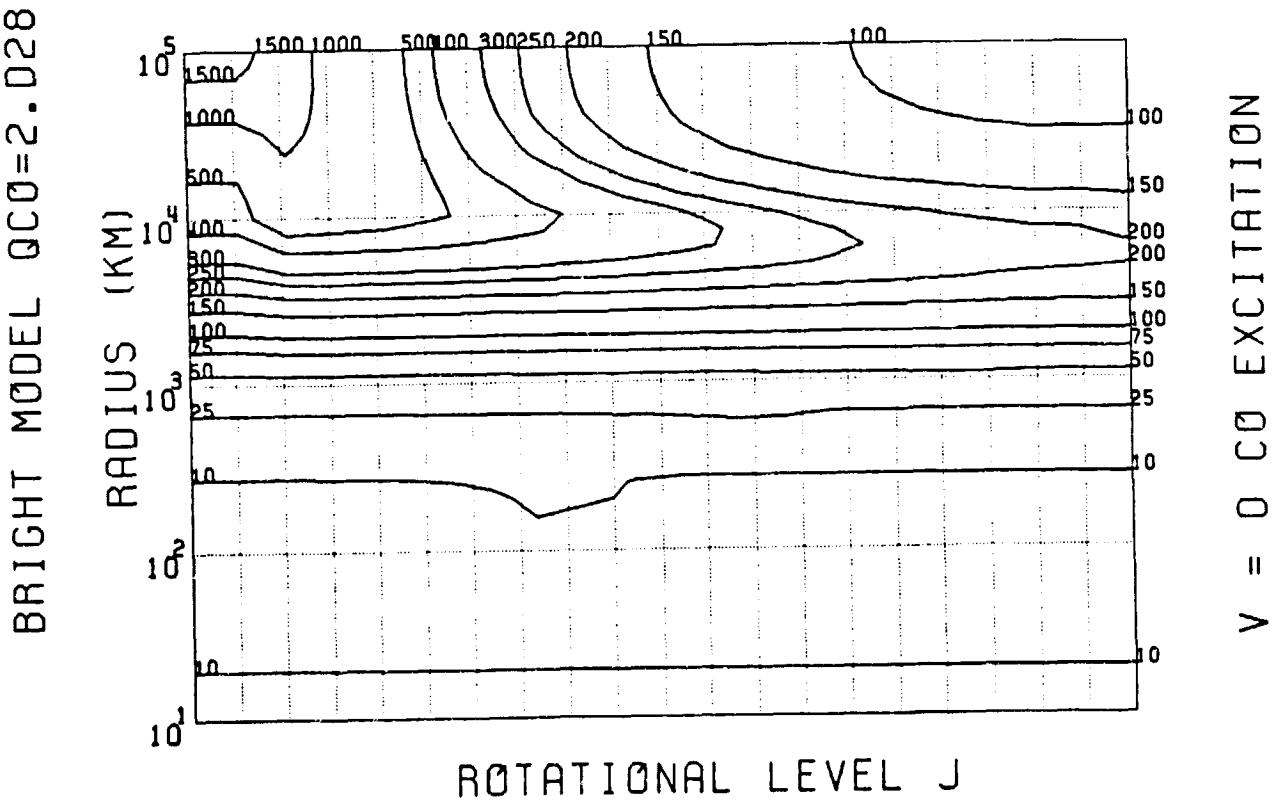

Figure Ib2.

ORIGINAL PAGE IS
OF POOR QUALITY

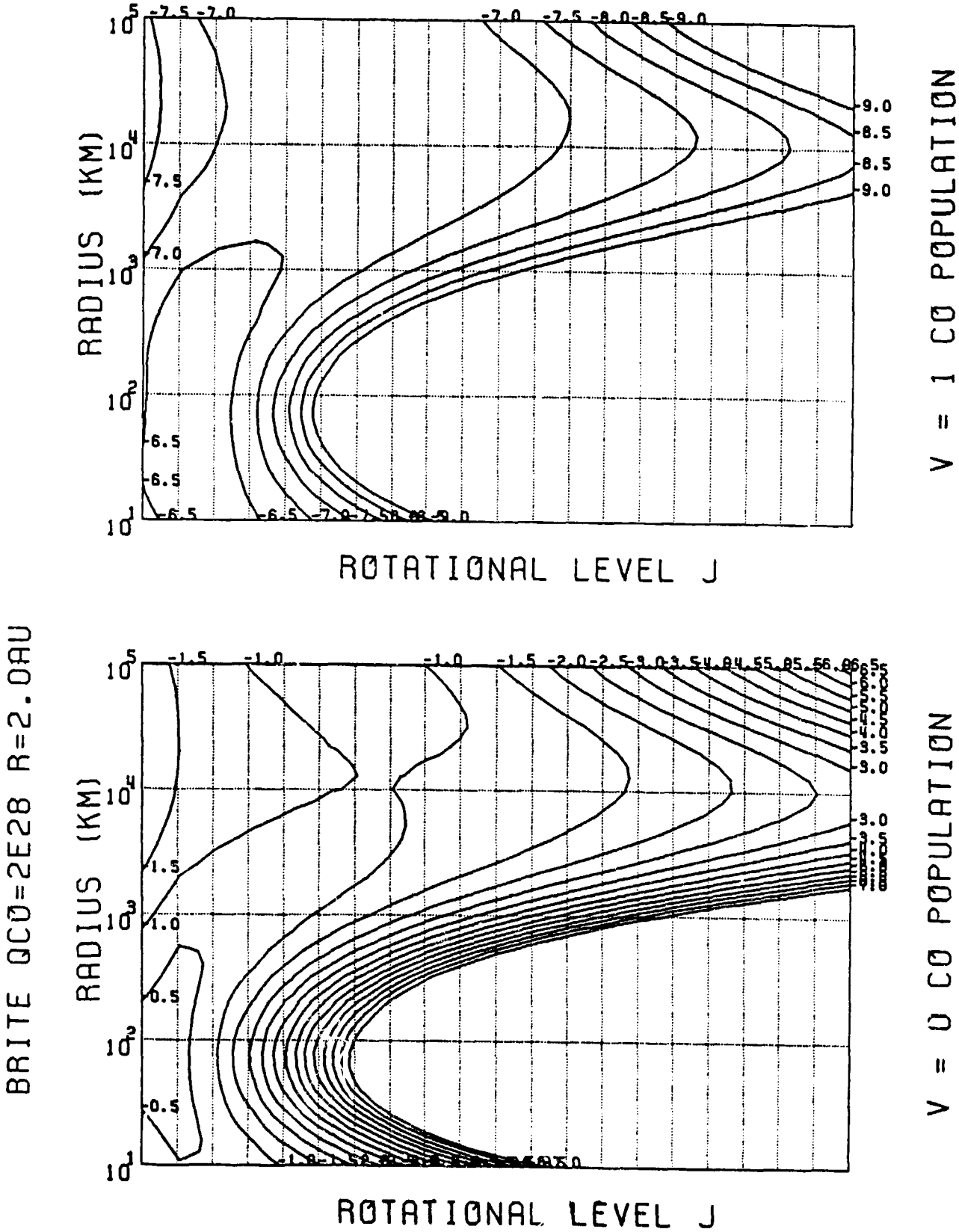

Figure Ic1.

ORIGINAL PAGE IS
OF POOR QUALITY

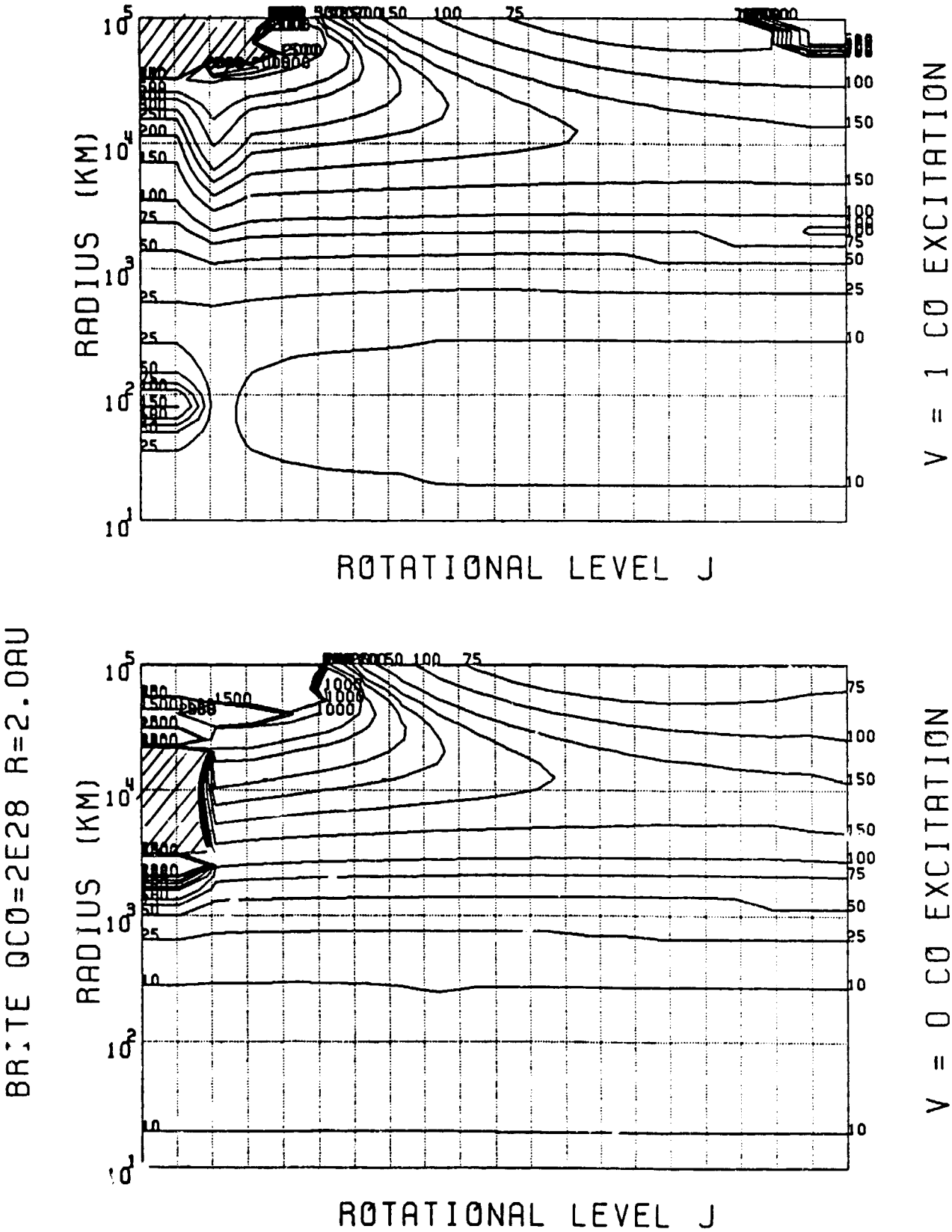

Figure Ic2.

ORIGINAL PAGE IS
OF POOR QUALITY

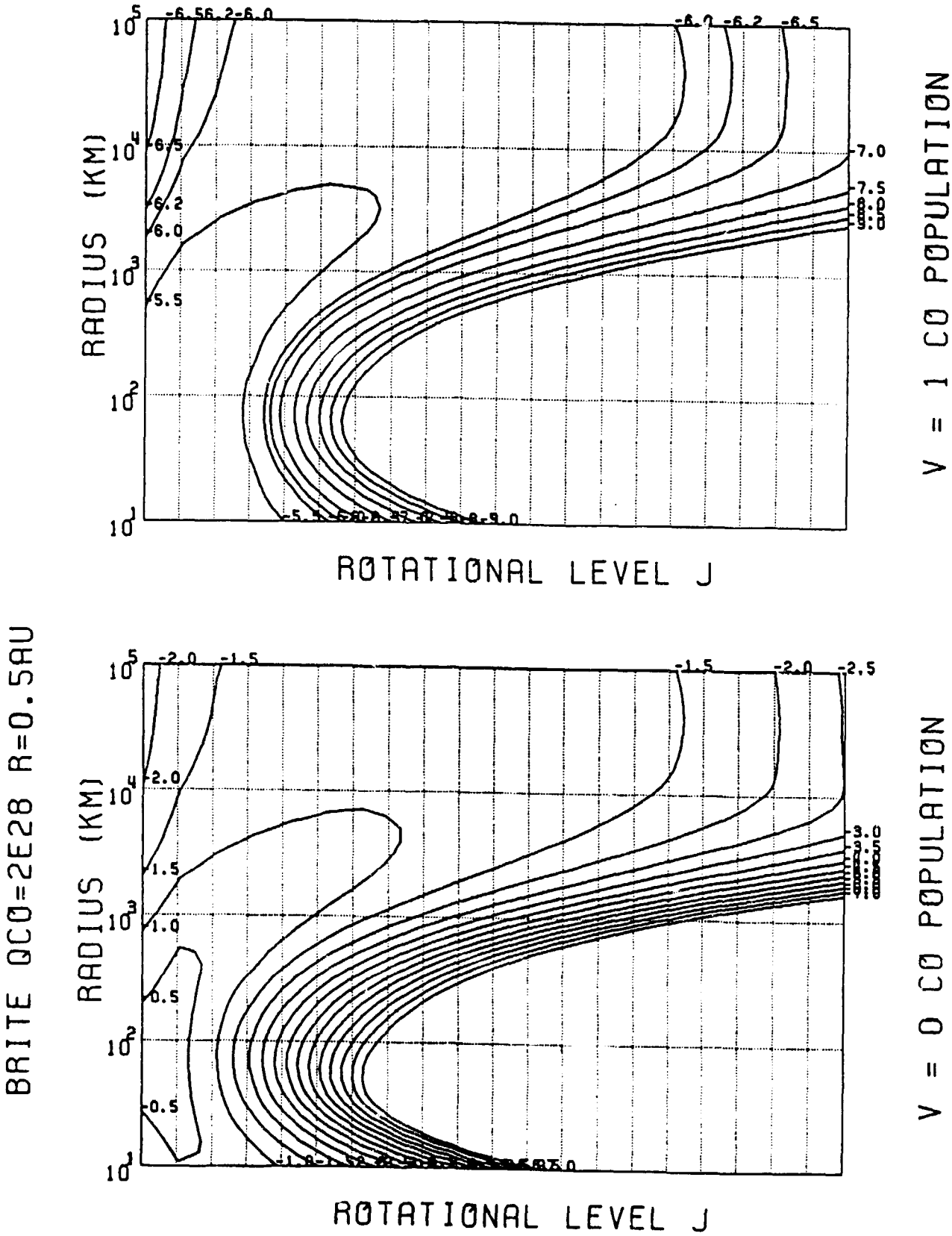

Figure Id1.

ORIGINAL PAGE IS
OF POOR QUALITY

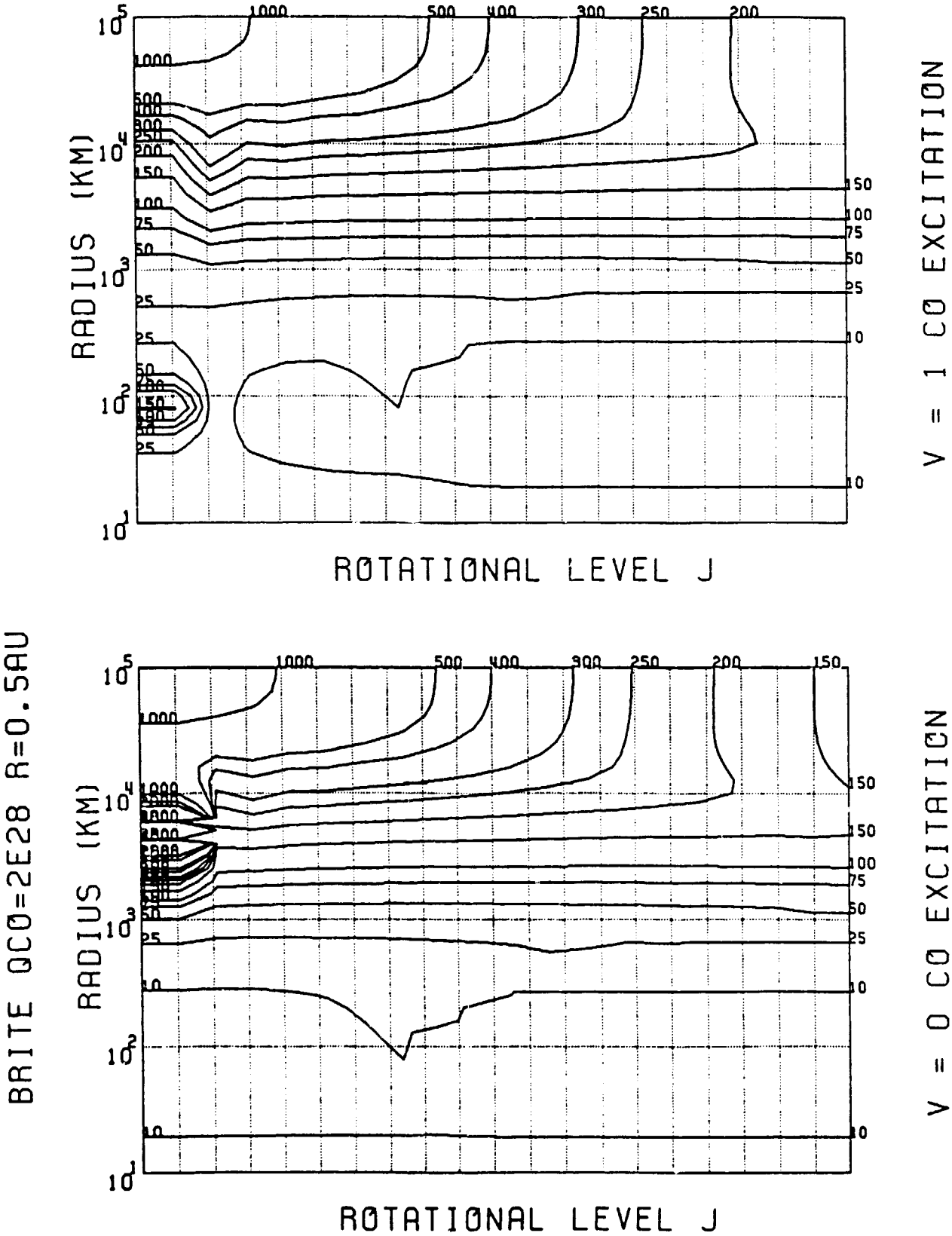

Figure Id2.

ORIGINAL PAGE IS
OF POOR QUALITY

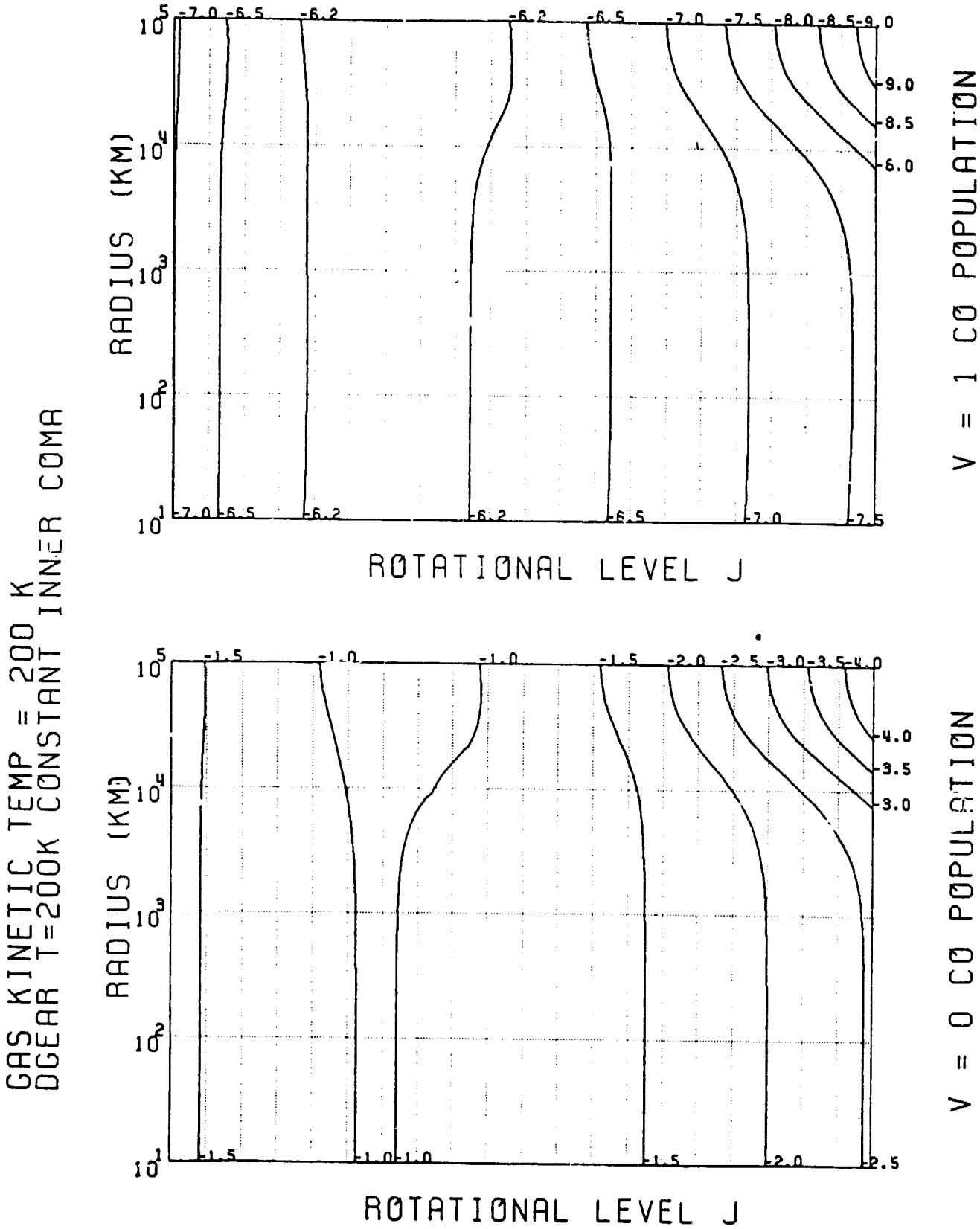

Figure Iel.

ORIGINAL PAGE IS
OF POOR QUALITY

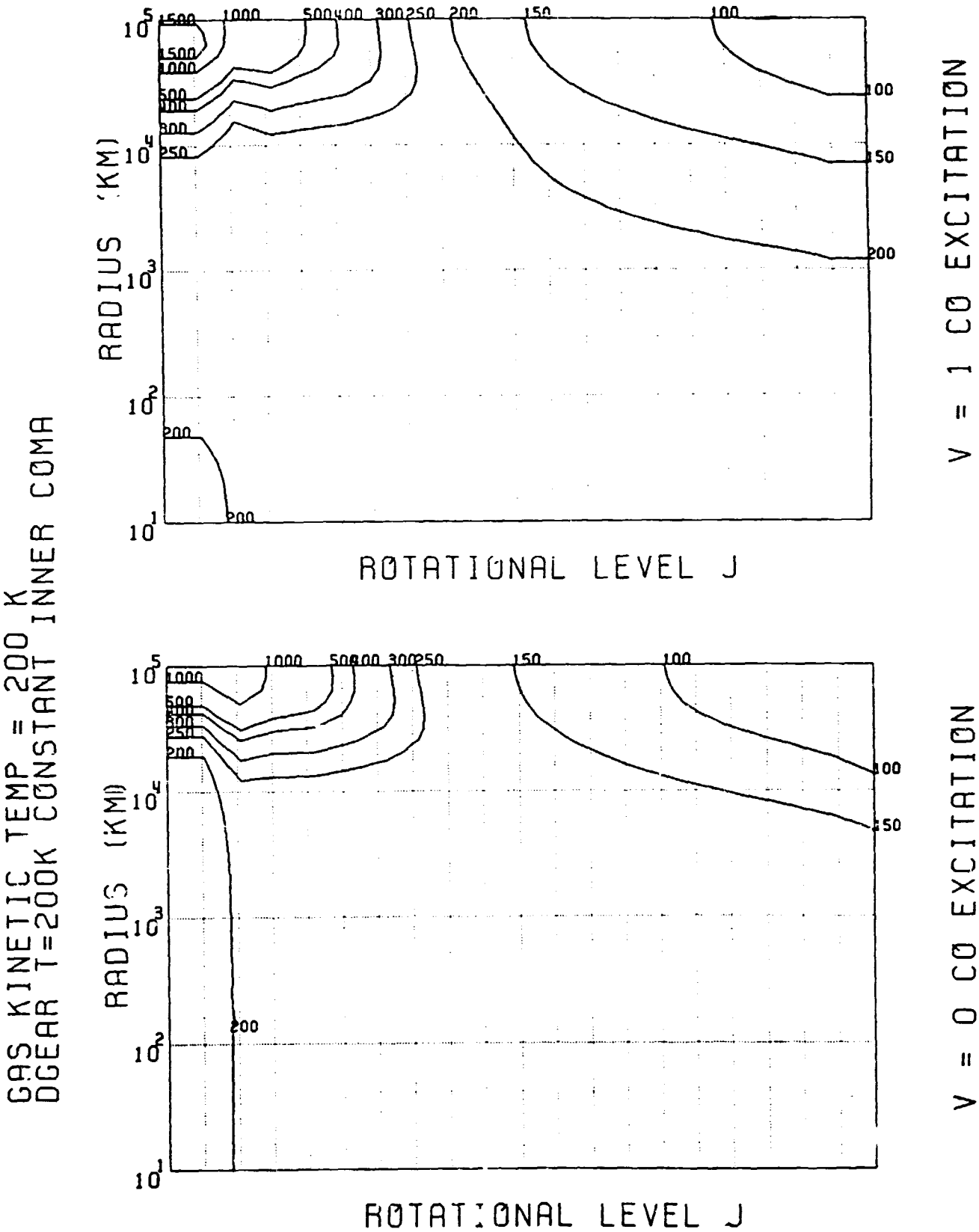

Figure Ie2.

ORIGINAL PAGE IS
OF POOR QUALITY

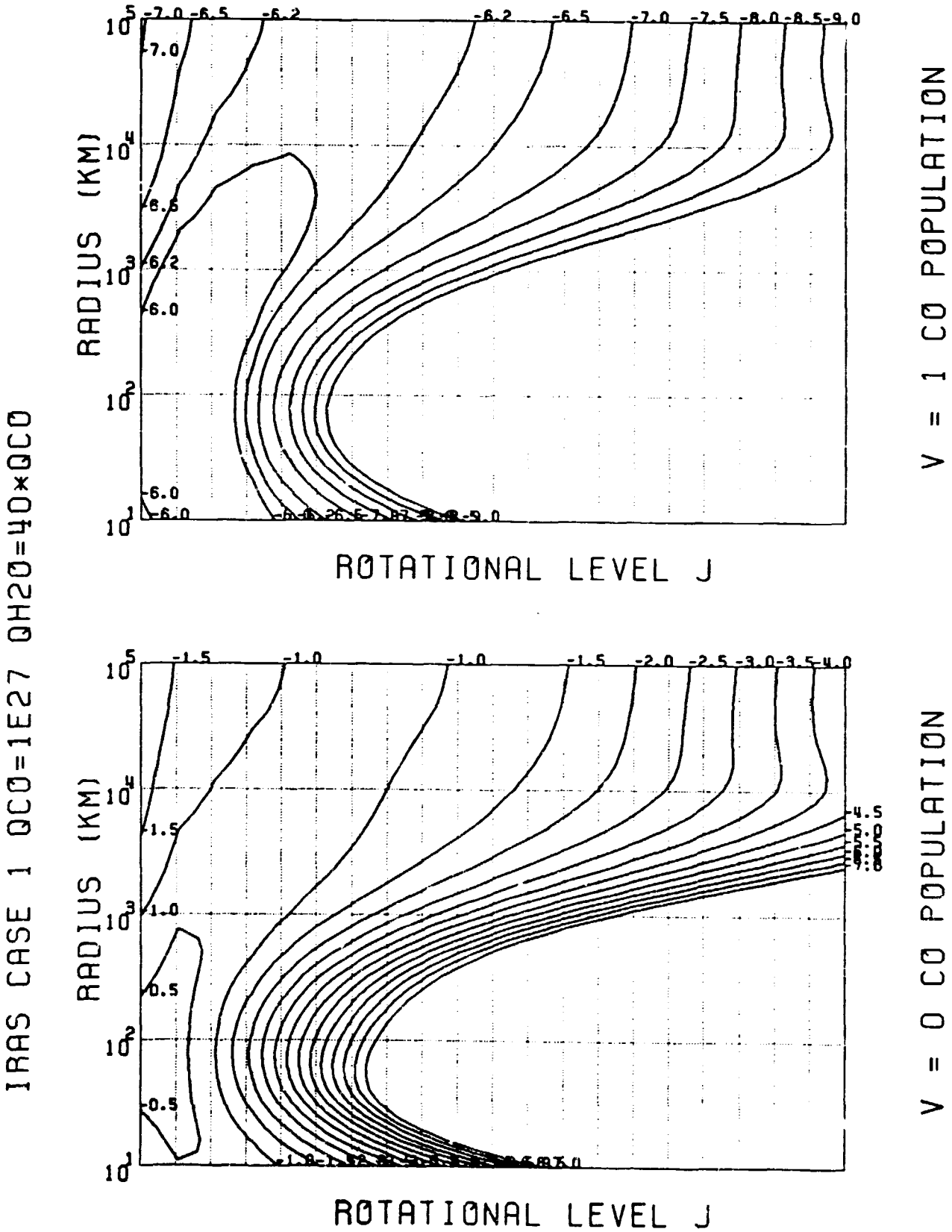

Figure If1.

ORIGINAL PAGE IS
OF POOR QUALITY

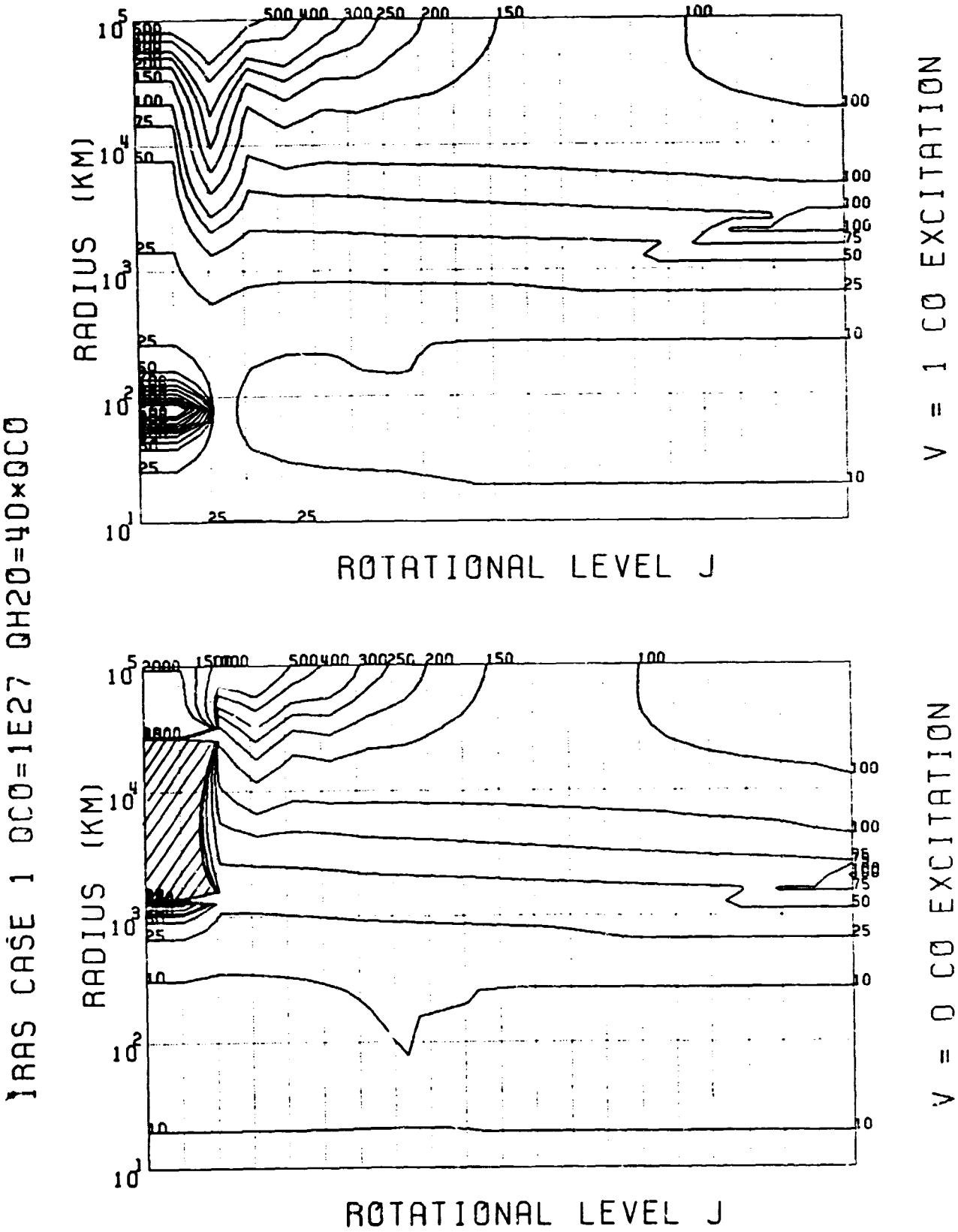

Figure If2.

ORIGINAL PAGE IS
OF POOR QUALITY

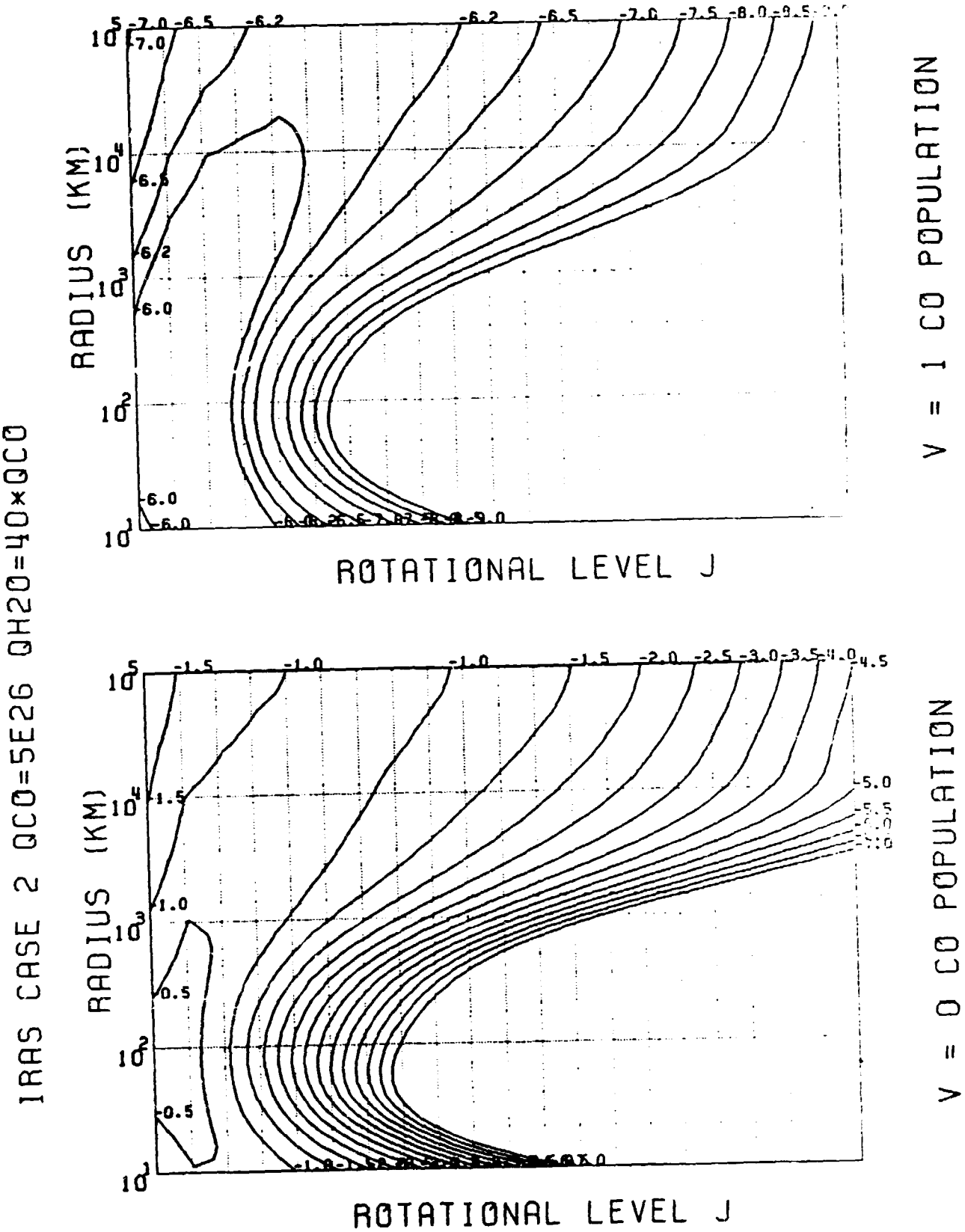

Figure Igl.

ORIGINAL PAGE IS
OF POOR QUALITY

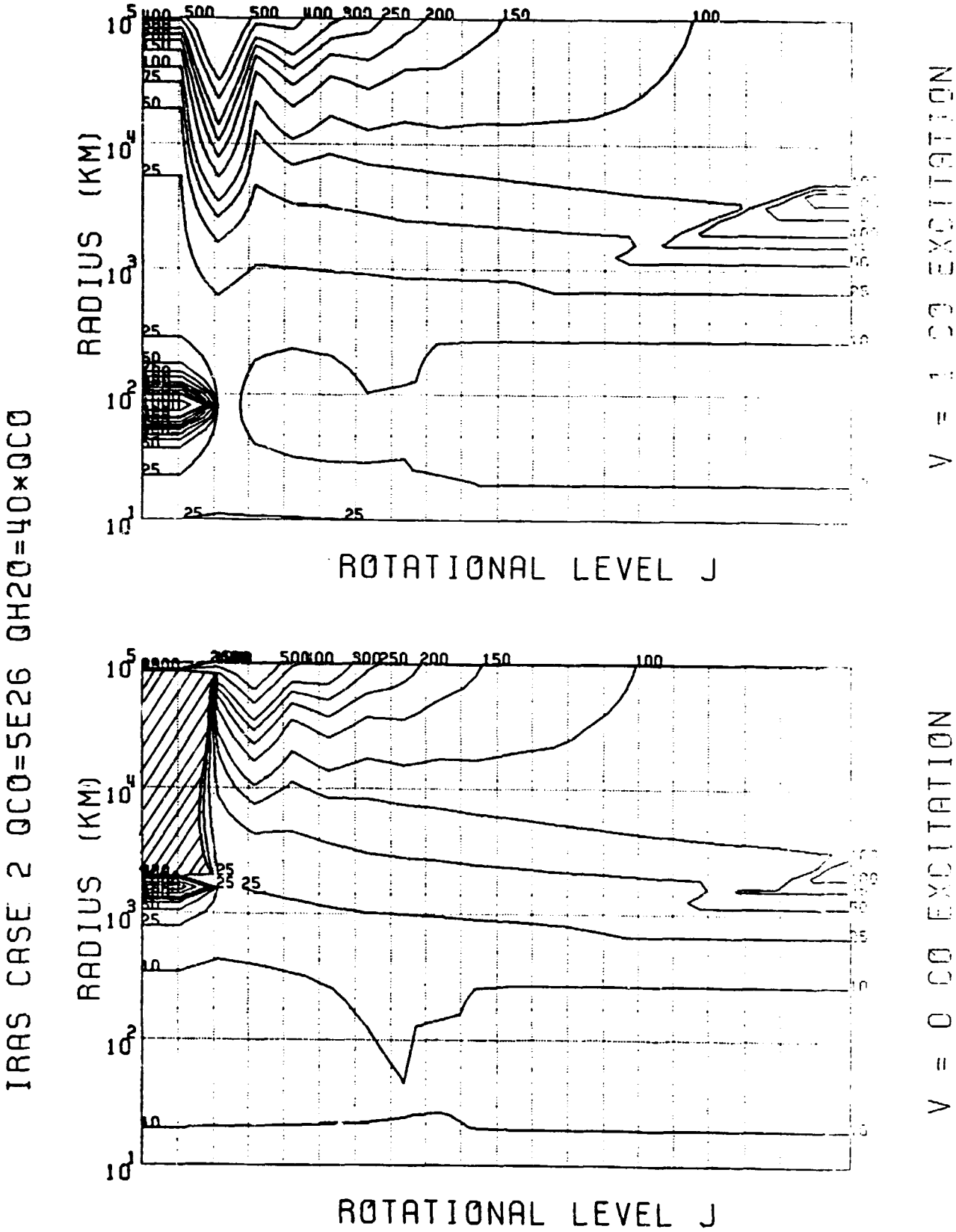

Figure Ig2.

ORIGINAL PAGE IS
OF POOR QUALITY

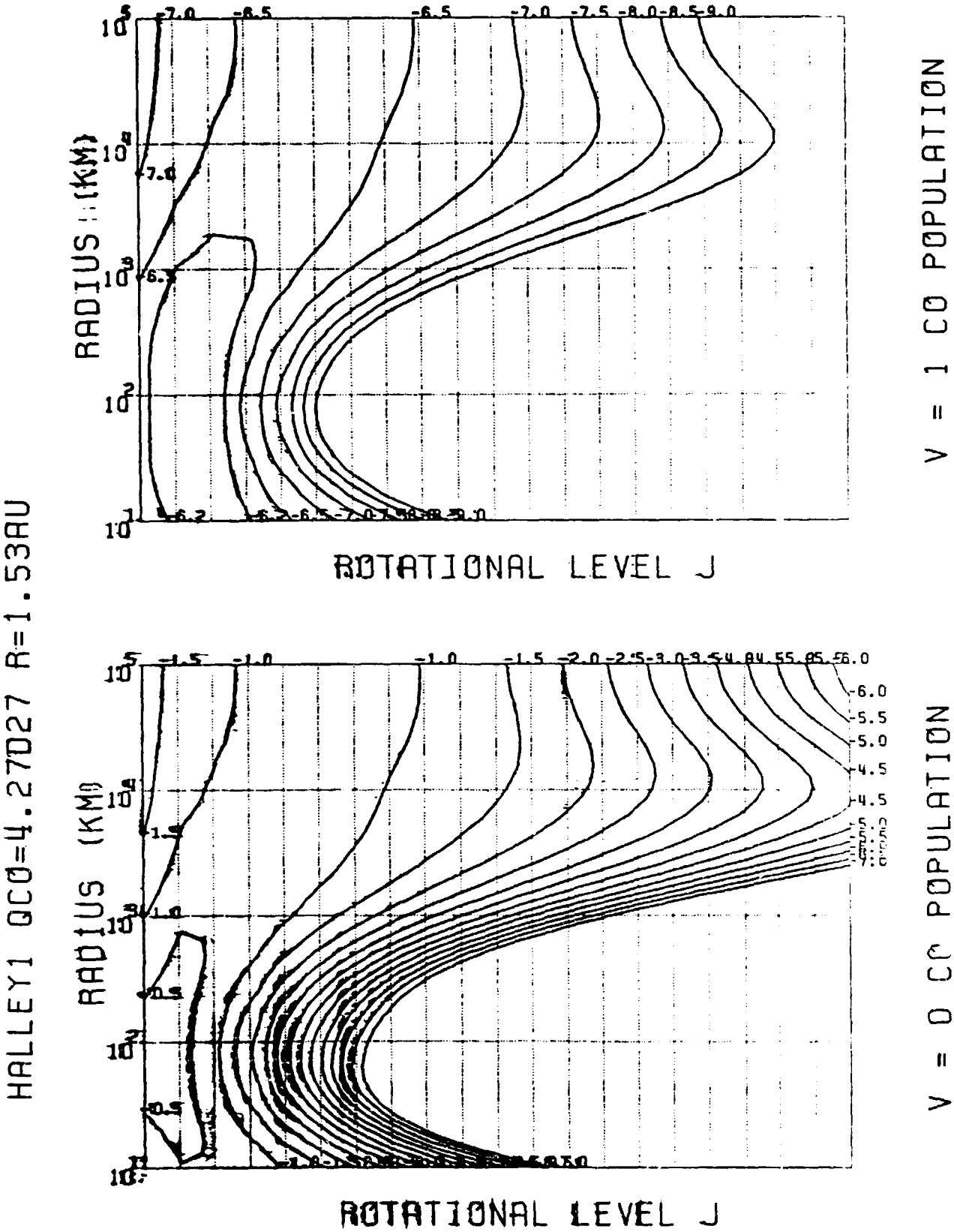

Figure Ihl.

ORIGINAL PAGE IS
OF POOR QUALITY

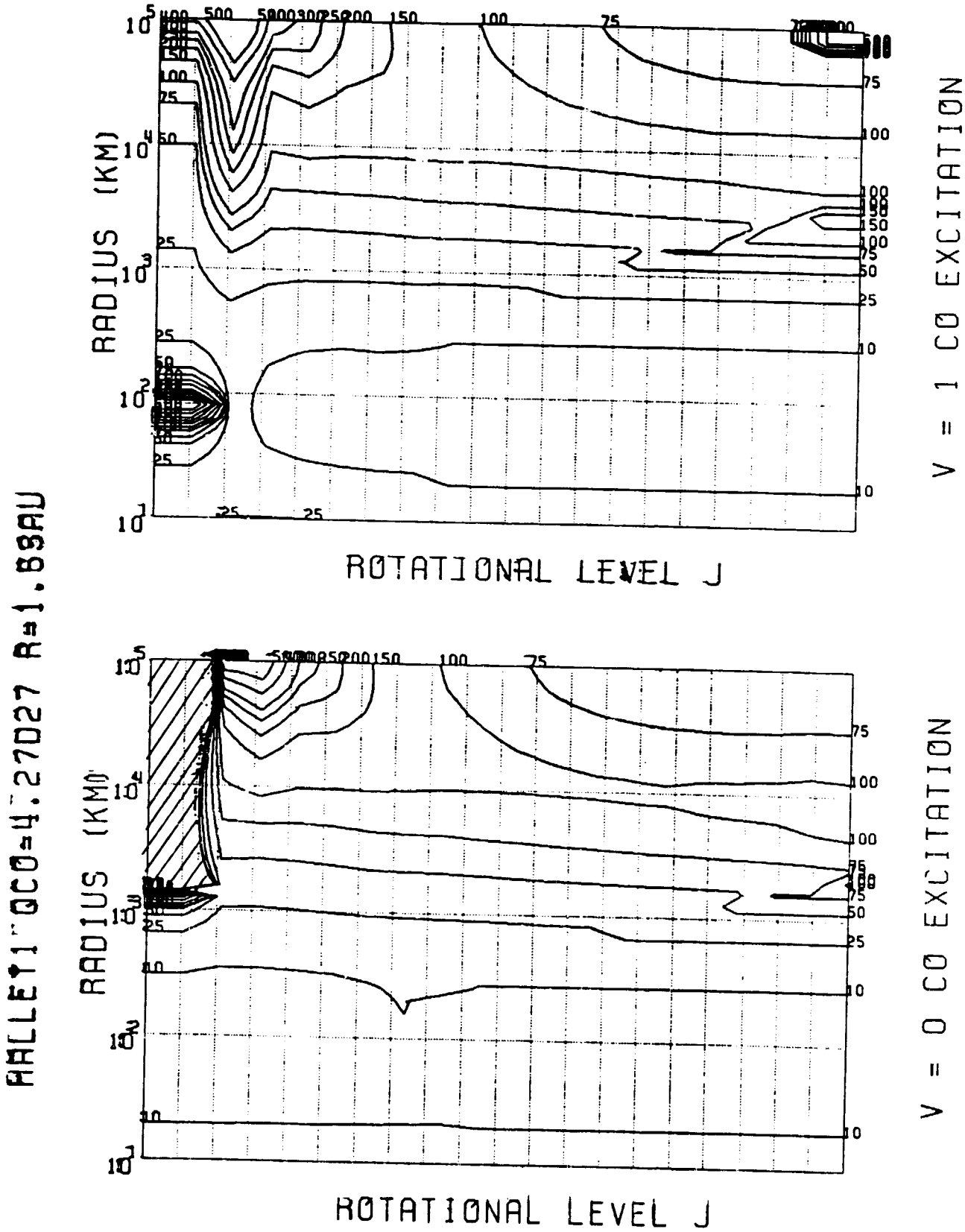

Figure Ih2.

ORIGINAL PAGE IS
OF POOR QUALITY

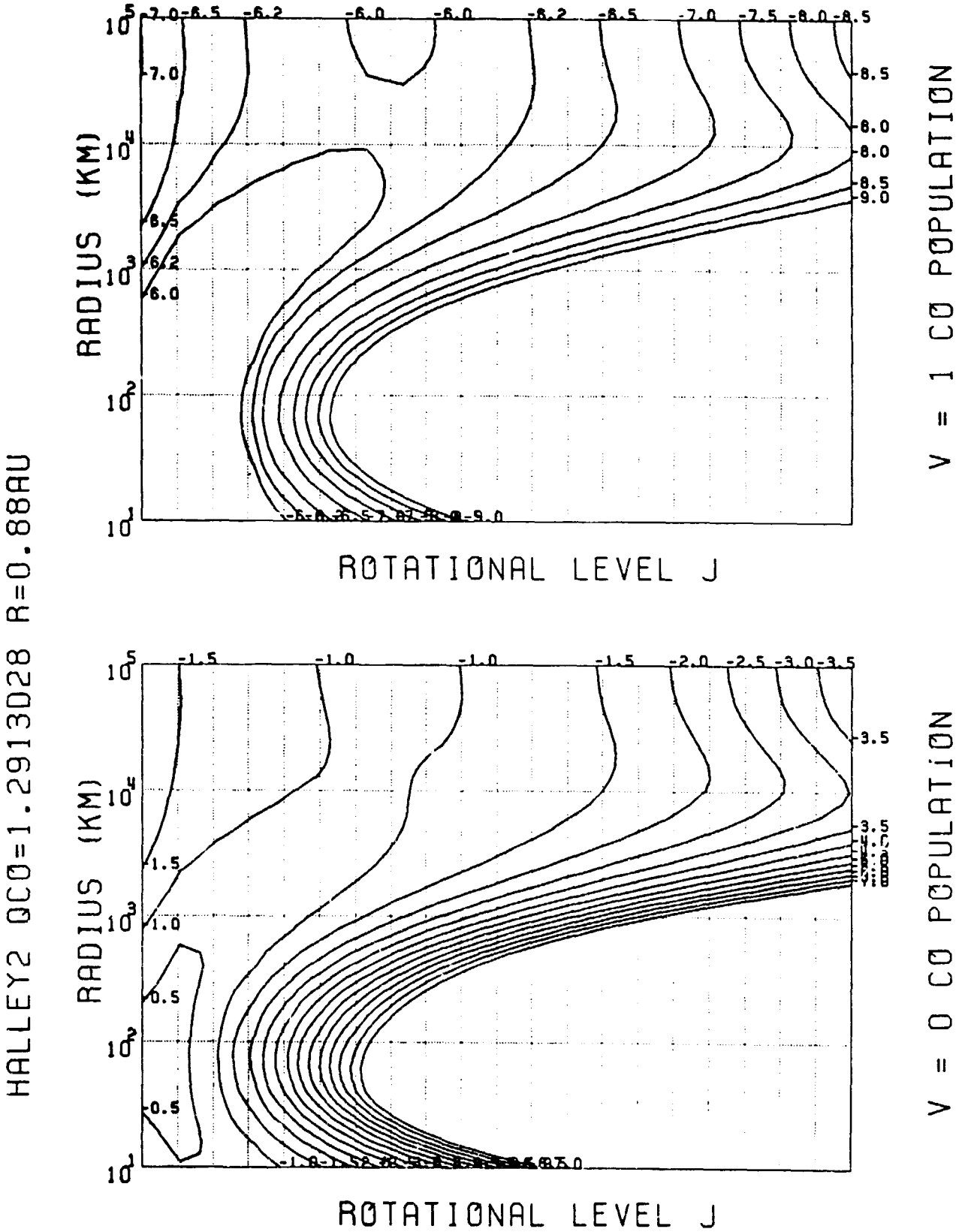

Figure Ii1.

ORIGINAL PAGE IS
OF POOR QUALITY

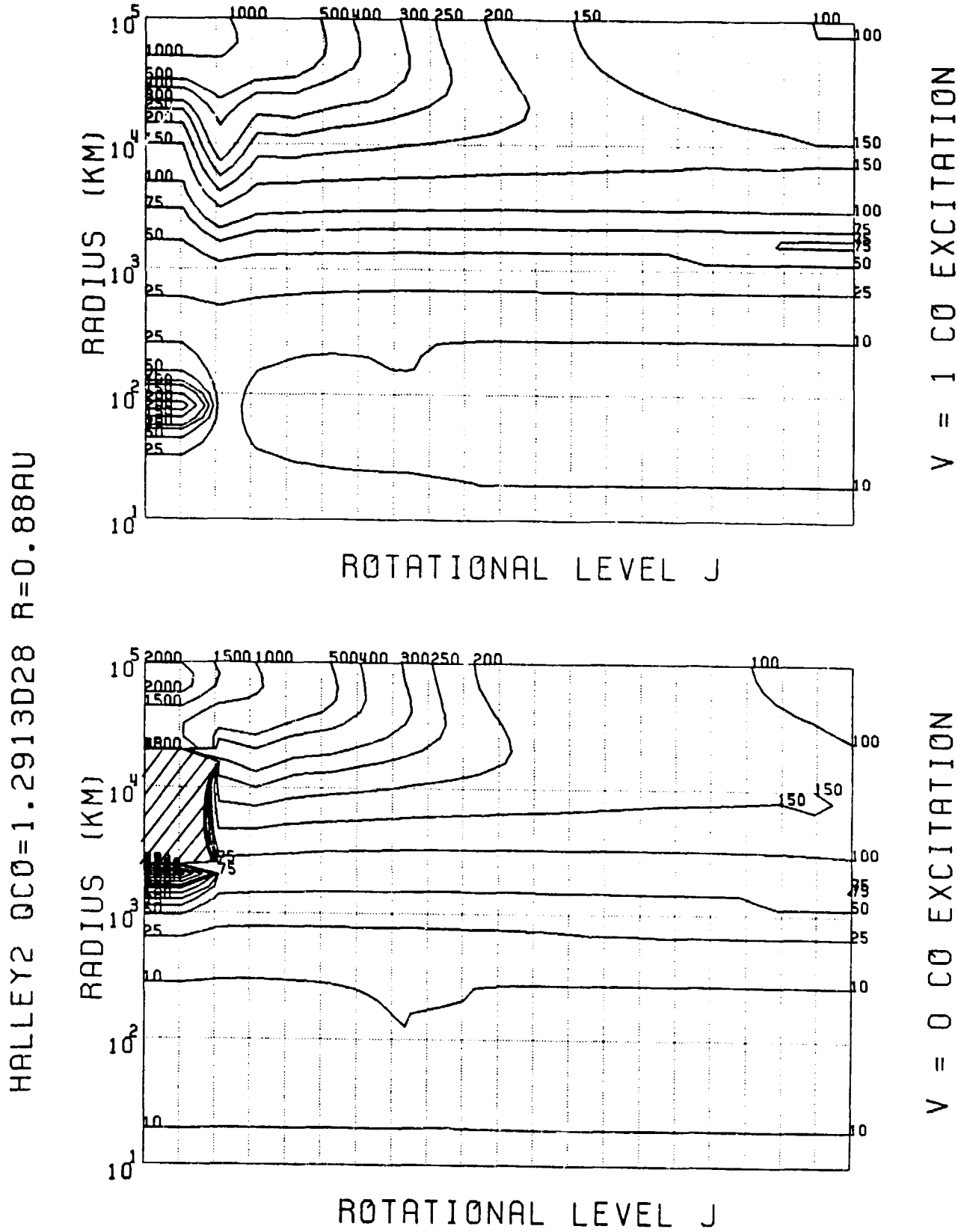

Figure I12.

ORIGINAL PAGE IS
OF POOR QUALITY

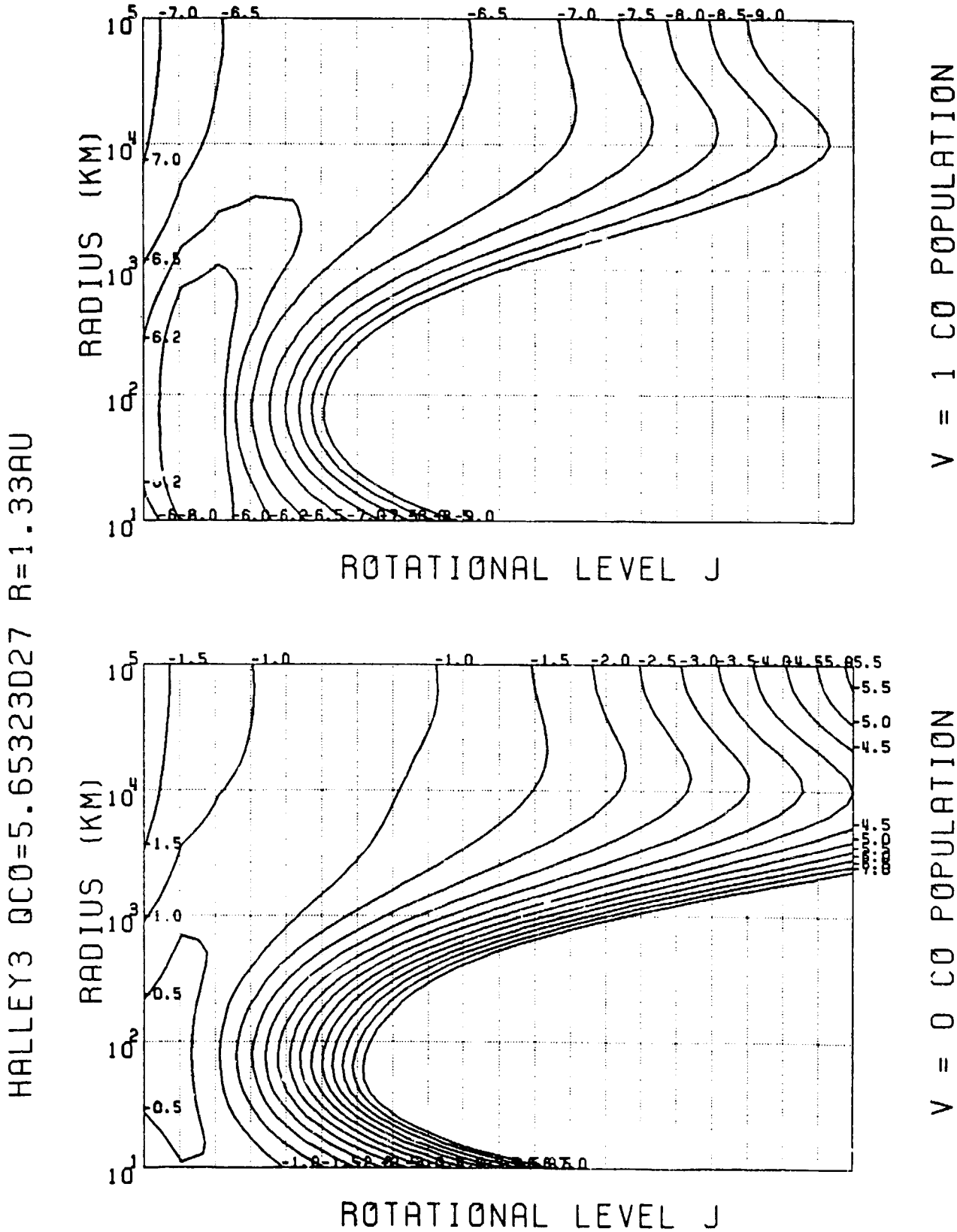

Figure Ij1.

ORIGINAL PAGE IS
OF POOR QUALITY

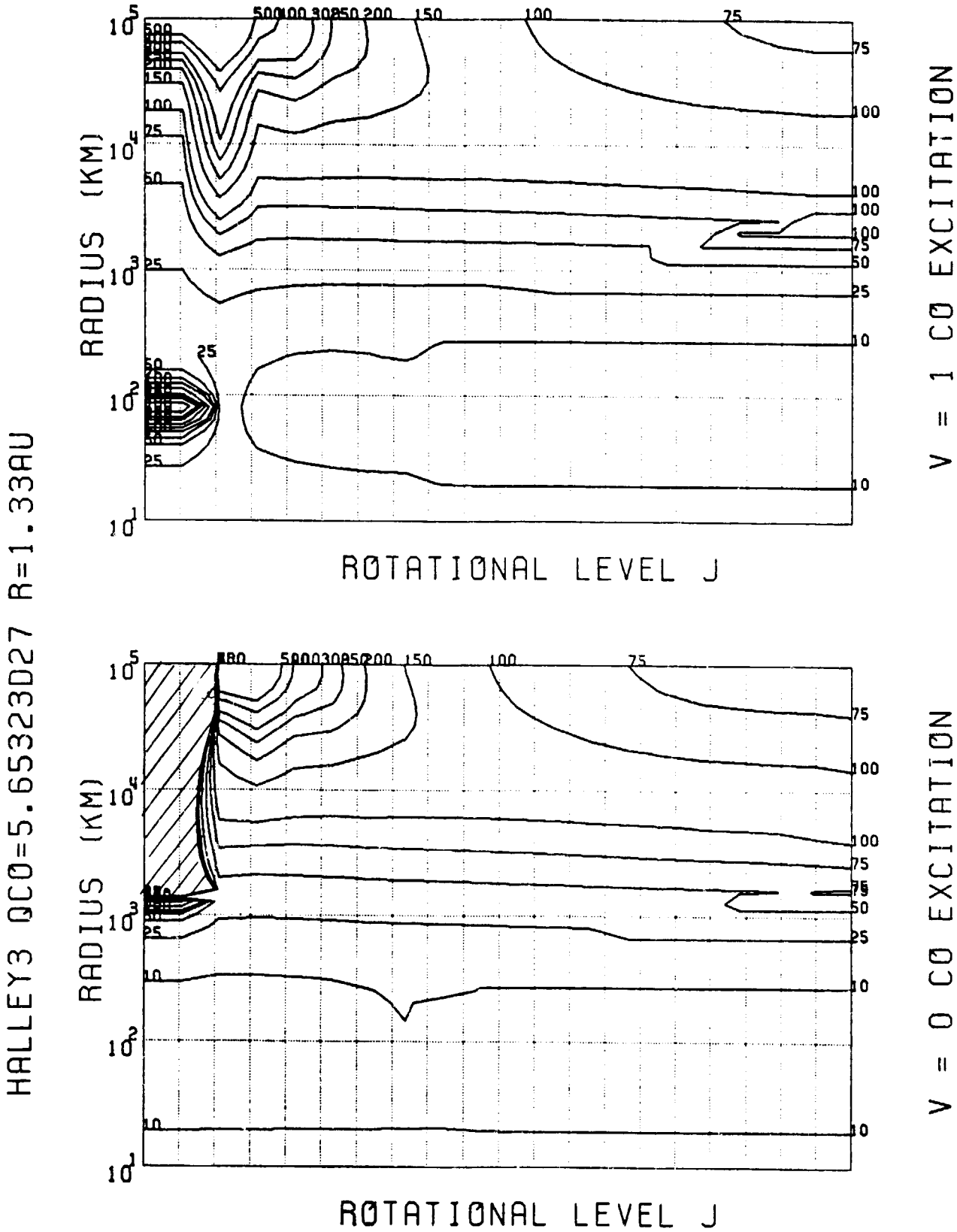

Figure Ij2.

ORIGINAL PAGE IS
OF POOR QUALITY

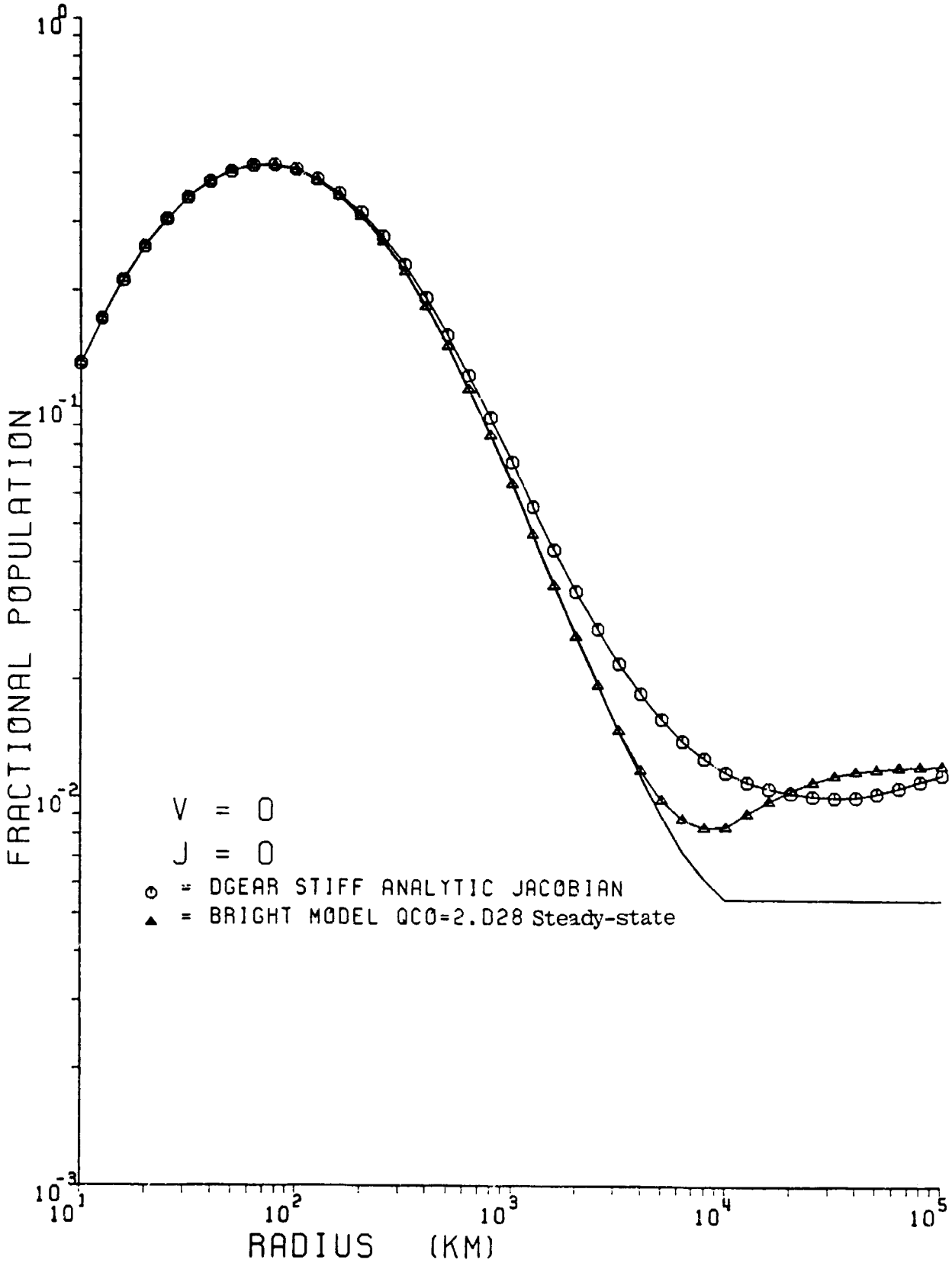

Figure IIa1.

ORIGINAL PAGE IS
OF POOR QUALITY

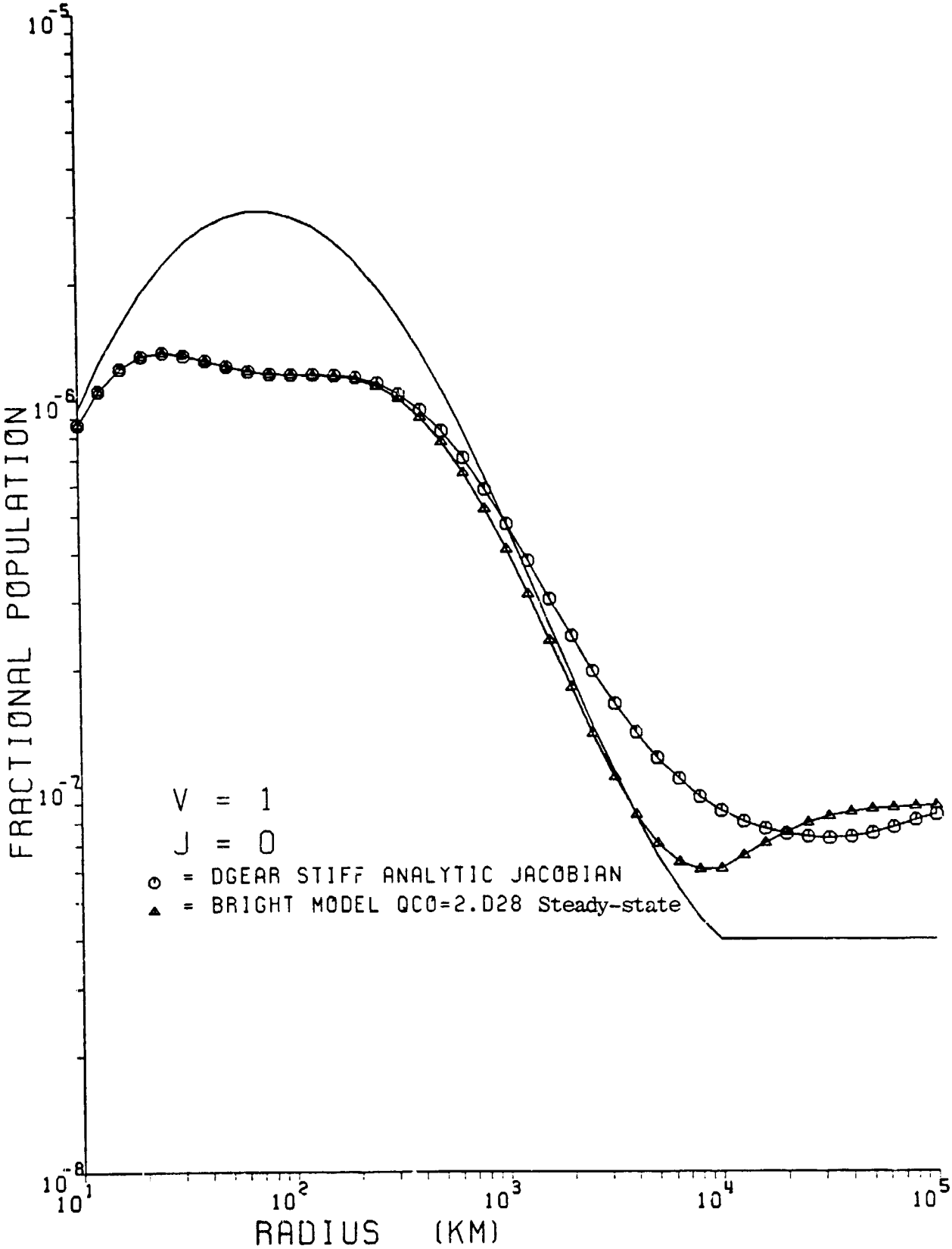

Figure IIa2.

ORIGINAL PAGE IS
OF POOR QUALITY

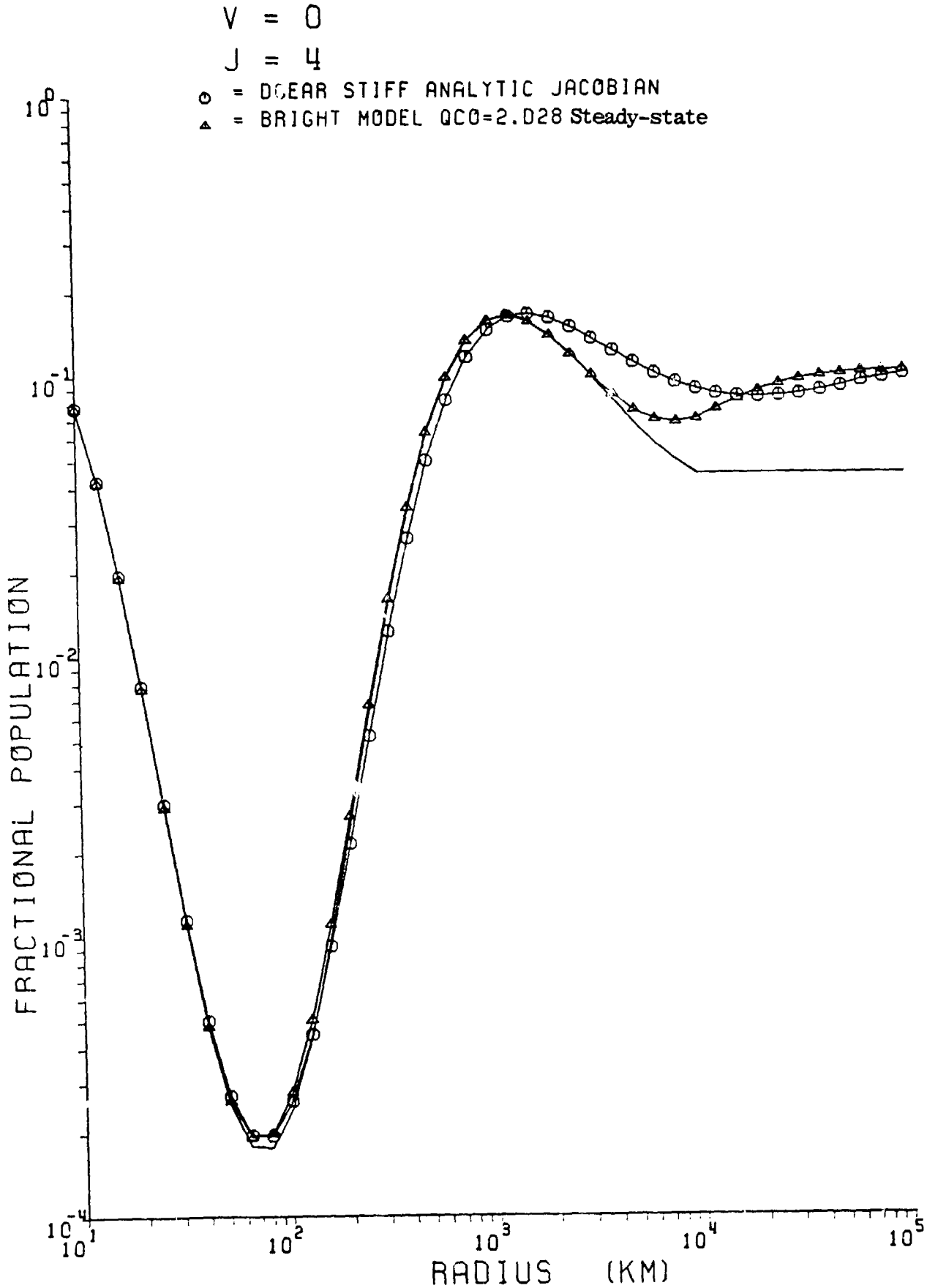

Figure IIa3.

ORIGINAL PAGE IS
OF POOR QUALITY

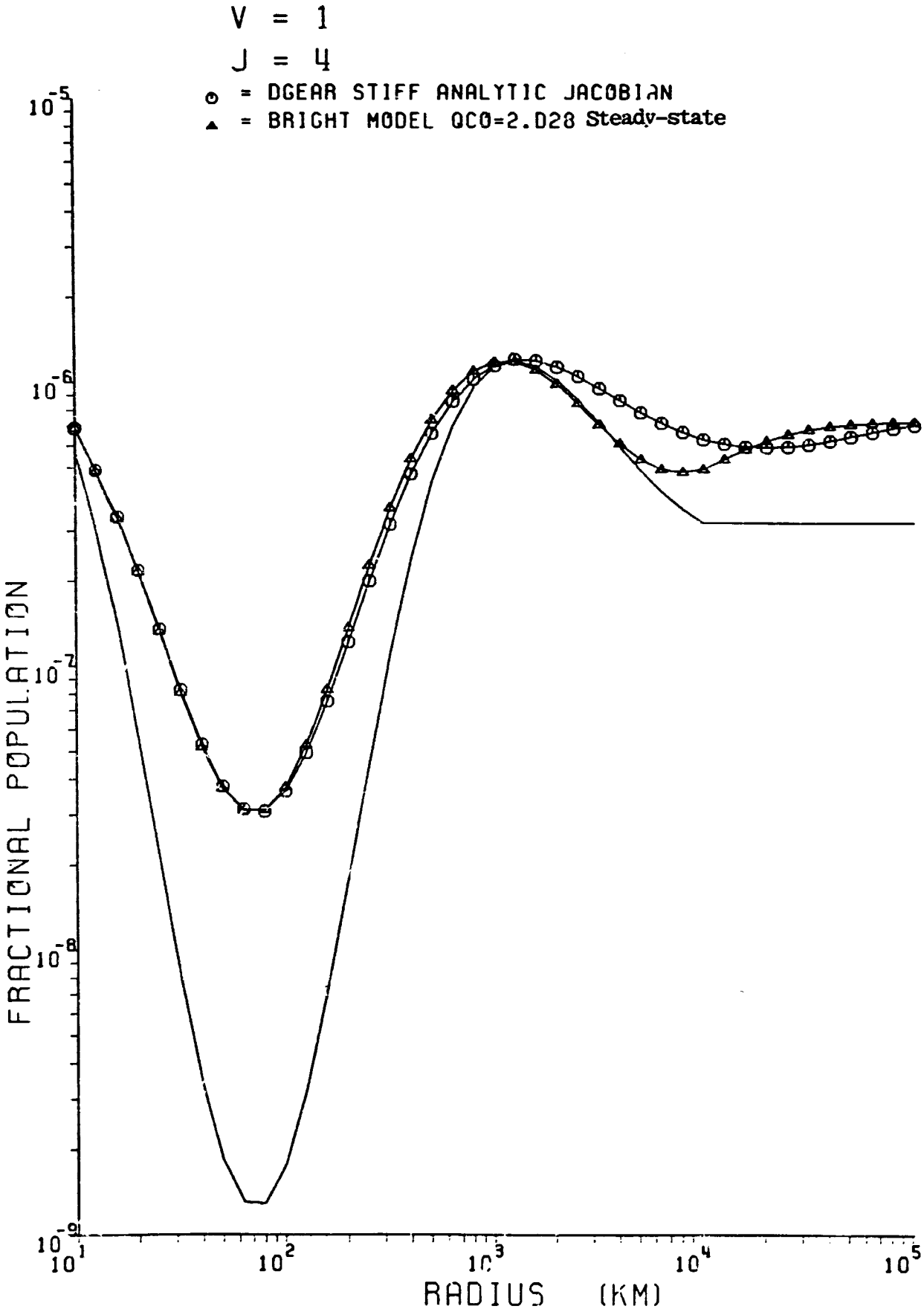

Figure IIa4.

ORIGINAL PAGE IS
OF POOR QUALITY

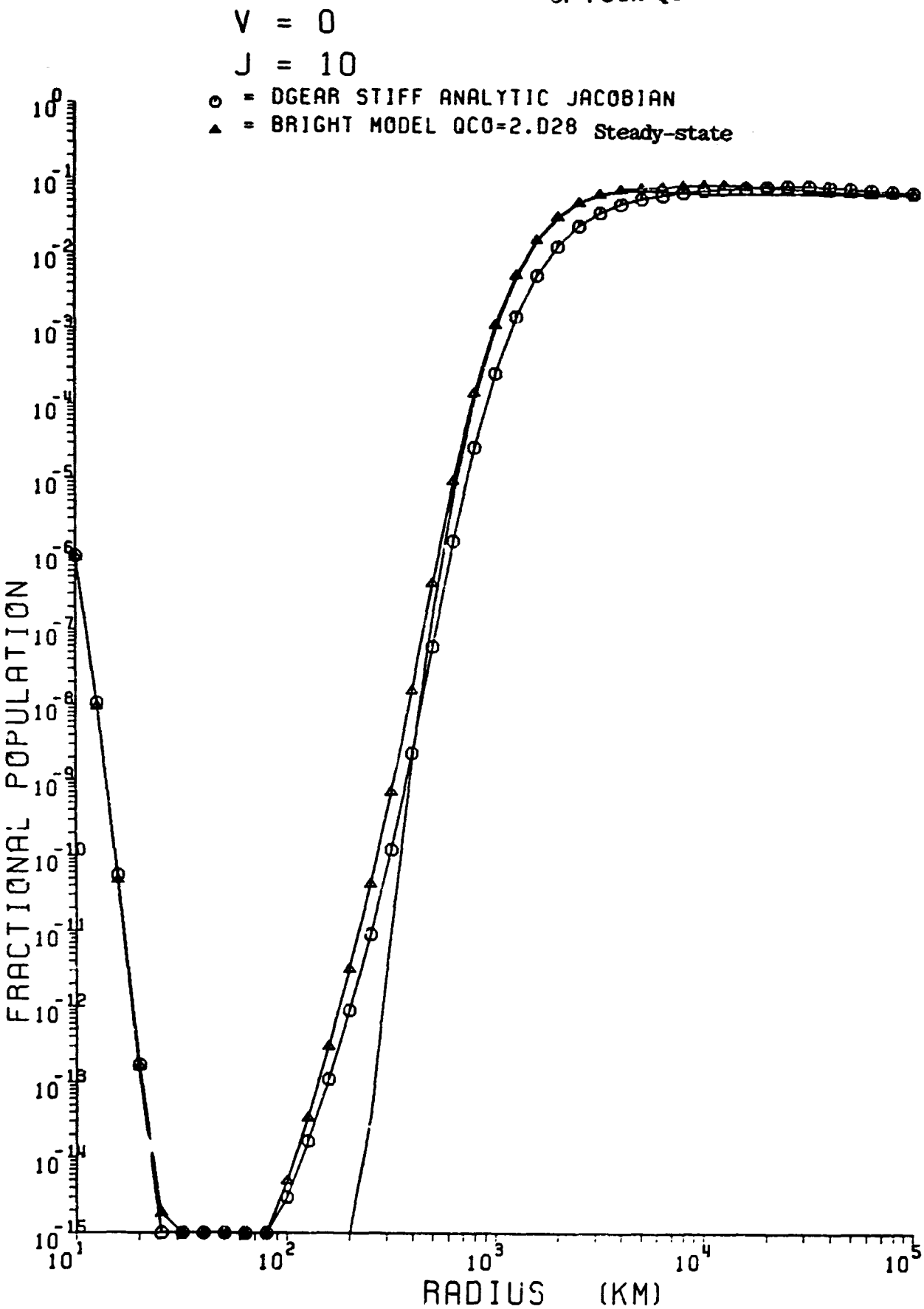

Figure IIa5.

ORIGINAL PAGE IS
OF POOR QUALITY

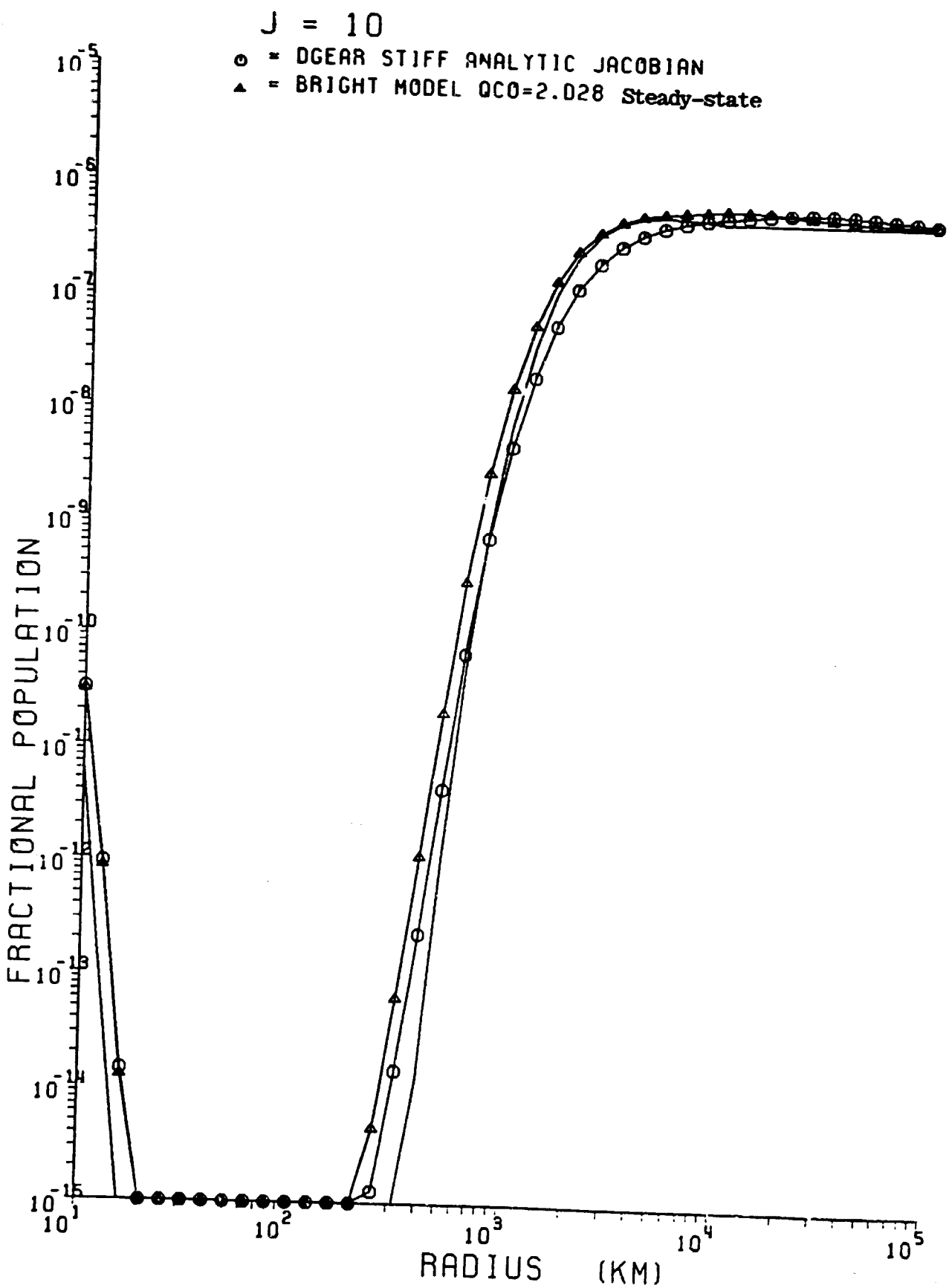

Figure IIa6.

ORIGINAL PAGE IS
OF POOR QUALITY

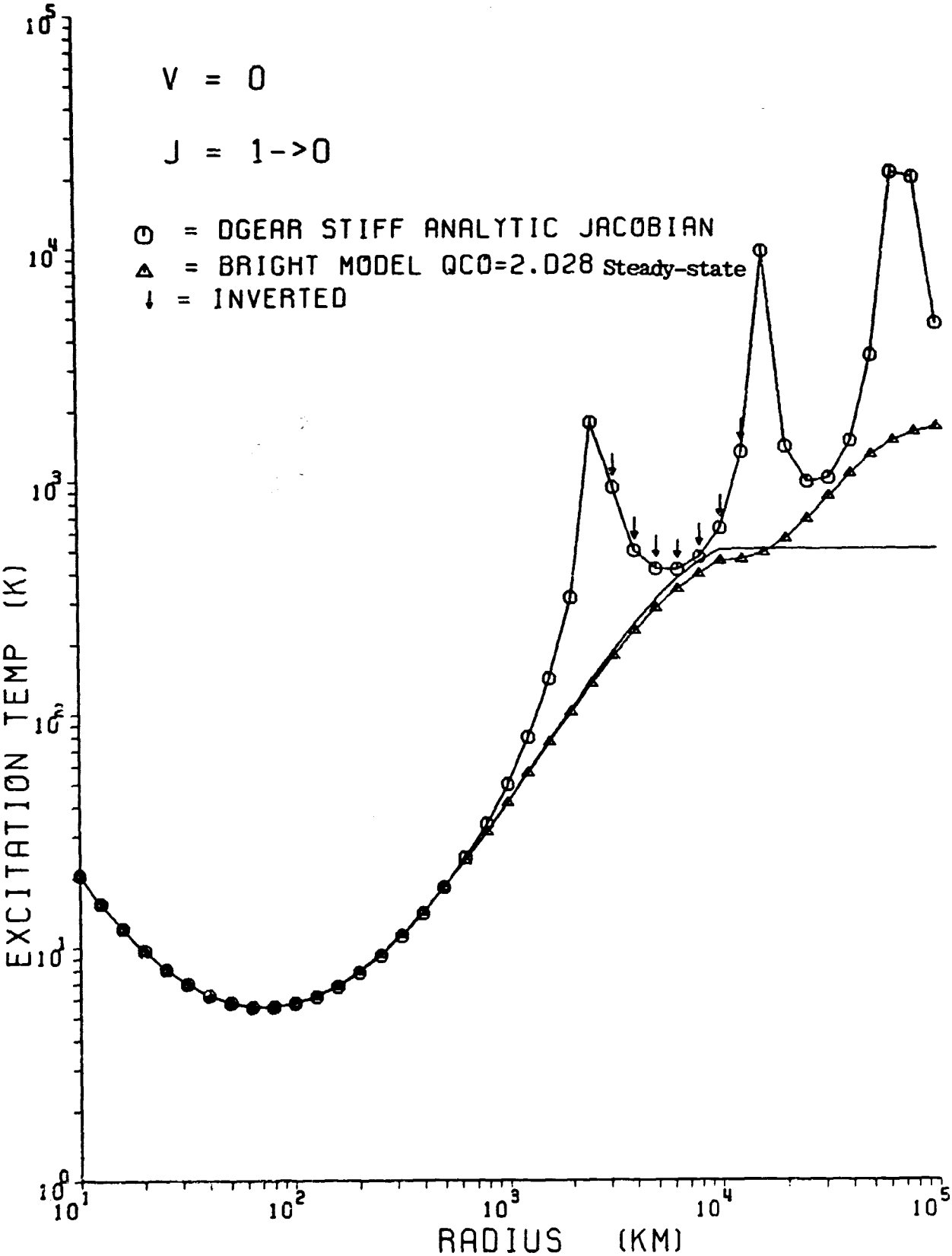

Figure IIa7.

ORIGINAL PAGE IS
OF POOR QUALITY

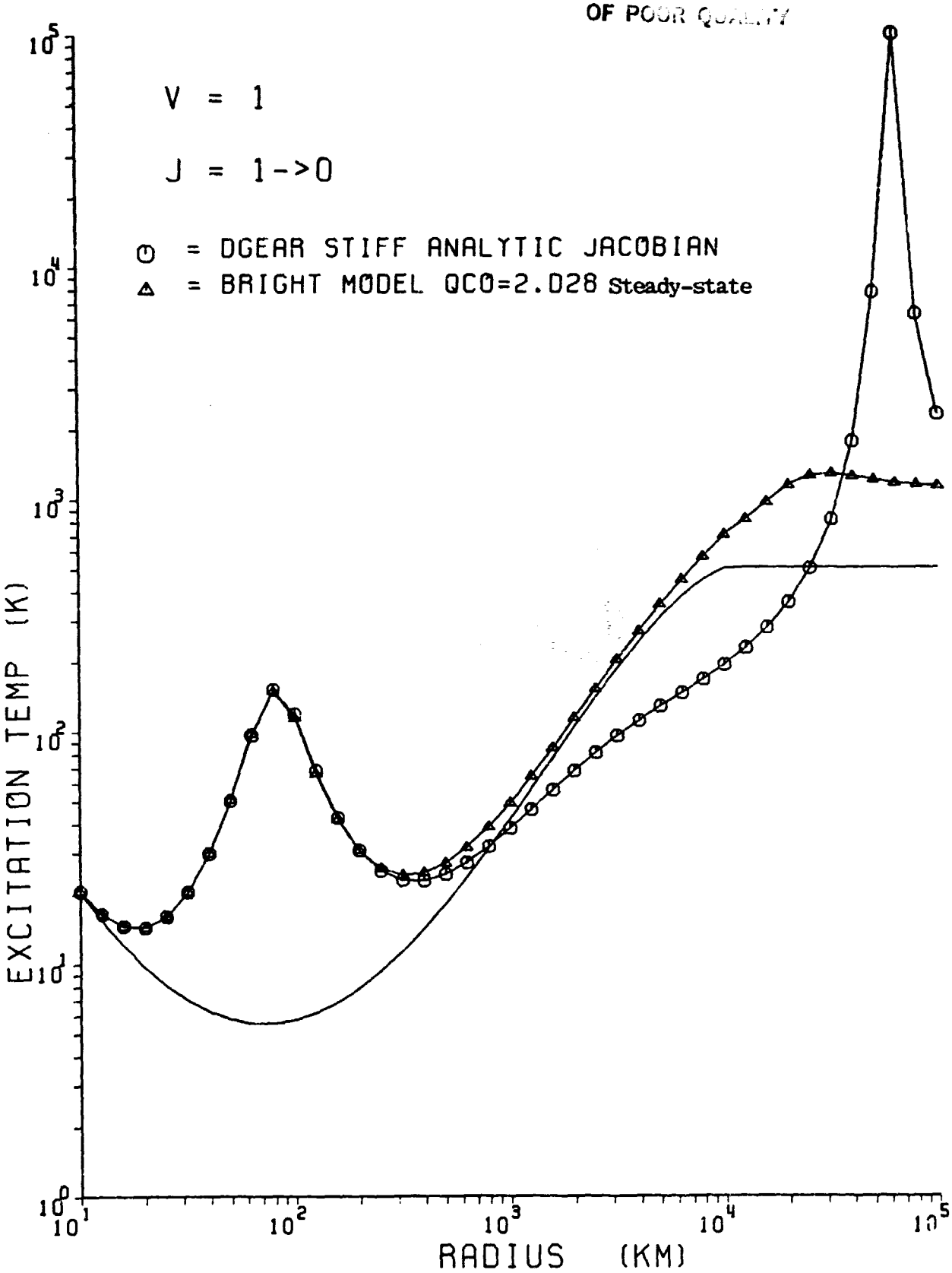

Figure IIa8.

ORIGINAL PAGE IS
OF POOR QUALITY

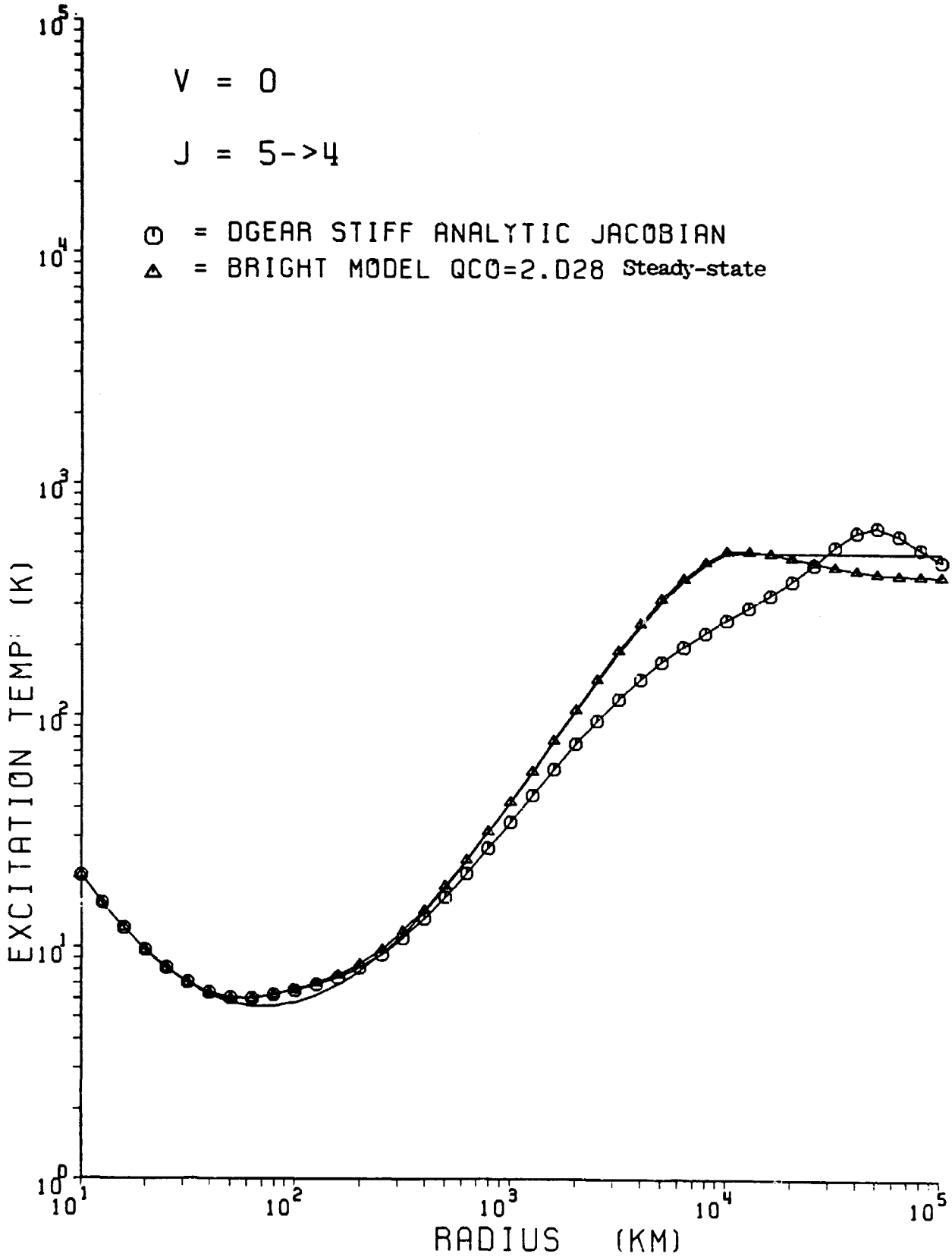

Figure IIa9.

ORIGINAL PAGE IS
OF POOR QUALITY

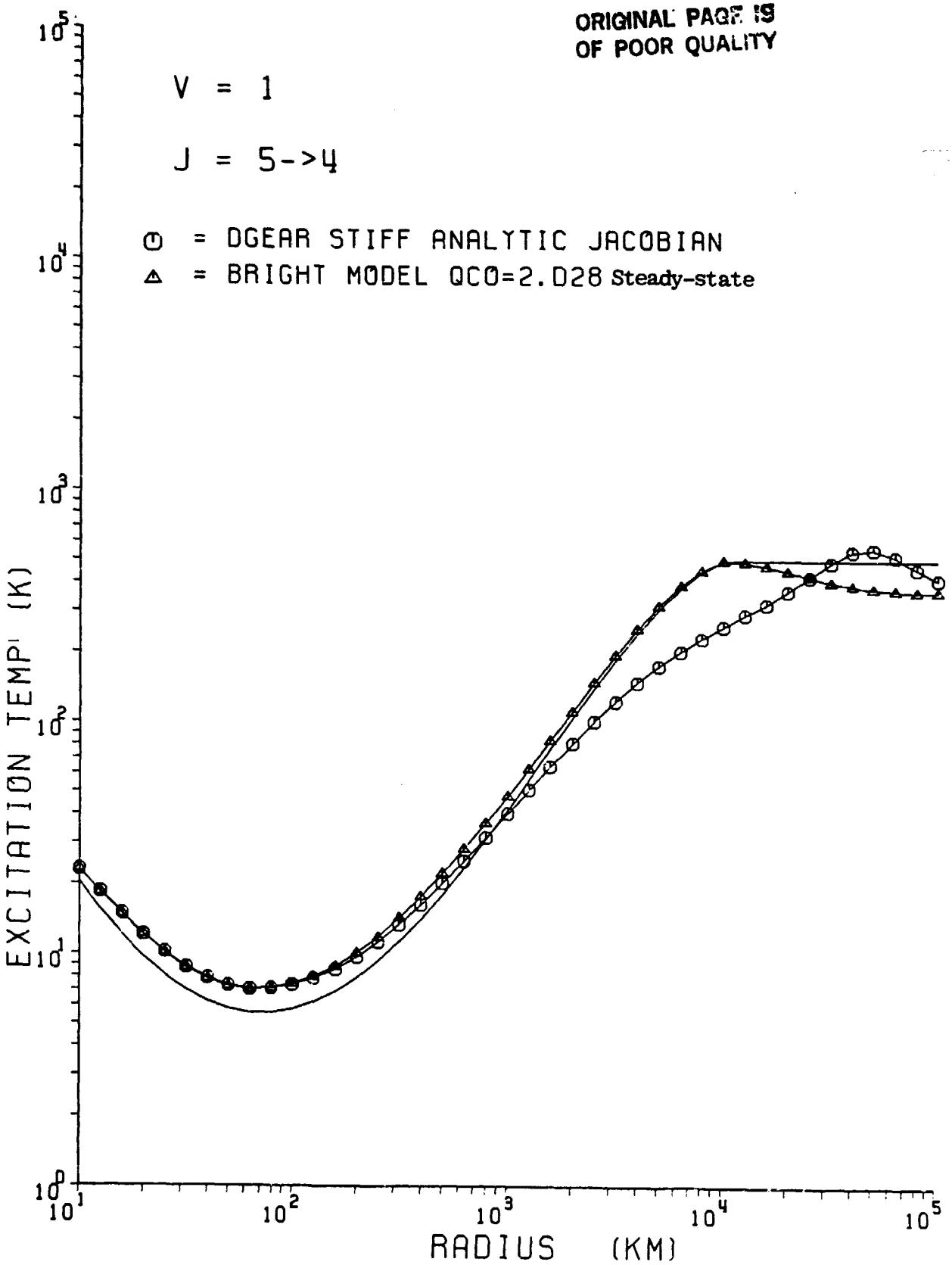

Figure IIa10.

ORIGINAL PAGE IS
OF POOR QUALITY

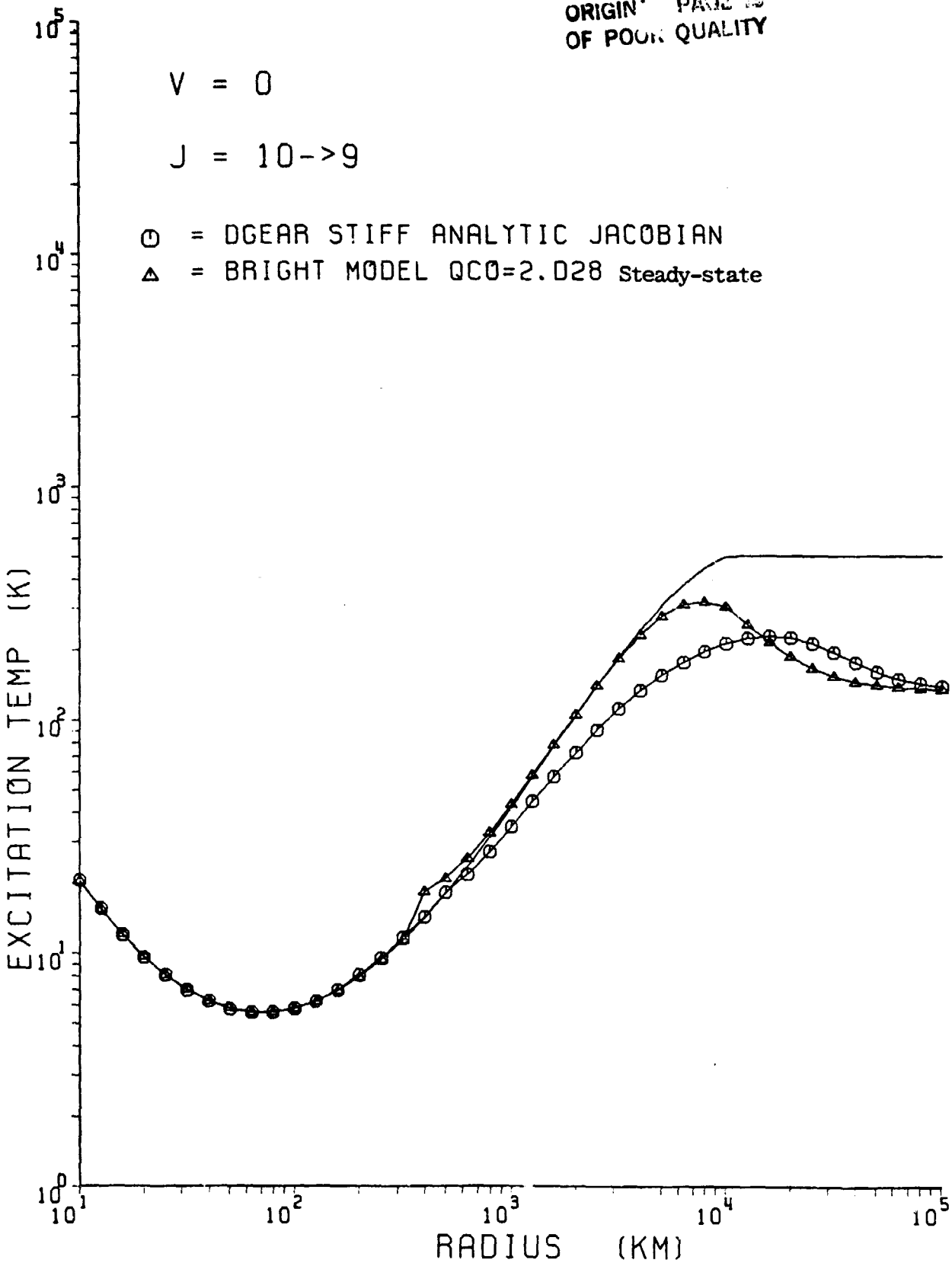

Figure IIall.

ORIGINAL PAGE IS
OF POOR QUALITY

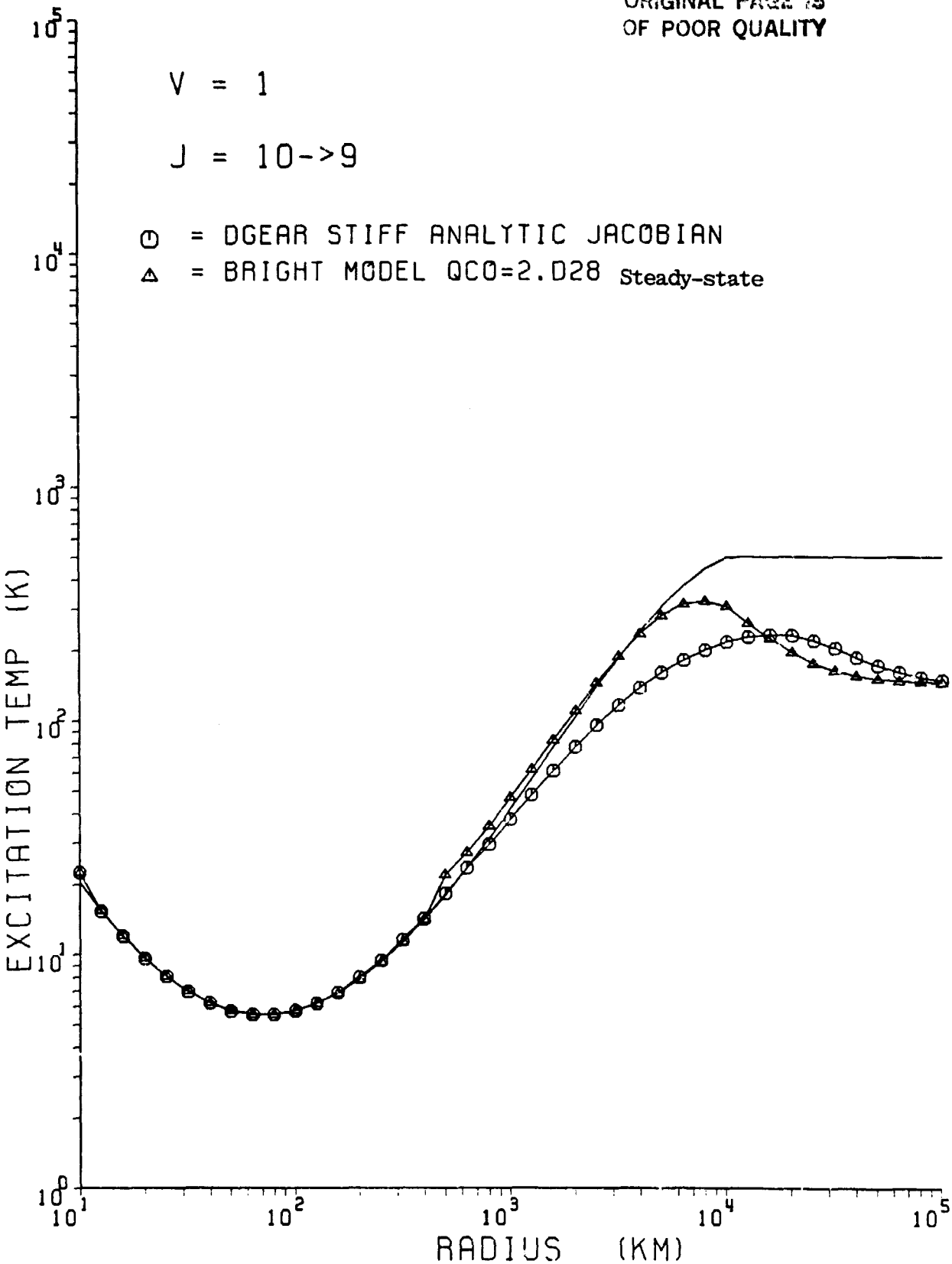

Figure IIa12.

ORIGINAL PAGE IS
OF POOR QUALITY

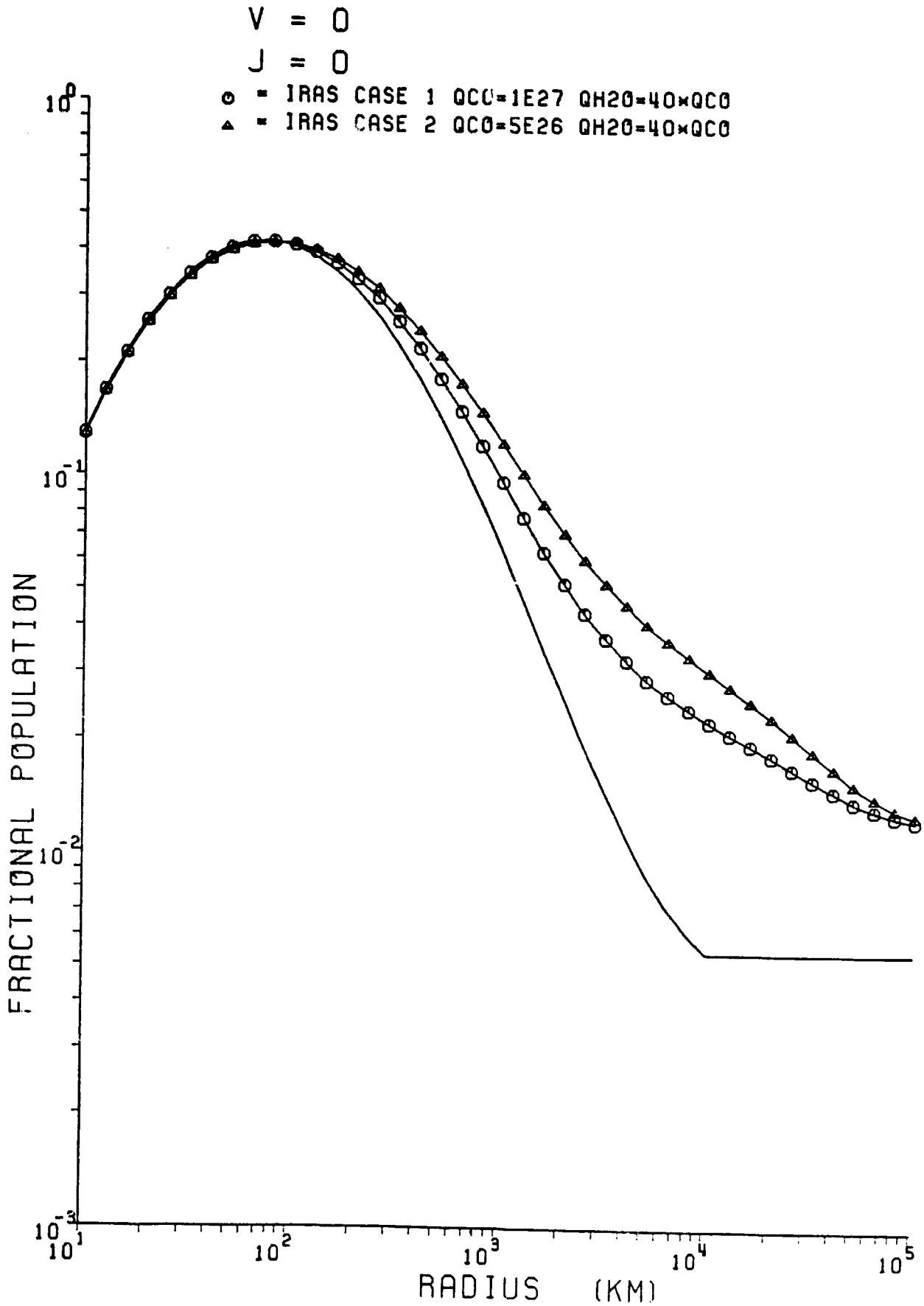

Figure IIb1.

ORIGINAL PAGE IS
OF POOR QUALITY

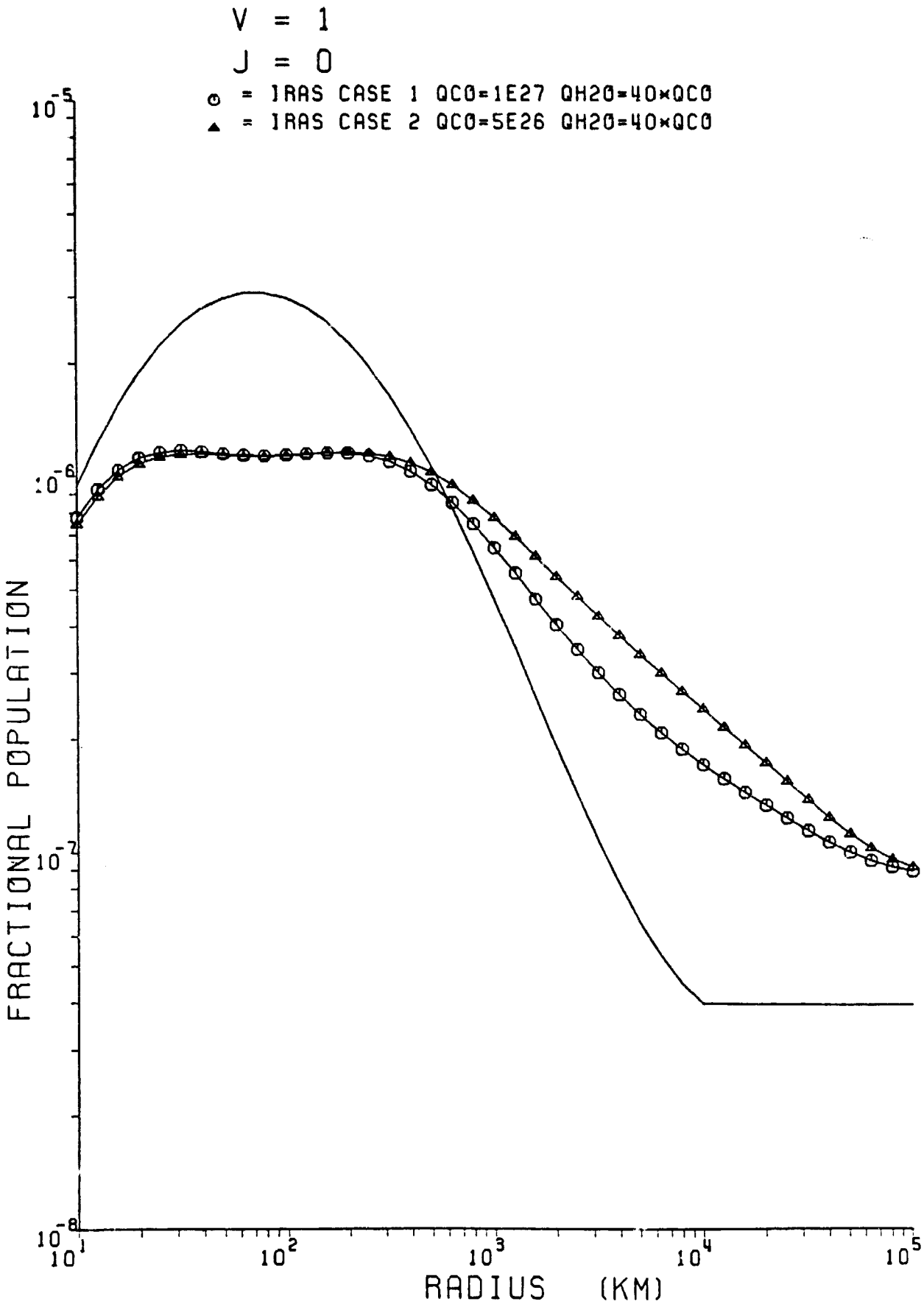

Figure IIb2.

ORIGINAL PAGE IS
OF POOR QUALITY

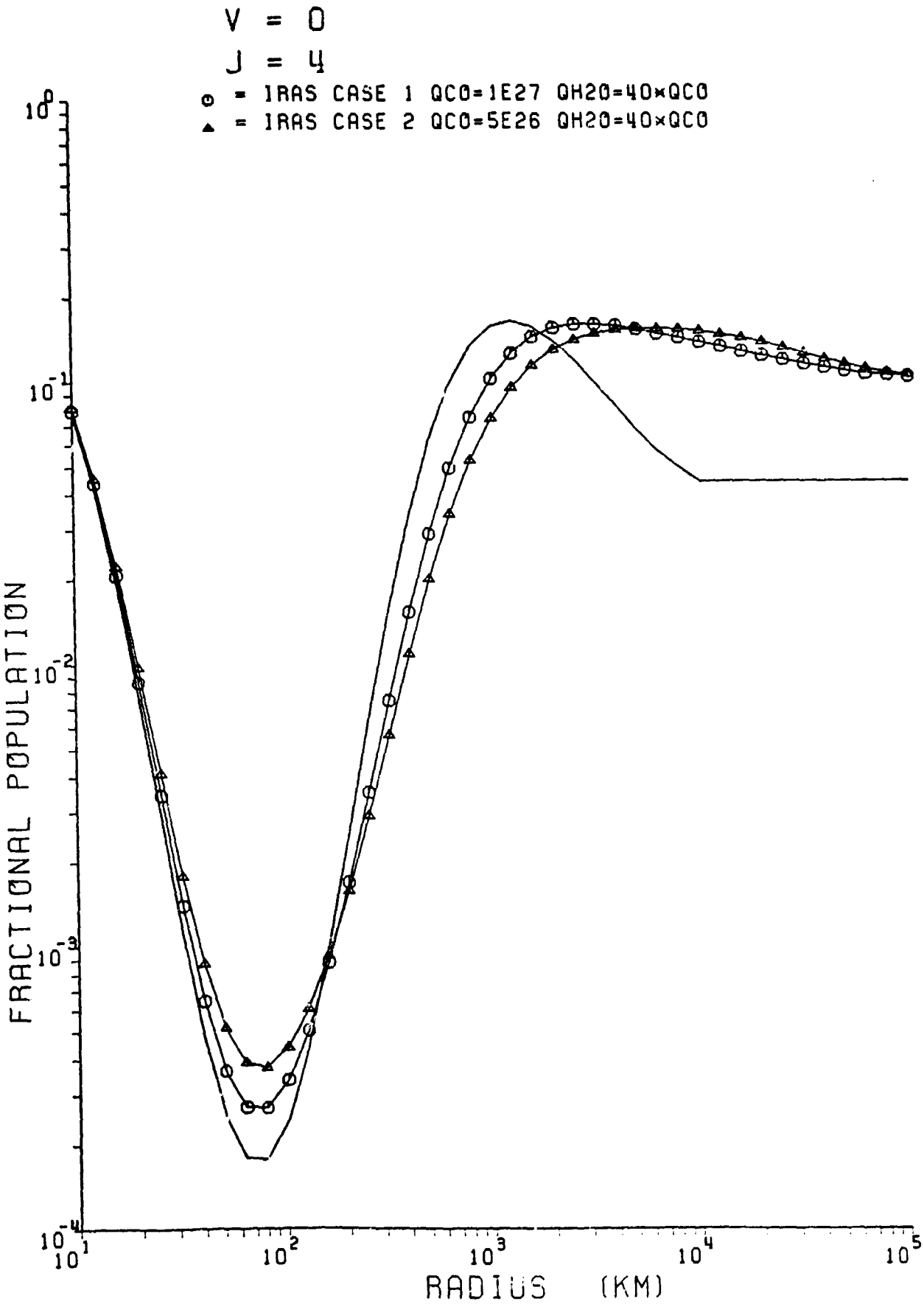

Figure IIb3.

ORIGINAL PAGE IS
OF POOR QUALITY

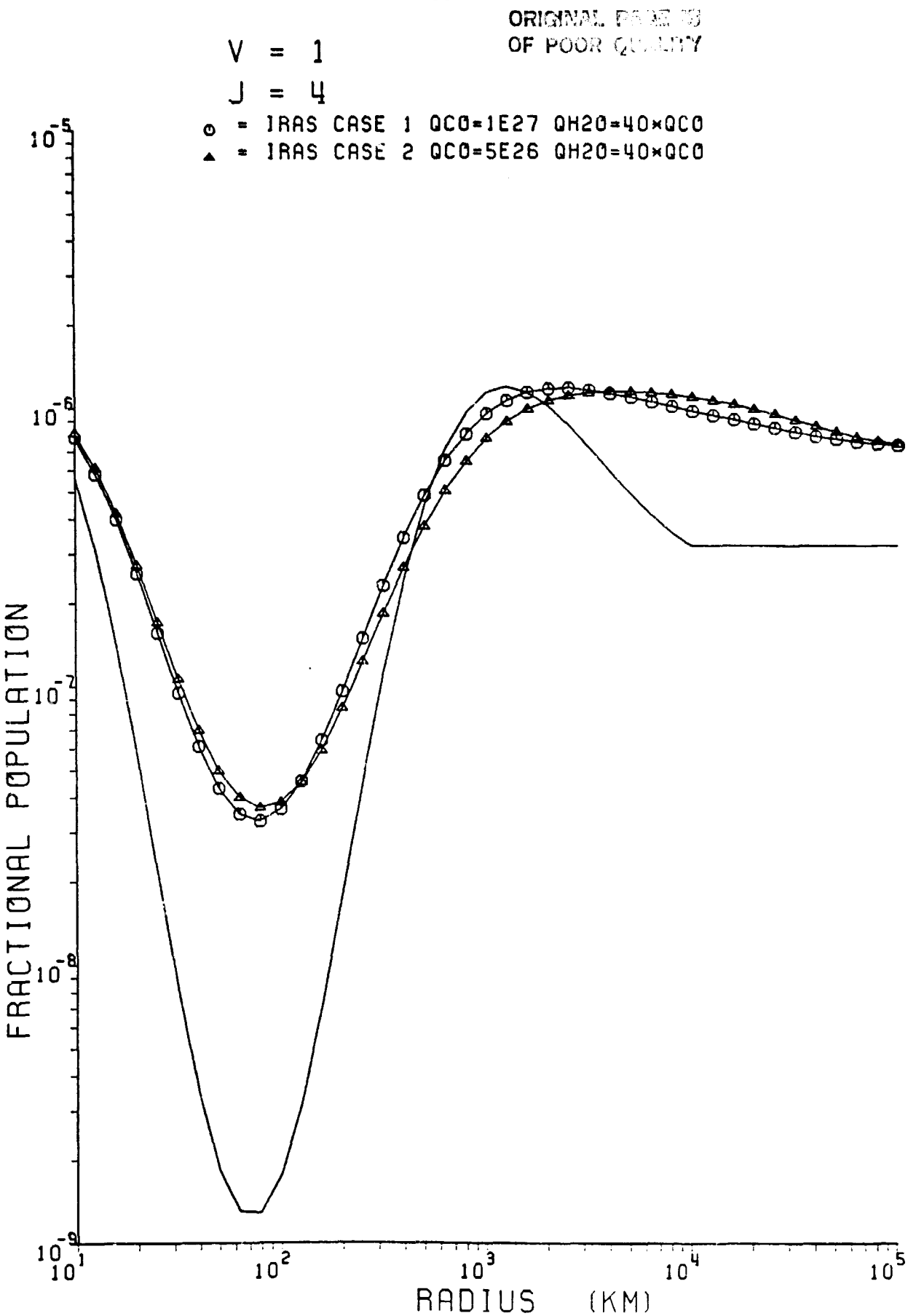

figure IIb4.

ORIGINAL PAGE IS
OF POOR QUALITY

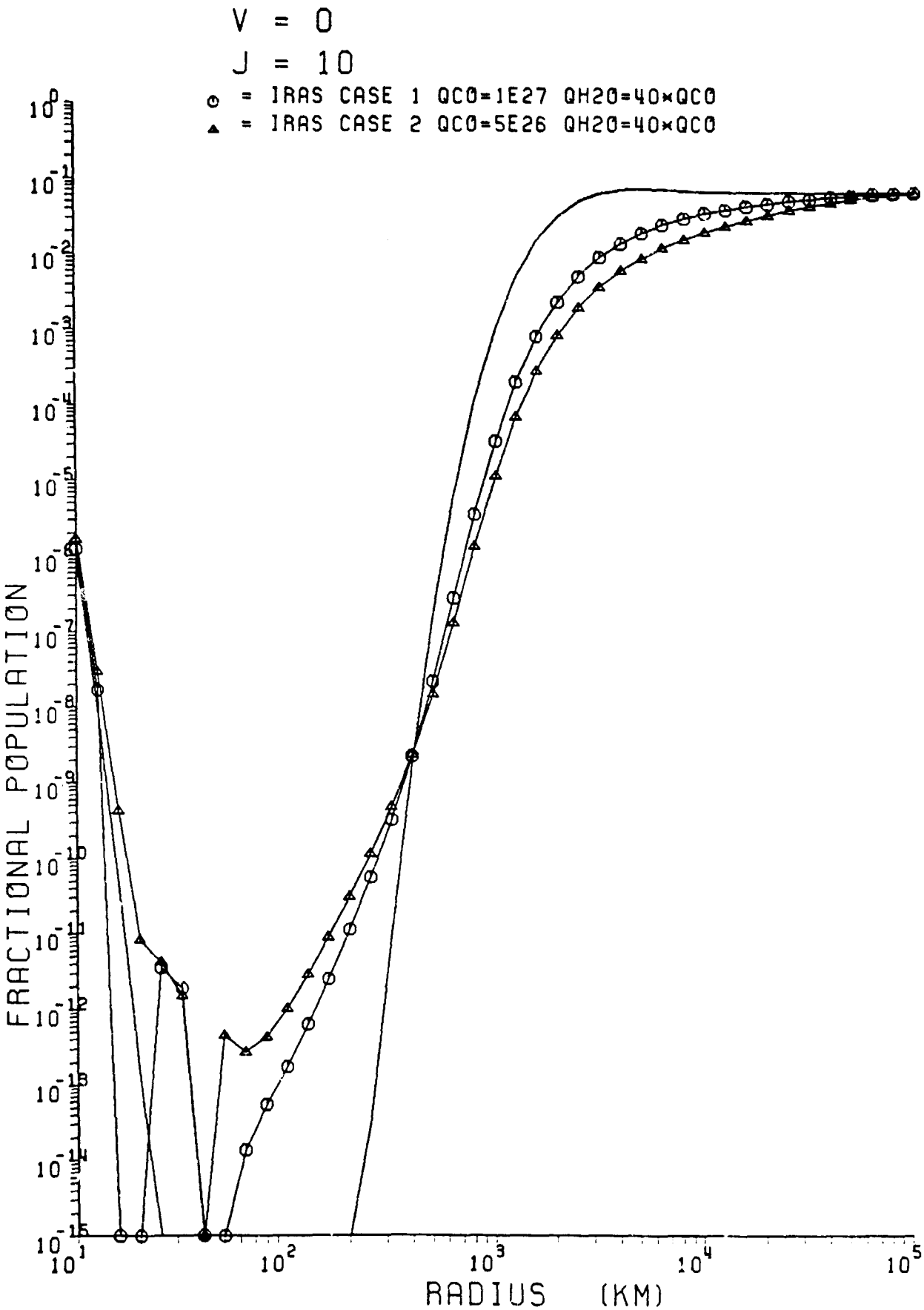

Figure IIb5.

ORIGINAL PAGE IS
OF POOR QUALITY

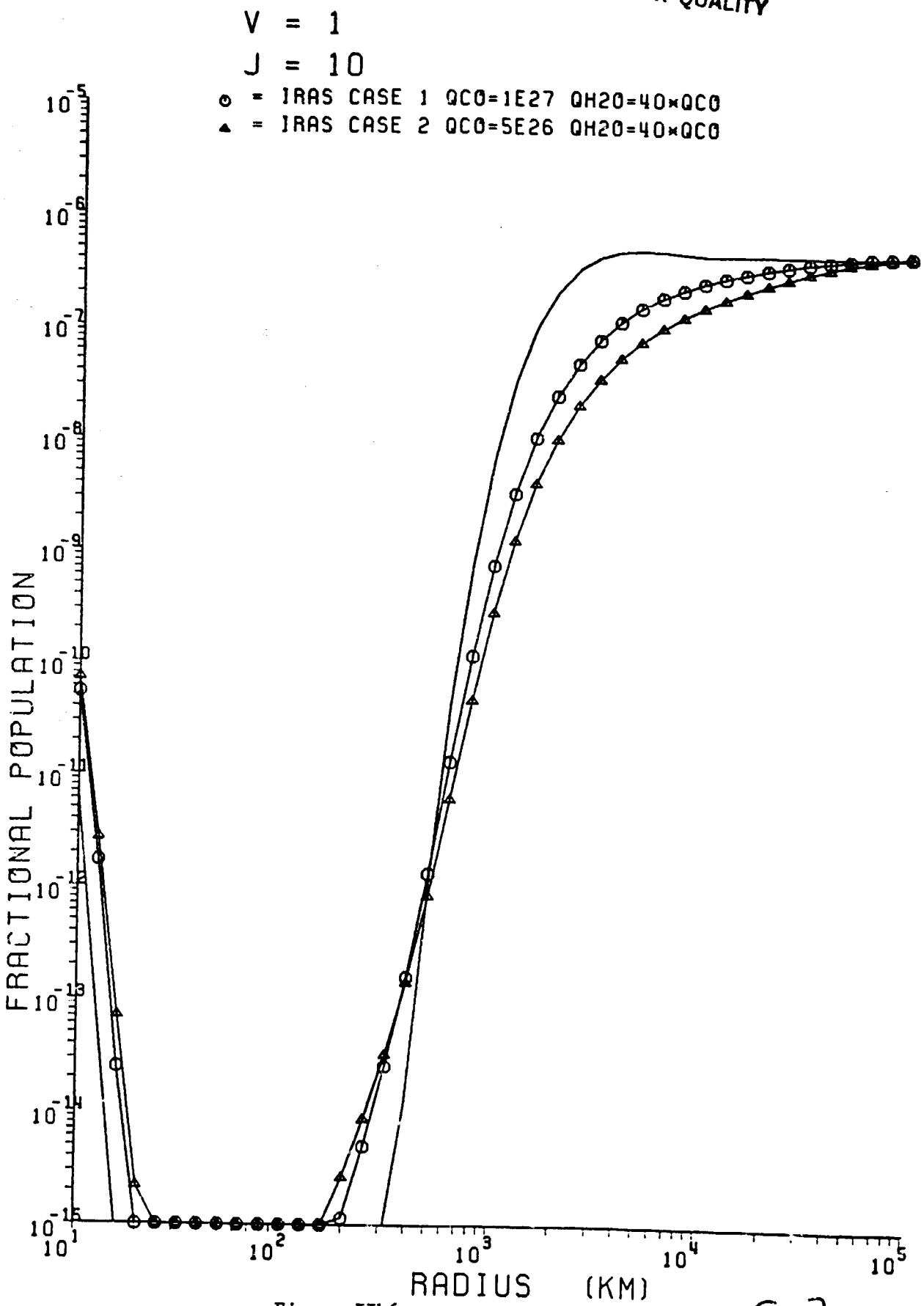

Figure IIb6.

C-2

ORIGINAL PAGE IS
OF POOR QUALITY

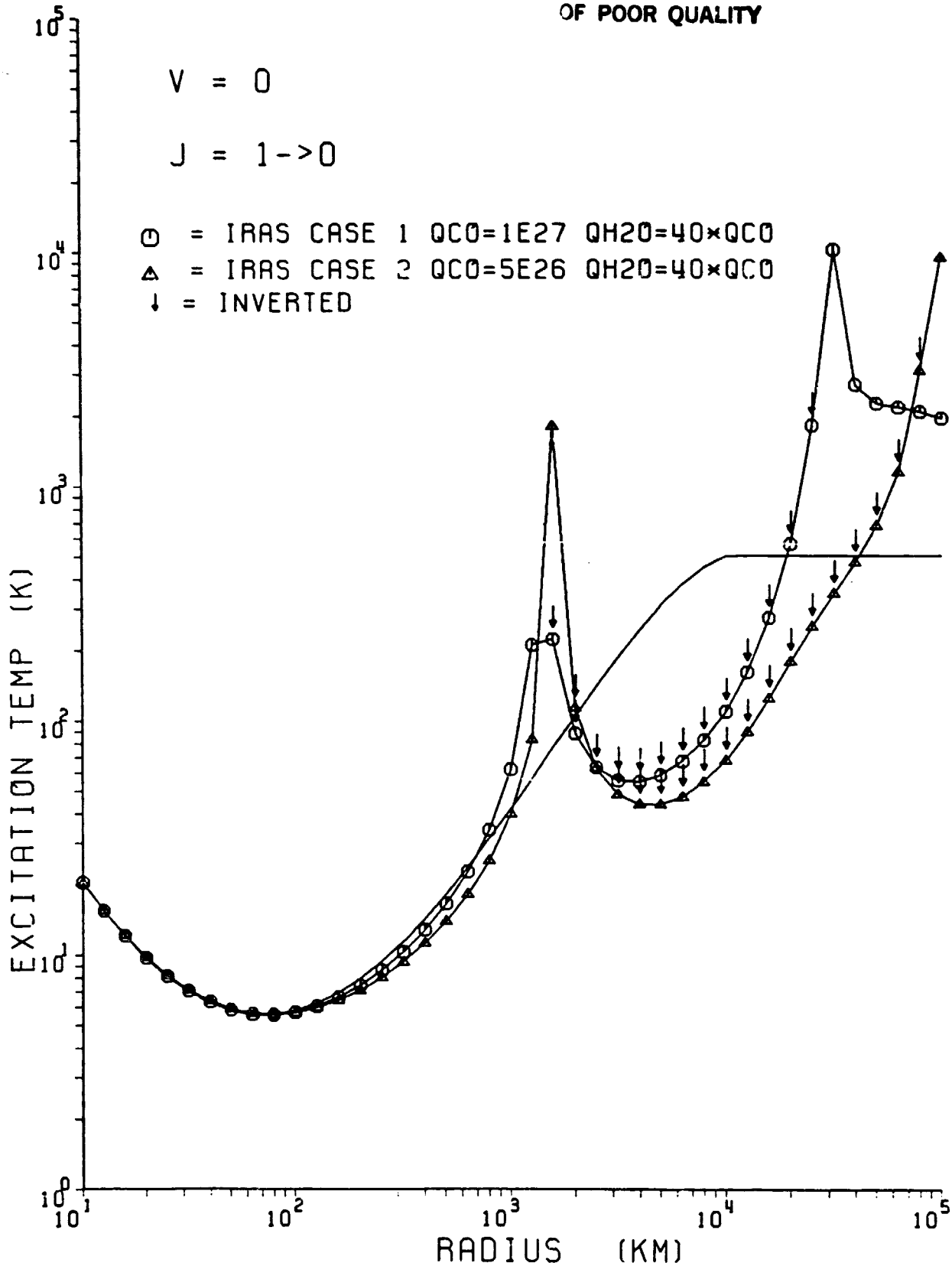

Figure IIb7.

ORIGINAL PAGE IS
OF POOR QUALITY

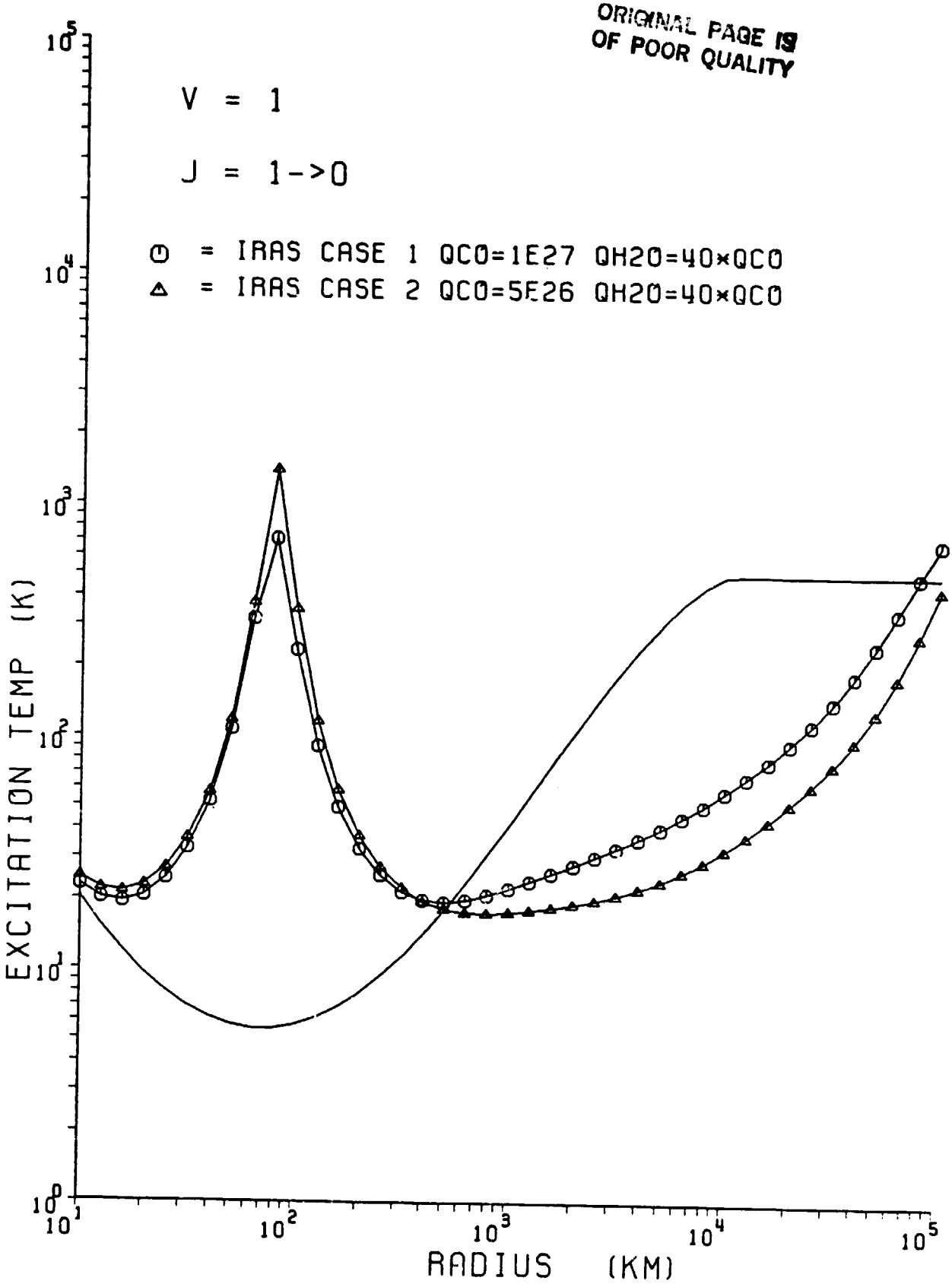

Figure IIb8.

ORIGINAL PAGE IS
OF POOR QUALITY

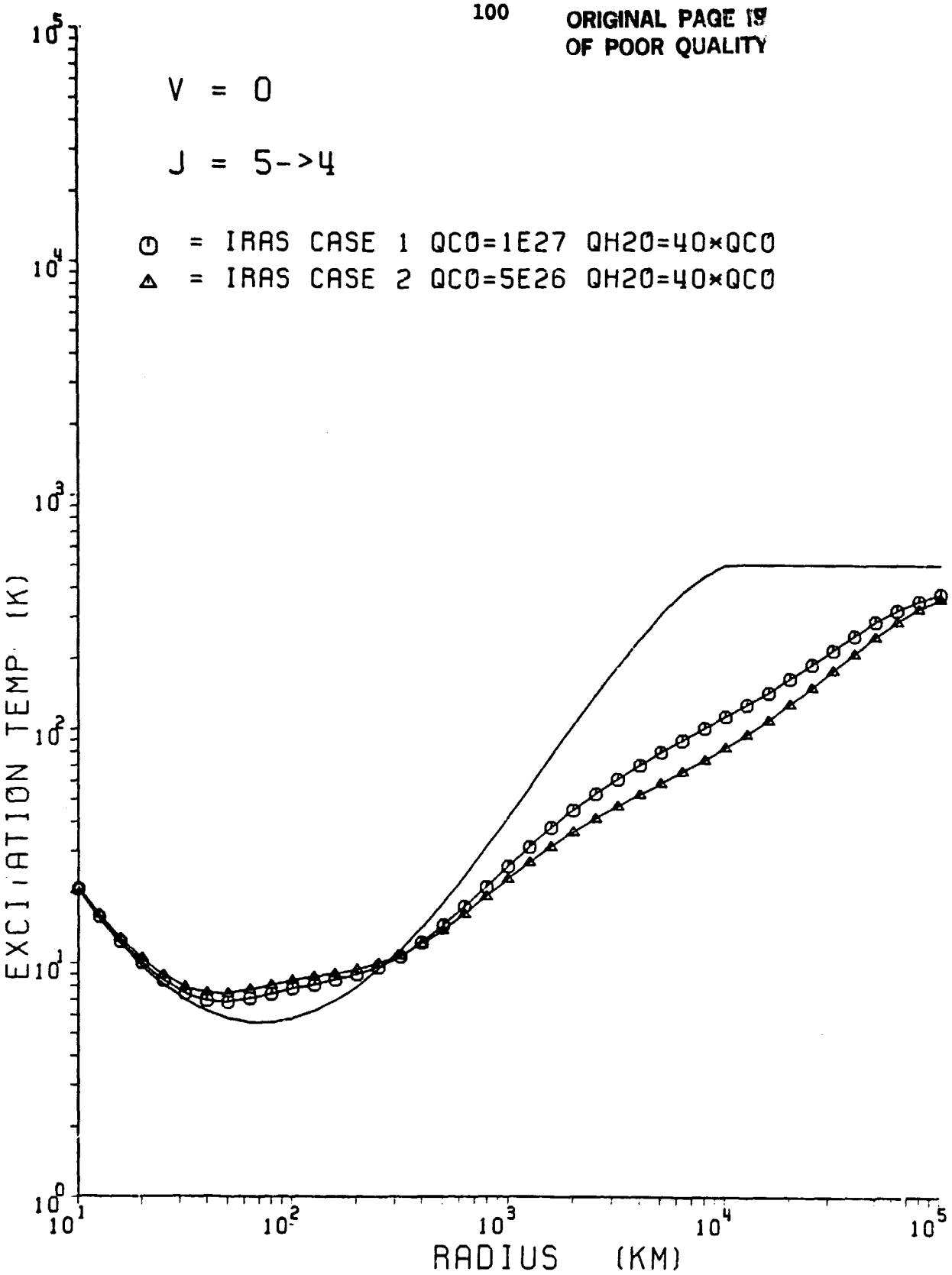

Figure IIb9.

ORIGINAL PAGE IS
OF POOR QUALITY

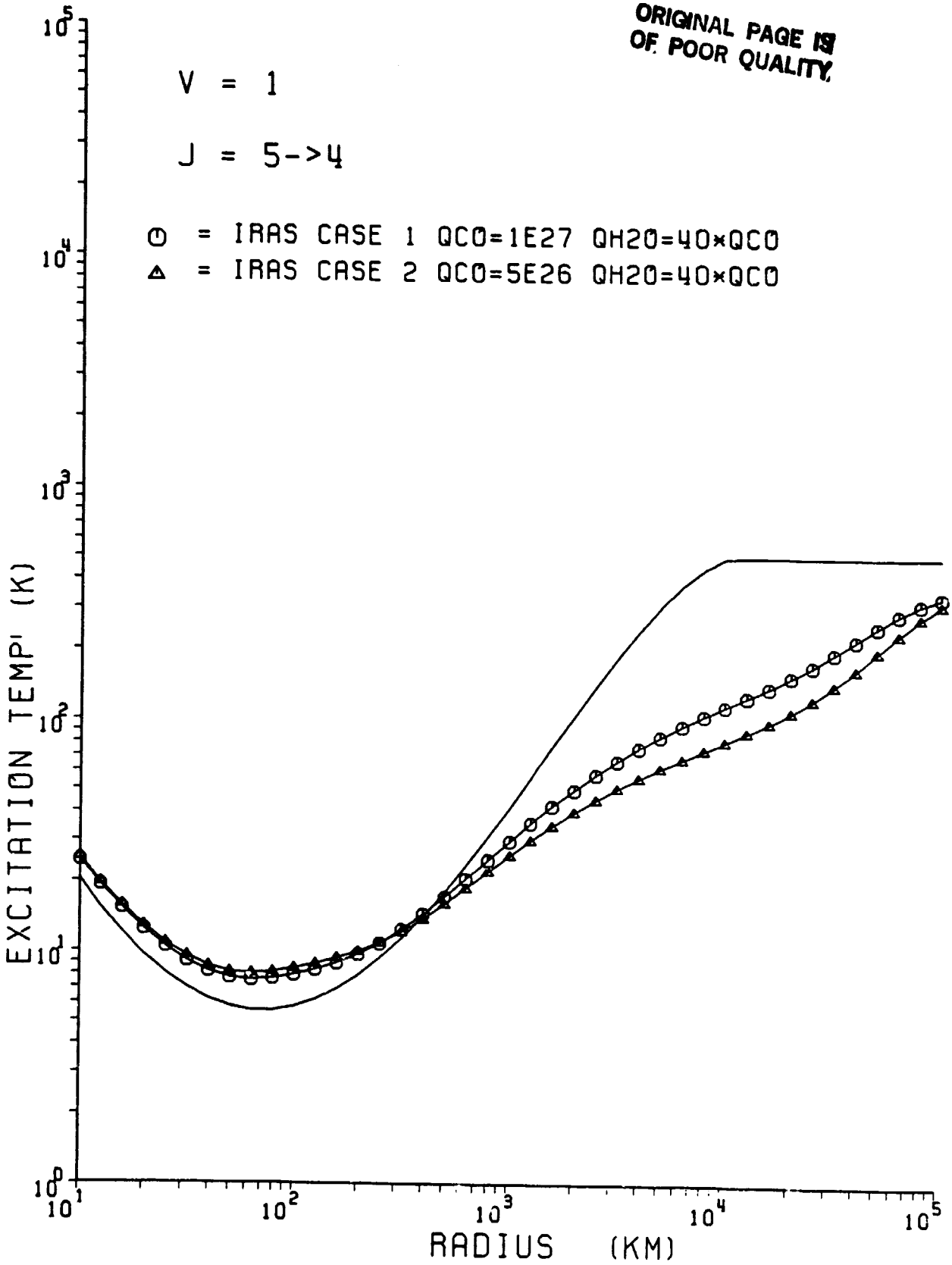

Figure IIb10.

ORIGINAL PAGE IS
OF POOR QUALITY

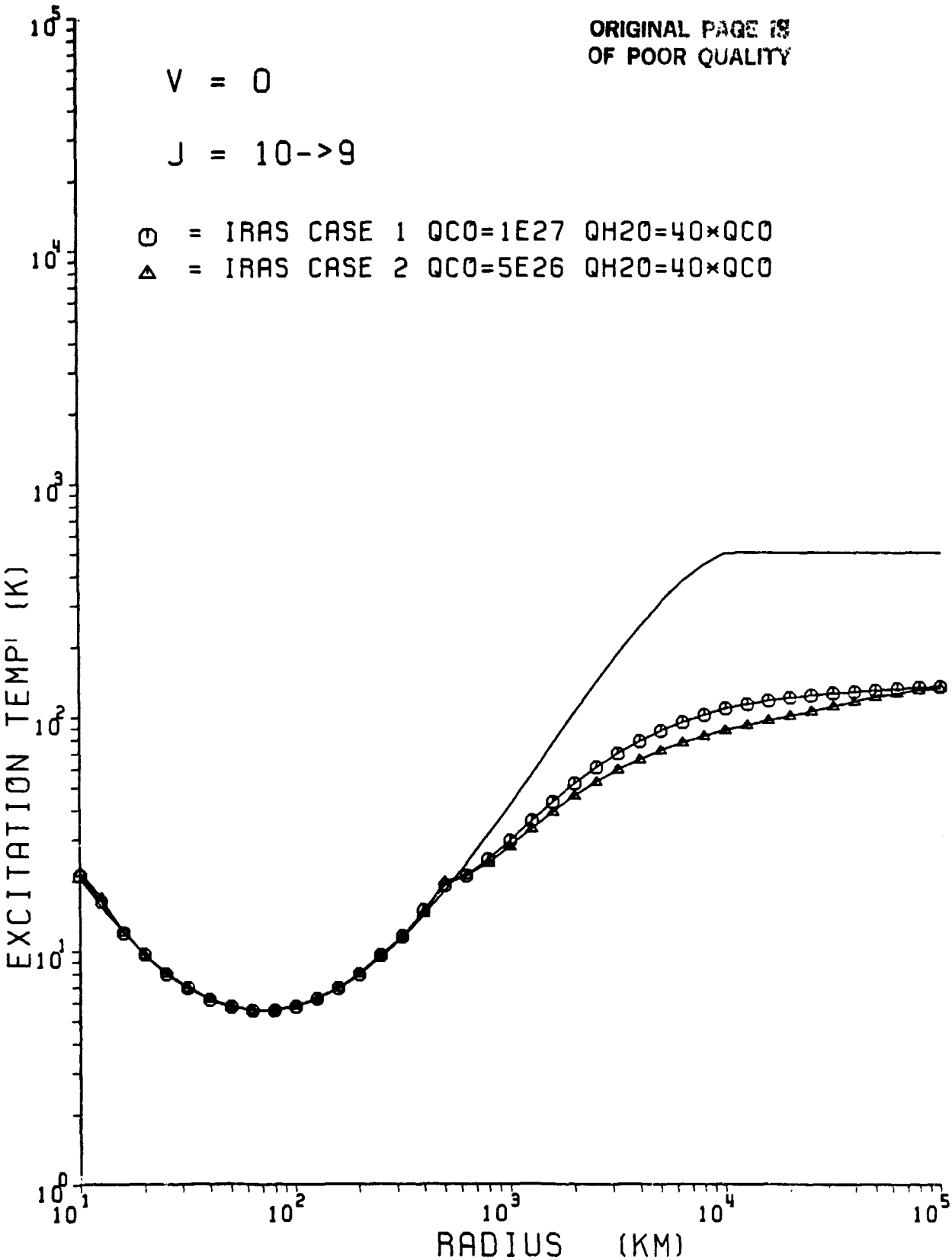

Figure IIb11.

ORIGINAL PAGE IS
OF POOR QUALITY

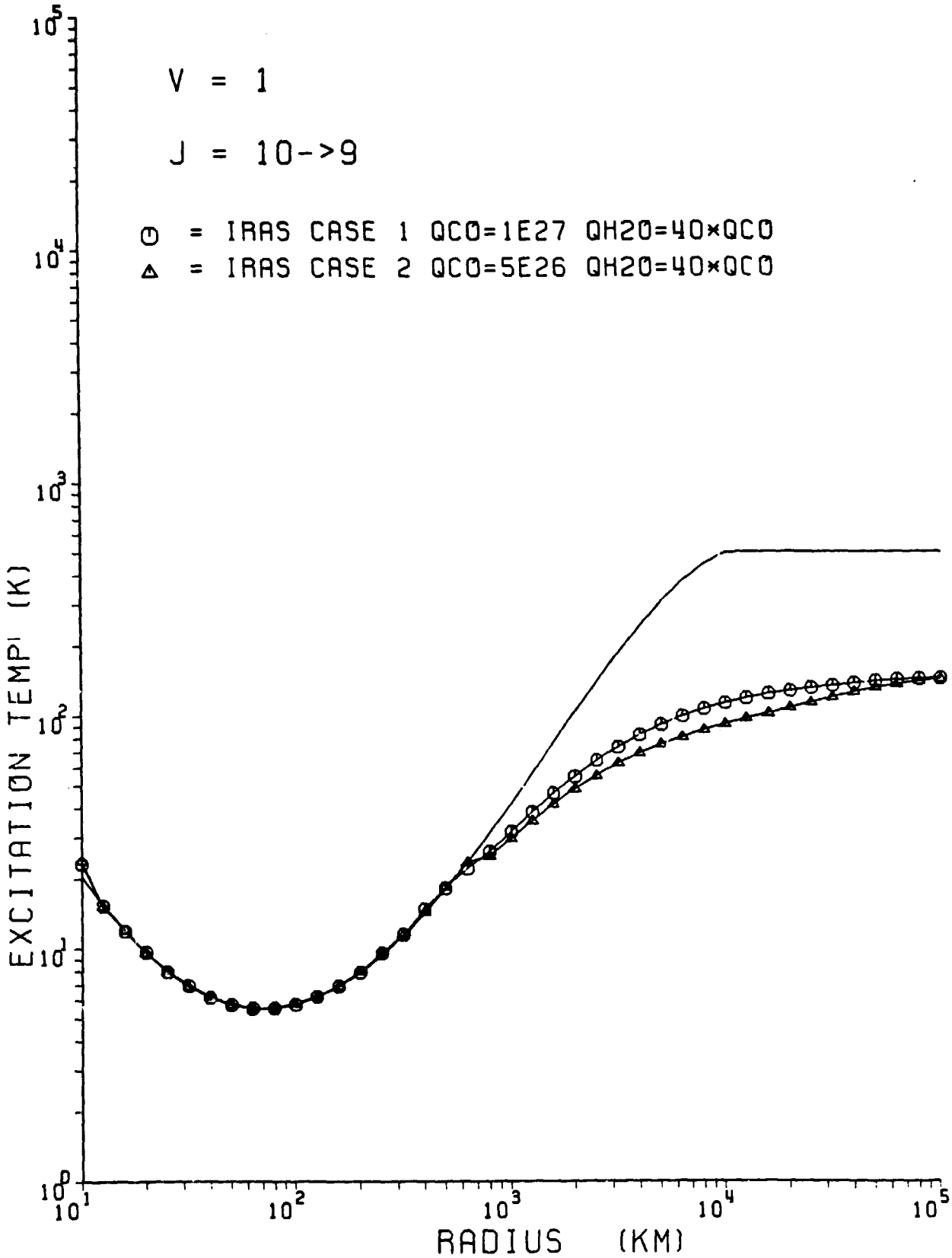

Figure IIb12.

ORIGINAL PAGE IS
OF POOR QUALITY

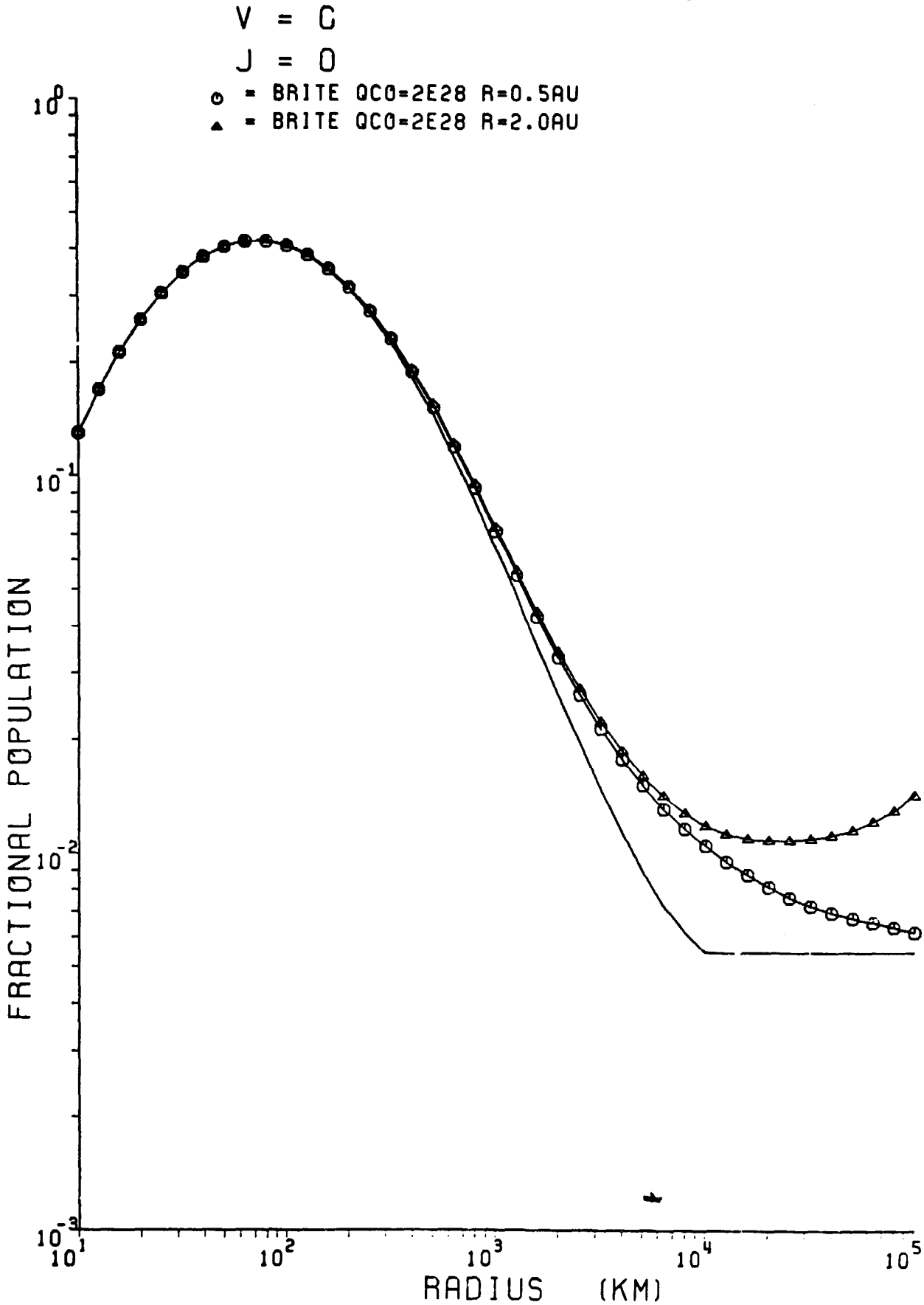

Figure IIc1.

ORIGINAL PAGE IS
OF POOR QUALITY

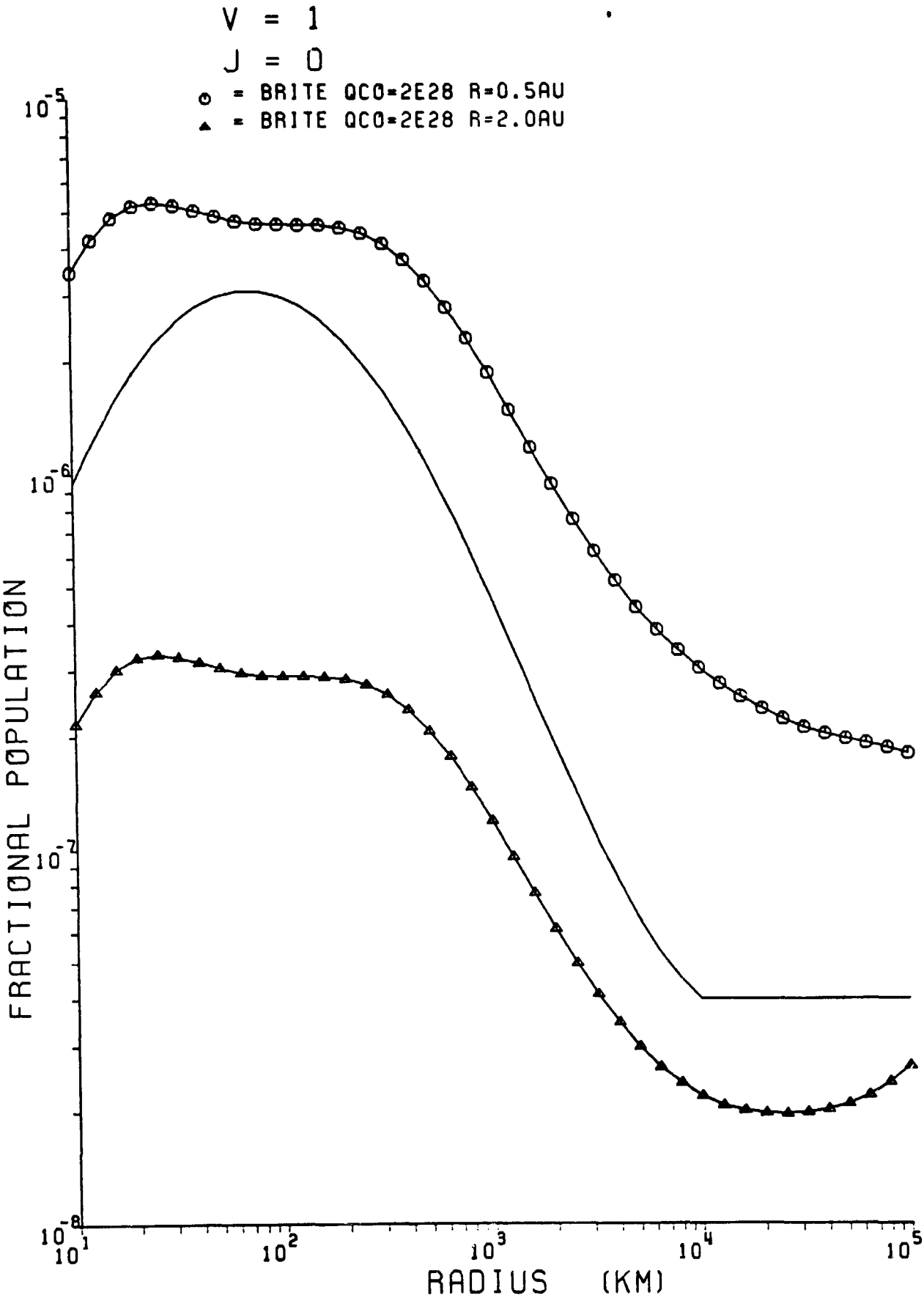

Figure IIc2.

ORIGINAL PAGE IS
OF POOR QUALITY

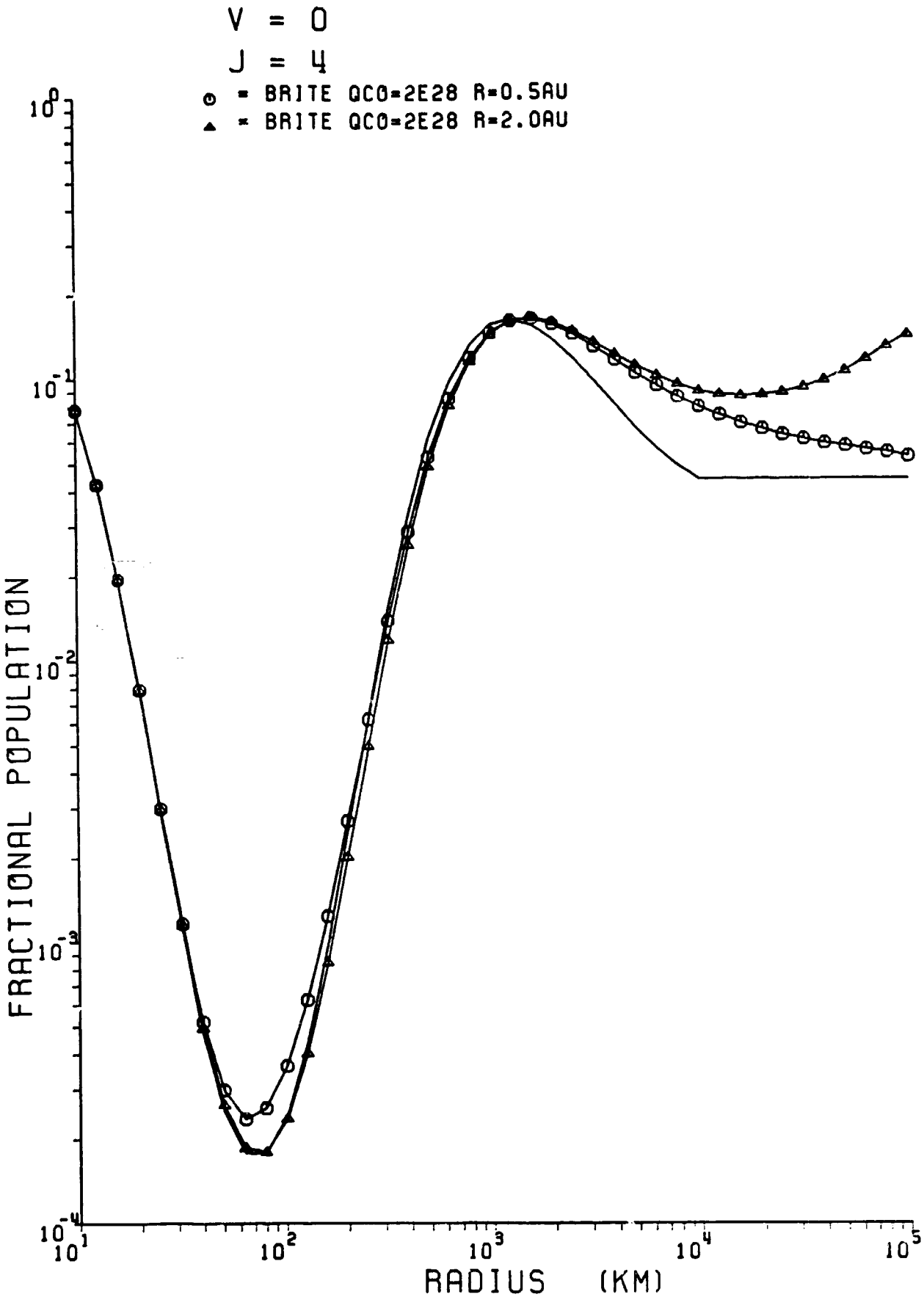

Figure IIc3.

ORIGINAL PAGE IS
OF POOR QUALITY

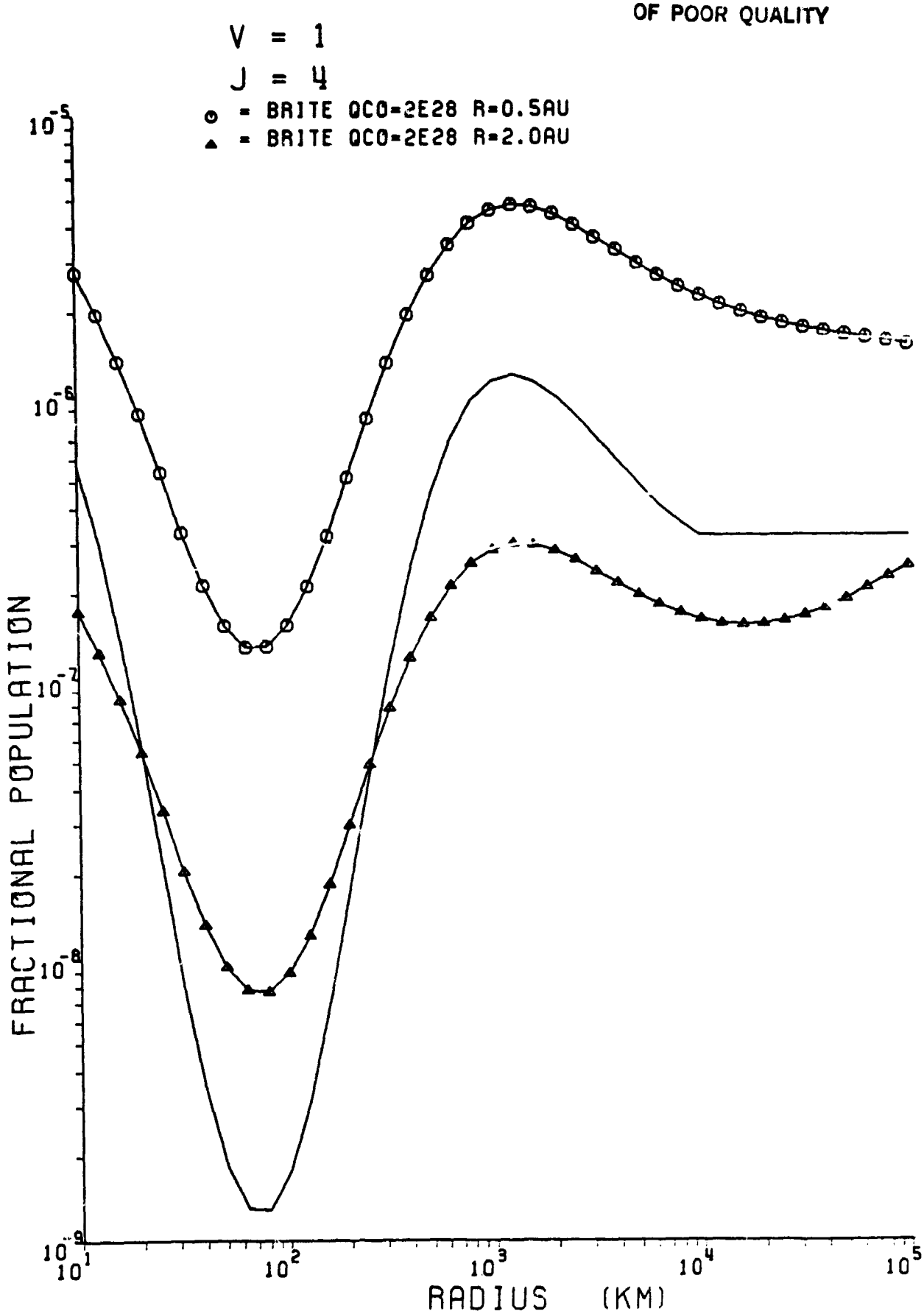

Figure IIc4.

ORIGINAL PAGE IS
OF POOR QUALITY

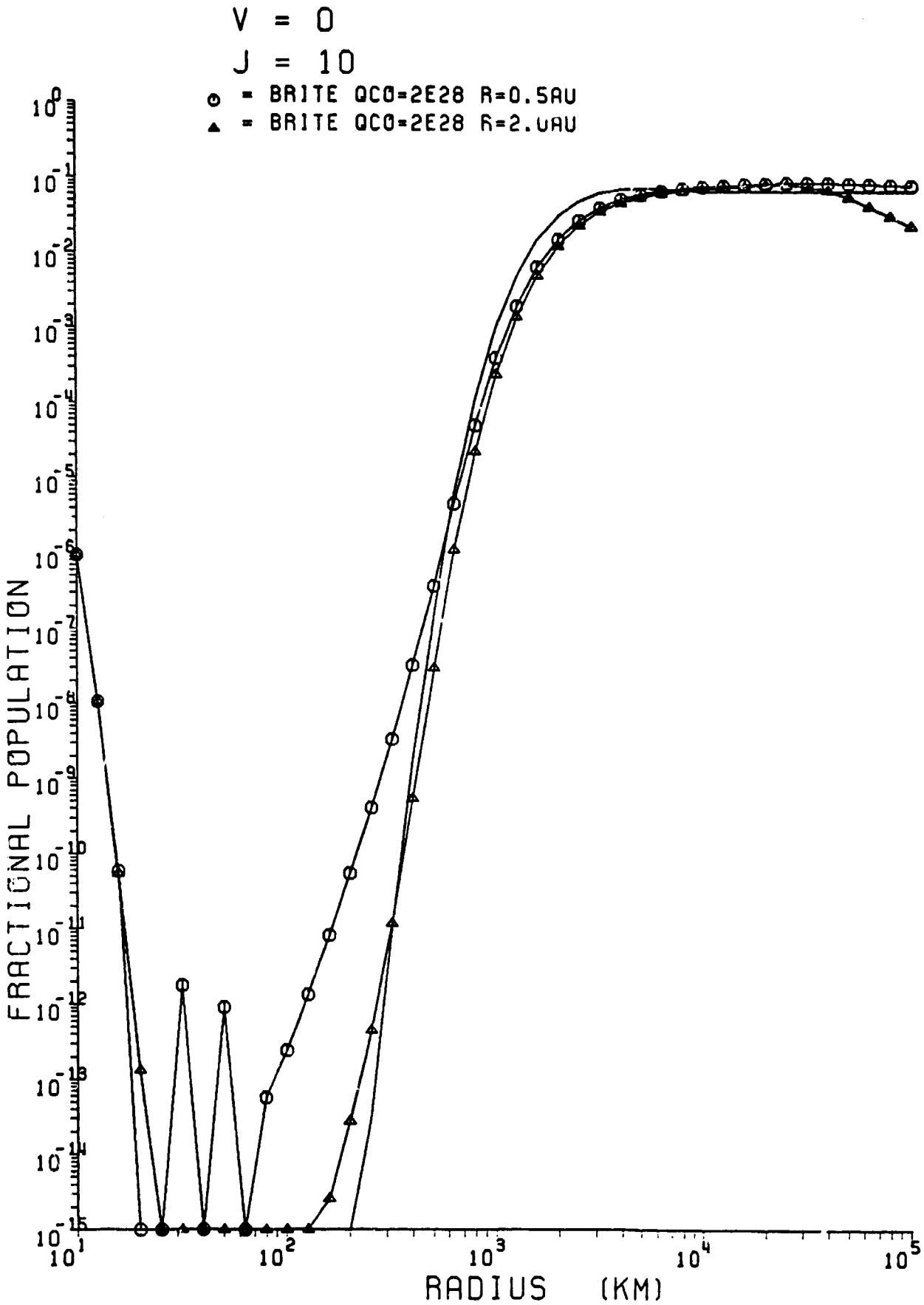

Figure IIc5.

ORIGINAL PAGE IS
OF POOR QUALITY

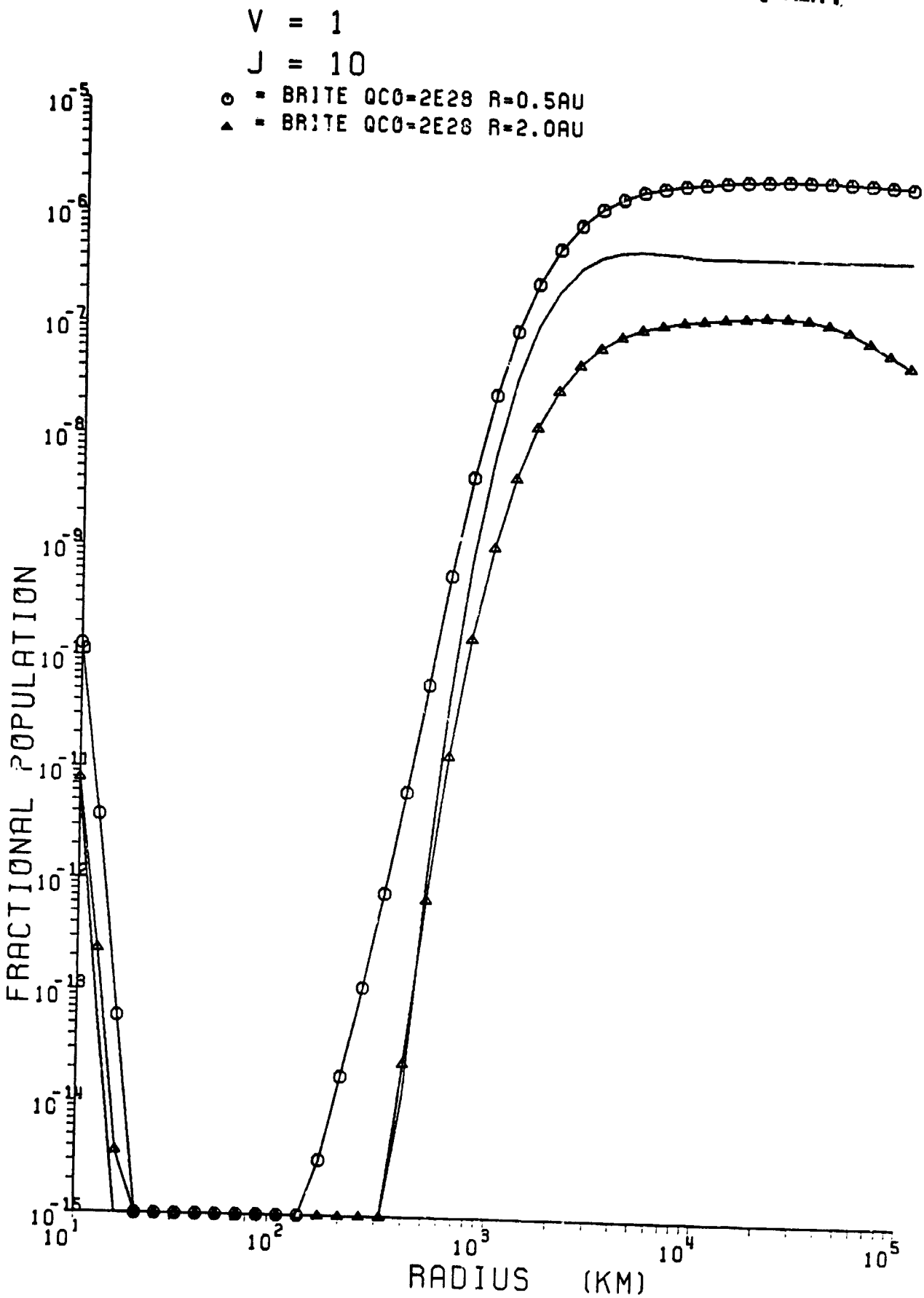

Figure IIc6.

ORIGINAL PAGE IS
OF POOR QUALITY

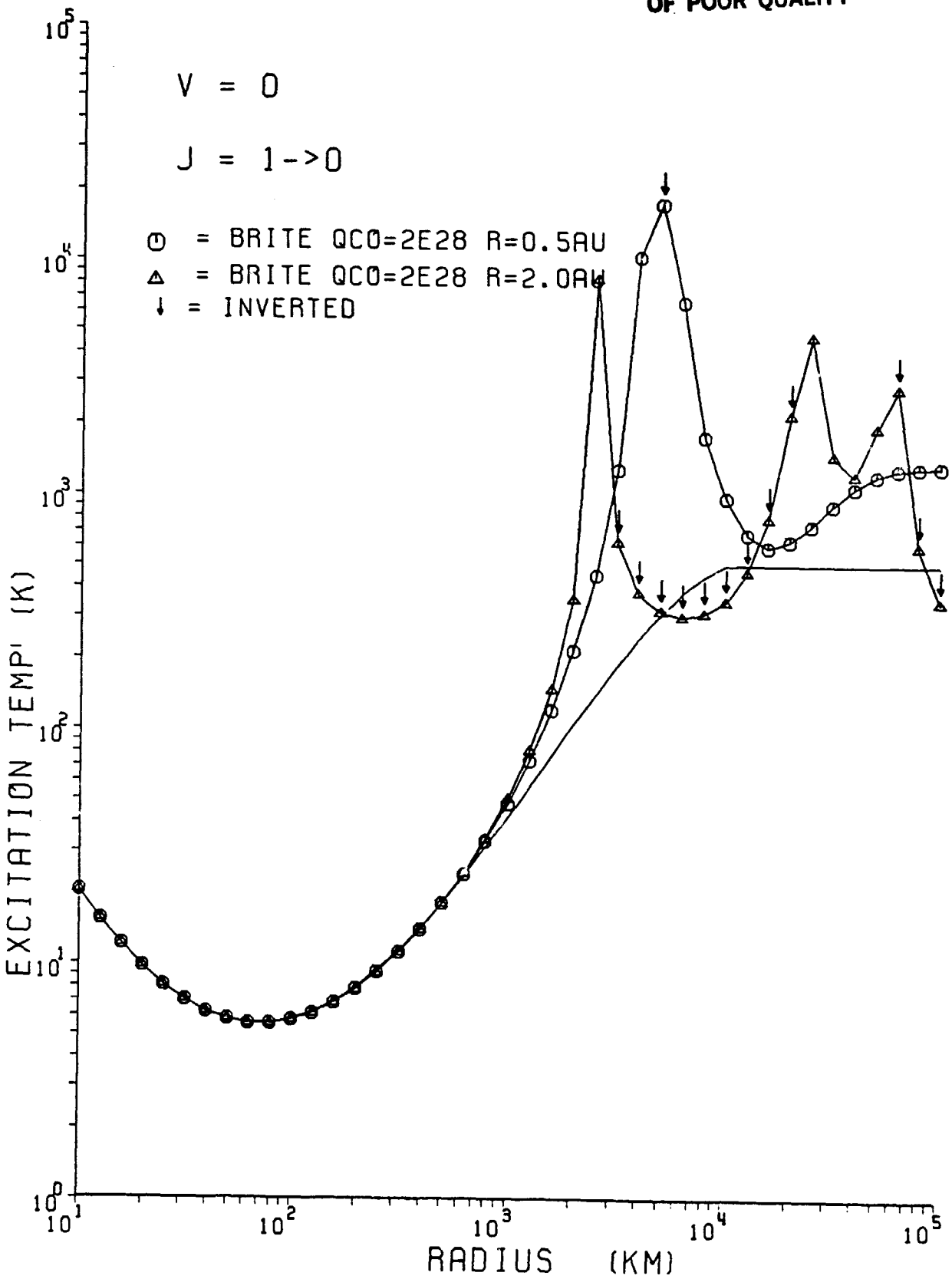

Figure IIc7.

ORIGINAL PAGE IS
OF POOR QUALITY

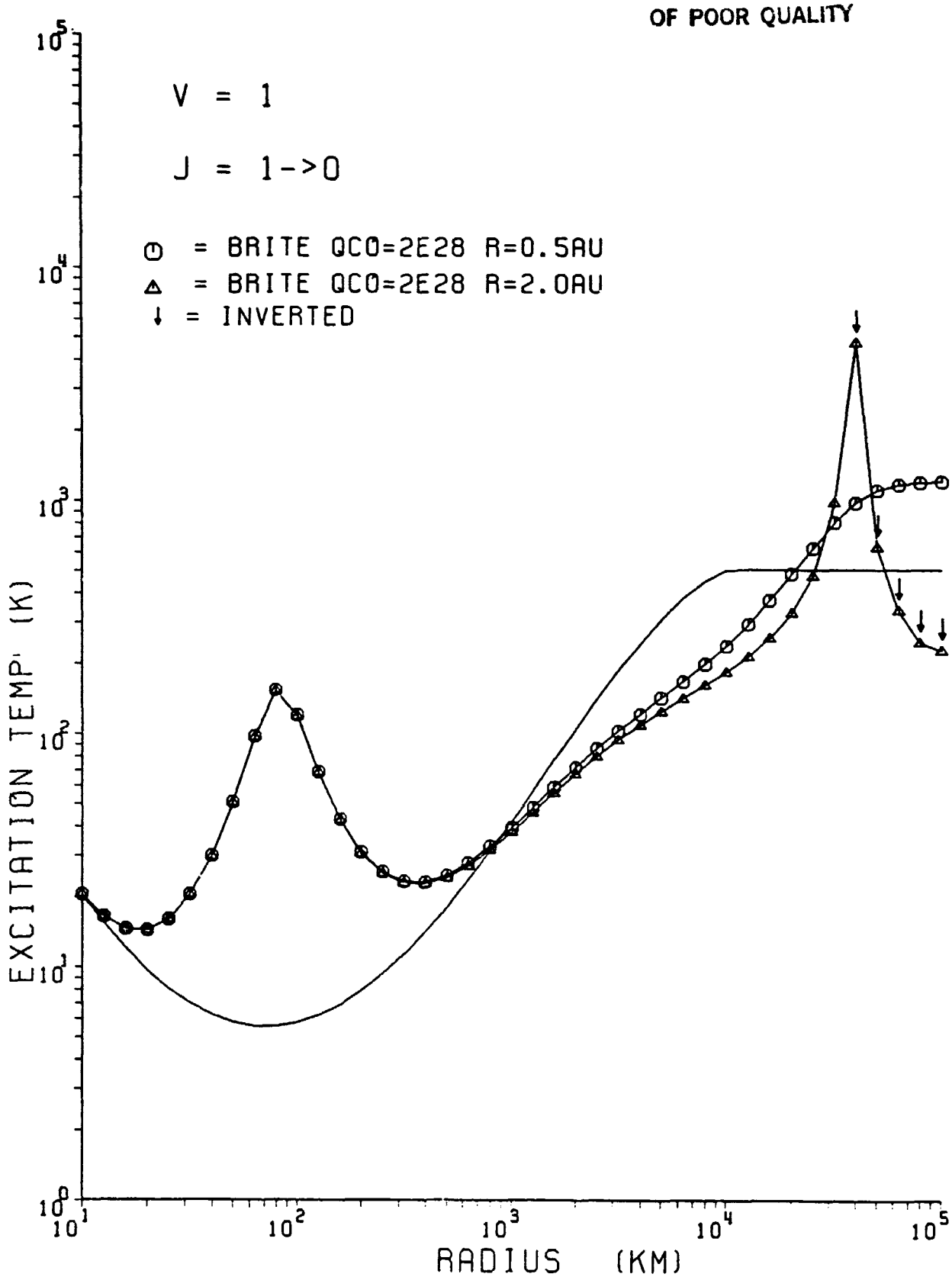

Figure IIc8.

ORIGINAL PAGE IS
OF POOR QUALITY

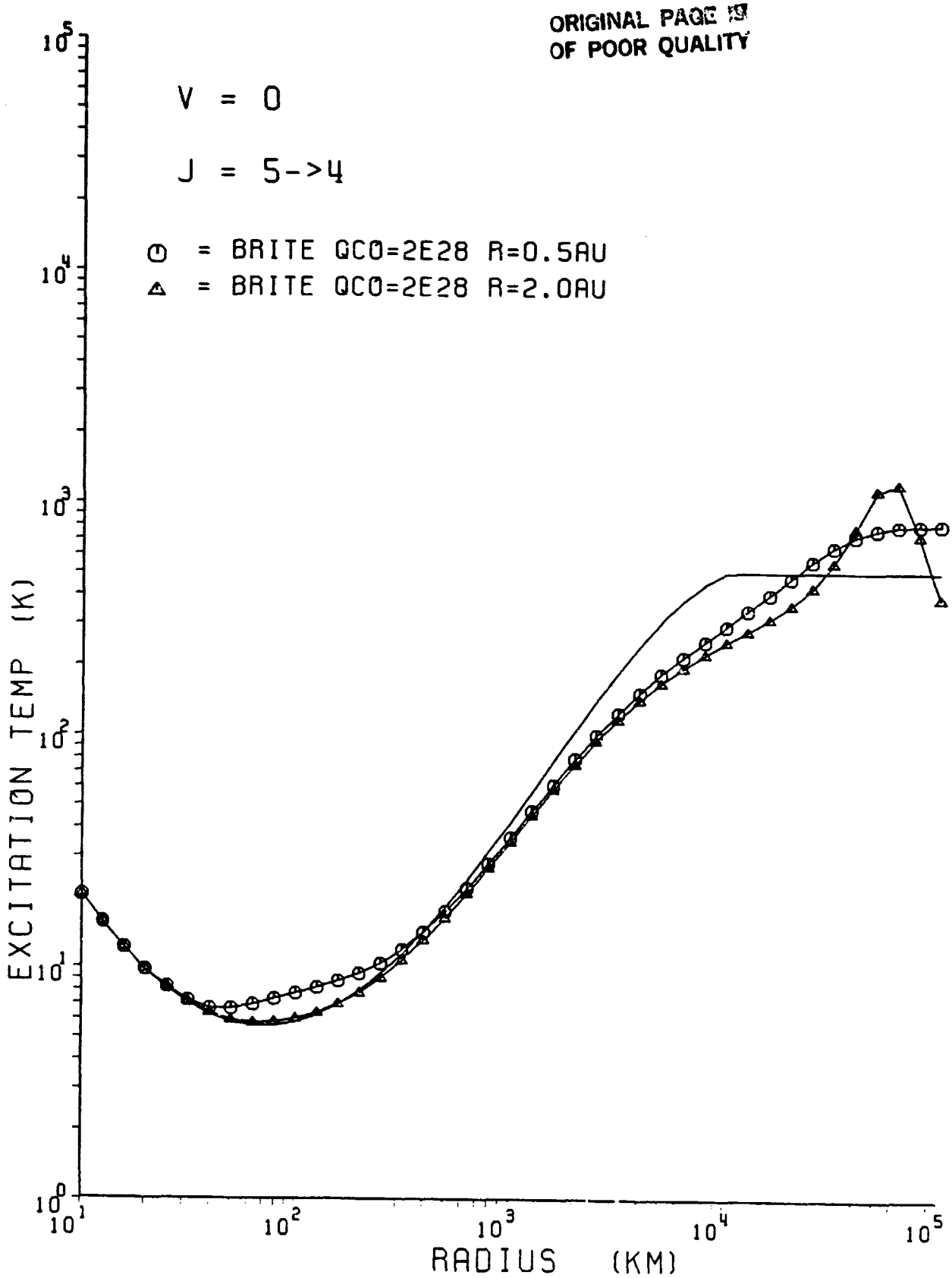

Figure IIc9.

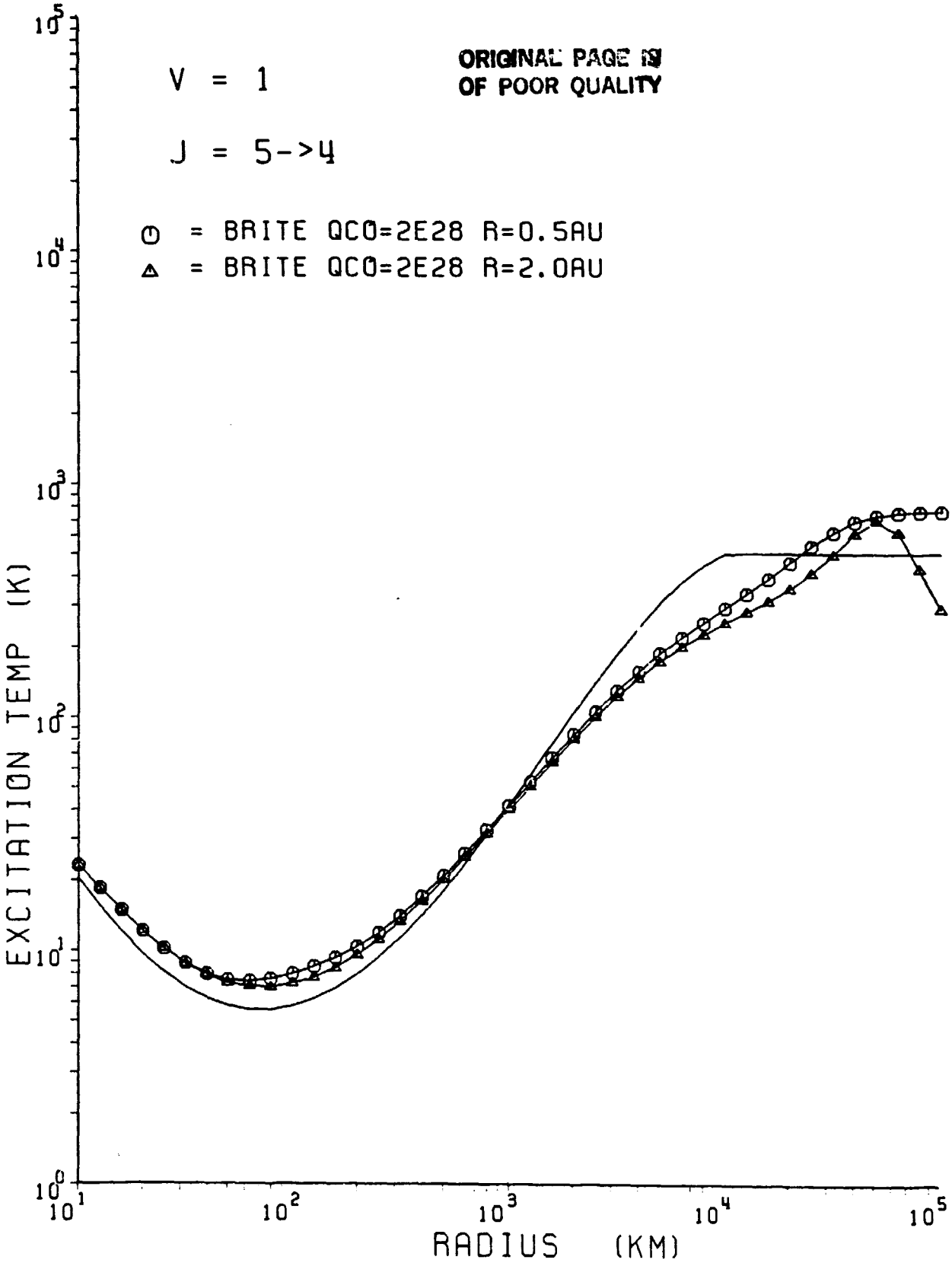

ORIGINAL PAGE IS
OF POOR QUALITY

Figure IIc10

ORIGINAL PAGE IS
OF POOR QUALITY

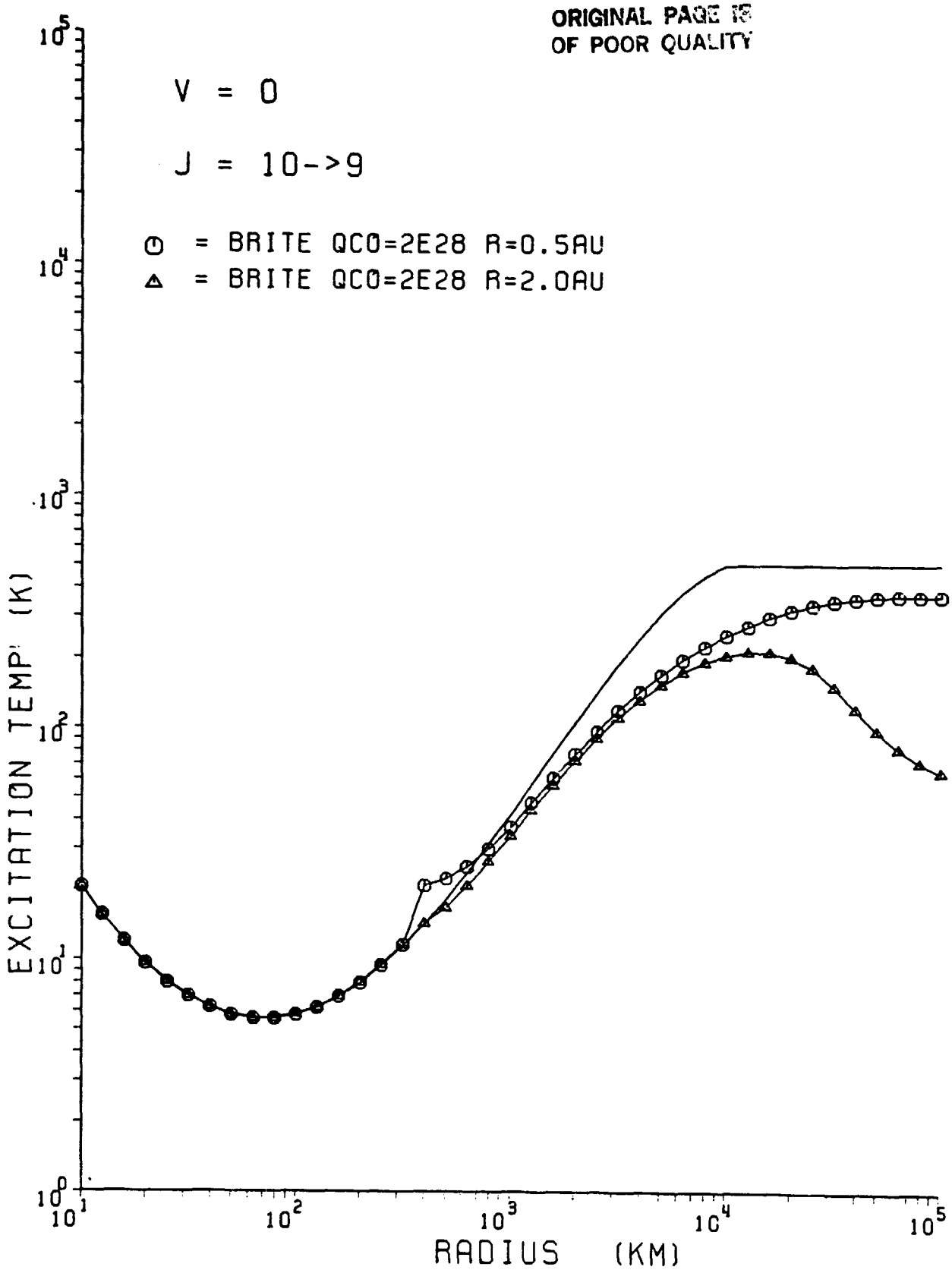

Figure IIc11.

ORIGINAL PAGE IS
OF POOR QUALITY

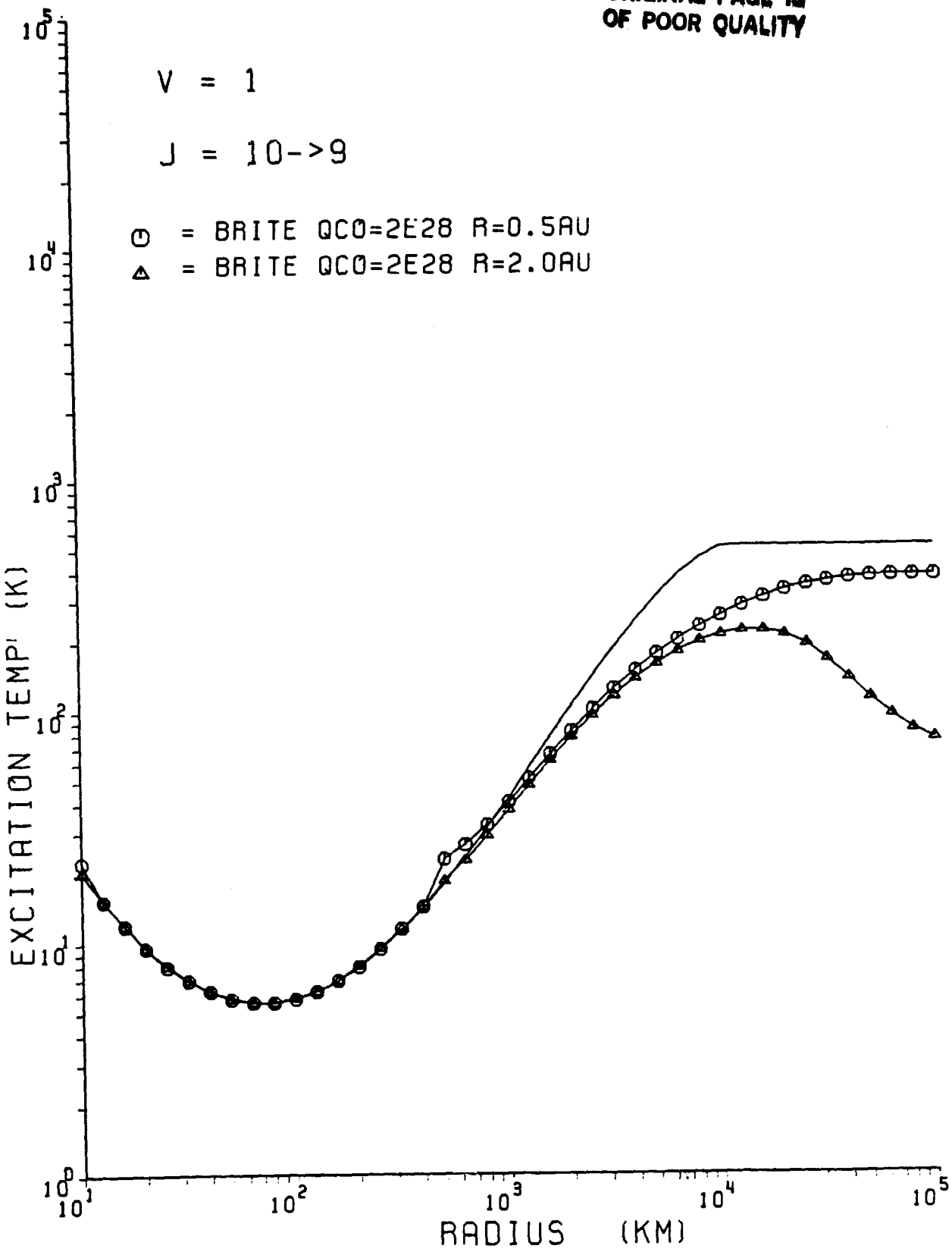

Figure IIc12.

ORIGINAL PAGE IS
OF POOR QUALITY

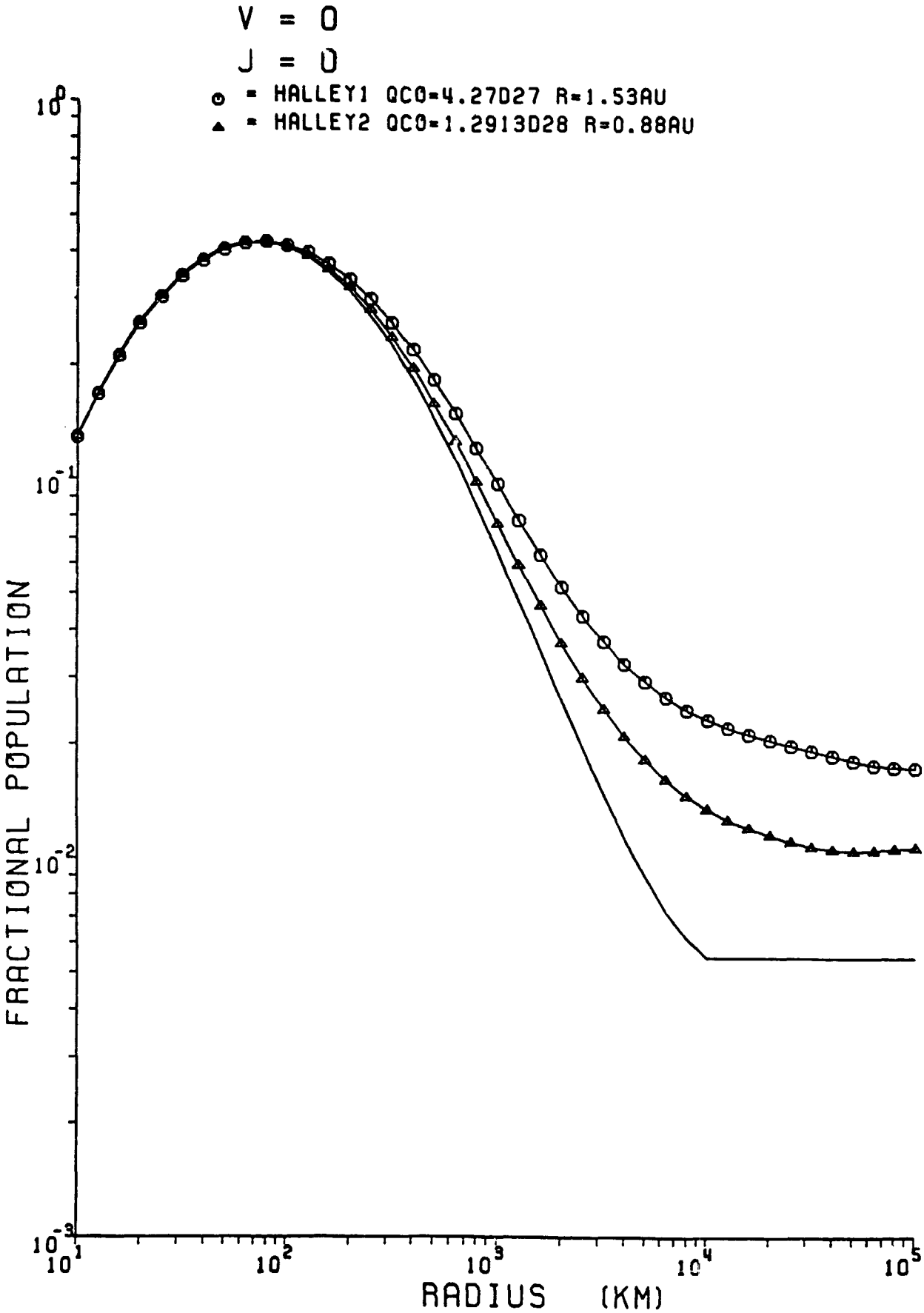

Figure IId1.

ORIGINAL PAGE IS
OF POOR QUALITY

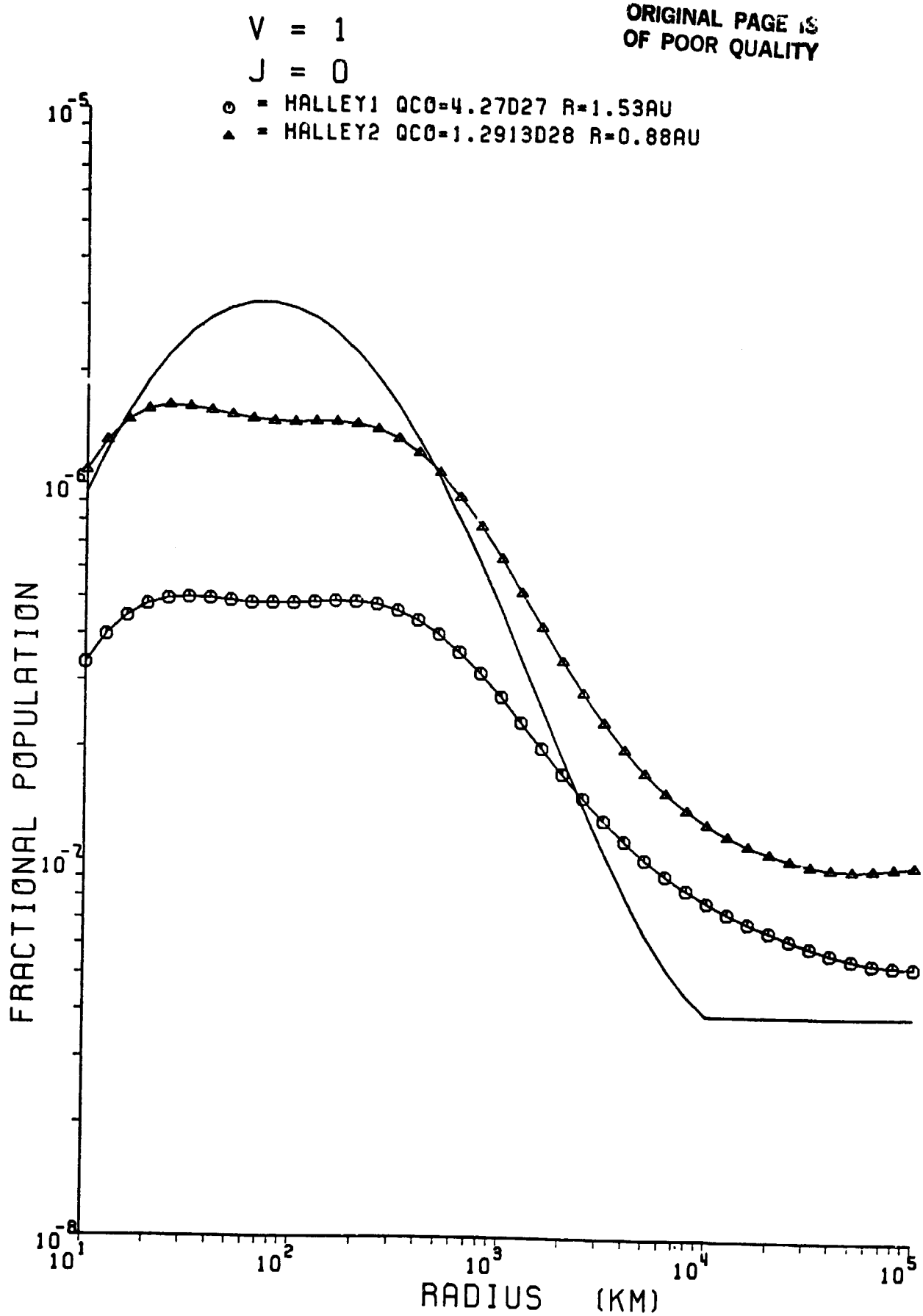

Figure IId2.

ORIGINAL PAGE IS
OF POOR QUALITY

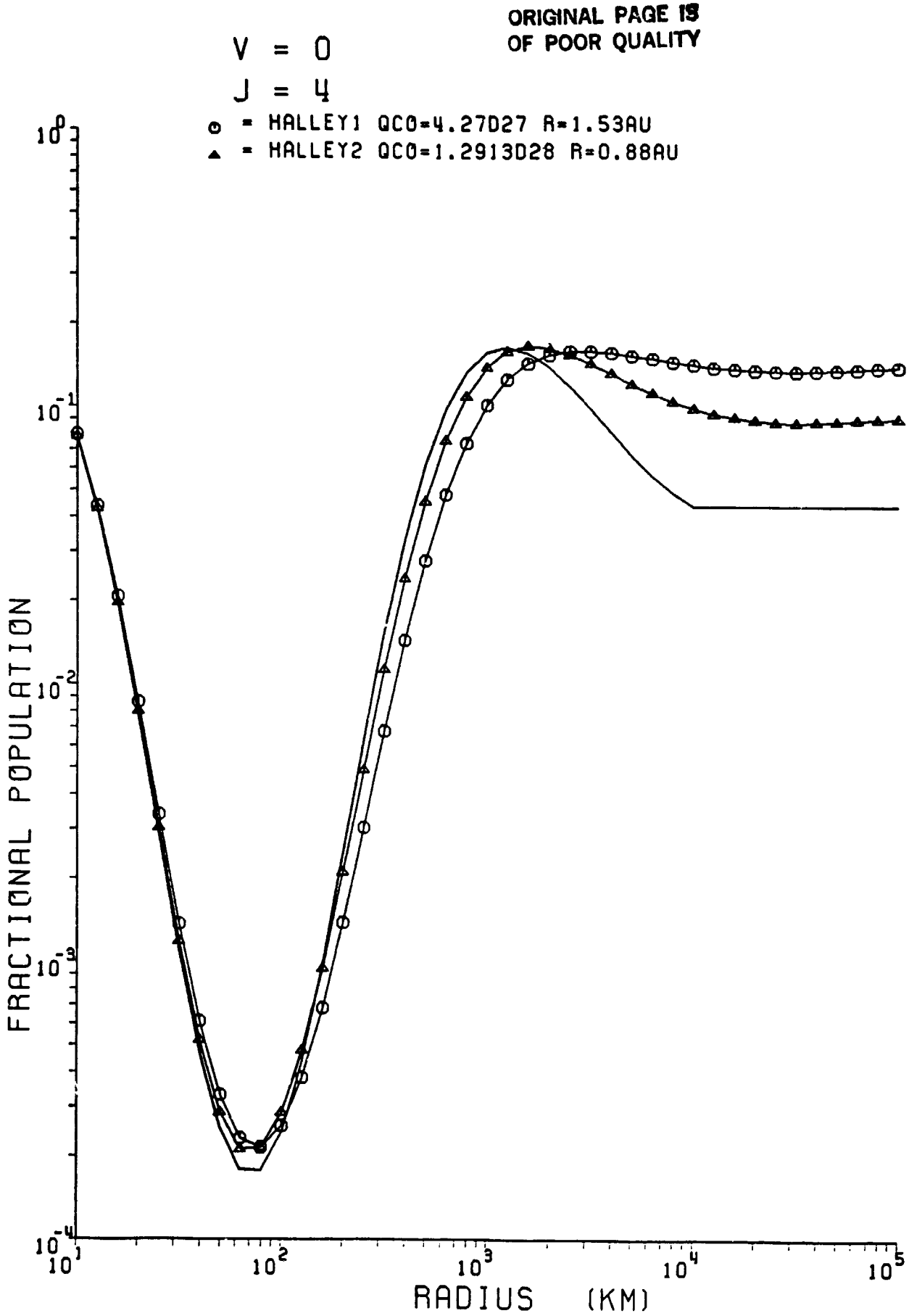

Figure IId3.

ORIGINAL PAGE IS
OF POOR QUALITY

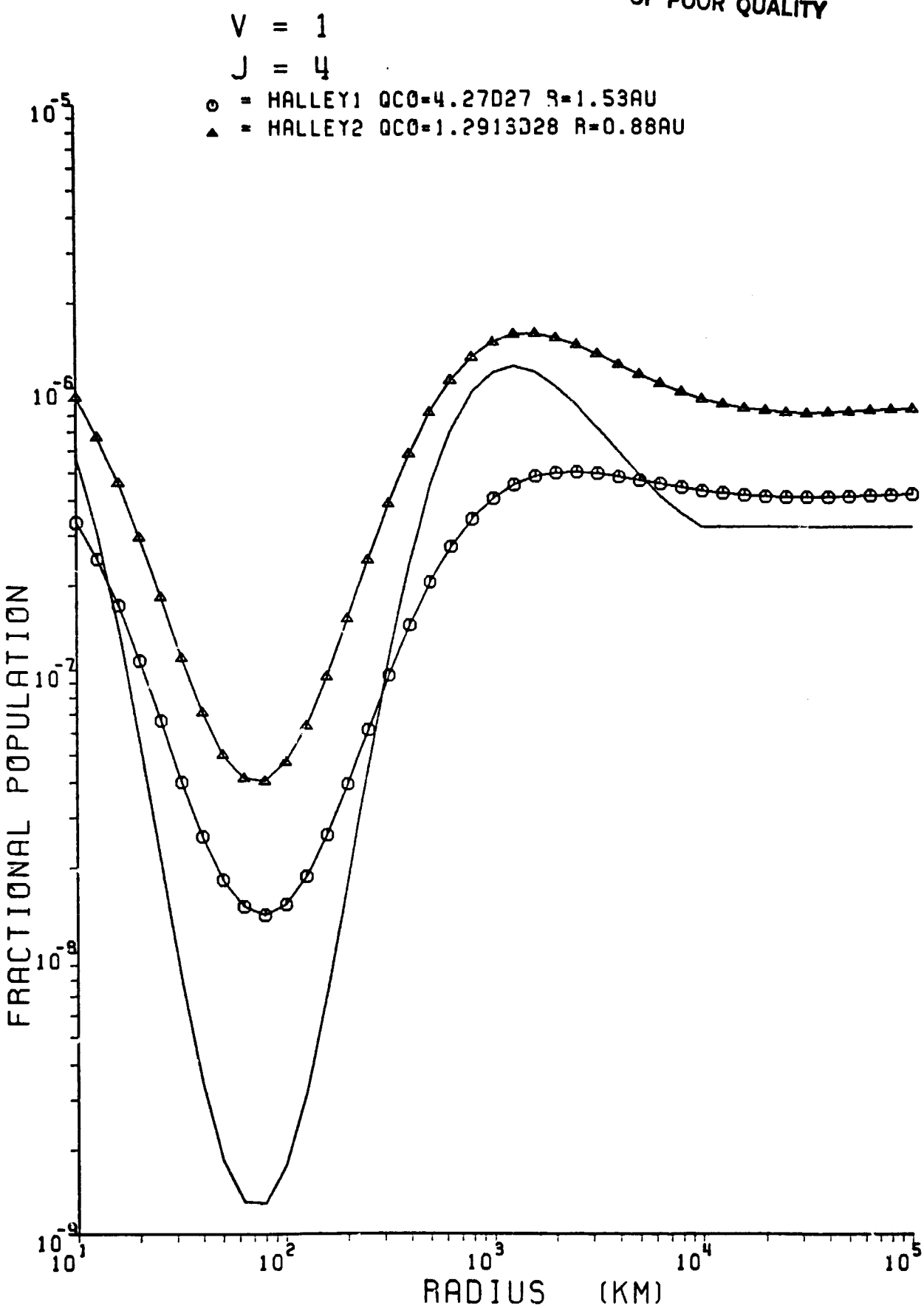

Figure IId4.

ORIGINAL PAGE IS
OF POOR QUALITY

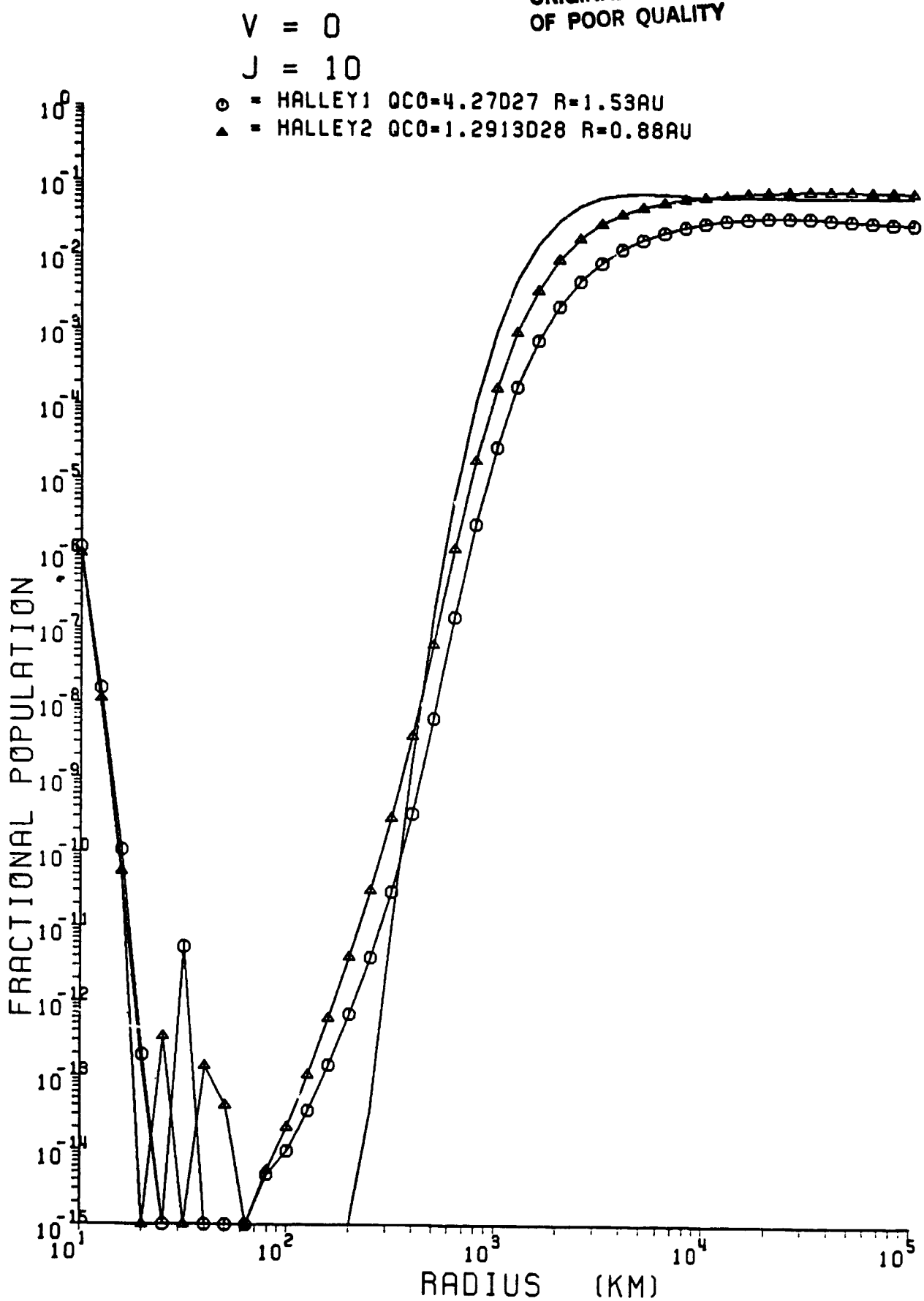

Figure IId5.

ORIGINAL PAGE IS
OF POOR QUALITY

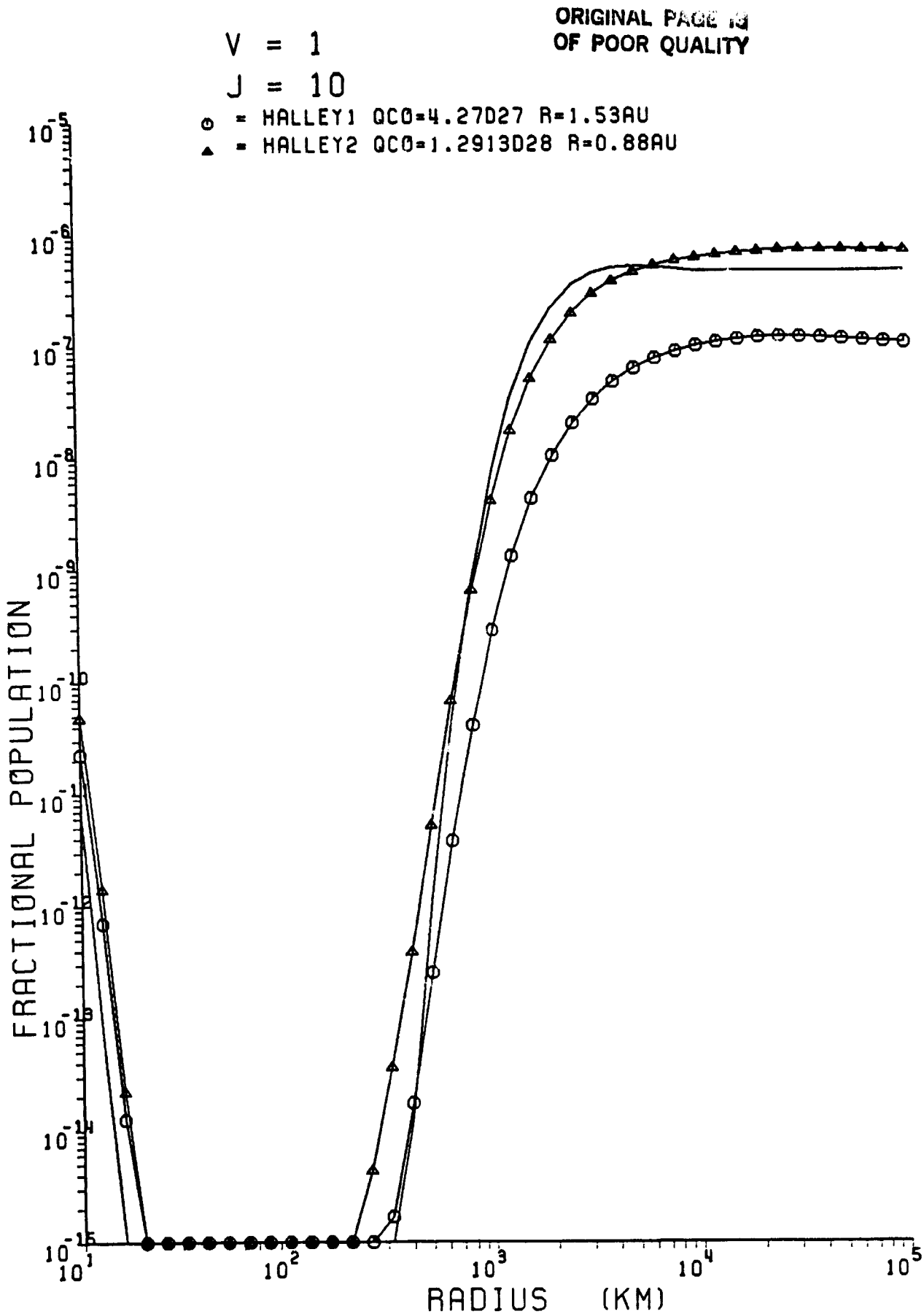

Figure IId6.

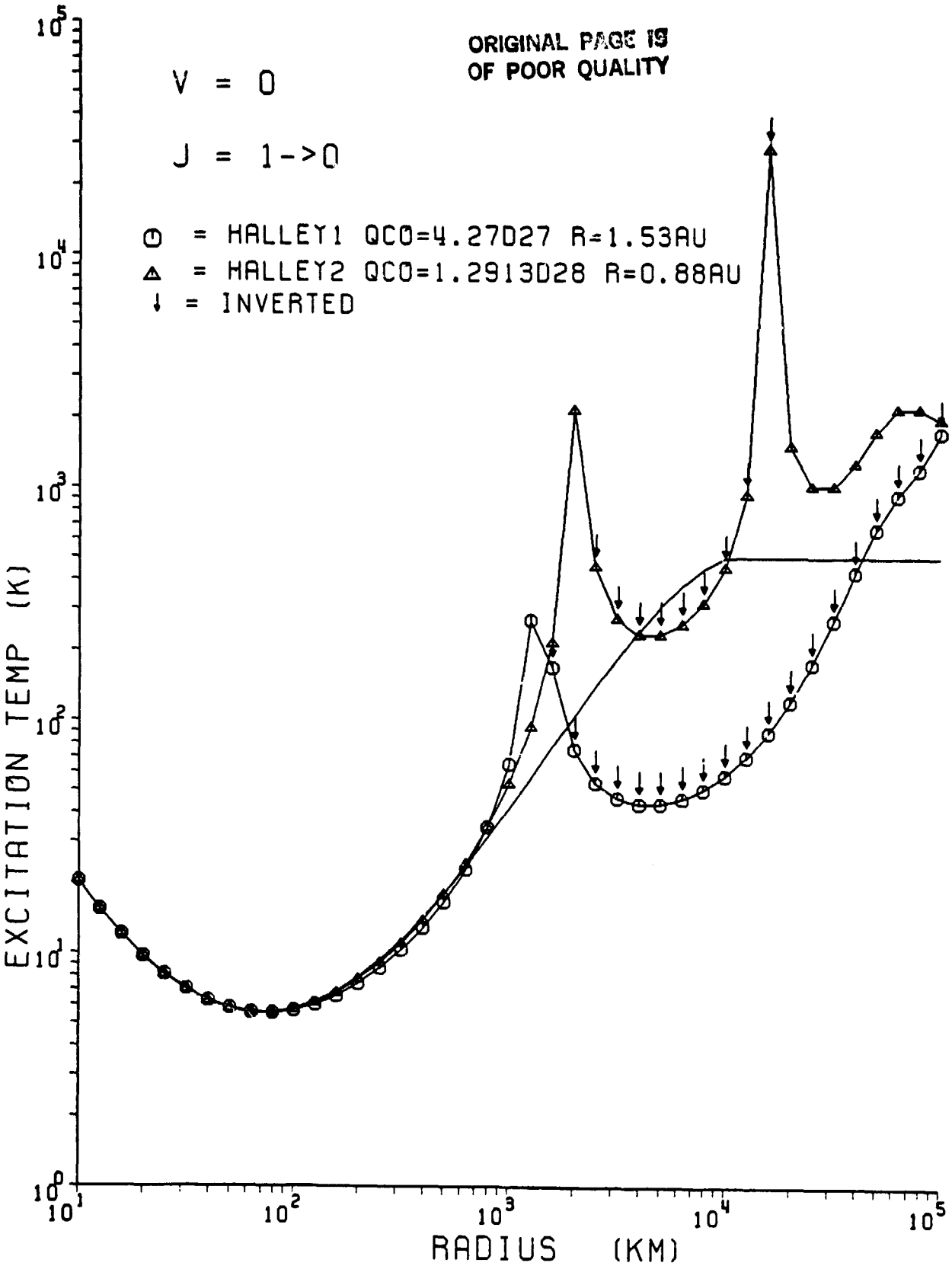
ORIGINAL PAGE IS
OF POOR QUALITY
V = 0
J = 1->0
⊙ = HALLEY1 QCO=4.27D27 R=1.53AU
△ = HALLEY2 QCO=1.2913D28 R=0.88AU
↓ = INVERTED
EXCITATION TEMP (K)
RADIUS (KM)
10^0
10^1
10^2
10^3
10^4
10^5

Figure IId7.

ORIGINAL PAGE IS
OF POOR QUALITY

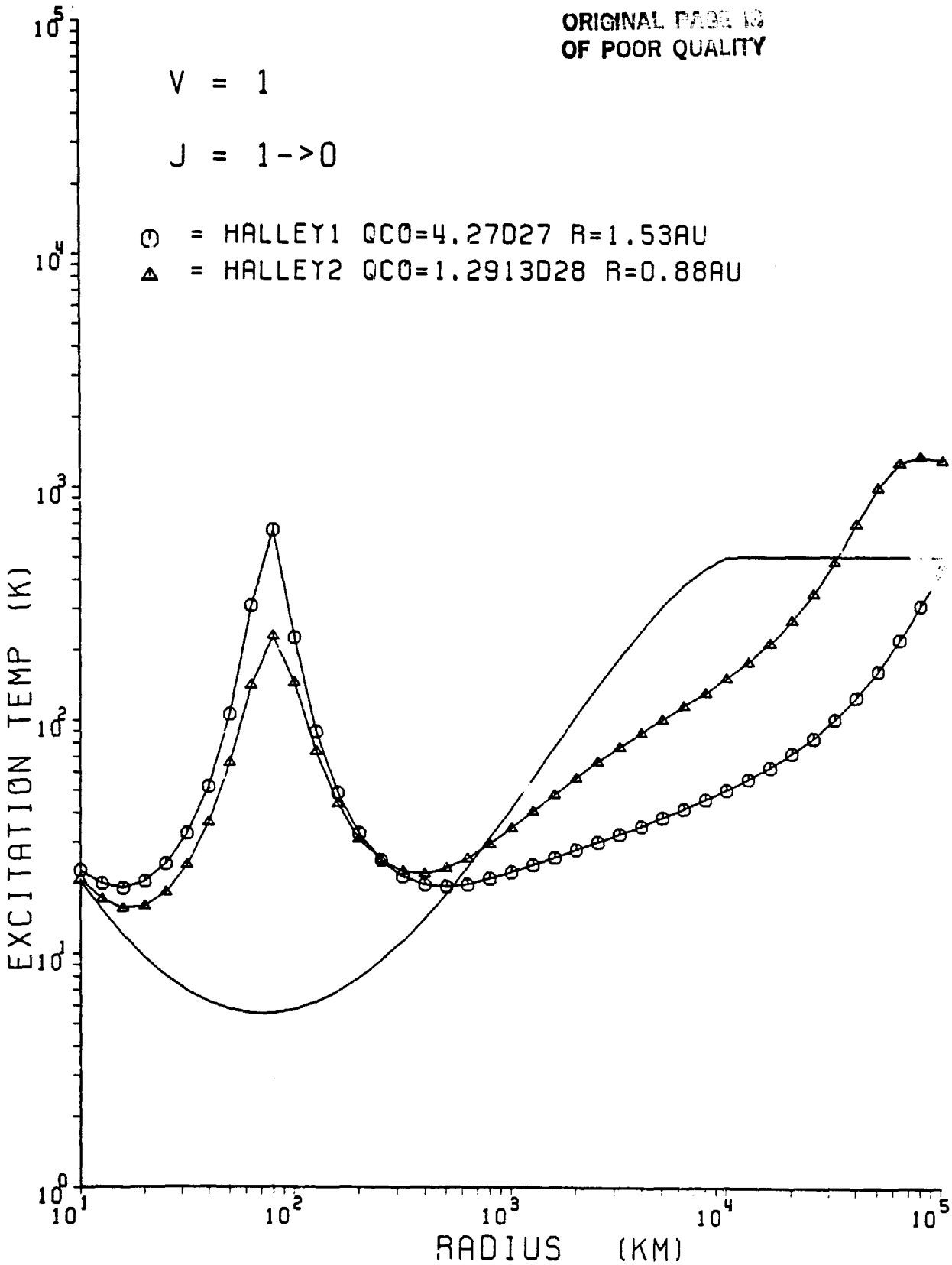

Figure IId8.

ORIGINAL PAGE IS
OF POOR QUALITY

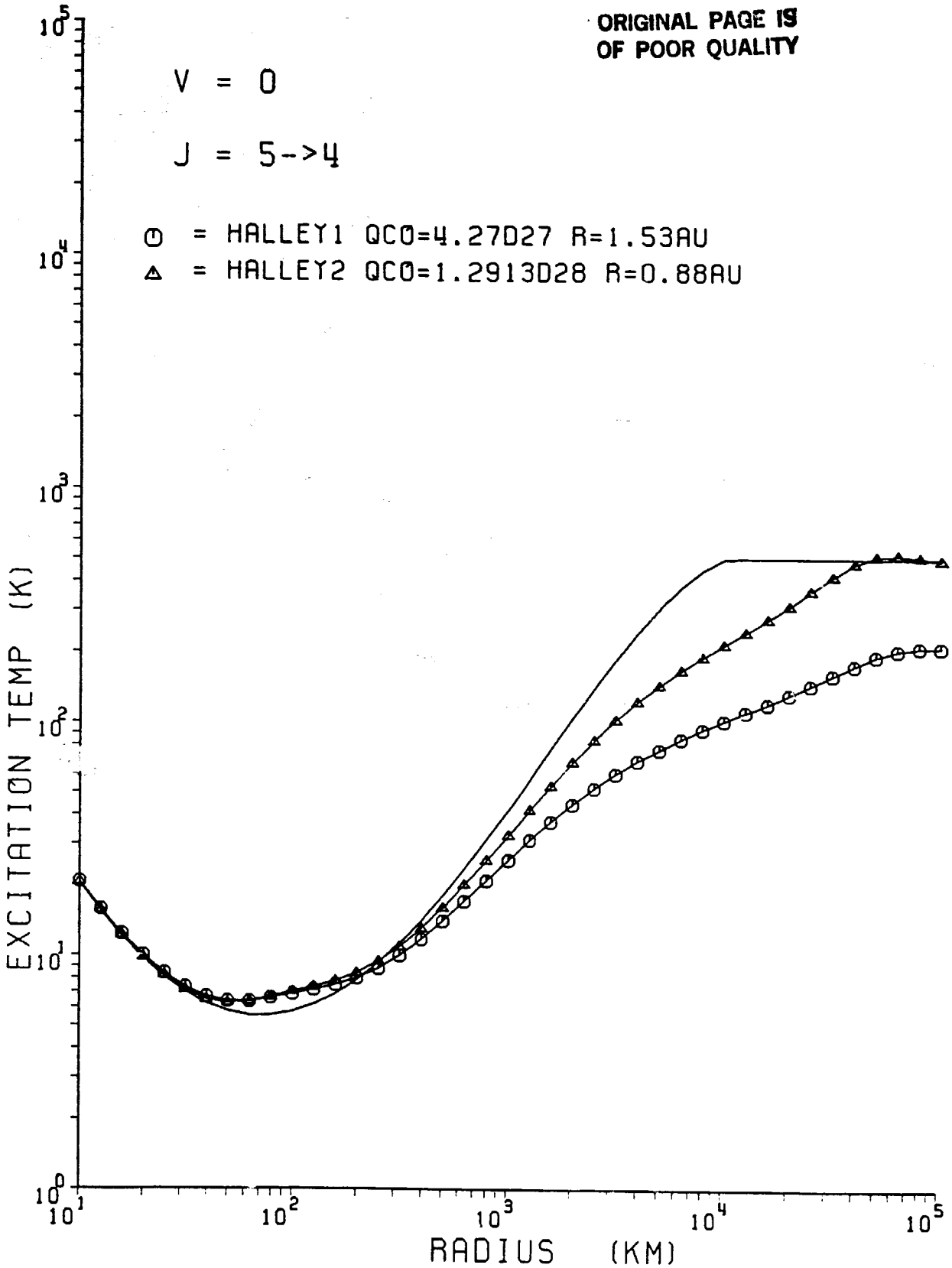

Figure IId9.

ORIGINAL PAGE IS
OF POOR QUALITY

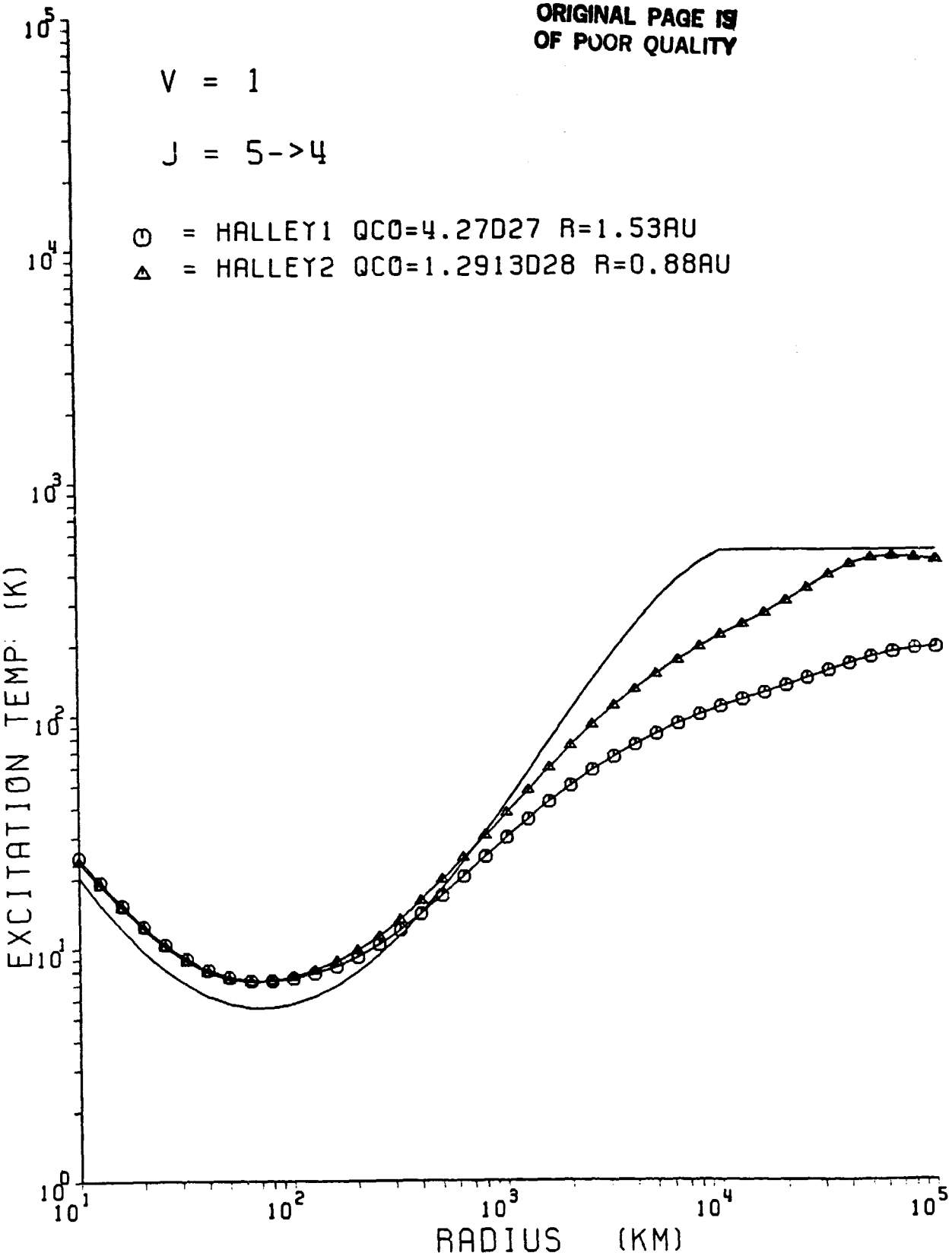

Figure IId10.

ORIGINAL PAGE IS
OF POOR QUALITY

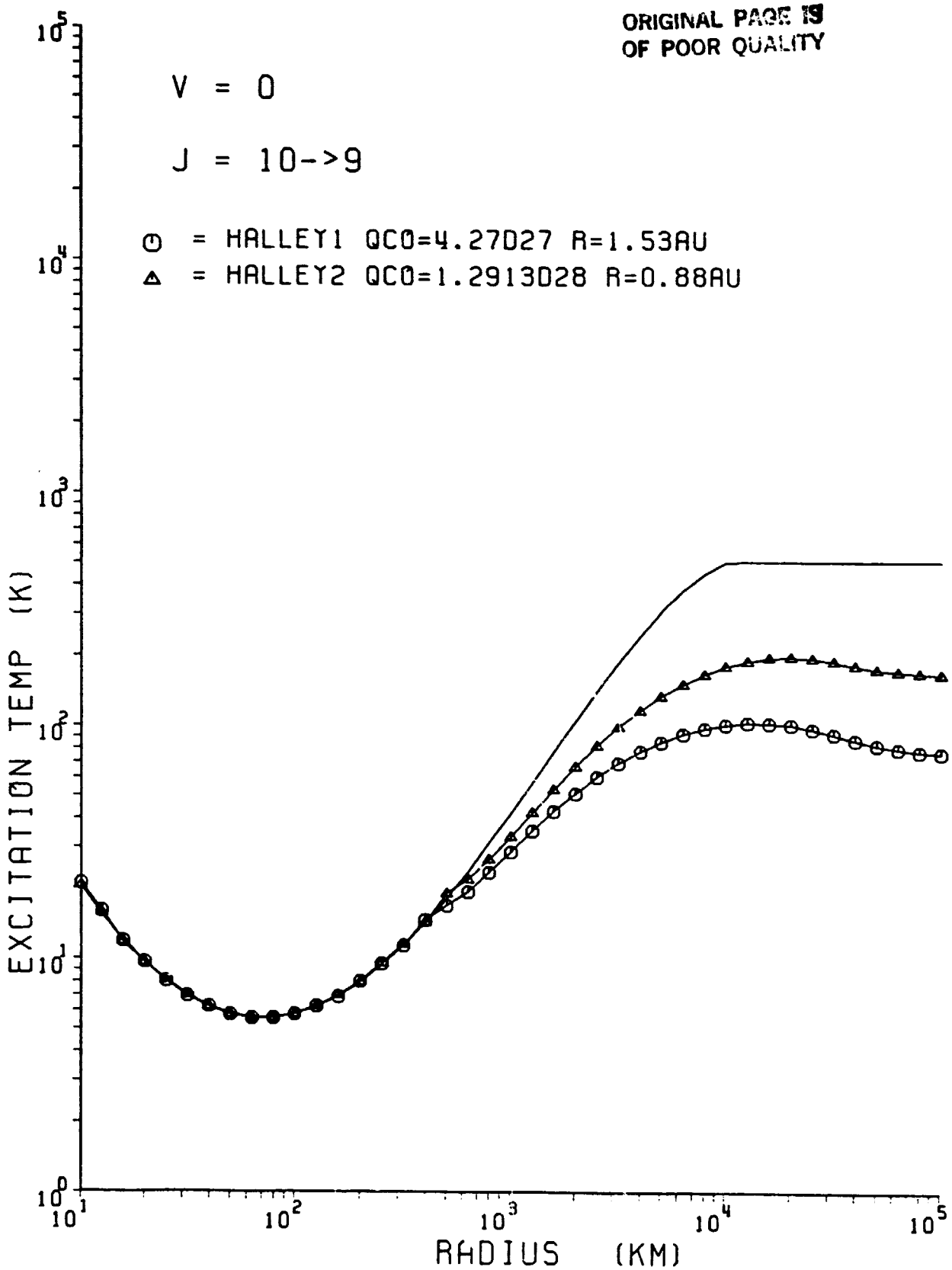

Figure IId11.

ORIGINAL PAGE IS
OF POOR QUALITY

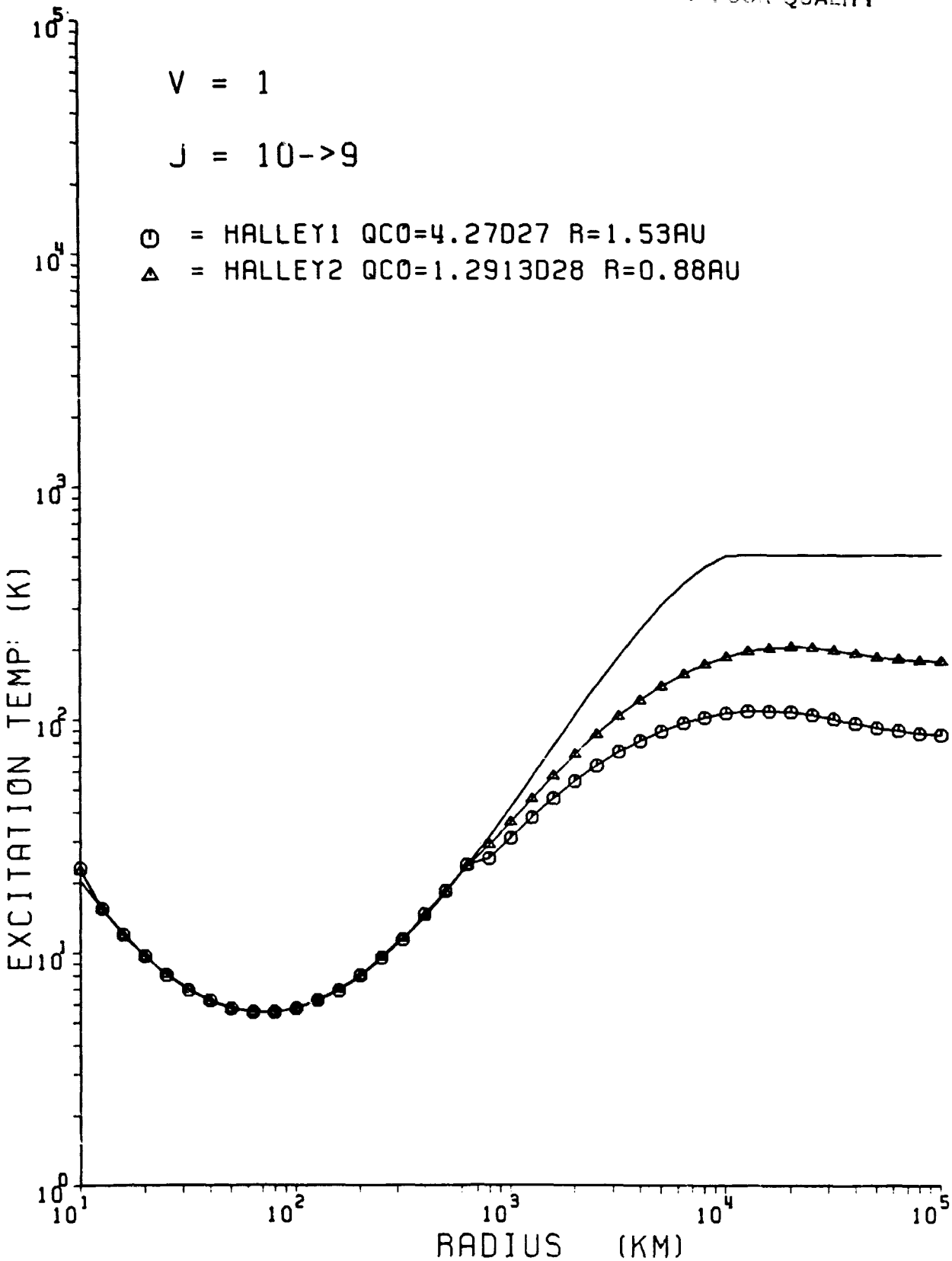

Figure IId12.

ORIGINAL PAGE IS
OF POOR QUALITY

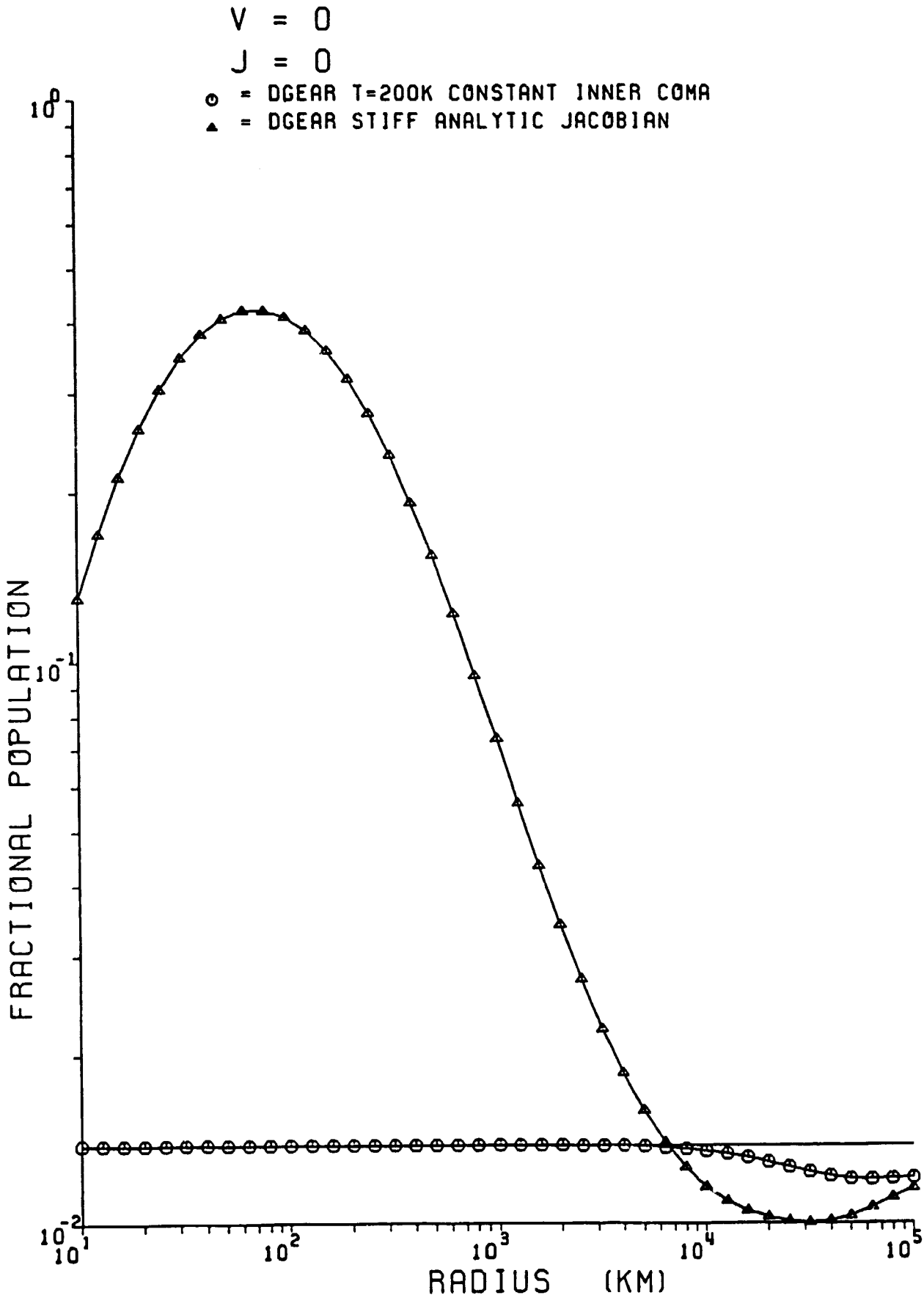

Figure IIe1.

ORIGINAL PAGE IS
OF POOR QUALITY

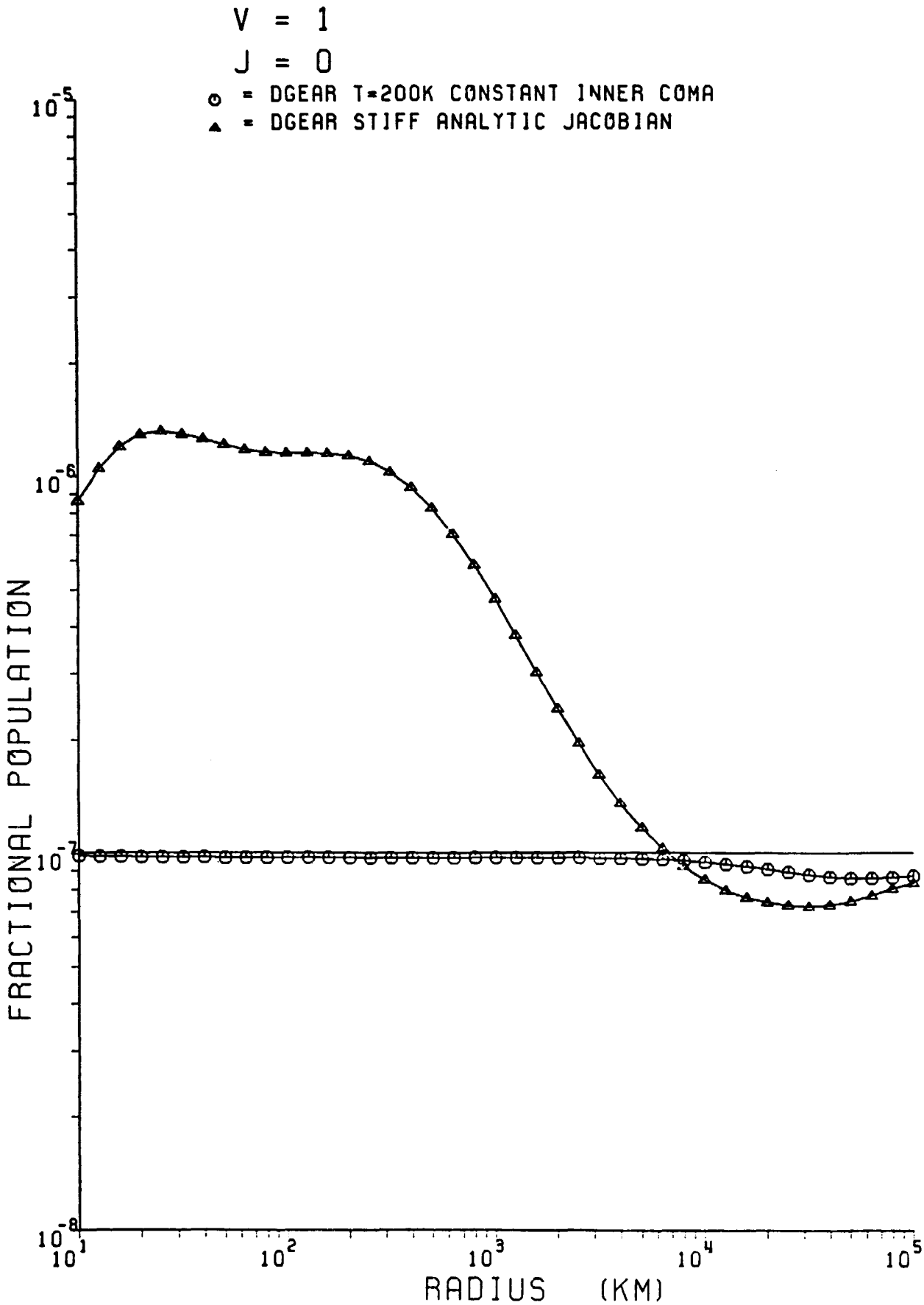

Figure IIe2.

ORIGINAL PAGE IS
OF POOR QUALITY

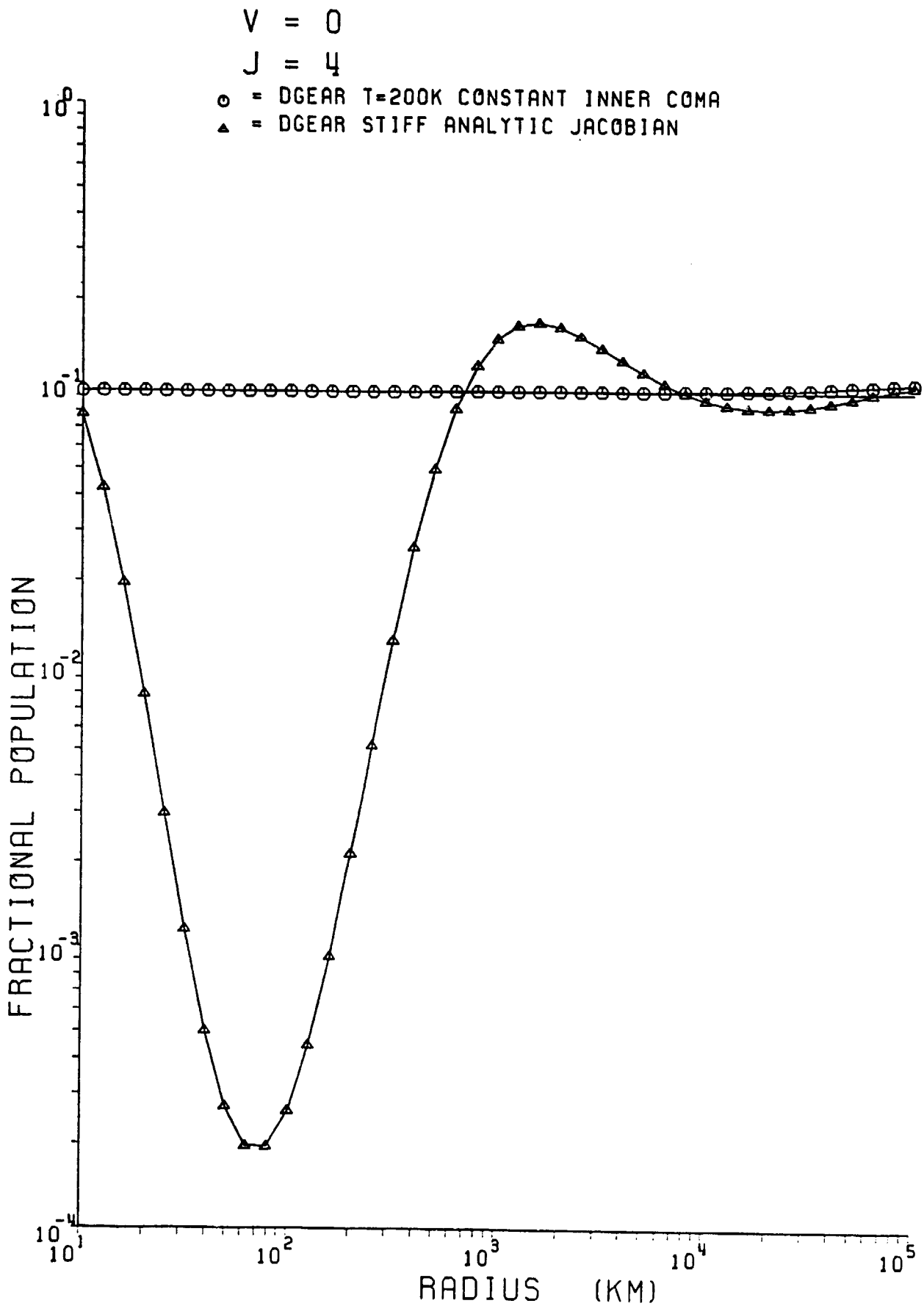

Figure IIe3.

ORIGINAL PAGE IS
OF POOR QUALITY

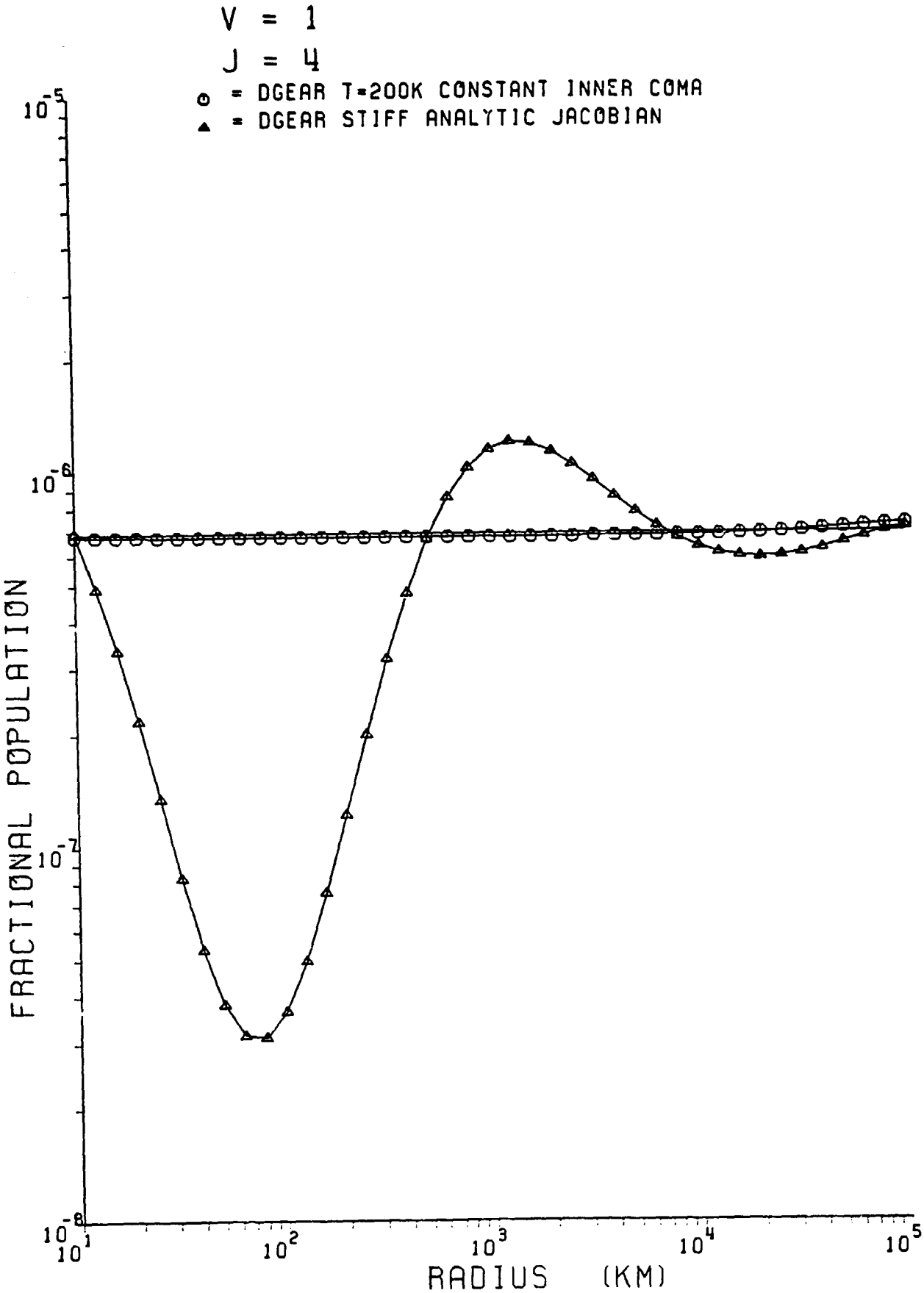

Figure IIe4.

ORIGINAL PAGE IS
OF POOR QUALITY

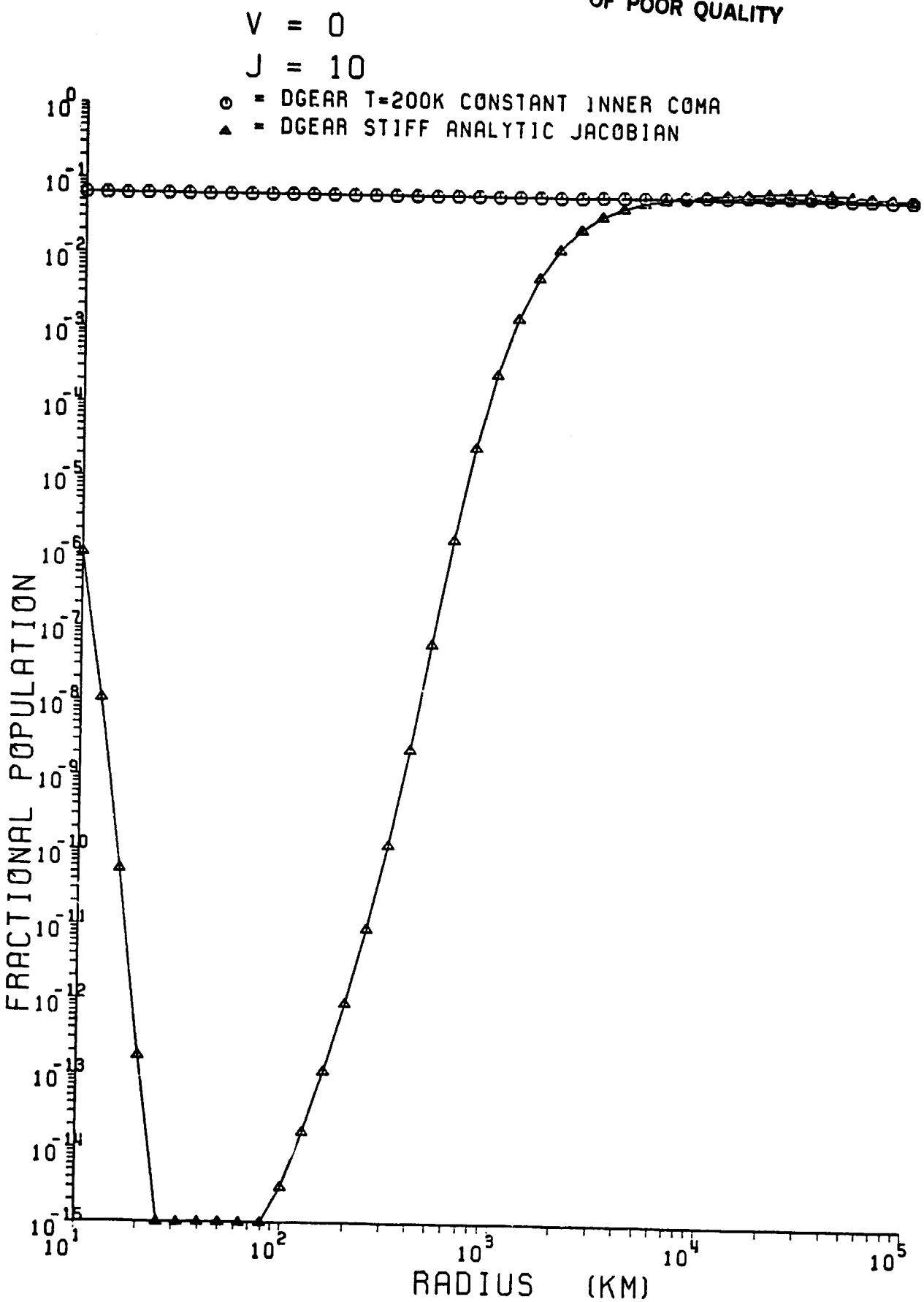

Figure IIe5.

ORIGINAL PAGE IS
OF POOR QUALITY

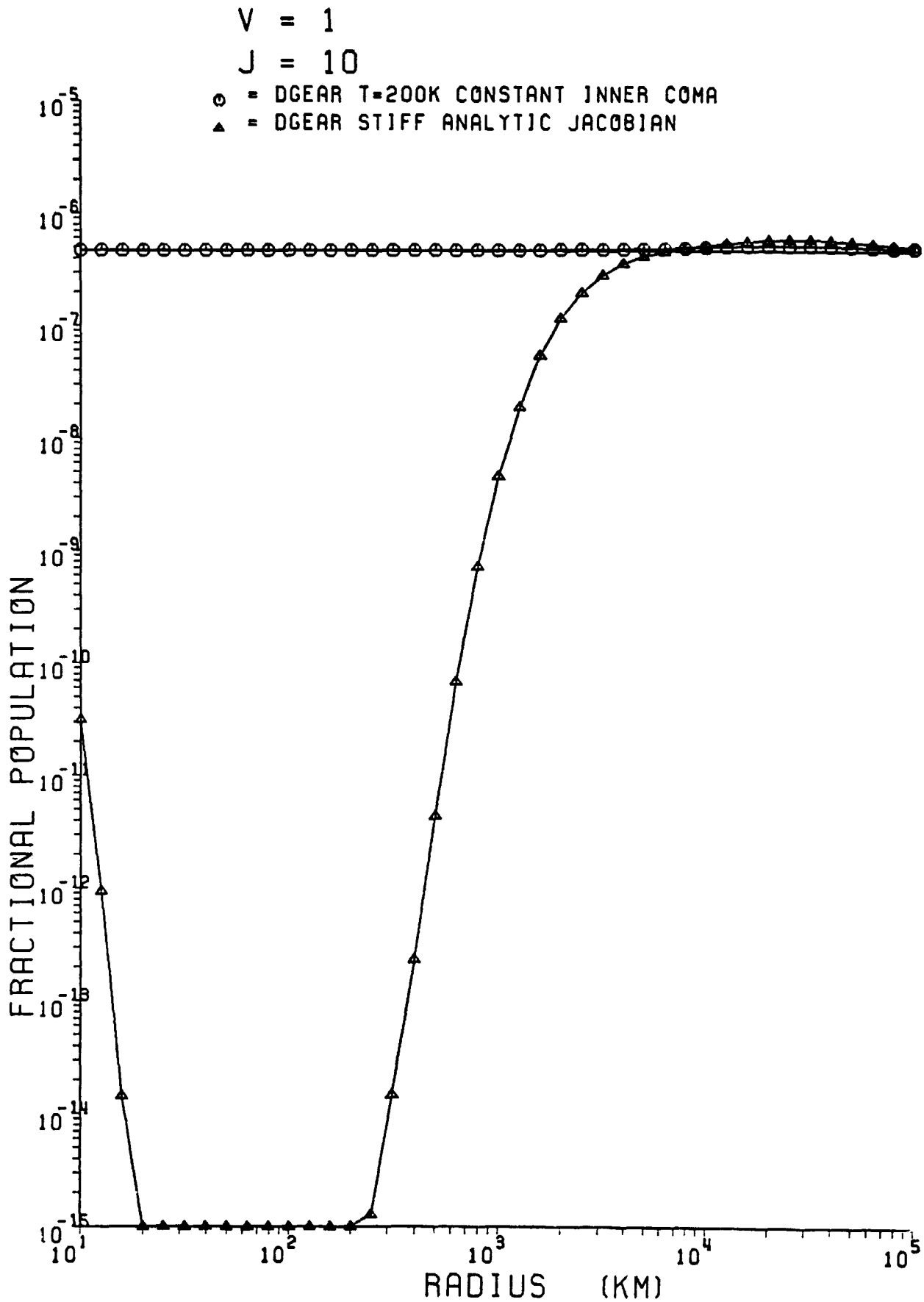

Figure IIe6.

ORIGINAL PAGE IS
OF POOR QUALITY

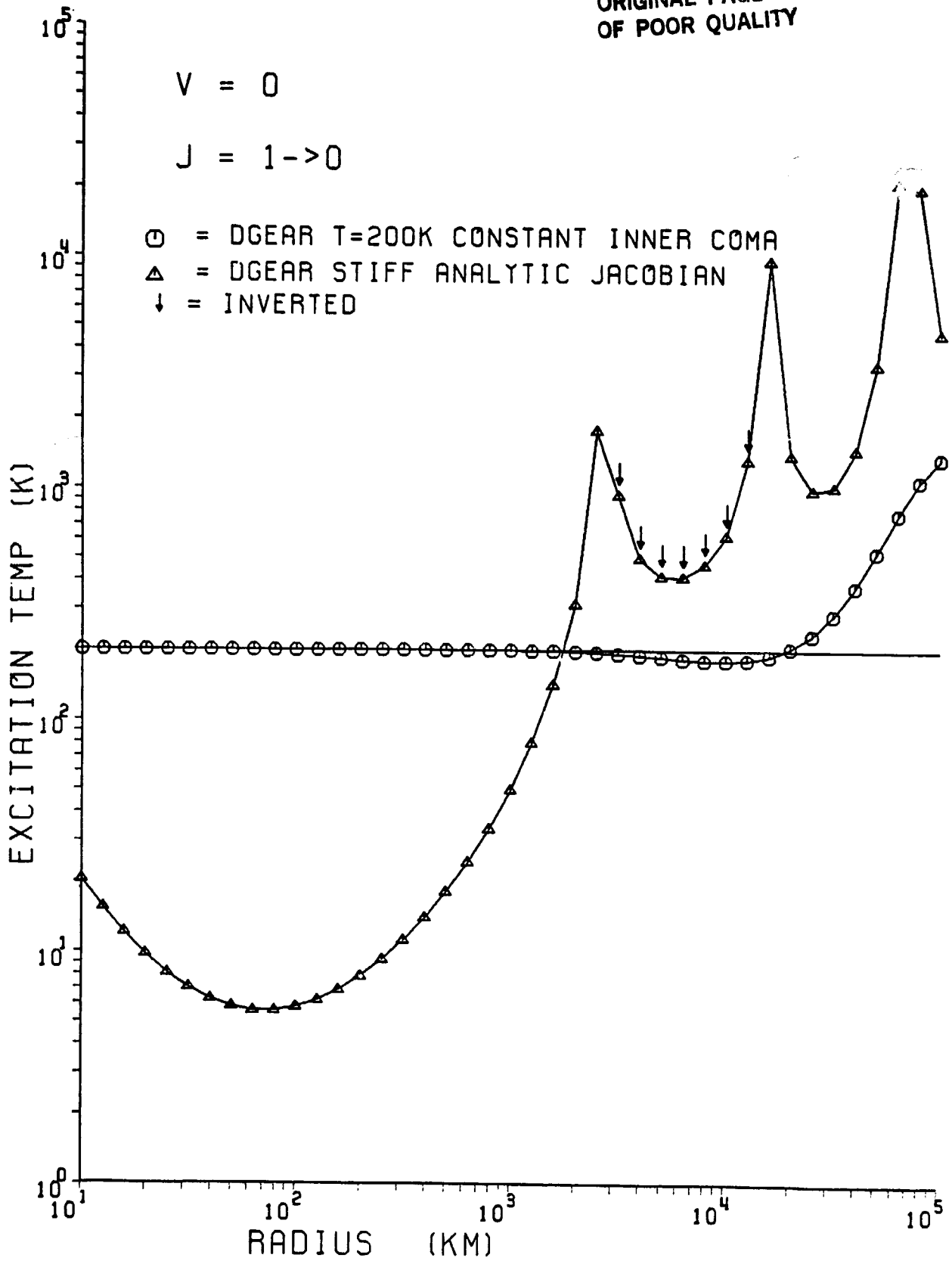

Figure IIe7.

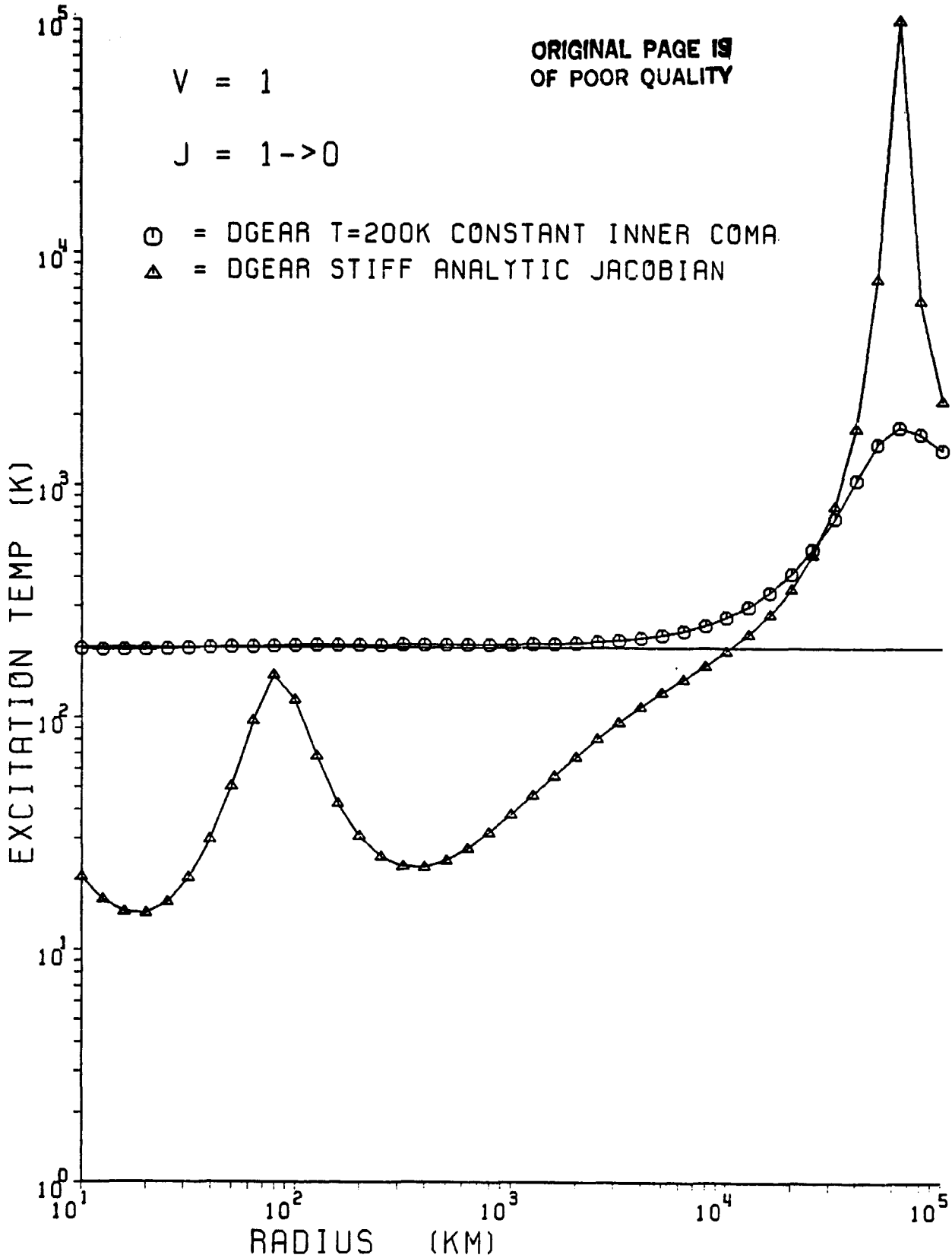
ORIGINAL PAGE IS
OF POOR QUALITY
V = 1
J = 1->0
⊙ = DGEAR T=200K CONSTANT INNER COMA
△ = DGEAR STIFF ANALYTIC JACOBIAN
EXCITATION TEMP (K)
RADIUS (KM)
10^0
10^1
10^2
10^3
10^4
10^5

Figure IIe8.

ORIGINAL PAGE IS
OF POOR QUALITY

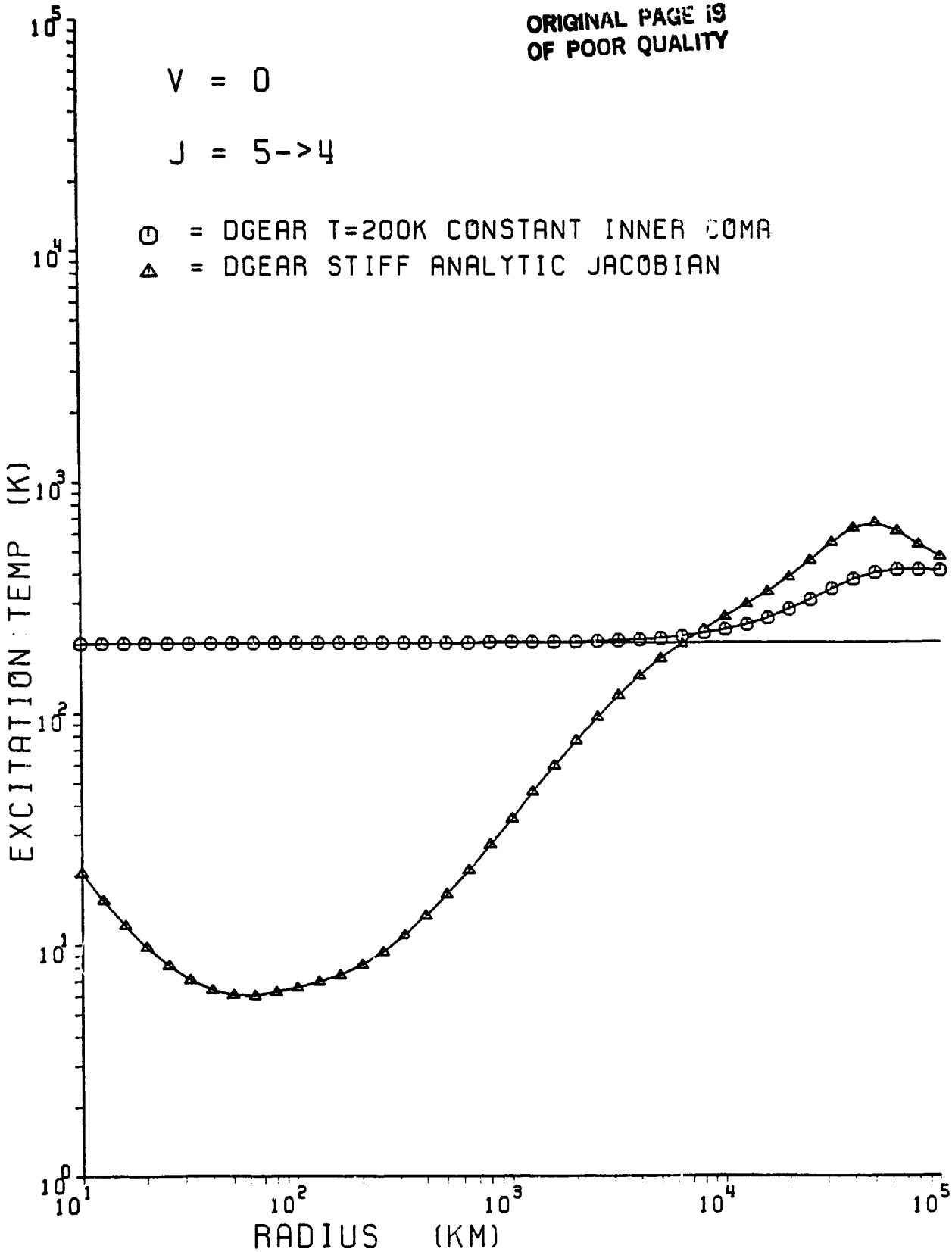

Figure IIe9.

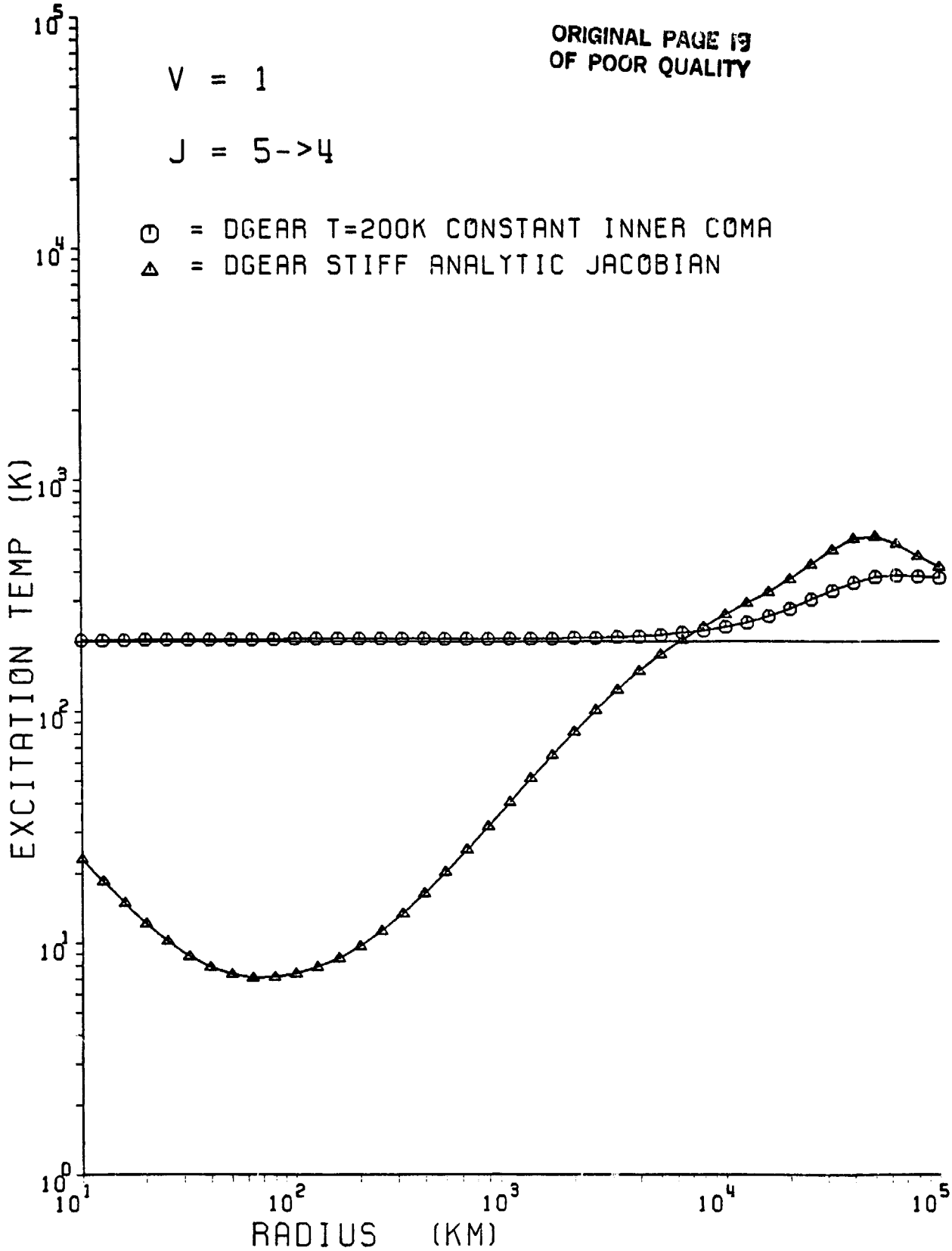

Figure IIe10.

ORIGINAL PAGE IS
OF POOR QUALITY

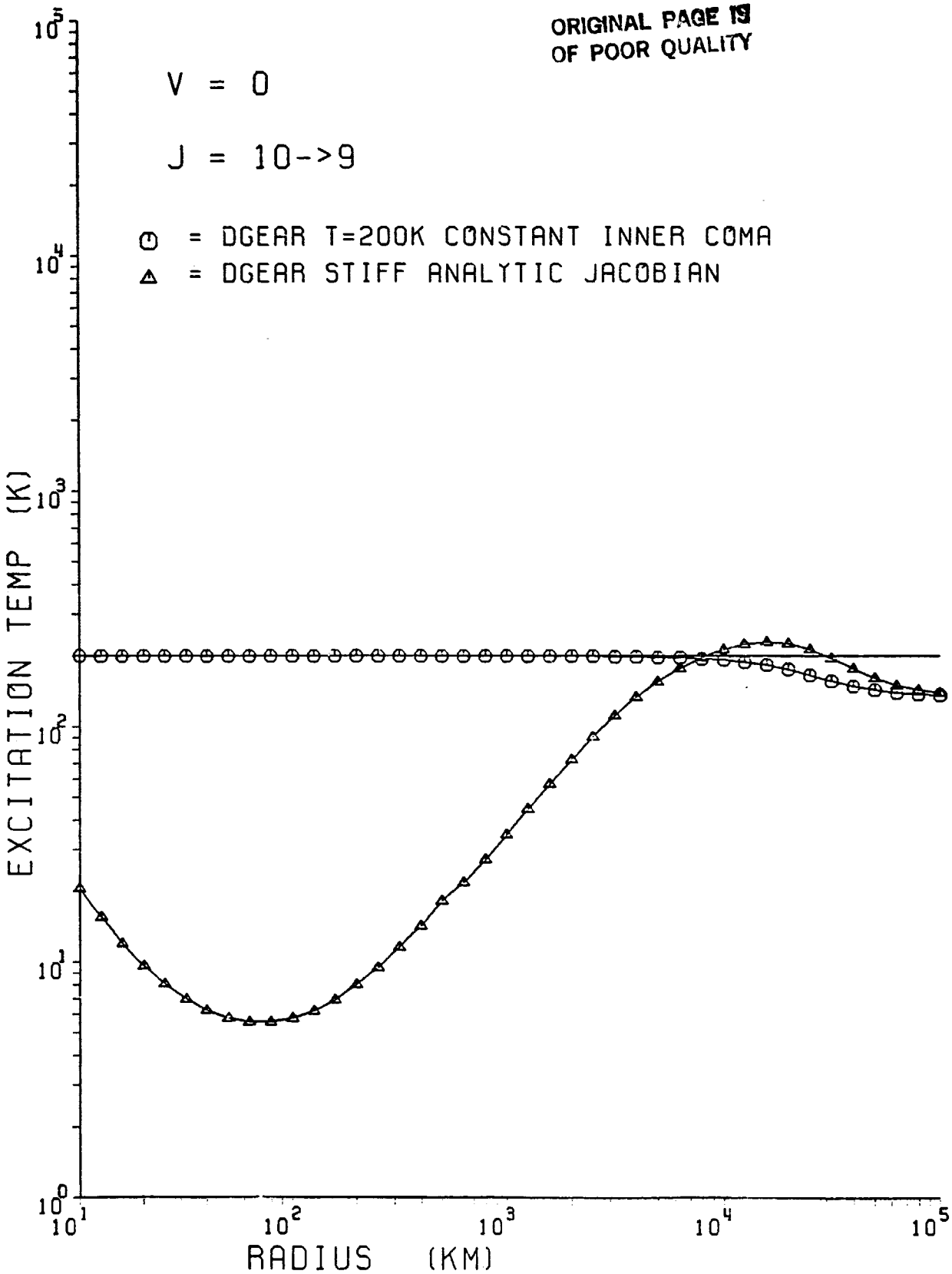

Figure IIe11.

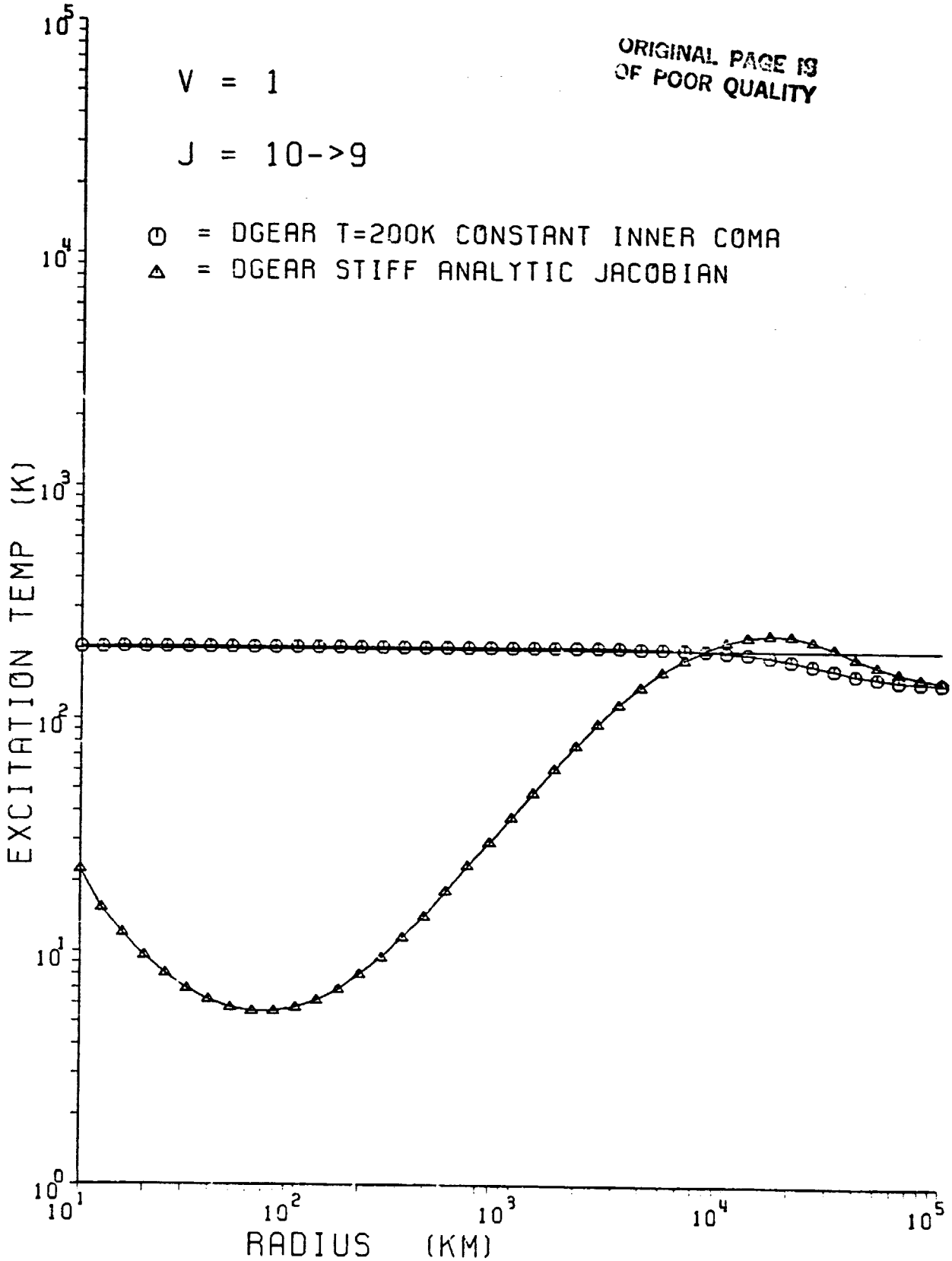

Figure IIe12.

ORIGINAL PAGE IS
OF POOR QUALITY

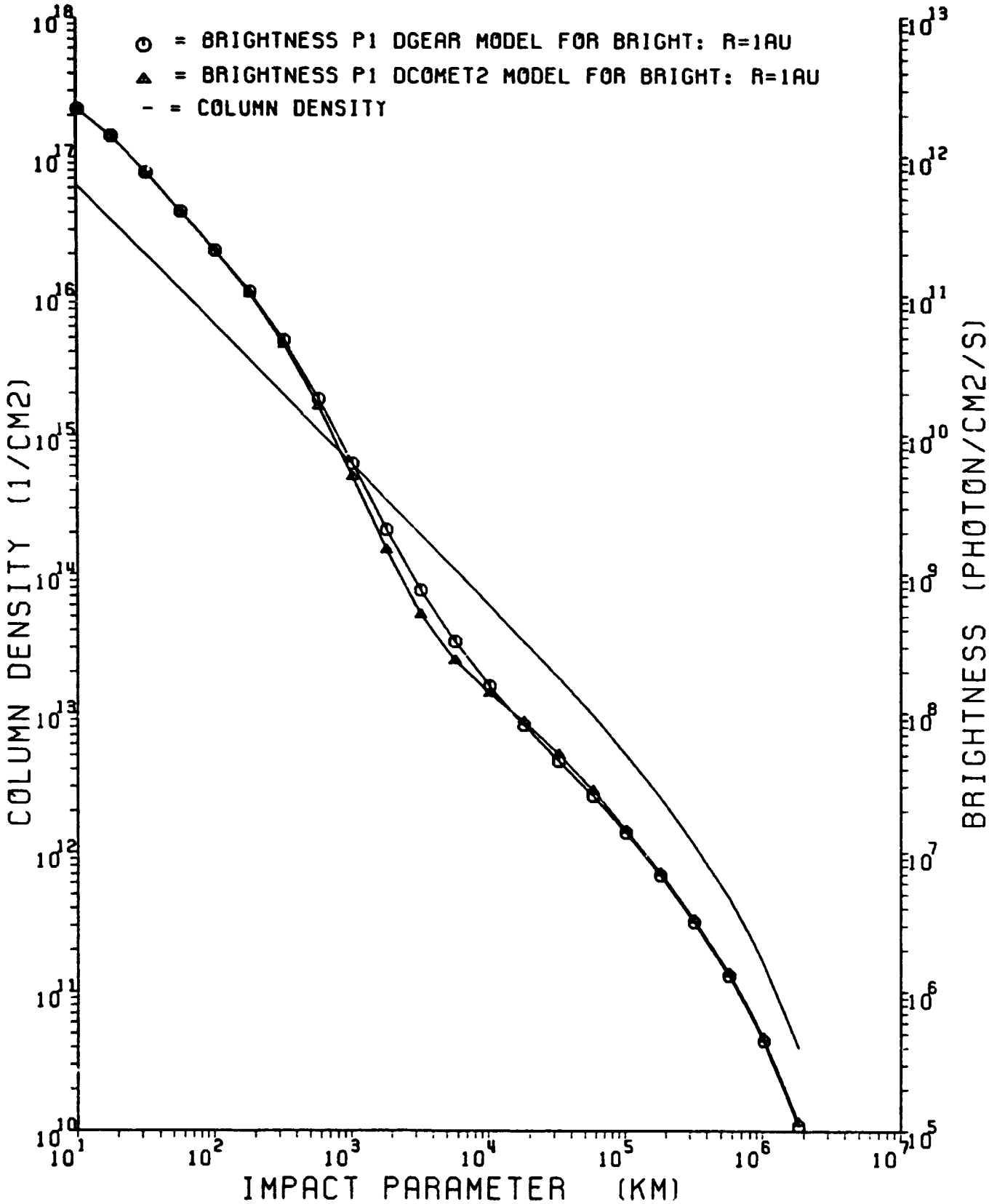

Figure IIIa.

ORIGINAL PAGE IS
OF POOR QUALITY

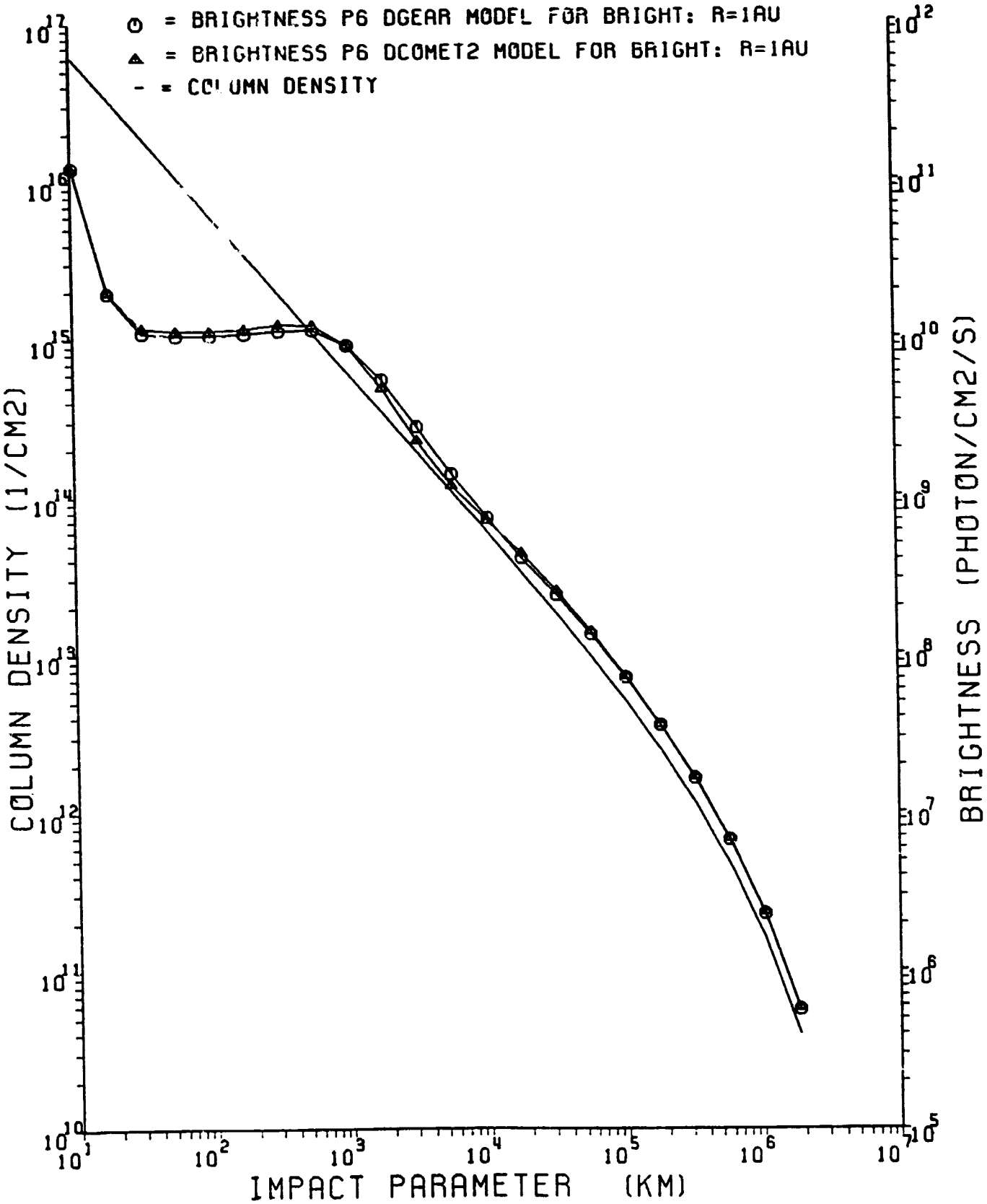

Figure IIIb.

ORIGINAL PAGE IS
OF POOR QUALITY

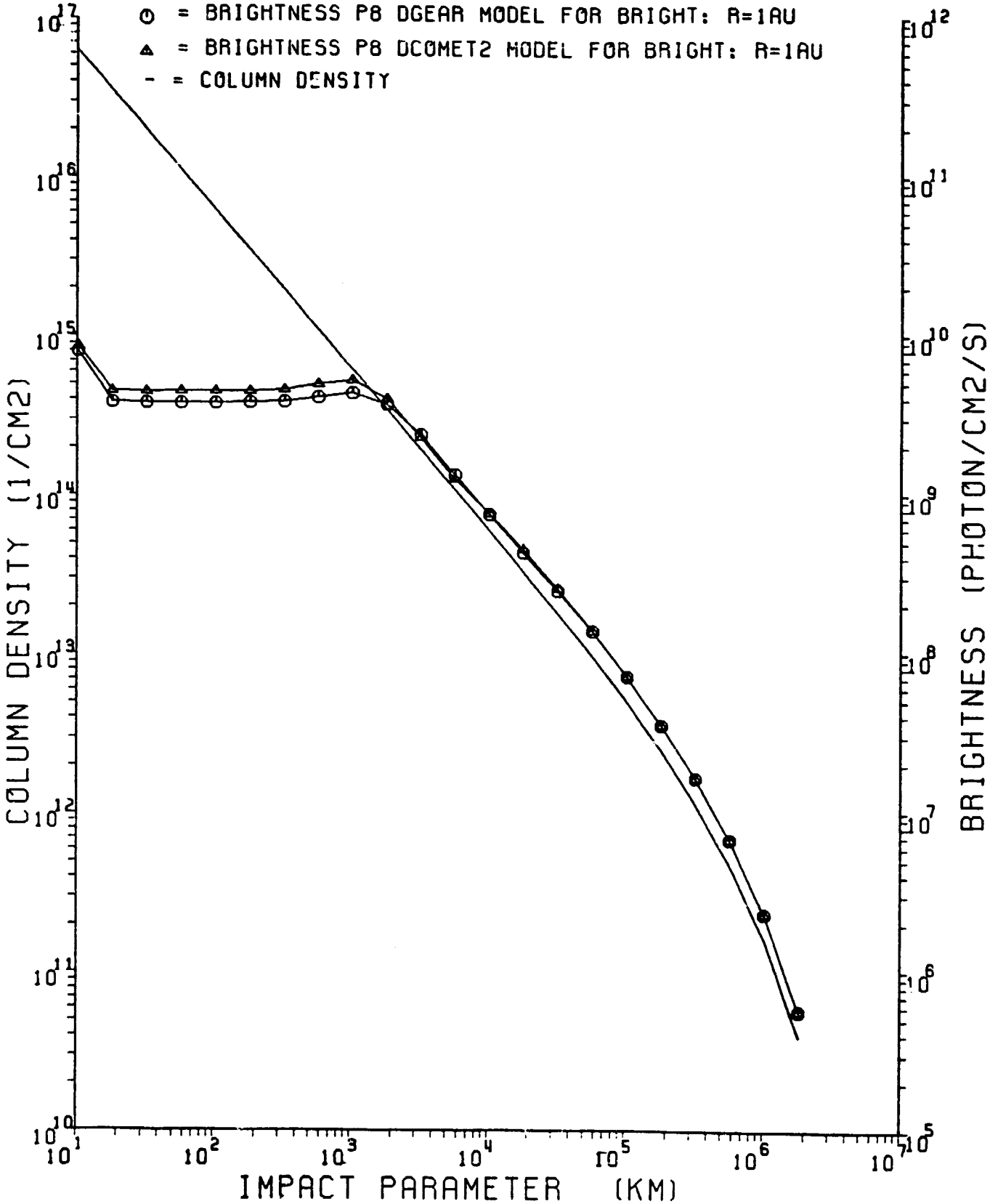

ORIGINAL PAGE IS
OF POOR QUALITY

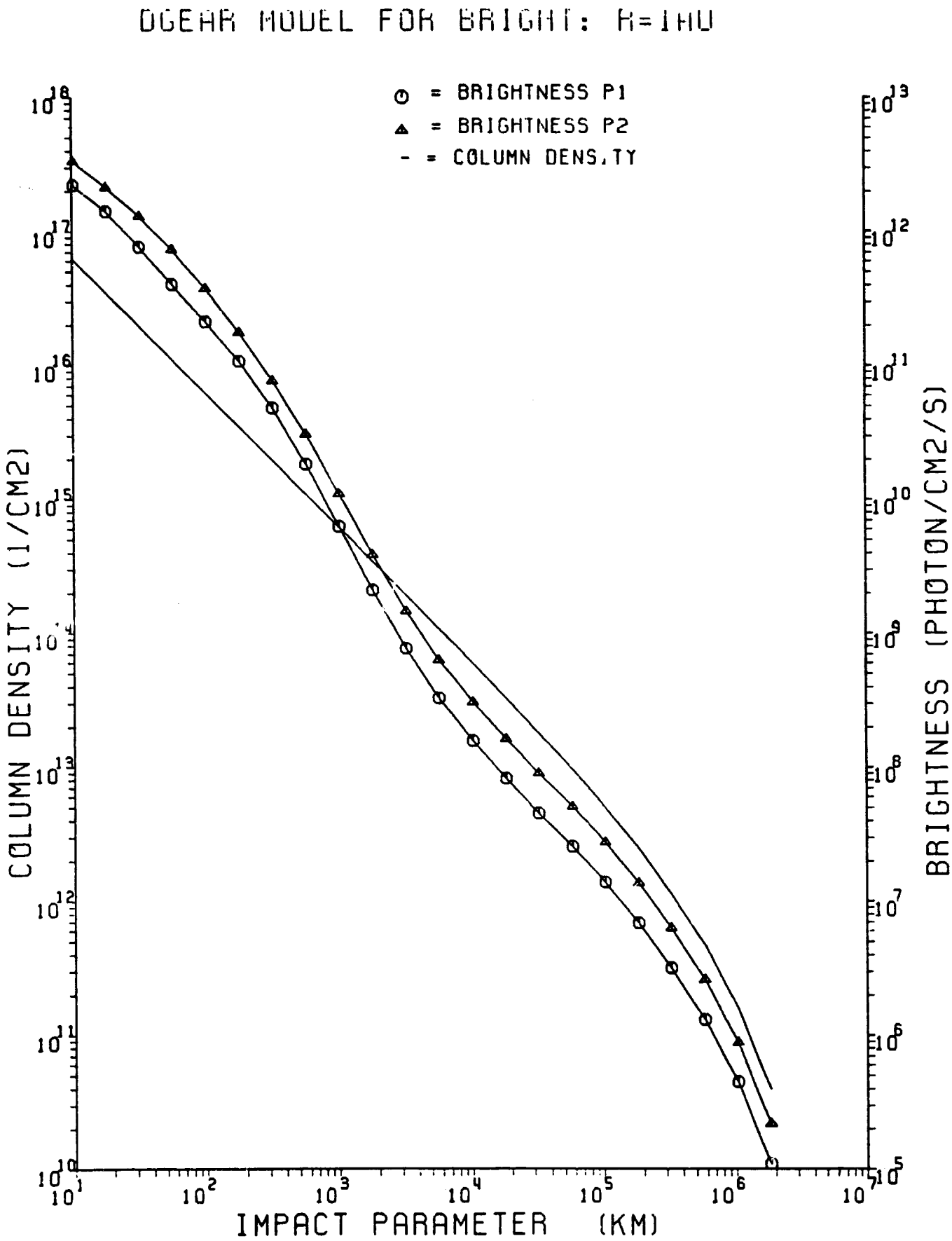

Figure IIId.

ORIGINAL PAGE IS
OF POOR QUALITY

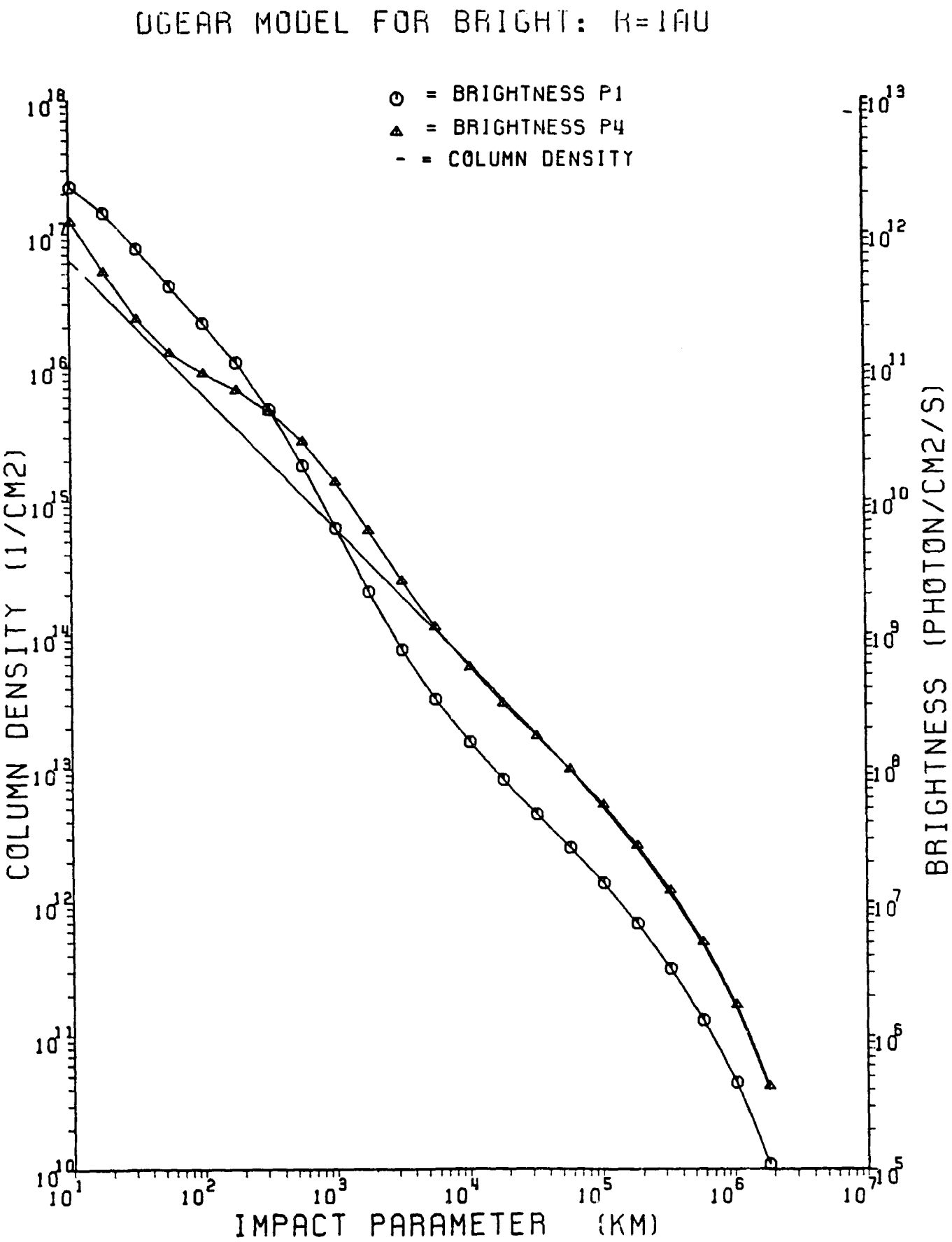

Figure IIIe.

ORIGINAL PAGE IS
OF POOR QUALITY

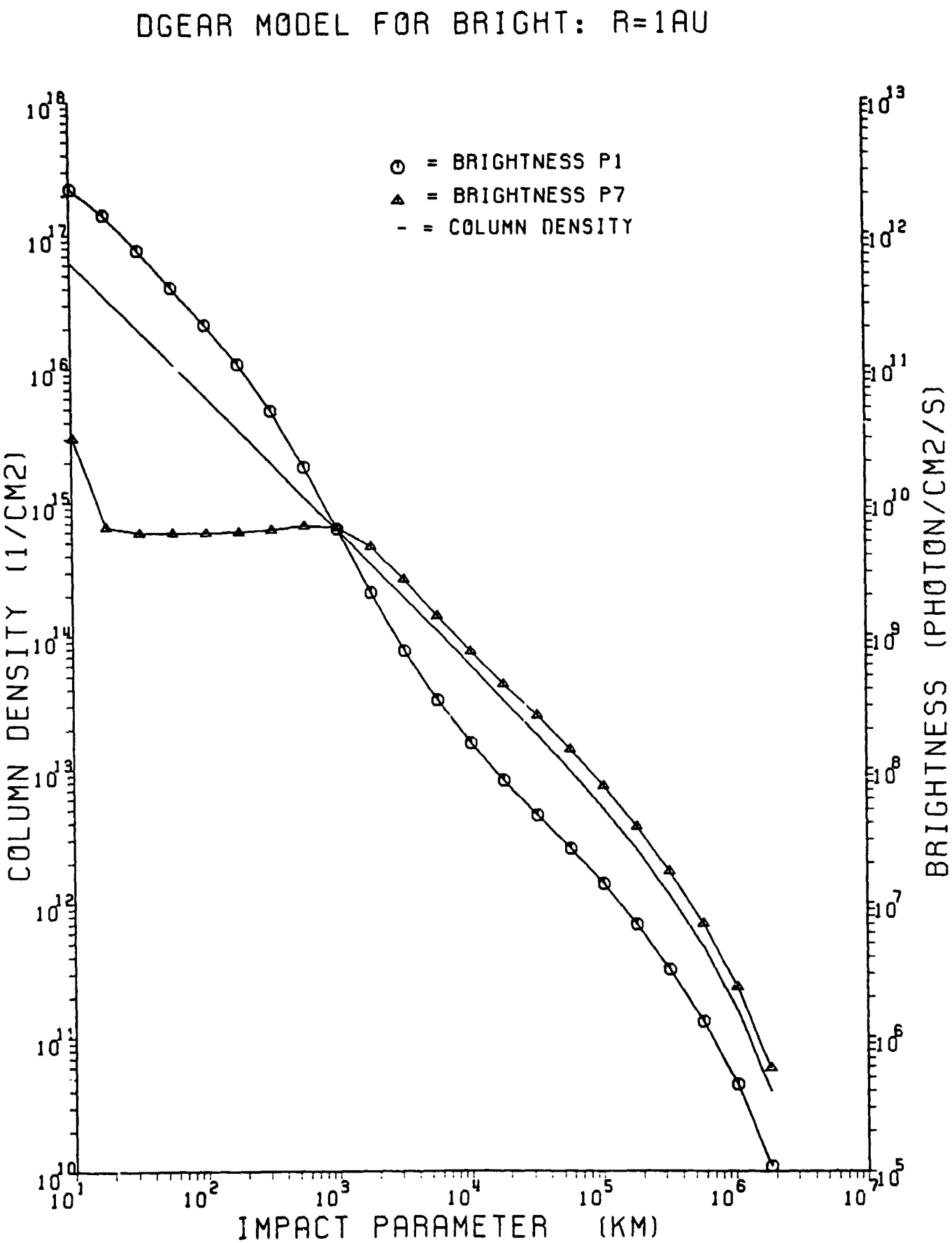

Figure IIIf.

ORIGINAL PAGE IS
OF POOR QUALITY

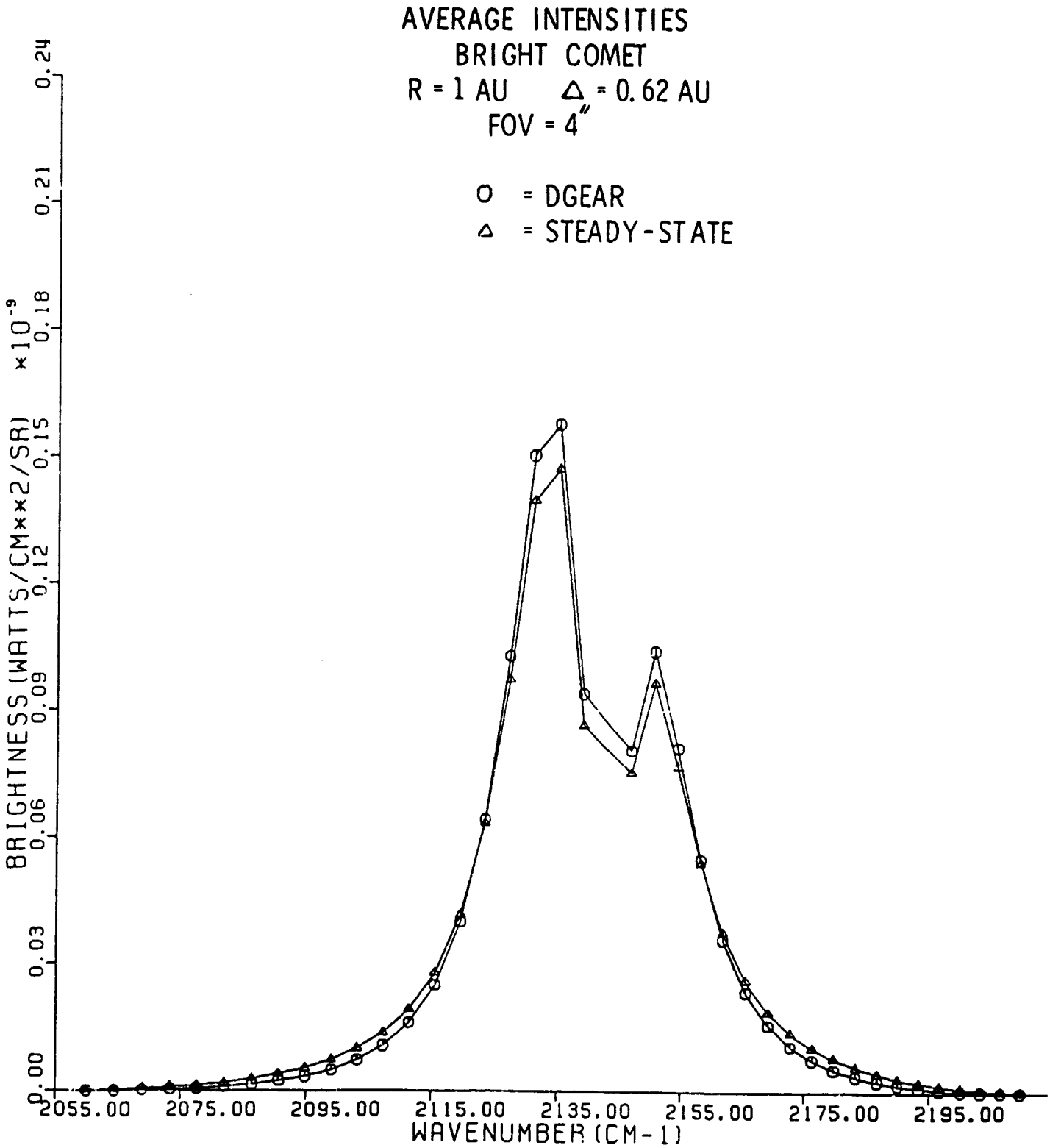

Figure IVa.

ORIGINAL PAGE IS
OF POOR QUALITY

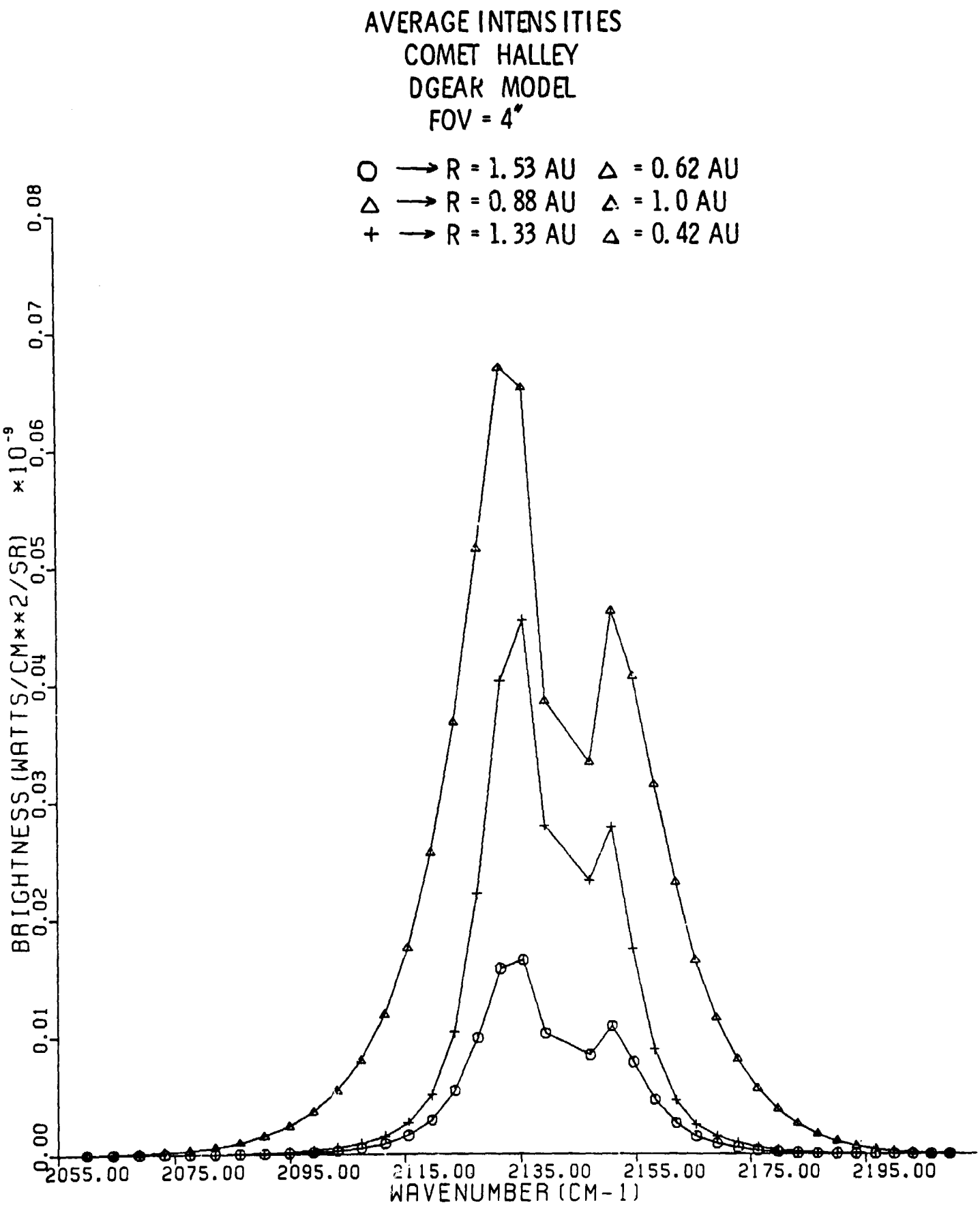

Figure IVb.

ORIGINAL PAGE IS
OF POOR QUALITY

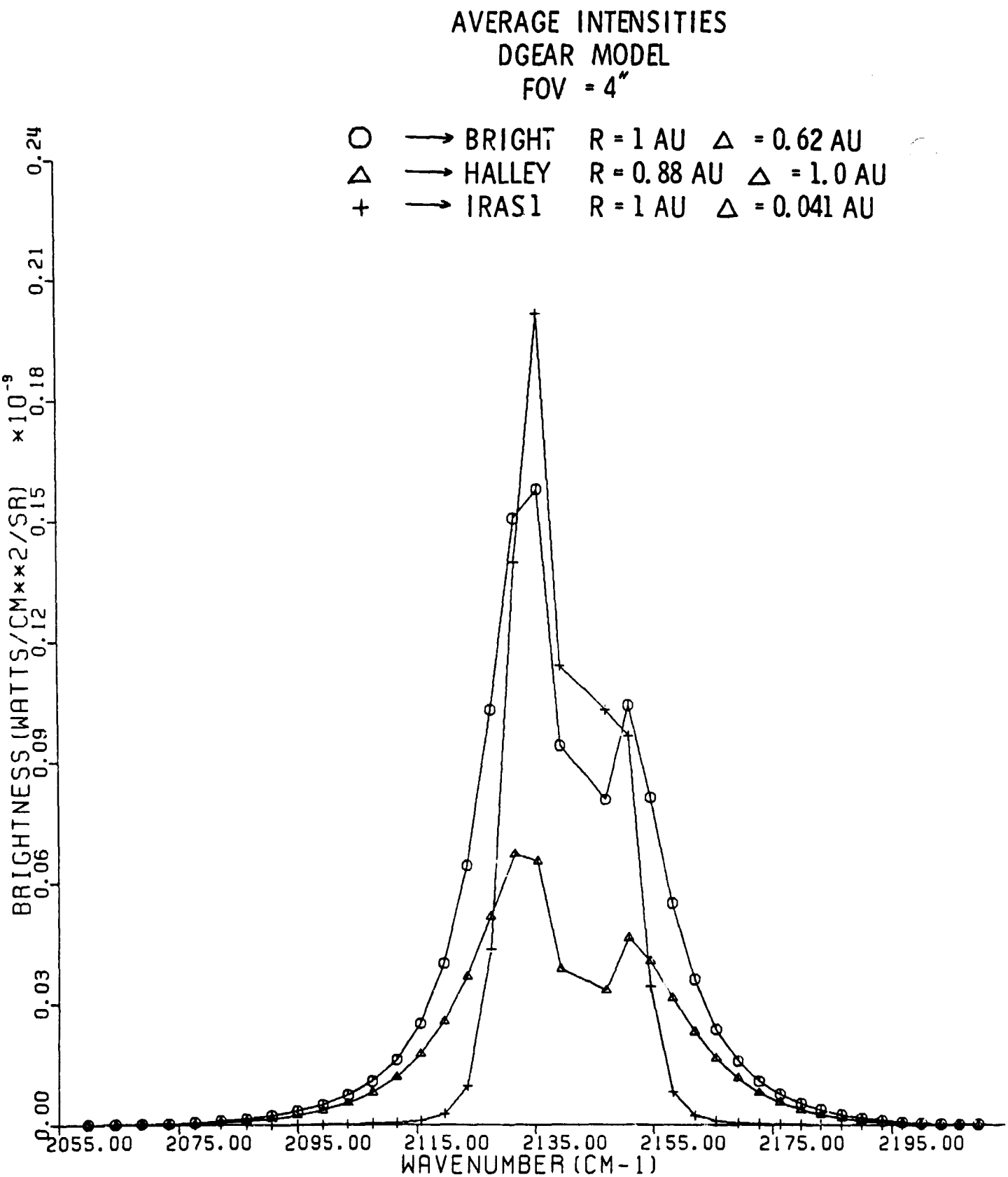

Figure IVc.

ORIGINAL PAGE IS
OF POOR QUALITY

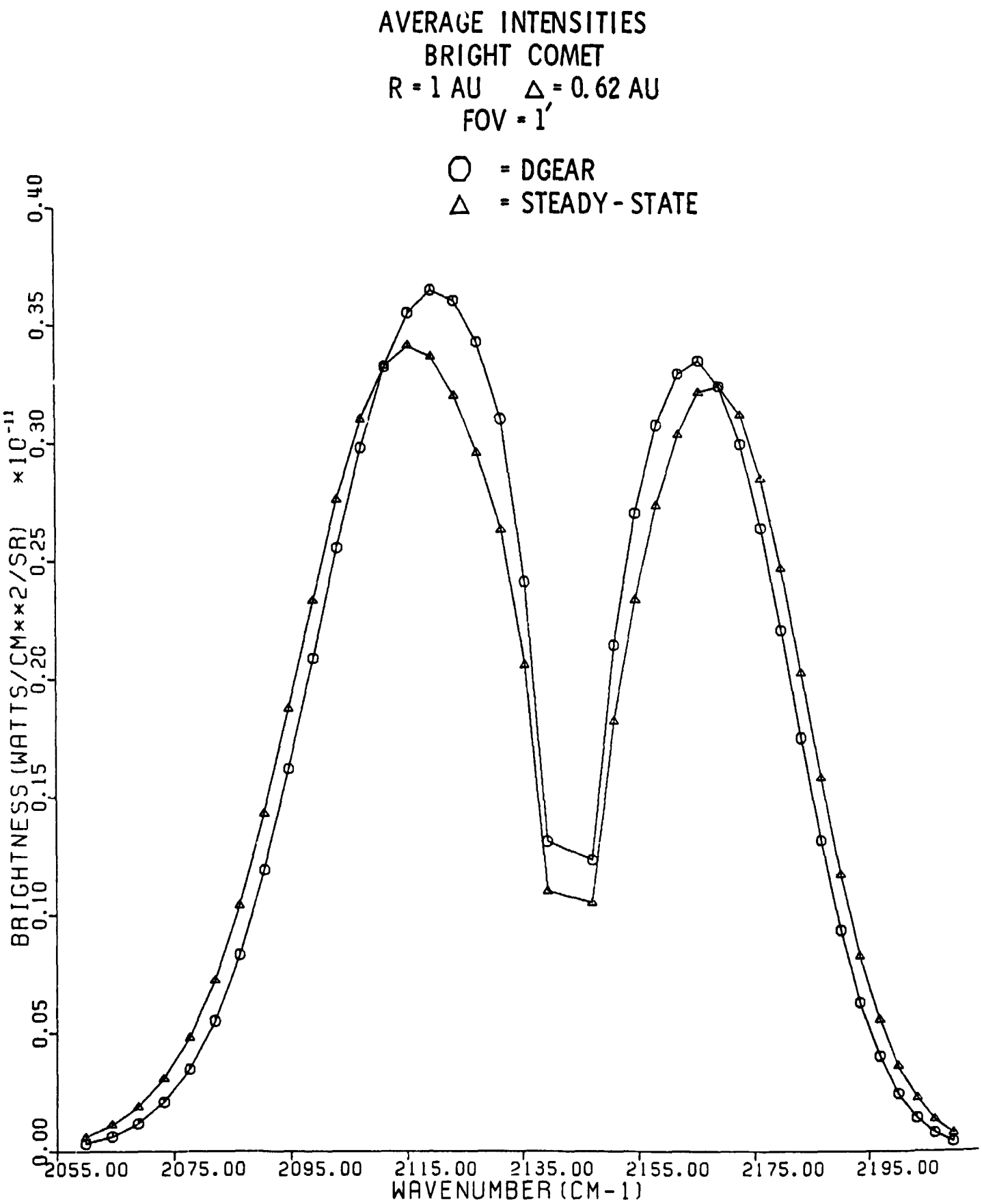

Figure IVd.

ORIGINAL PAGE IS
OF POOR QUALITY

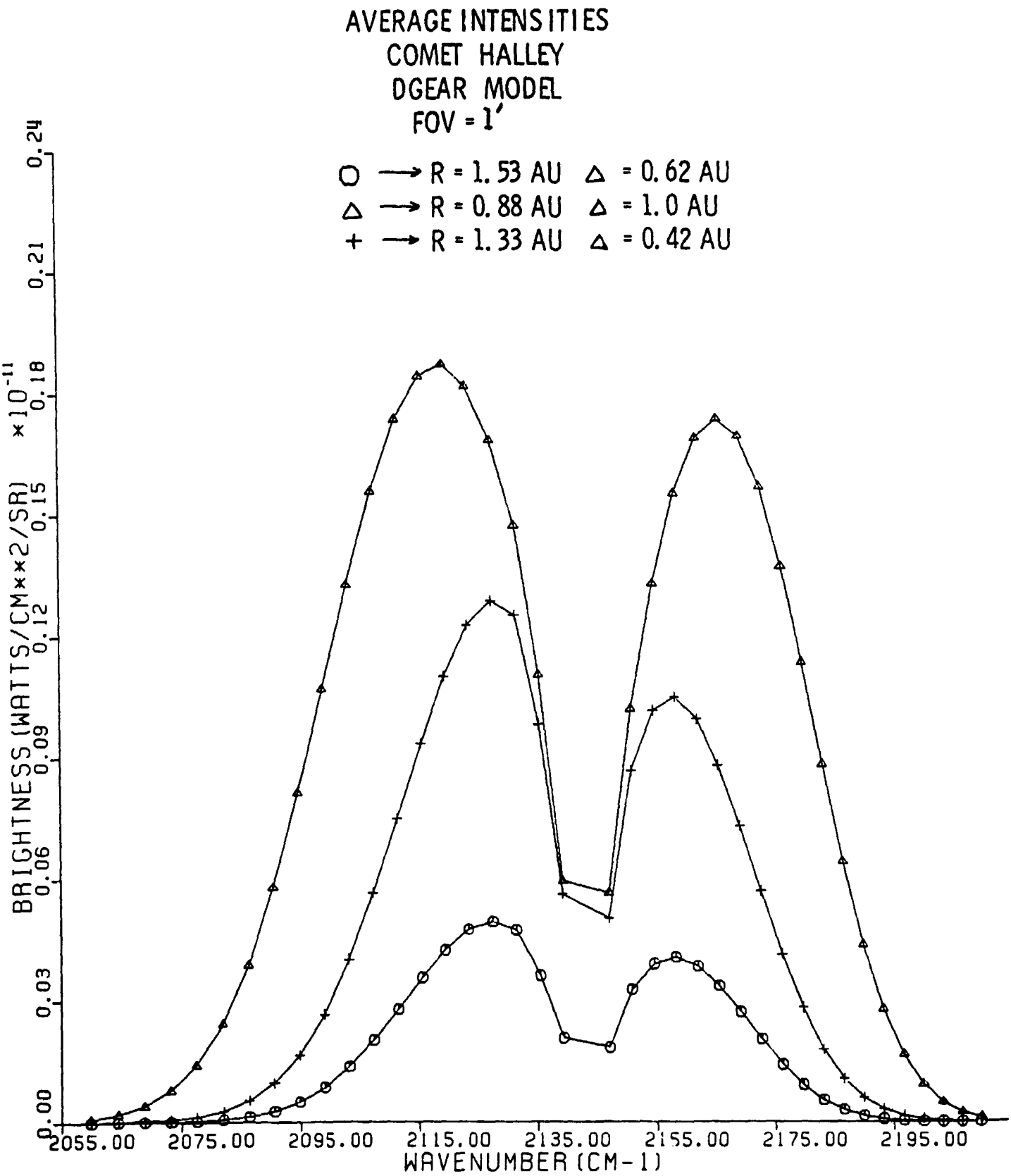

Figure IVe.

ORIGINAL PAGE IS
OF POOR QUALITY

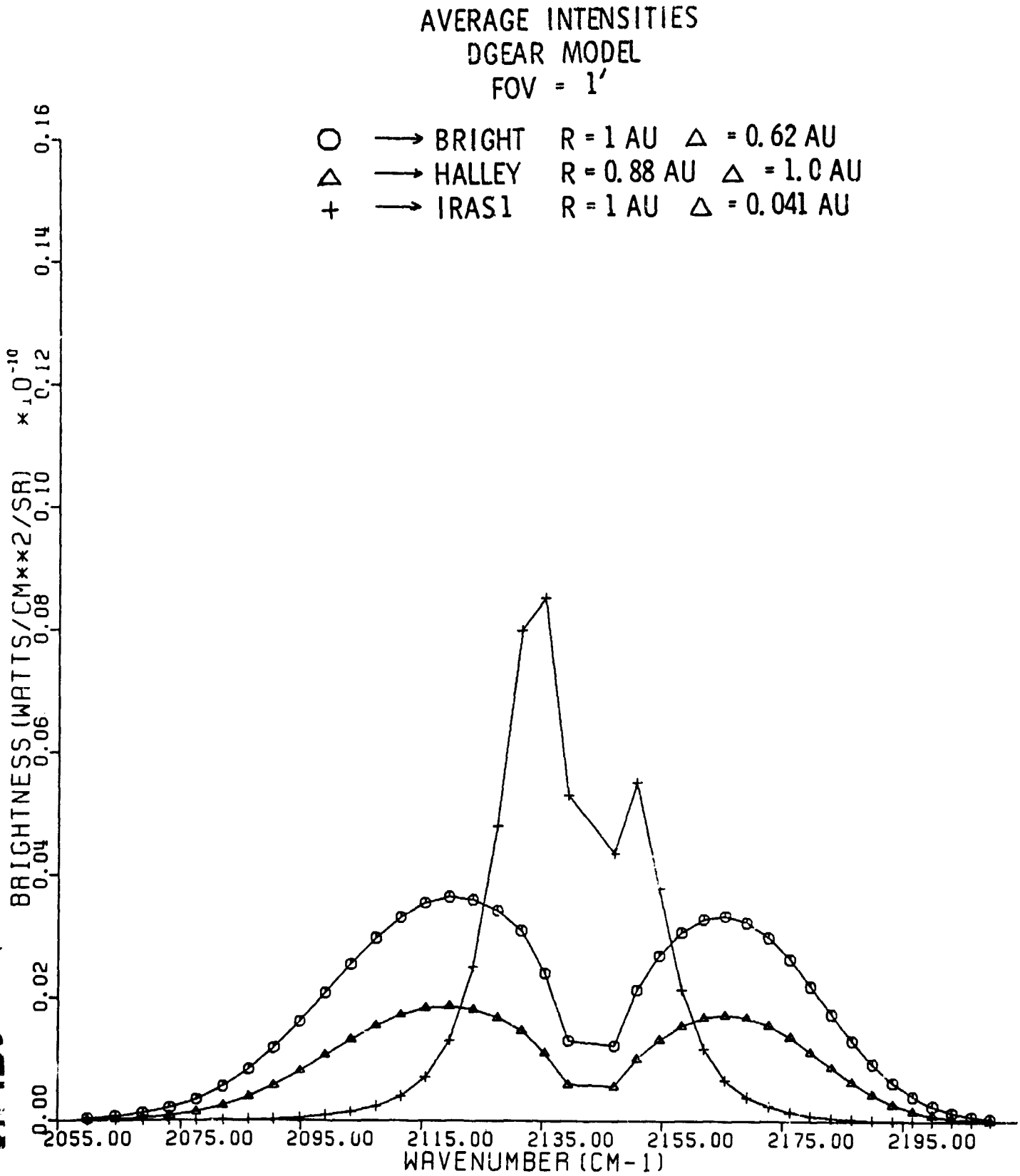

Figure IVf.

ORIGINAL PAGE IS
OF POOR QUALITY

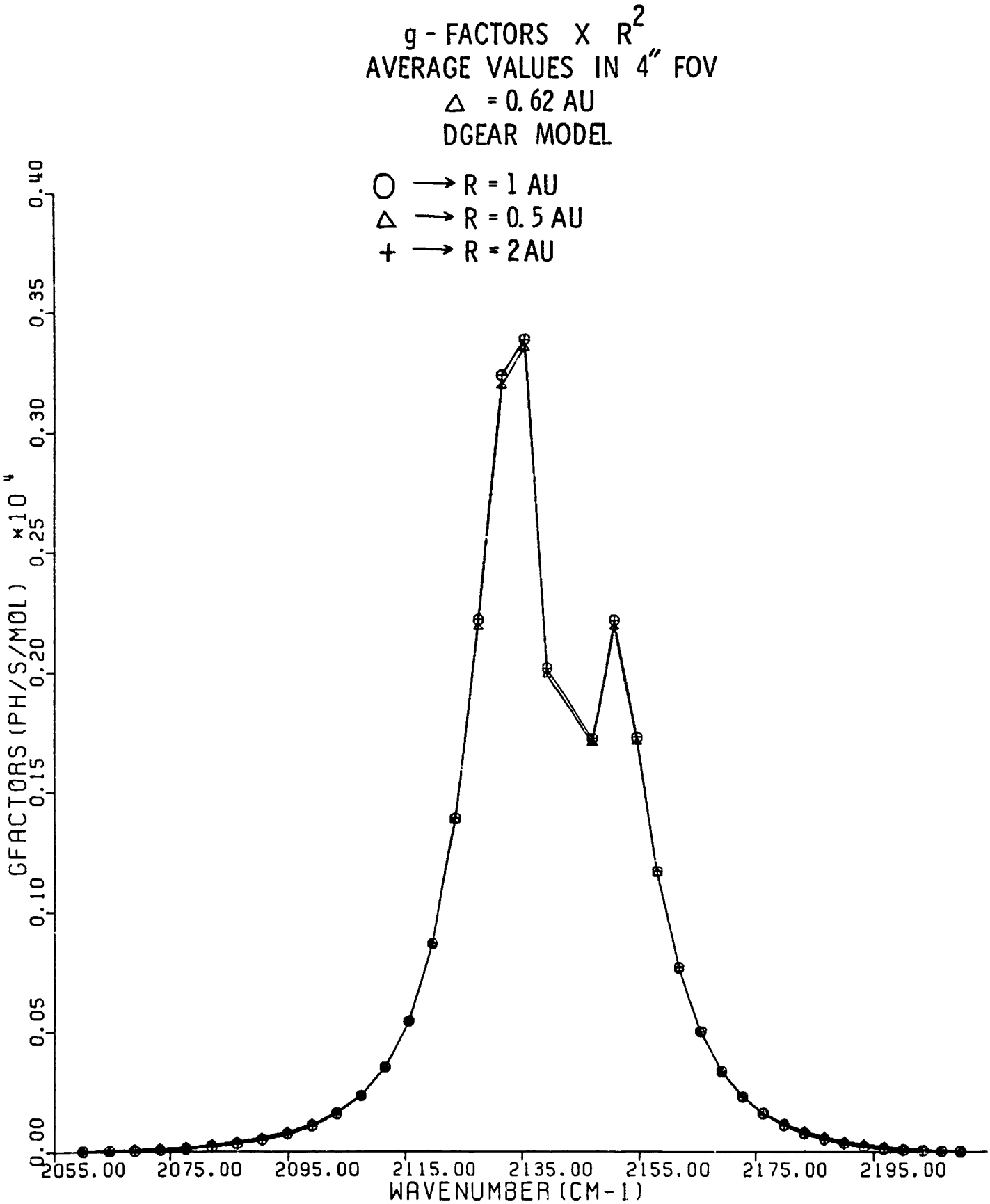

Figure IVg.

ORIGINAL PAGE IS
OF POOR QUALITY

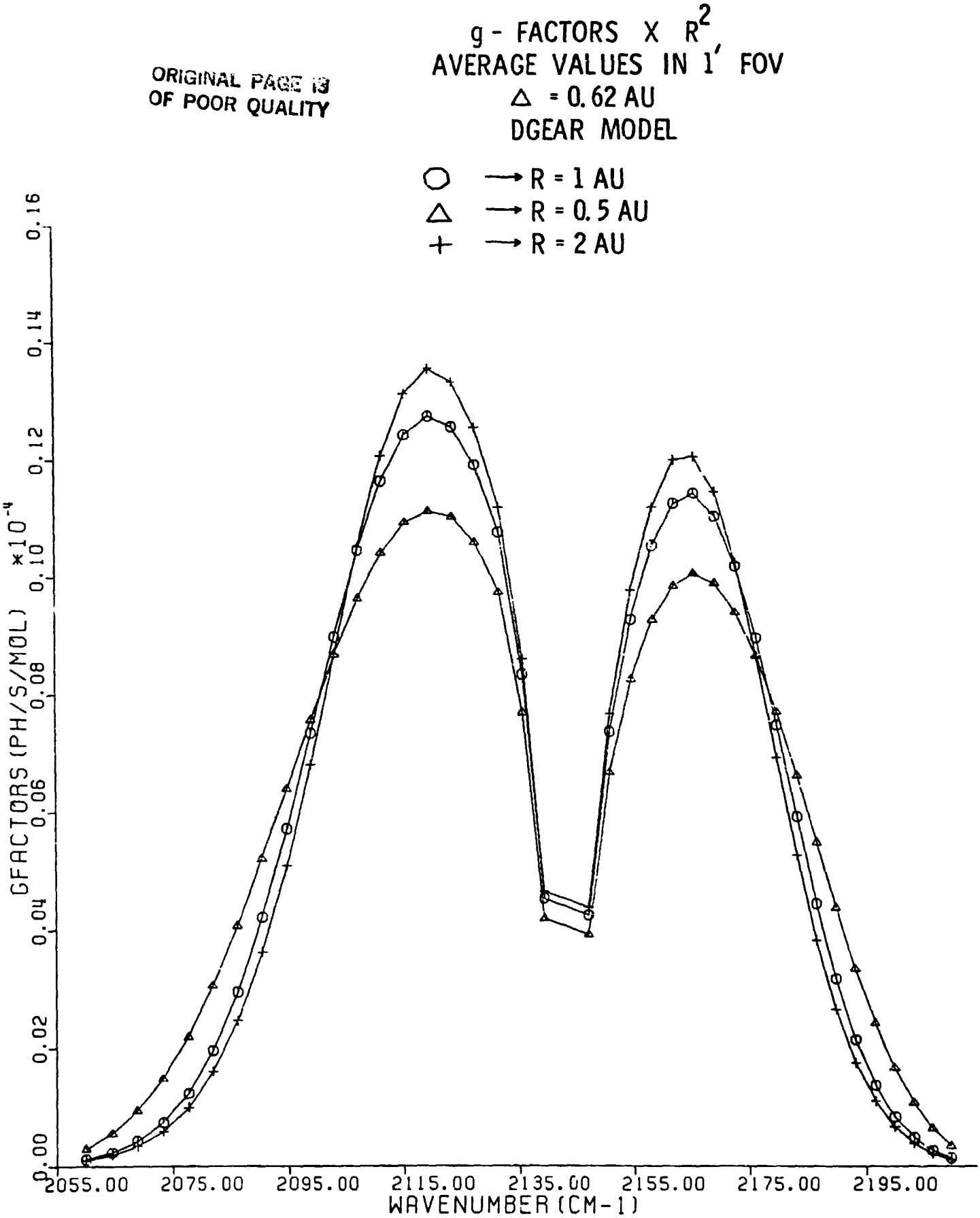

Figure IVh.